UNIVERSITAT POLITÈCNICA DE CATALUNYA BARCELONATECH

Conducting polymers and hybrid materials for technological applications

Guillem Ruano i Torres

UNIVERSITAT POLITÈCNICA DE CATALUNYA BARCELONATECH

Conducting polymers and hybrid materials for technological applications

Guillem Ruano i Torres

Thesis for the degree of Doctor from Universitat Politècnica de Catalunya

Directed by **Dr. Carlos Alemán Llansó** and **Dr. Joan Torras Costa**

Doctoral program in Polymers and Biopolymers

Barcelona, July of 2021

This thesis has been funded by the Ministerio de Ciencia e Innovación:

GRANT FOR THE RECRUITMENT OF NEW RESEARCH STAFF (FPI-BES-2016-077664)

I+D Projects: MINECO-FEDER (MAT2015-69367-R and RTI2018-098951-B-I0), and the Agència de Gestió d'Ajuts Universitaris i de Recerca (2017SGR359)

Agraïments

M'agradaria començar agraint de forma general a totes les persones que d'alguna manera o altra han contribuit a que pugui presentar aquesta tesi. Com és evident, el que s'està presentant aquí no només és fruit del meu treball, sinó que és el resultat dels esforços de moltes persones que han aportat el seu coneixement, la seva expertesa o simplement el seu suport.

Per començar m'agradaria agrair als meus dos directors de tesi, el Dr Carlos Alemán i Dr. Joan Torras per la seva ajuda a cada pas. Sense la seva guia mai hauria arribat a apendre tantes coses com les que he après en els últims quatre anys, ni molt menys podria haver elaborat i presentat una tesi com la que estic presentant avui. Al Carlos, agrair-li la seva comprensió pels meus ritmes i necessitats, i el seu inestimable coneixement i esforç, sense els quals el meu doctorat no hauria ni començat. Al Joan, agrair-li la seva paciència i ajuda pas a pas que ha permès que, tot i que m'equivoqui algunes vegades (moltes), mai deixi d'apendre.

En segon lloc, m'agradaria agrair-li a la Xènia, la meva companya, que també esta fent el doctorat. Sense ella i tota la seva ajuda, suport i estima res del que tinc avui seria possible. Moltes gràcies per ajudar-me a cada pas i donar-me suport quan no em veia capaç de continuar.

També, agraïr a la resta de professores, post-docs i companyes del grup per acollir-me i aconsellar-me. Les vostres paraules, comentaris i bromes han fet que aquests 4 anys es passin en un moment. A l'Angélica, la Georgina i la Neudys, per acollir-me i presentar-me al grup i ajudar-me als primers moments de començar el doctorat. A l'Anna i la Brenda, les dues més cracks del laboratori, per ser el suport quan no sabia on anar, la Sonia, l'Ina, la Maricarmen, la Mar, la Ludka, a en Manolo, n'Hamid, en Vitor per la seva amistat i companyerisme. Al Jordi, en Dídac,

a l'Adrian i el Marc, per totes les converses i discussions que hem tingut de ciència i de no tan ciència. Al Jordi, l'Isma, la Fio i l'Steffi, no podria haver demanat millors projectistes. A l'Elaine, el Lucho, el Jordi, la Lourdes, el Francesc, el David, la Núria i la Margarita, per tota l'ajuda prestada i fer del departament un lloc mes maco.

Finalment, i no per això menys important a tota la meva família i amics, i en especial als meus pares, Carlos i Maria Jesús, que m'han inspirat i m'han servit de guia durant tots aquests anys, al meu germà Miquel i a la Gina, pel seu suport i amor que m'han servit per seguir endavant. Al Iuri i al Diego, els meus companys de pis, per fer la vida més agradable.

A nosotros no nos dan miedo las ruinas porque llevamos un mundo nuevo en nuestros corazones. Y ese mundo está creciendo en este instante-

Buenaventura Durruti (Sindicalista i revolucionari anarquista 1986-1936)

Resum

Degut al desenvolupament de l'economia globalitzada i la industrialització, s'ha accelerat l'esgotament de recursos naturals i fonts d'energia no renovables. En els últims anys, la comunitat científica ha dedicat una gran part dels seus esforços a desenvolupar i millorar les fonts d'energia renovable. En aquest context, els capacitors electroquímics, o supercapacitors, han rebut un gran interès degut a les seves propietats i potencials aplicacions. El principal camp de treball d'aquesta tesis són els supercapacitors i les diferents parts que els constitueixen, més concretament la tesis estudia l'ús d'hidrogels en diverses funcions diferents. El treball fet a la tesis s'ha desenvolupat tant a nivel experimental com corroborat mitjançant estudis teòrics basats en la mecànica quàntica i la dinàmica molecular.

El cos principal de la tesis està dividit en 3 parts. La primera part inclou la síntesis i caracterització d'un hidrogel derivat d'una poliesteramida insaturada com a electròlit sòlid en un supercapacitor. Aquesta part consta de la caracterització electroquímica de l'hidrogel obtingut, evaluant el rendiment de l'hidrogel a l'hora d'actuar com un electròlic sòlid, així com també consta d'un estudi de difusió dels ions a través d'aquest dut a terme amb dinàmica molecular. Aquests estudis permeten obtenir les condicions òptimes per la síntesis i ús d'aquest hidrogel.

La segona part està dedicada a la preparació i caracterització d'un sistema multicapa com a elèctrode en un supercapacitor. Més concretament, es basa en la preparació d'un sistema multicapa format per PVA i el polímer conductor PEDOT, preparat mitjançant un procés capa per capa. El capítol consta tambe d'un estudi teòric de mecànica quàntica en el que s'estudia el moviment i canvis d'una monocapa de PEDOT, i permet elucidar els mecanismes i propietats electròniques que no s'havien entès completament a nivel exeprimental.

Finalment, l'última part es tracta de la preparació d'un sistema multifuncional format completament per hidrogels. El capítol comença detallant la preparació d'un elèctrode d'un supercapacitor basat en un hidrogel de PEDOT i alginat. Després de la seva caracterització com a electrode, s'exploren les altres funcionalitats que se li poden donar a aquest sistema. Es prepara un sensor de pressió reutilitzable i reciclable que permet detectar canvis de pressió linealment i amb una gran sensibilitat, i també es prepara un sistema d'alliberament controlat de fàrmacs, concretament l'alliberament controlat mitjançant estímul elèctric de curcumina.

Abstract

Depletion of natural resources and non-renewable energy sources has recently accelerated due to the development of globalized economy and industrialization. During the last years, the scientific community has devoted much of its efforts to developing and improving renewable energy sources. In this context, electrochemical capacitors, or supercapacitors, have received great interest owing to their properties and potential applications. Supercapacitors and their different components constitute the main line of work of the present thesis. More specifically the thesis investigates the use of hydrogels in various distinct functions. The work done in the thesis has been developed both experimentally and corroborated by theoretical studies based on quantum mechanics and molecular dynamics.

The main body of the thesis is divided into three parts. The first one includes the synthesis and characterization of a hydrogel derived from an unsaturated polyesteramide as a solid electrolyte in a supercapacitor. This part consists of the electrochemical characterization of the hydrogel obtained, evaluating the performance of the hydrogel when acting as a solid electrolyte, as well as a study of ion diffusion through the hydrogel carried out with molecular dynamics. These studies allow to obtain the optimal conditions for the synthesis and use of this hydrogel.

The second part is based on the preparation and characterization of a multilayer system as an electrode in a supercapacitor. More specifically, it covers the preparation of a multilayer system consisting of PVA and the conductive polymer PEDOT, prepared by a layer-by-layer process. The chapter also consists of a theoretical study of quantum mechanics in which the movement and changes of a PEDOT monolayer are studied, and allows to elucidate the mechanisms and electronic properties that had not been fully understood at the experimental level.

Finally, the third and last part incorporates the preparation of a multifunctional system consisting entirely of hydrogels. The chapter begins by detailing the preparation of an electrode of a supercapacitor based on a PEDOT hydrogel and alginate. After its characterization as an electrode, other functionalities that can be given to this system are explored. Among them, a reusable and recyclable pressure sensor is prepared to detect pressure changes linearly and with great sensitivity, as well as a controlled drug release system, in particular a controlled release by electrical stimulation of curcumin.

TABLE OF CONTENTS

Agraïments **1**

Resum **3**

Abstract **5**

List of abreviations and symbols **11**

1. Introduction **15**

1.1 Introduction **16**

1.2. Fundamentals of electrochemical capacitors **20**

1.2.1. Properties 20

1.2.2. SC performance evaluation 24

1.2.3 Electrode materials 26

1.2.4 Electrolytes 30

1.3 Hydrogels for energy applications **35**

1.4 Hydrogels as solid state electrolyte for supercapacitors **40**

1.4.1 Inorganic hydrogels as SSE for SCs 40

1.4.2 Organic hydrogels as SSE for SC 44

References 52

2. Objectives **77**

3. Results **81**

3.1 Biohydrogel from Unsaturated Polyesteramide: Synthesis, Properties and Utilization as Electrolytic Medium for Electrochemical Supercapacitors **82**

3.1.1 Summary 83

3.1.2 Introduction 84

3.1.3 Methods 86

3.1.4 Results and discussion 97

3.1.5 Conclusions 117

References 119

3.2 Doped photo-crosslinked polyesteramide hydrogel as solid electrolyte for supercapacitors **125**

3.2.1 Summary 126

3.2.2 Introduction 127
3.2.3 Methods 129
3.2.4 Results and Discussion 133
3.2.5 Conclusions 160
References 161
3.3 Electrical and Capacitive Response of Hydrogel Solid-Like Electrolytes for Supercapacitors 169
3.3.1 Summary 170
3.3.2 Introduction 171
3.3.3 Methods 174
3.3.4 Results and Discussion 178
3.3.5 Conclusions 190
References 191
3.4 Free-standing, flexible nanofeatured polymeric films as electrodes for supercapacitors 195
3.4.1 Abstract 196
3.4.2 Introduction 197
3.4.3 Methods 200
3.4.4 Results and discussion 203
3.4.5 Conclusions 213
References 214
3.5 Study on the Control of Porosity in Films of Polythiophene Derivatives 219
3.5.1 Summary 220
3.5.2 Introduction 221
3.5.3 Methods 224
3.5.4 Results and Discussion 229
3.5.5 Conclusions 247
References 248
3.6 Self-Healable and Eco-Friendly Hydrogels for Flexible Supercapacitors 255
3.6.1 Summary 256
3.6.2 Introduction 257
3.6.3 Methods 260
3.6.4 Results and discussion 264
3.6.5 Conclusion 279

References 280
3.7 Conductive, self-healable and reusable poly(3,4-ethylenedioxythiophene)-based hydrogels for highly sensitive pressure arrays 285
3.7.1 Summary 286
3.7.2 Introduction 287
3.7.3 Methods 291
3.7.4 Results and discussion 296
3.7.5 Conclusions 320
References 321
3.8 Electroresponsive Alginate-Based Hydrogel for Controlled Release of Hydrophobic Drugs 329
3.8.1 Summary 330
3.8.2 Introduction 331
3.8.3 Methods 333
3.8.4 Results and discussion 339
3.8.5 Conclusions 364
References 365
4. Conclusions 371

List of abreviations and symbols

κC	κ-carreginan
(I)CPs	(intrinsically) Conducting polymers
AA	Alginic Acid
ACP	Activated carbon powder
AFM	Atomic force microscopy
ALD	Atomic layer deposition
Alg	Alginate
ATR	Attenuated total reflection
BMSCs	Bone marrow-derived mesenchymal stem cells
CA	Chronoamperometry
CLD	Crosslinking degree
CMC	Carboxymethil cellulose sodium salt
CNF	Cellulose nanofibers
CNTs	Carbon nanotubes
CPE	Constant phase element
CS	Chitosan
CUR	Curcumine
CV	Cyclic voltammetry
DCA^-	Dicyanamide
DFT	Density functional theory
DMA	Dimethyl acetamide
DMC	Dimethyl carbonate
DMEM	Dulbecco's modified eagle medium
DMSO	Dimethyl sulfoxide
EC	Ethylene carbonate
EDC	1-[3-(dimethylamino)propyl]-3-ethylcarbodiimide methiodide
EDL	Electric double layer
EDLCs	Electrical double layer capacitors
EDS	Energy dispersive spectroscopy
EDX	Energy dispersive X-ray
EF	Electric Field
EIS	Electrochemical impedance spectroscopy
ESCs	Electrochemical supercapacitors

ESPW	Electrochemical stable potential window
ESR	Equivalent series resistance
FBS	Fetal bovine serum
FSI^-	Bis(fluorosulfonyl)imide
FTIR	Fourier transform infrared
GCD	Galvanostatic charge/discharge
GGA	Generalized gradient approximation
GO	Graphene oxide
GPEs	Gel polymer electrolytes
HD	Hydration degree
hMSC	human mesenchymal stem cells
HOMA	Harmonic oscillator model of aromaticity
ILs	Ionic liquids
ITO	Indium tin oxide
LC	Leakage current
LEA	Loss of electroactivity
LIBs	Lithium ion batteries
MD	Molecular dynamics
MSD	Mean squared displacement
MTT	[3-(4, 5-dimethylthiazol-2-yl)-2, 5-diphenyltetrazolium bromide]
NCs	Nanocrystals
NMR	Nuclear magnetic resonance
OCP	Open circuit potencial
PA	PEDOT/Alginate
PAA	Poly(acrylic acid)
PAAK	Potassium polyacrylate
PAM	Polyacrylamide
PANI	Polyaniline
PAP	PEDOT/Alginate/ PHMeDOT
PBC	Periodic boundary conditions
PBE	Perdew−Burke−Ernzerhof
PBS	Phosphate buffer saline
PC	Propylene carbonate
PDI	Polydispersion index
PEDOT	Poly(3,4-ethylenedioxythiophene)

PEEK	Poly(ether ether ketone)
PEG	Polyethylene glycol
PEGDA	Polyethyleneglycol diacrylate
PEMs	Polymer electrolyte membranes
PEO	Poly(ethyl oxide)
PGGA	Poly-γ-glutamic acid
PHMeDOT	Poly(hydroxymethyl-3,4-ethylenedioxythiophene
PMMA	Poly(methylmethacrylate)
PPy	Polypyrrole
PS	Pore size
PSS	Poly styrene sulfonate
PTh	Polythiophene
PVA	Poly(vinyl alcohol)
PVDF	Polyvinylidene fluoride
RCS	Refrigerated cooling system
RDF	Radial distribution function
RMS	Root mean squared roughness
SC	Specific capacitance
SCs	Supercapacitors
SD	Self-discharging
SE	Solid electrolyte
SEM	Scanning electron microscopy
SERS	Surface-enhanced Raman scattering
SPEs	Solid polymer electrolytes
SR	Swelling ratio
SSEs	Solid-state electrolytes
SWCNT	Single-walled carbon nanotube
TCPS	Tissue culture polystyrene
$TEABF_4$	Tetraethylammonium tetrafluoroborate
TEM	Transimision electron microscope
$TFSI^-$	Bis(trifluoromethanesulfonyl)imide
TGA	Thermogravimetric analysis
UPEA	Unsaturated polyesteramide
XRD	X ray difraction

1. Introduction

1.1 Introduction

The fast development of globalized economy and continuous worldwide industrialization over the last decades has accelerated the depletion of non-renewable energy sources (fossil fuel reserves) and, consequently, increased life-threatening environmental hazards such as greenhouse gas emissions and water pollution [1]. The increasing concern about an anthropogenic impact on global climate has therefore stimulated ongoing research in the field of renewable energy technologies. Indeed, high performance electrochemical energy storage devices such as batteries [2–4], electrochemical capacitors [5] and fuel cells are being extensively researched owing to their high efficiency, stability and environmental friendliness [6–8]. Currently, electrochemical capacitors receive considerable interest from both the scientific community and industry owing to their highly tunable properties and their potential applications, which extend for stop-start systems in hybrid vehicles, regenerating braking, cranes, etc [9]. Electrochemical capacitors, also named supercapacitors (SCs), are constituted by two non-reactive porous electrodes which are in contact with an electrolytic medium and electrically isolated through a porous separator that enables the migration of ions (see Figure 1.1). Usually, both electrodes are electrically connected to their terminals via a metallic collector.

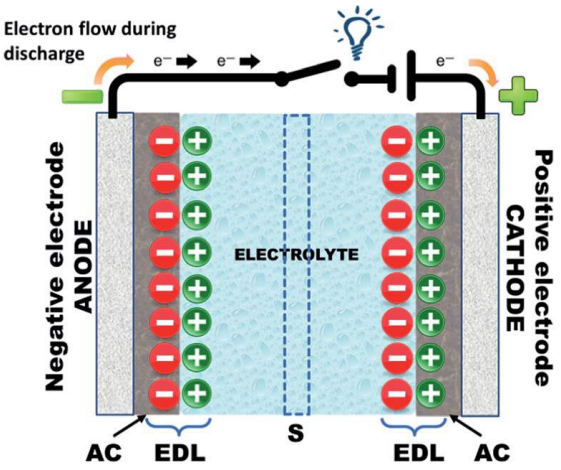

Figure 1.1 Sketch of a charged EDLC, which is a specific category of SC. AC, EDL and S refer to activated carbon, electrical double layer and separator/porous membrane, respectively [10].

SCs can be differentiated into three categories according to the charge storage mechanisms: electrical double layer capacitors (EDLCs), redox capacitors, and hybrid electrodes [5,11]. All of them include an electrolyte and an interface (electric double layer, EDL) between the electronic conductor and the ionic conductor. Typically, EDLCs storage mechanism occurs by physisorption of charges, via the formation of an EDL at the interface between the electrode and the electrolyte [12–14]. High porosity carbon allotropes, such as activated carbons [15–17], aerogel or xerogel carbons [15,16,18], carbon nanotubes [15,16,19,20] and exfoliated graphite [21], are the preferred option as EDLC electrode materials due to their high electrical conductivity, which confers high energy-density to EDLCs, but also to their price, disposal and possibility of modification. Furthermore, their high power density is achieved by the fast diffusion of ions in the electrolyte to the electrode surface. Alternatively, charge storage in redox capacitors, also known as pseudocapacitors, mainly occurs via reversible oxidation-reduction reactions with fast insertion of the electrolytes on the surface of the electrode [22–24]. Among these reactions, fast Faradaic reactions occur in or near metal oxides [15,25], conducting polymers [15,26–28], and hybrid organic-inorganic nanocomposite materials [29], which are attractive

materials for pseudocapacitor electrodes. Lastly, hybrid SCs are those which store charge through both of the aforementioned mechanisms, that is, via the formation of EDL and also Faradaic reactions.

Due to the physical nature of charge storage and discharge, SCs have multiple advantages over secondary batteries. Since SCs do not store electrical charge within the entire electrode but only at its surface, they commonly have lower energy densities compared to batteries. Nevertheless, SCs can operate at high rates and provide high specific power because the charge–discharge reaction is not limited by ionic conduction into the electrode bulk. Moreover, most of the SCs components do not contribute in redox reactions, fact that prevents electrode maintenance due to the little deterioration. SCs and batteries have some similarities in spite of the aforementioned differences. For example, the reaction takes place at the interface between electrode and electrolyte for both, and their ionic and electronic transport are physically separated [30,31]. The Ragone plot in Figure 1.2 illustrates all the described differences. As displayed, electrochemical capacitors present higher specific power (P_S > 10 kW·kg^{-1}) than batteries and fuel cells, fast charge/discharge capability (within seconds) and long cycling stability (>10^5 cycles) [32–34]. SCs cycle efficiency is high (around 95 %) throughout their complete operating voltage range, even when operating at rates above 1 kW·kg^{-1}, since the energy dissipation to heat during each cycle is relatively small and easily removed [35].

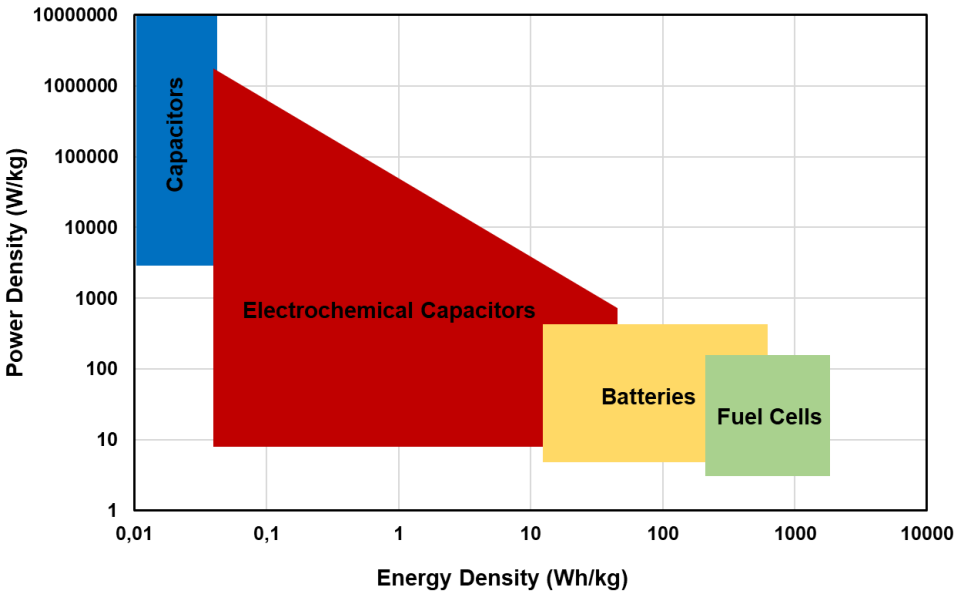

Figure 1.2 A Ragone plot comparison of power and energy densities for electrochemical capacitors, storage batteries and fuel cells.

As for the operational advantages, SCs excel at exhibiting long shelf life, operating in a wide range of temperatures, and being safe environmentally friendly. Unlike batteries, which usually will degrade and corrode if left unused on the shelf for months and, consequently, will lose their functionality, SCs are capable of maintaining the capacitance and being recharged to the original condition with almost complete voltage retention. Moreover, the operating temperature window is much higher for the SCs, with typical working temperatures ranging from -40 to 70 °C. Additionally, SCs are safer and environmentally friendlier than batteries due to the absence of hazardous and toxic materials and the ease of the material disposal. To sum up, SCs outstand among other energy storage devices owing to their life expectancy (long-term stability and cyclability, wide temperature range, use and disposal safety) and their energy efficiency (high specific power, fast reversibility, high cycle efficiency) [15,36–39].

1.2. Fundamentals of electrochemical capacitors

Many reviews have already discussed in depth the fundamentals of SCs [12,13,30,40–44], so the present work only provides an overview of them.

1.2.1. Properties

1.2.1.1. Capacitance

Briefly, SC is a special type of capacitor whose energy storage process is based on the electrostatic interactions between ions and polarized electrodes, preceded by the accumulation of the charged species (electrolyte ions) nearby the electrode surface [45], which do not get absorbed into it. As already described, this phenomenon is known as the EDL formation, where a nanometric layer of ions counterbalances the charge of the oppositely polarized electrode (see Figure 1). The described interface is usually treated as a capacitor with an electrical double-layer capacitance that depends on the specific surface area of the electrode and follows the Equation 1:

$$C = \frac{\varepsilon_0 \varepsilon_r A}{d} \qquad (1)$$

where C is the capacitance of the EDL, ε_0 is the vacuum permittivity, ε_r the relative electrolyte dielectric constant, A is the surface area of the electrode and d the effective thickness of the double layer. Concurrently, Figure 1 also shows that the entire SC could be understood as two capacitors in series, since each electrode/electrolyte interface represents a capacitor. Expressing the capacitances of the two electrodes, *i.e.* positive and negative, as C_p and C_n, respectively, the overall capacitance (C_T) of the cell can be expressed as [30,45]:

$$\frac{1}{C_T} = \frac{1}{C_p} + \frac{1}{C_n} \qquad (2)$$

For a symmetric SC, C_p is equal to C_n and therefore the overall capacitance (C_T) would be half of either one's capacitance. In the case of an asymmetric SC, that is, $C_p \neq C_n$, C_T is primarily dominated by the electrode with a smaller capacitance. The capacitance and stored charge fundamentally depend on the electrode material used. To evaluate the capacitance of an electrode material, another definition often used is the specific capacitance (C_s), with a unit of Faraday per gram ($F \cdot g^{-1}$), which follows the Equation 3:

$$C_s = \frac{C_i}{W_{em}} \qquad (3)$$

where W_{em} is the weight in grams of the electrode material in the electrode layer and C_i corresponds to the electrode capacitance (anode or cathode). Therefore, different electrode materials can be compared by means of their C_s values. The same expression can be used to define the total specific capacitance of a SC (C_{TS}), which should be the device's total capacitance (C_T) normalized by the entire weight of the device (W_{TM}, the sum weight of all elementary components including the anode, cathode, electrolyte solution, current collector and others), as follows:

$$C_{TS} = \frac{C_T}{W_{TM}} \qquad (4)$$

The specific capacitance of an electrode is the intrinsic capacitance of the material. However, it is worth mentioning that a higher specific capacitance does not necessarily imply this material to be better SC electrode material, since electrode capacitance value (C_i) can also be affected by the electrolyte solution. For example, electrode capacitance will be larger if the electrolyte solution has better contact with the electrode material, as the area of the double-layer will be increased. For this reason, the development of an electrolyte which satisfactorily fills pore areas inside the electrode material and, consequently, maximizes the

material utilization for the generation of capacitance, is crucial in order to improve the SC performance.

1.2.1.2. Energy density and power density

When the SC is charged, a voltage (V) will accumulate across the two electrodes. Equations 5 and 6 express the theoretical (or maximum) energy density (E) and power density (P) of the SC cell, respectively.[42,43,46].

$$E = \frac{1}{2} C_{TS} V^2 \qquad (5)$$

$$P = \frac{1}{4 W_{TS} R_S} V^2 \qquad (6)$$

In Eq. 6, R_S denotes the equivalent series resistance (ESR) of the SC cell. Generally, the energy density (Eq. 5) has a unit of $W \cdot h \cdot kg^{-1}$, while the power density has a unit of $W \cdot kg^{-1}$ [15,47]. These two equations evidence that V, C_{TS}, W_{TS} and R_S are all important factors that determine the SC's performance. Specifically, energy and power densities of a SC can be improved by increasing the values of both V and C_{TS} and, simultaneously, reducing the value of W_{TS} or R_S. However, since both energy and power densities are proportional to the square of the operating voltage, an increase of the latter parameter would be more efficient to the improvement of the SC's energy and power densities than increasing capacitance or reducing inner resistance. It is worth mentioning that the value of the SC voltage (V) is subjected to the electrode and electrolyte materials (*e.g.* cell voltage window is about 1 V when a carbon electrode is used for aqueous electrolytes, whereas is in the range of 3–3.5 V in organic electrolytes) and, simultaneously, the operating voltage is determined by the electrochemical stable potential window (ESPW) of the electrolyte.

1.2.1.3. Equivalent series resistance

Generally, the ESR corresponds to the sum of distinct types of resistances, including intrinsic resistance of the electrode and electrolyte materials, mass transfer resistance of the ions and contact resistance between the electrode and the current collector [42]. As indicated by Eq. 6, ESR is an important parameter that determines the SC's power density, so that a high ESR value limits the charging/discharging rate, leading to low power densities. Although an electrolyte with high ionic conductivity is suitable in order to attain a high SC's power density, the operating potential window of the electrolyte must be also taken into consideration, so there is often a trade-off between both parameters. For instance, high ion conductive electrolytes such as aqueous H_2SO_4 and KOH exhibit low operating potential windows. Oppositely, non-aqueous electrolytes such as organic and ionic liquids (ILs) often offer high operating voltages but lower ionic conductivities than aqueous electrolytes, leading to a higher ESR and, as a result, limiting the power density [48]. On account of that, the development of electrolytes with a wide operating voltage and a small ESR (high ion conductivity) is crucial to achieve both high SC energy and power density.

1.2.1.4. Cycle-life

Cycle-life or stability analysis tests of SC entail cyclic charge and discharge of the electrode in a certain electrolyte in order to compare the initial and final capacitance, and are essential to measure the overall SC performance. It is known that SC stability depends on various factors such as cell type, electrode and electrolyte materials, charging/discharging rate and operating voltage and temperature. For instance, EDLCs with carbon electrodes habitually have a very high cyclic stability [15]. Nevertheless, it is generally reduced when pseudocapacitive

reactions are introduced, since interactions between electrolyte ions and electrode materials appear.

1.2.1.5. Self-discharge rate

Summarily, self-discharge rate is related to cell potential losses of a charged electrode throughout a period of storage time [49,50], so it may limit the use of SCs for applications demanding a constant amount of energy retention over a relatively long time. Again, they are determined by the type of electrolyte used, its impurities and residual gases.

1.2.1.6. Thermal stability

The temperature-dependent performance of SCs is strongly related to the nature of its electrolyte, such as the concentration and the type of conducting salt, and particular properties of the solvent (*i.e.* viscosity, freezing and boiling points). Typically, most potential applications for SCs take place in the temperature range of -30–70 °C, so widening this range can further broaden the spectrum of applications.

1.2.2. SC performance evaluation

Overall capacitive performance of SCs can be evaluated by means of several electrochemical techniques, being cyclic voltammetry (CV), galvanostatic charge discharge (GCD) and electrochemical impedance spectroscopy (EIS) the most common ones [51]. They are habitually used complementarily, since only a correlation between different techniques can provide a comprehensive insight into the reactions and processes taking place in the EDL [30,43,52].

1.2.2.1 Cyclic voltammetry

CV is performed in two or three electrode cell configuration. Usually, three electrode configurations are used to calculate the electrode capacitance as only one of the electrodes, the working electrode, contains the materials being analyzed. [51,53,54]. Two electrode configurations habitually study the whole packaged SC capacitive performance, with the measurements being conducted between both electrodes containing the analyzed materials [30,53].

1.2.2.2 Galvanostatic charge discharge

GCD is one of the most accepted methods in the industry to determine the capacitance of the whole SC [55]. Nevertheless, GCD measurements can be used either to calculate the capacitive performance of a single electrode, with a three electrode configuration, or of the packaged SC with a two-electrode configuration [53,54,56,57]

1.2.2.3 Electrochemical impedance spectroscopy

EIS is habitually conducted by applying an small amplitude of interrupting potential over a wide range of frequency (f) while the impedance data (|Z|) is being collected [30,58,59]. This experiment can show insights into the relationship between the imaginary part of the impedance and the frequency. It is arguably one of the most complex and sophisticated techniques to study the SC capacitance, which can be calculated through the Bode plot (log (|Z|)vs log (f)) or the Nyquist plot, where the imaginary part of the impedance Z(f)'' is represented against the real part Z(f)' [30,60].

1.2.3 Electrode materials

Electrode materials and electrolyte are the key elements of SCs. As already explained, charge storage and capacitance of a SC are closely related to the electrode–electrolyte interaction, their properties and their morphology [23,61]. The development of new capacitive devices must take into account the role of efficient charging of the electrode/electrolyte interface [12]. In this sense, most researchers focus on the surface area of the electrode to improve the overall SC capacitance. Even though a higher specific accessible area gives a higher capacitance to the SC, the most influential parameter is the electrochemical active surface area. Regarding this, the pore size of the electrode material, or more precisely, the pore size–pore distribution for a given specific area plays a major role in the SC. Nevertheless, improvement that can be made tuning the electrode morphology is limited by the intrinsic electronic properties of the material [45,62]. In general, electrode materials in a SC can be classified into three main groups: carbon materials, conducting polymers and metal oxides.

1.2.3.1 Carbon materials

Carbon materials are one of the most intensively researched materials [61]. Their high abundance, low cost, easy processing, non-toxicity, high specific area, high stability and wide operating temperature range make them really interesting industrywide. Carbon based SC are similar to EDLC, so that charge storage occurs in the interface between the electrode and the electrolyte. This means that the capacitance of such a SC depends mainly on the surface area accessible to the electrolyte ions and on the pore size distribution, and to a lesser extent on the pore shape and structure, electrical conductivity and surface functionality. Activated carbon [63–65], carbon nanotubes (CNTs) [13,19,28,46,66,67], graphene [31,68–71], carbide-derived carbons [72,73], carbon aerogels [16,18], carbon nanofibres [32,39,74,75] and

templated nanoporous carbons [76–79] are the main types of enhanced surface area carbon materials, and their performance has been extensively described in literature [80]. In terms of specific power and cycle-life, high surface carbon materials with porous structures appear to be optimal materials for SCs, but a reduction of their performance results unavoidable owing to the high internal series resistance caused by the contact resistance between carbon particles [39]. Moreover, capacitance performance of carbon materials is limited due to the surface area inaccessible to electrolyte ions [81] (*e.g.* capacitance values of only 40–160 $F \cdot g^{-1}$ for both activated carbon and carbon aerogels [82] and 10–35 $F \cdot g^{-1}$ for CNTs [83]). The development of carbon electrodes with higher specific surface area, rational pore distribution and moderate surface modification with the aim to reach a compromise between an optimized capacitance and conductivity and electrode stability will be a future research area.

1.2.3.2 Conducting polymers

Since pseudocapacitance values can be 10–100 times greater than the capacitance achieved from an EDL, SCs composed of redox-active materials bearing pseudocapacitance are highly attractive as the next generation of SC. They not only accumulate charge in the double layer, but also undergo fast and reversible surface redox reactions (faradaic reactions). For this reason, efforts dedicated to develop electrode materials with pseudocapacitance have grown considerably in recent years. These materials are commonly divided into two types, briefly described in this report: conducting polymers (CPs) and electroactive metal oxides/hydroxides.

Since the 1980s, the chance to synthesize new CPs with improved and specific properties began to attract the attention of researchers for a wide variety of applications, mainly in the energy applications field [84–86]. CPs are considered as the "*fourth generation of polymeric materials"*, as designated by Prof. Bengt Rånby

in 1991 [86]. The two prerequisites for a polymer to be conducting are: the presence of double bond (π) conjugations along its backbone chain, creating electron delocalization, and the presence of charge carriers (electrons or holes), also known as doping. Such doping induces these carriers into the electronic structure and, consequently, leads to carrier delocalization and charge carrier mobility into three dimensions through interchain electron transfer. The control of the electrical conductivity can be accomplished either by chemical or electrochemical doping [86]. The doping process causes simultaneously a change in the Fermi level (electrochemical potential) through the chemical reaction (redox or acid-base) to a region with a high density of electronic states. Therefore, the electrical conductivity arises from these two phenomena: the creation of carriers through the doping process and the electron delocalization of the backbone chain, which allows these carriers to move three dimensionally. The doping process can induce either a reduced state or n-type doping, or an oxidized state, also known as p-type doping [86].

Several characteristics of CPs make them ideal candidates for SCs electrode materials: low environmental impact, conductivity in the doped state and high voltage window and storage capacity achieved through the redox reaction. Oxidation makes ions move to the polymer backbone and reduction releases those ions into the electrolyte. This reaction takes place not only on the surface but in the entire polymer bulk [87].

Polyaniline (PANI) [28,88,89], polypyrrole (PPy) [28,90–92], poly(3,4-ethylenedioxythiophene) (PEDOT) [56,93–96] and other polythiophene (PTh) derivatives are the most habitual CPs used in SCs. Three configurations of SCs with CPs electrodes are possible [27,58,88,91,97]. Type I is a symmetric SC and both of its electrodes consist on the same p-dopable polymer, one electrode being in the charged state and the other in the uncharged state. Type II is an asymmetric SC

where two different p-dopable polymers are arranged, and Type III is a symmetric type in which the polymer used can be p-doped but also n-doped.

1.2.3.3 Metal oxides

As CPs, metal oxides not only store charge in the EDL but also undergo fast electrochemical faradaic reactions within appropriate potential windows [98]. Therefore, they can provide higher energy density for SC than conventional carbon materials and are electrochemically more stable than polymer materials. As SC's electrode material, metal oxides should meet the following prerequisites: (1) the metal oxide should exhibit electronic conductivity, (2) it presents two or more oxidation states which coexist over a continuous range with no irreversible modifications of the 3-dimensional structure associated with phase changes, and (3) the material allows free intercalation of the protons into its oxide lattice on reduction (and proton releasing on oxidation), enabling facile interconversion of $O^{2-} \leftrightarrow OH^{-}$. Among the used materials, ruthenium oxide has been, to date, the most extensively investigated candidate owing to multiple advantageous properties, including its wide potential window, highly reversible redox reactions, three different oxidation states attainable within a 1.2 V voltage window, high proton conductivity and specific capacitance, long cycle life, good thermal stability and high rate capability [99–101]. Nevertheless, utilization of RuO_2 is limited due to its high cost. Comprehensive research has been conducted in order to reduce Ru usage, and the synthesis of Ru-based composites by combining base metal oxides (*e.g.* MnO_2, NiO, etcetera) with ruthenium oxide [58,102–104], or employing directly other metal oxides are two approaches widely demonstrated in literature. Among these other oxides, manganese, cobalt, nickel and vanadium oxides have been the most investigated ones and, to a lesser extent, iron and tin oxides.

1.2.4 Electrolytes

As stated before and as depicted in Fig. 1.1, the electrolyte is an essential constituent in SCs which resides inside the separator and plays a key role providing ionic conductivity and thus enhancing charge balance on each cell electrode [105]. Constituted by an electrolyte salt dissolved in a solvent, the electrolyte is a crucial component in the EDL formation (in EDLCs) and in the reversible redox processes for the charge storage (in pseudocapacitors), thus determining the SC performance [106]. Indeed, cell performance is influenced by multiple factors of the electrolyte nature, including (a) the type and size of the ions, (b) the ion concentration, (c) the ion–solvent interaction, (d) the electrolyte–electrode interaction and (e) the potential window. Generally, the requirements for an ideal electrolyte are: wide voltage window, high chemical and electrochemical stability, high ionic conductivity and low solvated ionic radius, high chemical and electrochemical inertness to SC components (*e.g.* electrodes, current collectors and packaging), wide operating temperature range, low resistivity and viscosity, low volatility and flammability, environmentally friendly and low cost [30,43]. The choice of a proper electrolyte is fundamental to obtain a safe and high performance SC device. Nevertheless, there is no electrolyte meeting all of these requirements to date, so each one has its own advantages and drawbacks. In general, different types of electrolytes have been developed and reported in literature, and a general accepted classification is shown in Figure 1.3.

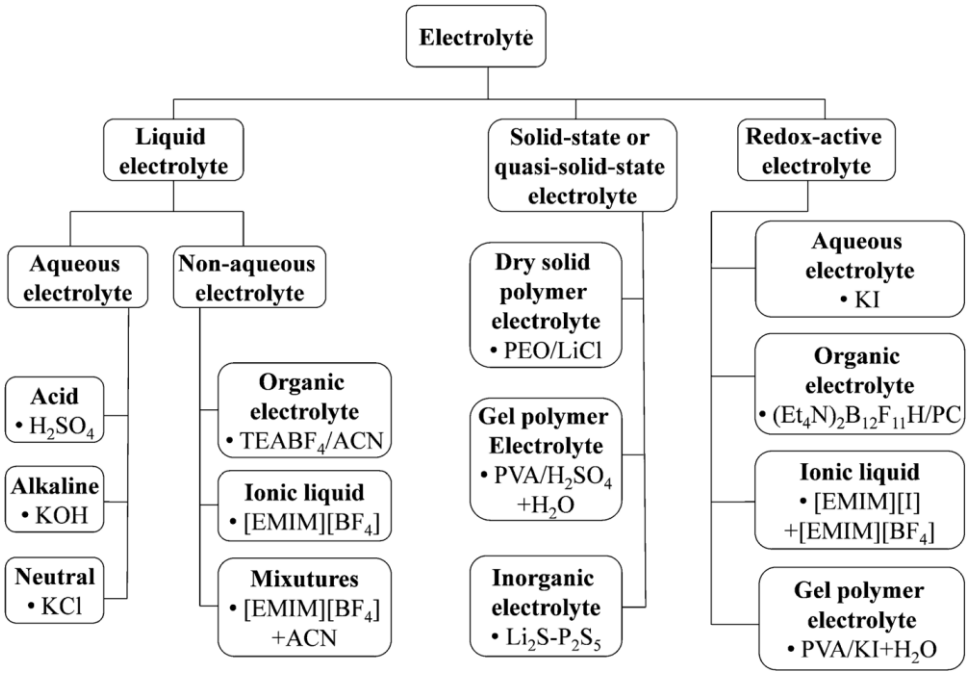

Figure 1.3 Electrolyte classification for electrochemical capacitors [43].

1.2.4.1 Liquid Aqueous electrolytes

Aqueous electrolytes have been used considerably in research and development due to their low cost, their simple fabrication and assembly processes, and their easy handing in the laboratory as compared to organic electrolytes and ILs, which require special purification procedures. Aqueous electrolytes (such as H_2SO_4, KOH, Na_2SO_4, NaOH, etc) [107] exhibit higher ionic conductivities than their organic counterparts, which lowers the ESR and leads to better power delivery of SCs [108]. The criteria followed for the electrolyte selection must take into account not only the size and mobility of the hydrated ion, but also how they influence the ionic conductivity and the specific capacitance of the SC. Unfortunately, the narrow voltage window (ESPW, typically of 1.2V) [109] of aqueous electrolytes constitutes a large disadvantage, and for this reason most commercial SCs use organic electrolytes instead of aqueous ones. In general, aqueous electrolytes can be divided into acid, alkaline and neutral solutions, in which H_2SO_4 [110], KOH [111] and Na_2SO_4 [112] are representatives and also the most frequently used ones,

respectively. Other commonly used aqueous electrolytes are KOH [113], NaOH, LiOH, $(NH_4)_2SO_4$, K_2SO_4, Li_2SO_4, $MgSO_4$, $CaSO_4$, KCl, NaCl, LiCl, $CaCl_2$, KNO_3, $LiNO_3$, $Na(CH_3COO)$, $Mg(CH_3COO)_2$, Na_2HPO_4, $NaHCO_3$ and $Na_2B_4O_7$ [114].

1.2.4.2 Liquid Organic electrolytes

Organic electrolytes for SCs are usually constituted by a conducting salt dissolved in an organic solvent. Organic electrolyte-based SCs are commercially available and currently prevailing in the commercial market due to their high operating potential window, habitually in the range of 2.5 to 2.8V [43]. Similar to aqueous electrolyte-based SCs, the performance of the organic electrolyte-based SCs is strongly dependent on the nature of the solvents and salts, the ion size and ion-solvent interaction, the viscosity of the solvent, the conductivity and the ESPW. The increased operation cell voltage can yield an improvement in both the energy and power densities, and cheaper materials (*e.g.,* Al) can be used for the current collectors and packages when employing organic electrolytes. However, due to their large size molecules, organic electrolytes display higher resistivity, smaller capacitance and lower conductivity than aqueous electrolytes. Furthermore, they are usually more expensive and exhibit safety concerns related to the flammability, volatility and toxicity. Unlike aqueous solvents, organic electrolytes require complicated purification and assembling steps in order to remove any residual impurities (*e.g.,* water) that can cause severe self-discharge issues and performance degradation [115]. Typical organic electrolytes for the commercial EDLCs consist of a conductive salt such as tetraethylammonium tetrafluoroborate ($TEABF_4$) dissolved in acetonitrile or propylene carbonate, the most commonly used solvents [30].

1.2.4.3 Ionic Liquid electrolytes

ILs are salts constituted exclusively by cations and anions (organic cations and organic/inorganic anions) with a melting point below 100 °C [116]. The ions that compose ILs or molten salts, which are usually large and asymmetric, are the main contribution to the low melting point [117] and their combination results in unique structures and properties that make them significantly interesting as alternative electrolytes for SCs [118]. These properties include low vapor pressure, high thermal, chemical and electrochemical stability, negligible volatility, low flammability and wide voltage window (>3 V) [117,119–121]. Both physical and chemical properties of ILs can be tuned easily owing to the large diversity of cation/anion combinations [117,122]. Therefore, SCs performance can be improved by optimizing or customizing ILs composition [123,124]. Regarding their composition, ILs can be classified as aprotic, protic and zwitterionc types [117]. Whereas aprotic ILs are the perfect candidates for SCs applications, protic and zwitterionic ILs are suitable for fuel cells and membranes, respectively [117]. The main ILs studied for SCs applications are based on imidazolium, pyrrolidinium, ammonium, sulfonium and phosphonium cations, and tetrafluoroborate (BF_4^-), hexafluorophosphate (PF_6^-), bis(trifluoromethanesulfonyl)imide ($TFSI^-$), bis(fluorosulfonyl)imide (FSI^-), and dicyanamide (DCA^-) anions [108,125]. Generally, imidazolium-based ILs yield higher ionic conductivity, but larger ESPWs are achieved with pyrrolidinium-based ILs. In fact, there is a trade-off between the ionic conductivity and the ESPW of ILs. Although solvent-free IL-based SCs avoid the safety issues associated with commercially employed organic solvents, such as their volatile and flammable nature, their commercial use can be restricted by their high viscosity, low ionic conductivity and high cost [126–129]. For this reason, considerable efforts have been undertaken to improve ILs performance. The selection of IL composition and design of the cell has been optimized by means of both experimental and

theoretical understanding [130–132], and useful reviews have been published establishing insights into the electrochemical and capacitive behavior of the EDL at the IL/electrode interface [133–135].

1.2.4.4 Solid State Electrolytes

Solid-state electrolytes (SSEs) exhibit multiple advantages over other electrolytes, but the major ones are a manageable packaging and fabrication processes of SCs and liquid-leakage free [136]. SSEs play not only the ionic conducting media role, but also the electrode separator role. To date, SSEs engineered for SCs have been focused on polymer electrolytes, and only a few works have based their research on inorganic solid materials (*e.g.,* ceramic electrolytes [136,137]). The polymer-based SSEs can be further classified into three groups: dry polymer electrolytes (also known as solid polymer electrolytes, SPEs), polyelectrolytes and gel-polymer electrolytes (GPEs).

Dry polymer-based electrolytes have a limited usage as SSEs. Generally, dry polymer electrolytes are composed of a polymer and a salt, with no presence of solvents. They have low ionic conductivities due to the hampered salt movement through the polymer. Nevertheless, dry polymer electrolytes have excellent mechanical strength and a wide operative temperature range [138]. Similar to dry polymer electrolytes, polyelectrolytes are composed of a polymer and a salt but, alternatively, their ionic conductivity is provided by the charged polymer chains. Regardless, both types of SSE end up with similar issues that must be addressed: low ionic conductivity and limited contact surface area between electrode materials (especially for the nanoporous materials) and SSE.

Gel polymer electrolytes arose to partially overcome these limitations. In contrast to dry polymer and polyelectrolyte electrolytes, GPEs consist of a polymer host (*e.g.,* PVA, PEG, PEO, etc) and a conducting salt dissolved in a solvent or an

aqueous electrolyte (*e.g.,* H_2SO_4, KOH, K_2SO_4, etc) [139]. Due to the presence of a liquid phase in them, GPEs are also known as quasi-solid state electrolytes [140,141]. In GPEs, the solvent that swells the polymeric matrix allows rapid ionic transport, conferring them the highest ionic conductivity among the three types of SSEs. For this reason, GPEs are the most used and reported ones, currently dominating the SC market. When water is used as the solvent, the prepared gel is called hydrogel, and water is usually trapped in the polymer matrix through surface tension [142]. To achieve an efficient electrochemical performance, the interaction between the electrode and the hydrogel must be favourable. In spite of this, it is worth mentioning that the presence of water as a solvent in GPEs can cause them relatively poor mechanical strength, as well as a narrow operative temperature range. Multiple polymeric hosts have been investigated and reported to prepare GPEs, such as poly(acrylic acid) (PAA), poly(vinyl alcohol) (PVA), poly(ethyl oxide) (PEO), potassium polyacrylate (PAAK), poly(ether ether ketone) (PEEK), poly(methylmethacrylate) (PMMA), among others. GPEs can be further classified regarding the solvent used to enhance ionic transport. In organogels an organic solvent such as ethylene carbonate (EC), dimethyl carbonate (DMC) or propylene carbonate (PC) swells the polymer host and, similarly to organic liquid electrolytes, organogels exhibit a large working cell voltage [143–147]. Ionogels are prepared with the incorporation of an IL to the polymer host matrix in order to profit the large ESPW and thermal stability of IL and, simultaneously, safety and fabrication processes of a GPE [148,149].

1.3 Hydrogels for energy applications

The interest for gel polymer electrolyte-based SCs has remarkably increased in recent years due to the rapid growth of power demand for wearable electronics,

portable electronics, microelectronics, pintable electronics and particularly flexible electronic devices [150–153]. GPEs can provide SCs with enough flexibility to develop bendable structures and tunable shapes for multiple functionalities, such as roll-up displays or smart mobile devices, among others [154–161]. Moreover, the rapid development of biomedical devices, such as drug delivery systems [162–165], molecular actuators [166–168] or even soft robotics [169], have pointed out the necessity of biocompatible devices to power such applications. In this sense, hydrogels represent the most promising and sustainingly desirable alternative among GPEs since water can be replaced for organic solvents and other hazardous reagents, simplifying the processing and assembling steps, as well as substantially minimizing the device cost. Hydrogels have been widely studied and applied as electrolytes in energy storage devices, and the large number of publications in this field reveals their increasing importance in recent years. Indeed, different types of hydrogels have been extensively reported due to their outstanding electrochemical capabilities, which will be overviewed in the next section [43,114,142]. This chapter will first provide an outline of the characteristics of hydrogels, especially of the beneficial features for their successful application in the energy storage field.

As stated before, hydrogels mainly consist of a cross-linked polymeric network with abundant hydrophilic groups in its backbone chains that is able to trap water by the effect of surface tension, so that they exhibit properties ranging from soft to hard and tough. The presence of physical interactions or chemical cross-linkages induces the formation of a three-dimensional network that can be swollen in water without being dissolved, so hydrogels usually contain large amounts of water while maintaining their shape [170,171]. As illustrated in Fig 1.4, hydrogels with physical crosslinking are different from those in which the crosslinking is chemical in the type of established bond, but also in network formation mechanics that induces changes in the rigidity and elastic moduli. In physical hydrogels, polymer helices

stabilize the network through the formation of junction zones wherein typical non-covalent interactions such as physical entanglements, electrostatic charges and hydrogen bonding play crucial roles in the hydrogel formation. Contrarily, cross-linkages in chemical hydrogels are established between the polymer and the crosslinking agent and have a covalent nature, which provide them with enhanced mechanical stability. Chemical crosslinking methods include radical polymerization, high-energy irradiation, chemical reaction of complementary groups and the use of other functional crosslinking agents.

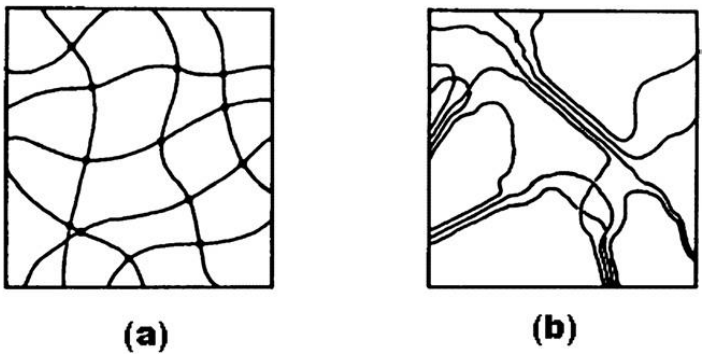

Figure 1.4 Schematic diagram of (a) a chemical hydrogel with point cross-links and (b) a physical hydrogel with multiple-junction zones. In (a) the solid lines represent polymer chains that constitute the hydrogel matrix. The solid dots in the cross-link points of the polymer helices represent the cross-links formed by chemical reaction between the polymer such as PVA and a cross-linking reagent such as glutaraldehyde. In (b) the solid lines represent the polymer helices aligning themselves literally in extended junction zones [142].

There are several useful classifications for hydrogels regarding different aspects of their composition. Based on the nature of the pendant groups in the precursor, hydrogels can be divided in neutral or ionic, or in affine or phantom networks when classifying them according to their structural or mechanical properties. Moreover, hydrogels can be homopolymeric or copolymeric concerning the polymer nature. Ultimately, based on the physical structure of the network, hydrogels can be further

grouped into amorphous, semicrystalline, hydrogen-bonded structures, supramolecular structures or hydrocolloidal aggregates [172].

Additionally, hydrogel's unique chemical and physical structures make them particularly suitable for bio-related fields and indeed have been applied in biological sensors [173], controlled drug delivery [174,175], tissue engineering devices [176] and even diagnostic imaging [175,177]. The cross-linked nature of hydrogel networks provides great affinity with the solvent and avoids its dissolution simultaneously. Solvents are able to penetrate the polymer matrix between the chains, giving the hydrogel the capability of modulating mechanical and structural properties through the modification of the molecular architecture and morphology. This highly interconnected nature results in a large surface area and allows the incorporation of biologically active substances such as cells and enzymes into the network, providing biocompatibility. Moreover, molecular tailoring enables gel network to interact with certain environments in an intelligent way.

As mentioned earlier, these attractive characteristics of hydrogels are also highly desirable for energy storage devices. Effectively, the hydrogel matrix promotes the electronic transport along the backbone and enhances the ionic transport through hierarchical pores. This structure can also avoid clustering, aggregation or stacking of materials by screening the effect of strong π-π interactions responsible for it, and can accommodate the volume changes induced by reactions, thereby protecting the transport pathways. Surface area and surface chemistry play a key role in energy conversion and storage processes, since the latter involve physical interactions and/or chemical reactions at surfaces and interfaces [178]. The hierarchical pore structure of hydrogels implies an enhanced surface area and higher active site density for electronic and ionic transport. Furthermore, hydrogel's high tunability of mechanical, chemical and electrochemical properties can be used to apply modifications in order to meet the desired characteristics, such as flexibility

or stretchability. Finally, hydrogels offer an excellent scaffold for the development of hybrid materials, since their matrix can act as a support for other active materials and permits the interpenetration with other networks.

Although gels, and specially hydrogels, have been described as an excellent constituent of SCs (not only as electrolyte but also as electrode) they have also been applied in other energy storage devices, such as lithium ion batteries (LIBs), solar cells and fuel cells. Unlike liquid electrolytes, GPEs are almost exempt from leaking and volatilization due to their quasi-solid-state-nature. Simultaneously, the liquid phase of GPEs confers them high ionic conductivity (10^{-4}–10^{-3} S/cm at room temperature), in comparison with other SSEs. In summary, the ease of handling and the excellent flexibility of GPEs, combined with their liquid-like ionic transport capability and good chemical, electrochemical and thermal stability, make GPEs a promising candidate for the development of less expensive energy devices, with improved safety and better packaging processability. Organogels, and more recently ionogels, have been emerging as types of GPEs to use in lithium ion batteries. To improve their performance, the addition of nanoparticles, copolymerization and chemical crosslinking have been applied, and several review articles have thoroughly discussed organogels and ionogels for LIBs [179–183]. The application of GPEs in solar cells is still limited because liquid electrolytes are still more efficient. Research is being conducted to overcome the problems by means of the proposal of new approaches such as a post-polymerization process after the penetration of the monomers [184,185]. Lastly, GPEs are used as polymer electrolyte membranes (PEMs) in fuel cells due to their improved resistance to dehydration and solvent evaporation. Ionogels also present an opportunity as separators in fuel cells because of their good thermal stability, high ionic conductivity and gas permeability [186,187].

Therefore, great progress has been achieved in the development of gel materials for energy applications in the last decades. The optimization of SC performance has attracted a lot of interest and, as a result, there is a knowledge of the relationships and synergies existing between the properties of gels and their performance in energy devices. While many reviews have been published in order to asses in the composition aspect on this field, like the electrode [30,39] and electrolyte selection [43,105,114], others have examined the fundamentals and performance [55,58,134,188], the utilization of different materials [3,42,49,108,132,161,189,190], the sustainability aspects [7,52,191] or the biocompatibility [85,192,193].

1.4 Hydrogels as solid state electrolyte for supercapacitors

Hydrogels can be differently categorized depending on the purpose of such classification or on the aspect to be remarked. Since one of the aims of this chapter is to provide insights into the utilization of hydrogel-based SSEs in biological systems remarking their sustainability and biocompatibility, the proposed classification highlights the important aspects for this kind of application. Therefore, hydrogels have been firstly divided into two self-explanatory categories regarding the nature of their matrix, that is, organic and inorganic. Afterwards, organic hydrogels will be further sorted into synthetics or biopolymer, concerning their origin.

1.4.1 Inorganic hydrogels as SSE for SCs

Inorganic 3D structures have received some attention due to their ease of integration into nanoscale systems but also because the low dimensionality and quantum effects of their building blocks at the nano level induce paramount properties. In this sense, inorganic hydrogels are promising in energy

conversion/storage applications since the large pore volume, which leads to high specific area and low densities, helps to ensure a good contact between the electrode and the electrolyte and a high density of active sites for electrochemical reactions. This porous structure also enables solvent movement and thus causes an increase in the reaction rate kinetics. Although the application of inorganic hydrogels is highly desirable in multiple fields such as sensing, catalytic conversion, selective absorption and thermal insulation, the related literature for such applications is still relatively scarce. Moreover, the utilization of inorganic hydrogels as SSE in SCs is an almost unexplored branch since most of the research has been conducted with the aim to explore the synthetic pathways and properties of the prepared hydrogels, but not their specific application. Taking this into account, the main synthesis strategies will be detailed in this chapter in order to highlight the reported hydrogels with characteristics that may be interesting as SSE in SCs.

Various synthetic pathways have been developed to prepare inorganic gels, among which the sol-gel method is the only one that has led to an inorganic SSE hydrogel. The work of Matsuda *et al.* reports the preparation of electric double-layer capacitors, which were fabricated using polyvinyl alcohol-containing silica gels doped with $HClO_4$ as an electrolyte, and activated carbon powders (ACP) hybridized with the silica gels as a polarizable electrode [194]. The prepared SC exhibited a capacitance up to 44 F/g, comparable to the capacitance of conventional capacitors with liquid electrolytes. The doped silica gel increased its conductivity upon increasing $HClO_4$ electrolyte concentration, indicating that the added $HClO_4$ enhanced proton conductivity of the gels and, in other words, acted as an effective proton donor. Thus, the large capacitance of the SC is attributed to the concentration-regulated proton conductivity of the $HClO_4$ doped silica gel and its hybridization by the sol-gel process. Gash *et al.* [195] reported the implementation

of a sol-gel method to systematically prepare inorganic gels by means of inexpensive precursors and highly controllable conditions such as solvent or type of epoxide. This method allowed the preparation of gels with high surface areas (up to 500 m^2/g), which can be used to prepare monolithic gels of transition metals as long as the transition metal has an oxidation state of 3 or more.

Template-assisted methods have been also used to prepare inorganic hydrogels. In the work of Wang *et al.* [196] a block copolymer scaffold was covered with alumina or titania particles by means of the atomic layer deposition (ADL) technique. The organic scaffold was removed by calcination and a highly mesoporous metal oxide nanotube network with a porosity up to 90 % was obtained. Similarly, the work of Ras *et al.* [197] features the preparation of an inorganic metal oxide porous nanotube network through the deposition of the metal oxide particles by ALD onto a nanofibrillated cellulose template. These inorganic hydrogels have already demonstrated humidity sensing capabilities and are expected to be important when applied in fields such as catalysis, photovoltaics, energy conversion and other pore related applications, and are expected to be promising candidates for SC technology.

Another used pathway to prepare inorganic hydrogels is the self-assembly method. This bottom-up strategy is based on the self-aggregation and distribution of various building blocks at the nanoscale in order to create macroscopic 3D integrated structures. Recently, inorganic self-assembled 3D macroscopic structures have received some attention due to their ability to form functional gels with hierarchical 3D porous macrostructures, controlled crystallinity and composition, and also because they maintain the physical and chemical characteristics of the assembled nanomaterials. An interesting study presented by Gao *et al.* reports the synthesis of Ag inorganic hydrogels through the self-assembly of Ag nanoshells via the oxidative removal of surface thiolates. The as-prepared hydrogels show very low

densities, high surface area and tunable porosity by varying the diameter of the precursor Ag nanoshells and the oxidant molar ratio. Additionally, the Ag hydrogels prepared with higher concentrations of oxidant remove the visible light scattering, displaying optical transparency. Therefore, these low-density mesoporous structures could be promising candidates for many applications, such as catalytic, electrocatalytic and SERS-based (surface-enhanced Raman scattering) sensing ones [198]. Instead of nanoshells, Jung *et al.* obtained highly porous inorganic hydrogels/aerogels through nanowire self-assembly. Specifically, the *in situ* hydrothermal synthesis of one-dimensional $K_{2-x}Mn_8O_{16}$ nanowires directly implied the formation of a cross-linked network and allowed nanowires to have longer length, which provided aerogels with exceptional porosity and surface area, remarkably low densities and mechanical robustness, properties that can be controlled by tuning the initial concentrations and reaction time. Although the obtained hydrogels/aerogels were investigated as water filters to remove heavy metal ions and toxic organic pollutants, their properties make them suitable for many application fields, such as catalysis or photocatalysis, environmental, sensing, energy storage, and beyond, since the nanowires act as both the structural support for the bulk monolith and the active functional sites [199]. Lastly, the work of Sayevich *et al.* reports a self-assembly of electrostatically stabilized semiconductor nanocrystals (NCs) by the linkage with appropriate ions into multibranched 3D structures. The formation of these gels is already available with a variety of NCs and represents a solution to the formation of interconnected inorganic 3D structures while maintaining the individual properties of the NCs. These inorganic gels, which exhibit the features of the individual quantum dots, are benefited from the strong coupling between particles that enhances the charge transport phenomena between different NCs [200].

1.4.2 Organic hydrogels as SSE for SC

As stated before, extensive research can be found in the literature about the use of organic hydrogels as GPEs. In this chapter, it has been collected the most representative peer-reviewed publications on biocompatible organic hydrogels as SEE for SC applications.

1.4.2.1 Synthetic polymer hydrogel electrolytes

Among the multiple kinds of polymers for hydrogel electrolytes, poly(vinyl alcohol) (PVA) has been the most widely studied one. Briefly, PVA-based hydrogels are generally mixed with different aqueous solutions such as strong acid (*e.g.*, H_2SO_4, H_3PO_4), strong alkaline (*e.g.,* NaOH, KOH) and neutral (*e.g.,* LiCl, NaCl, KCl) electrolytes to prepare hydrogels. However, and more recently, the use of poly(acrylate)- and poly(acrylic acid)-based in hydrogels for SCs have also been explored, obtaining promising results.

Since its discovery in 1924, PVA has been one of the most widely studied polymers as a matrix among all the host polymers for hydrogel electrolytes due to its low cost, non-toxicity, chemical stability and easy preparation [201–206]. The gel formation capability is a result of the reaction of the –OH groups of PVA with –CHO groups of certain aldehydes to form acetal or (hemi)acetal bonds under acidic conditions [207]. Usually, PVA-based hydrogels have good mechanical properties and high structural integrity, since they are able to trap large amounts of water without dissolving in it, enhancing the ionic conductivity. Additionally, they can be easily cast to form thin membranes with large surface-area, proper to use as electrolyte-separator in SCs. Precisely, Song *et al.* [208] reported a PVA electrolyte with excellent properties used for the preparation of a miniaturized integrated stretchable and biocompatible micro-SC, with functionalized graphene oxide (GO) hydrogels as electrodes. After coating the collector with the functionalized GO hydrogels, a thin

layer of PVA/H_2SO_4 was drop-casted on the electrodes to form the solid state gel electrolyte. The prepared SC exhibited a high performance and high durability, retaining up to 93 % of the initial capacitance after 10000 charge/discharge cycles and up to 96,8 % after 2000 bending and twisting cycles. Similarly, the work of Mangisetti *et al.* [209] features the preparation of a highly conductive, porous hierarchical structure made of exfoliated CNTs as the SC electrode. The SC performance was evaluated with various electrolytes, and the PVA/H_2SO_4 SSE appeared to exhibit a stable and remarkable performance, retaining a 77,12 % of the capacitance at currents as high as 5 A/g. More recently, Pullanchiyodan *et al.* [210] reported a study based on metal coated fabrics and GPE for SC. Their work studied the use of a metal coated fabric as the electrochemically active material and a PVA/KCl as the electrolyte in wearable SC. Electrochemical and capacitive tests were performed in order to characterize this novel SC, which displayed a specific capacitance up to 99.06 mF/ at a scan rate of 5mV/s and a stable capacitive response for 5000 charge/discharge cycles. Moreover, the biocompatibility of the PVA/KCl electrolyte was assessed and confirmed by an in vitro cytocompatibility study with adult human fibroblast cells.

Poly(acrylic acid) (PAA) presents a carboxylic group on each monomer unit. In aqueous media it becomes a polyelectrolyte via dissociation of the acidic groups, which promote the formation of hydrogen bonds between the polymer chains and water molecules. Additionally, the weak acidity of these carboxylic groups provides PAA-based hydrogels a sensitive behavior against pH and ionic strength [211]. For the reasons above, and together with poly(sodium acrylate) an other polyacrylate derivatives, PAA is one of the most profusely used water soluble anionic polyelectrolytes, being the basis of a type of materials named super absorbents. Since protons of the carboxylic acids can easily be extracted, PAA and PAA-based hydrogels enhance proton conduction and thus have been extensively tested as

SC electrolytes [43,68,89,114,212–215]. On one hand, Guo and coworkers [212] developed and characterized a self-healable and easily recyclable supramolecular PAA hydrogel electrolyte crosslinked by ferric ions (PAA/KCl-Fe^{3+}). The PAA/KCl-Fe^{3+} hydrogel is stabilized by both the ionic bond between Fe^{3+} and carboxylic acid ions and the intra- and inter-molecular hydrogen bonding, which give excellent mechanical performance with an extensibility up to 700 % and resisting a stress of 400 kPa. The prepared hydrogel displays also a good conductivity, with a value of 0.09 S/cm. The electrochemical performance of the PAA was tested by assembling a full SC with graphene foam supported polypyrrol (GF@PPy) electrodes. The assembled SC exhibited a specific capacitance of 87.4 F/g at a current density of 0.5 A/g and a capacitive retention of 89 % after 5000 charge/discharge cycles. In addition, owing to their eco-friendliness and already tested biocompatibility, no environmental or safety issues are related to the PAA/KCl-Fe^{3+} hydrogel electrolytes. On the other hand, the work of Jing *et al.* [216] focused on the biocompatibility and multifunctionality of a polyacrylamide (PAM) hydrogel inspired by the natural mussel adhesive mechanism. This hydrogel is able to integrate several desirable features, high stretchability, non-stimulated self-healing properties, strong and reversible adhesion ability, excellent biocompatibility in human fibroblasts, as well as conductivity, which makes it highly desirable for human-friendly biological devices. The hydrogel was prepared with a facile method by partially oxidizing dopamine coated talc fakes and introducing them into a traditional PAM hydrogel, using an ionic solution as the solvent. When the prepared hydrogel was used as a strain-sensor, it showed high sensitivity and was even able to monitor various human motions, such as bending of articulations or taking a deep breath. Closely related, the work of Fu *et al.* [217] features a tough and self-powered piezoelectric polyacrylonitrile hydrogel. This hydrogel, which is made by the incorporation of ferroelectric polyvinylidene fluoride (PVDF) into the conventional PAN matrix, is capable of not only generating an electrical signal

output (30 mV, 2.8 µA) with a rapid response (31 ms), but also of detecting physiological signal (gestures, pulse, words, etc.). These abilities make it extremely useful for human-friendly devices and, more precisely, for artificial skin development. Indeed, its mechanical properties resemble to those of the human skin, with almost skin-like Young's modulus and stretchability values (1.33-3.24 MPa, 90-175 %) and high toughness (1.23 MJ/m^2).

As explained above, PVA and PAA hydrogels are the most reported ones in terms of biocompatible synthetic polymers for SSE, but other polymers such as polyethyleneglycol diacrylate (PEGDA) or polyaniline (PANI) have also been used. More precisely, the work of Guarino *et al.* [218] reports a novel hydrogel prepared by an *in situ* precipitation of PANI in a PEGDA solution, followed by a UV photocrosslinking process. The resulting hydrogel exhibits a classic macro porous interconnected structure with the electrical conductivity reaching $(1.1 \pm 0.5) \times 10^{-3}$ S/cm and the proton conductivity $(2 \pm 0.1) \times 10^{-1}$ S/cm with a PANI content of 3 %wt. Finally, *in vitro* studies confirmed the biocompatibility of PEGDA/PANI hydrogels and its advantageous properties for cell proliferation with to different cell lines, PC12 and human Mesenchymal Stem Cells (hMSC).

1.4.2.2 Natural polymer hydrogel electrolytes

Hydrogels constituted of polymeric biomolecules from natural sources are known as biohydrogels. In the last years, and with the arise of green and sustainable chemistry, there has been a growing interest for the application of biopolymers and biohydrogels in a wide variety of research fields, usually more focused on biomedical applications such as drug delivery [163–165], tissue engineering [219,220], and molecular actuators[166,167,221], but also in other areas such as energy storage applications [53,209,222–235]. Among all the biopolymers, cellulose, chitin, gelatin, agarose and alginate are the most habitually used ones.

Indeed, as the primary structural component of the cell wall in green plants, cellulose constitutes the most abundantly used biopolymer. Specifically, cellulose fibers are employed in energy applications owing to their high aspect ratios, high surface area and porosity, excellent mechanical properties, and excellent flexibility. Cellulose can play three different key roles: firstly, as a mechanical and flexible reinforcement in electrode materials which are already formed by other electroactive components. Secondly, as a precursor of other electrically active carbonaceous materials, usually in a pyrolytic conversion, and finally as the separator between the electrodes and the SSE. While cellulose fibers are commonly used in either one of the two first roles (mechanical reinforcement or precursor for electroactive materials), cellulose hydrogels usually fulfill the third role, since their porous structure enhances ionic conductivity [57,236]. For instance, the work of Zhiyuan Peng *et al.* [223] explores the preparation of a fully flexible SC based on lignin and cellulose, both biomass. The prepared SC is composed of lignosulfonate/single-walled carbon nanotube (Lig/SWCNT) hydrogels as electrodes, prepared through a straightforward hydrothermal treatment, and cellulose hydrogels (cellulose/Li_2SO_4) as the electrode separator, synthesized through a phase–inversion mechanism. The electrochemical characterization of the assembled biomass-based SC shows high specific capacitance and a remarkable bendability, with a 292 F/g specific capacitance at current density of 0.5 A/g, and 98 % of capacitance retention after 1000 bending cycles. Similarly, but focusing on the electrode, Qinqin Ding *et al.* [235] developed a multifunctional hybrid hydrogel based on nanostructured cellulose nanofibers and PPy (CNF-PPy) complexes, and a PVA-borax gel matrix. The CNF-PPy complexes were prepared through an oxidative polymerization of PPy on the CNF templates. CNF-PPy complexes tangle with the PVA gel matrix, forming a hybrid hydrogel, but they also reversibly crosslink with the borate. The latter interaction leads to the formation of a robust and conducting network, which resulted in a hydrogel of high mechanical

properties, with a storage modulus of 0.1 MPa and a nominal compression stress of 22 MPa. When the hydrogel was electrochemically characterized in a three-electrode configuration, it exhibited a conductivity of 3.65 ± 0.08 S/m and a specific capacitance that reached up to 236.9 F/g and a 86 % retention after 1500 cycles. Ultimately, the multiple works of Saborio *et al.* [53,57] feature the preparation of a fully carboxymethyl cellulose (CMC) hydrogel SC. In these studies, a flexible, lightweight, robust and manageable symmetric supercapacitor was prepared by means of the assembly of two electrodes, constituted by a PEDOT-interpenetrated CMC hydrogel separated by a CMC/NaCl hydrogel. The electrodes were prepared with an anodic polymerization of the conducting polymer inside the CMC network, which originated a robust, flexible and conductive 3D hierarchical porous structure. The SC electrochemical performance was evaluated with CV, GCD and EIS experiments, resulting in values of specific capacitance ranging between 1.6 and 0.8 mF/g and a solid electrolyte resistance of 485 Ω. Such prototype represents a huge step forward as it opens a new window for the mass production of fully biohydrogel-based (cellulose) supercapacitors.

Another well-known polysaccharide, chitin, and its derivatives such as chitosan (CS), have been also explored as electrolytic medium in SC applications. After cellulose, chitin constitutes the most abundant natural polysaccharide, and it can be found in algae, fungus, the exoskeleton of some arthropods and crustaceans and even on insects' cuticles [225,237,238]. Cellulose and chitin are chemically similar, since they only differ in the hydroxyl at position C-2, which is replaced by an acetamide group [237,238]. In the work of Oliveira *et al.* [225], a chitosan-gellan gum assembly (CS/GG) hydrogel is prepared without any chemical or metallic crosslink agent. Such hydrogel has a resistance against dissolution/disintegration in physiological medium (PBS at pH 7.4), displays structural homogeneity, and an interconnected open structure, which is ideal for SC biomedical applications.

Indeed, hydrogel biocompatibility is also reported, and it demonstrates ability to promote adhesion and proliferation of bone marrow-derived mesenchymal stem cells (BMSCs) after four and nine days of cell culture. Moreover, the work of Lizhi Deng and coworkers [224] features the preparation of a chitin/KOH hydrogel through the dissolution of an ionic liquid and 1-butyl-3-methylimidazolium acetate ([BMIM]Ac), with a subsequent replacement of the ionic liquid for a KOH solution. Rheological properties were investigated and it was found that hydrogen bonds between chitin and [BMIM]Ac, as well as its chain flexibility, largely affected the rheological behavior. When a solid state capacitor was assembled and its performance was recorded, both specific capacitance and cycling capabilities were found better than those of a KOH solution SC.

Alginate, a natural polysaccharide habitually extracted from brown algae, is commonly found in form of a $(C_6H_7O_6Na)_n$ sodium salt, which contains many carboxylic groups in each monomer unit. This causes a strong interaction with water and, consequently, a viscous gel is formed. Due to alginate's natural source and its food and skin safety, it has been extensively employed in a wide variety of applications, from culinary ones (for the sferification techniques) to textile and pharmaceutical ones [231,232]. For instance, the work of Juan Zeng *et al*. [232] reports the preparation of a solid state SC in which every component comes from the same precursor, that is, electrolyte, separator and binder are constituted of kelp-extracted alginate extracted. The electrode is composed by activated carbon directly obtained from kelp, and presents a 3D open porous structure with a high surface area of 4425 m^2/g and a large pore volume of 3.22 cm^2/g. These qualities lead to a high performance SC (with a 277 F/g electrode capacitance), fast rate capability (with a capacitance of 156 F/g even at 20 A/g), and good cycling capabilities and stability. It is worth remarking that since it is an "all kelp" SC, it is

environmentally friendly, biocompatible and particularly suitable for medical and wearable electronics.

Wen Zhao *et al.* [231] fabricated a solid state, flexible, micro-supercapacitor in which MoO_{3-x} nanorods actuated as the cathode, a glucose-derived activated carbon as the anode, and alginate was used as the electrolyte. The prepared SC exhibited excellent electrochemical performance, with high areal capacitance of 47.20 mF/cm^2, an energy density of 0.18 mW/cm^2, and good cycling capabilities (with a 95 % of capacitance retention after 10000 cycles). The prepared SC also presented excellent mechanical stability, highlighting its potential in wearable/implantable electronics.

References

1. Bookchin, Murray. Ecology and Revolutionary Thought. *Antipode* **17**, 89–98 (1985).

2. Zhou, Chengtian, Bag, Sourav & Thangadurai, Venkataraman. Engineering Materials for Progressive All-Solid-State Na Batteries. *ACS Energy Lett.* **3**, 2181–2198 (2018).

3. Palakkathodi Kammampata, Sanoop & Thangadurai, Venkataraman. Cruising in ceramics—discovering new structures for all-solid-state batteries—fundamentals, materials, and performances. *Ionics (Kiel).* **24**, 639–660 (2018).

4. Thangadurai, Venkataraman, Narayanan, Sumaletha & Pinzaru, Dana. Garnet-type solid-state fast Li ion conductors for Li batteries: critical review. *Chem. Soc. Rev.* **43**, 4714–4727 (2014).

5. Aravindan, V., Chuiling, W., Reddy, M. V, Rao, G. V. Subba, Chowdari, B. V. R. & Madhavi, S. Carbon coated nano-LiTi2(PO4)3 electrodes for non-aqueous hybrid supercapacitors. *Phys. Chem. Chem. Phys.* **14**, 5808–5814 (2012).

6. Winter, Martin & Brodd, Ralph J. What Are Batteries, Fuel Cells, and Supercapacitors? *Chem. Rev.* **104**, 4245–4270 (2004).

7. Yang, Zhenguo, Zhang, Jianlu, Kintner-Meyer, Michael C. W., Lu, Xiaochuan, Choi, Daiwon, Lemmon, John P. & Liu, Jun. Electrochemical Energy Storage for Green Grid. *Chem. Rev.* **111**, 3577–3613 (2011).

8. Thackeray, Michael M., Wolverton, Christopher & Isaacs, Eric D. Electrical energy storage for transportation—approaching the limits of, and going beyond, lithium-ion batteries. *Energy Environ. Sci.* **5**, 7854–7863 (2012).

9. Miller, John R. & Simon, Patrice. Electrochemical Capacitors for Energy Management. *Science (80-.).* **321**, 651–652 (2008).

10. Armelin, Elaine, Pérez-Madrigal, Maria M., Alemán, Carlos & Díaz, David Díaz. Current status and challenges of biohydrogels for applications as supercapacitors and secondary batteries. *J. Mater. Chem. A* **4**, 8952–8968 (2016).

11. Aravindan, V., Reddy, M. V, Madhavi, S., Mhaisalkar, S. G., Subba Rao, G.

V & Chowdari, B. V. R. Hybrid supercapacitor with nano-TiP2O7 as intercalation electrode. *J. Power Sources* **196**, 8850–8854 (2011).

12. Béguin, François, Presser, Volker, Balducci, Andrea & Frackowiak, Elzbieta. Carbons and Electrolytes for Advanced Supercapacitors. *Adv. Mater.* **26**, 2219–2251 (2014).

13. Zhai, Yunpu, Dou, Yuqian, Zhao, Dongyuan, Fulvio, Pasquale F., Mayes, Richard T. & Dai, Sheng. Carbon Materials for Chemical Capacitive Energy Storage. *Adv. Mater.* **23**, 4828–4850 (2011).

14. Simon, Patrice, Gogotsi, Yury & Dunn, Bruce. Where Do Batteries End and Supercapacitors Begin? *Science (80-.).* **343**, 1210–1211 (2014).

15. Burke, Andrew. Ultracapacitors: why, how, and where is the technology. *J. Power Sources* **91**, 37–50 (2000).

16. Frackowiak, Elzbieta & Béguin, François. Carbon materials for the electrochemical storage of energy in capacitors. *Carbon N. Y.* **39**, 937–950 (2001).

17. Gamby, J., Taberna, P. L., Simon, P., Fauvarque, J. F. & Chesneau, M. Studies and characterisations of various activated carbons used for carbon/carbon supercapacitors. *J. Power Sources* **101**, 109–116 (2001).

18. Pekala, R. W., Farmer, J. C., Alviso, C. T., Tran, T. D., Mayer, S. T., Miller, J. M. & Dunn, B. Carbon aerogels for electrochemical applications. *J. Non. Cryst. Solids* **225**, 74–80 (1998).

19. Frackowiak, E., Metenier, K., Bertagna, V. & Beguin, F. Supercapacitor electrodes from multiwalled carbon nanotubes. *Appl. Phys. Lett.* **77**, 2421–2423 (2000).

20. Menzel, Jakub, Frąckowiak, Elżbieta & Fic, Krzysztof. Agar-based aqueous electrolytes for electrochemical capacitors with reduced self-discharge. *Electrochim. Acta* **332**, (2020).

21. Mitra, Sagar & Sampath, S. Electrochemical capacitors based on exfoliated graphite electrodes. *Electrochem. Solid-State Lett.* **7**, 264–268 (2004).

22. Sathiya, M., Prakash, A. S., Ramesha, K., Tarascon, J−M. & Shukla, A. K. V2O5-Anchored Carbon Nanotubes for Enhanced Electrochemical Energy Storage. *J. Am. Chem. Soc.* **133**, 16291–16299 (2011).

23. Aricò, Antonino Salvatore, Bruce, Peter, Scrosati, Bruno, Tarascon, Jean-Marie & Schalkwijk, Walter Van. Nanostructured materials for advanced energy conversion and storage devices. in *Materials for Sustainable Energy* 148–159 (2010). doi:10.1142/9789814317665_0022.

24. Augustyn, Veronica, Come, Jérémy, Lowe, Michael A., Kim, Jong Woung, Taberna, Pierre-Louis, Tolbert, Sarah H., Abruña, Héctor D., Simon, Patrice & Dunn, Bruce. High-rate electrochemical energy storage through Li+ intercalation pseudocapacitance. *Nat. Mater.* **12**, 518–522 (2013).

25. Kudo, T., Ikeda, Y., Watanabe, T., Hibino, M., Miyayama, M., Abe, H. & Kajita, K. Amorphous V2O5/carbon composites as electrochemical supercapacitor electrodes. *Solid State Ionics* **152**–**153**, 833–841 (2002).

26. Ghosh, S. & Inganas, O. Conducting polymer hydrogels as 3D electrodes:Applications for supercapacitors. *Adv. Mater.* **11**, 1214–1218 (1999).

27. Mastragostino, Marina, Arbizzani, Catia & Soavi, Francesca. Conducting polymers as electrode materials in supercapacitors. *Solid State Ionics* **148**, 493–498 (2002).

28. Frackowiak, E., Khomenko, V., Jurewicz, K., Lota, K. & Béguin, F. Supercapacitors based on conducting polymers/nanotubes composites. *J. Power Sources* **153**, 413–418 (2006).

29. Gómez-Romero, Pedro, Chojak, Malgorzata, Cuentas-Gallegos, Karina, Asensio, Juan A., Kulesza, Pawel J., Casañ-Pastor, Nieves & Lira-Cantú, Mónica. Hybrid organic–inorganic nanocomposite materials for application in solid state electrochemical supercapacitors. *Electrochem. commun.* **5**, 149–153 (2003).

30. Wang, Guoping, Zhang, Lei & Zhang, Jiujun. A review of electrode materials for electrochemical supercapacitors. *Chem. Soc. Rev.* **41**, 797–828 (2012).

31. Chee, W. K., Lim, H. N., Zainal, Z., Huang, N. M., Harrison, I. & Andou, Y. Flexible Graphene-Based Supercapacitors: A Review. *J. Phys. Chem. C* **120**, 4153–4172 (2016).

32. Simon, Patrice, Gogotsi, Yury, Simon, Patrice, Gogotsi, Yury & Materials, Nature. Materials for electrochemical capacitors. *Nat. Mater.* **7**, 845–854 (2008).

33. Gogotsi, Y. & Simon, P. True Performance Metrics in Electrochemical Energy Storage. *Science (80-.).* **334**, 917–918 (2011).

34. Naoi, Katsuhiko, Ishimoto, Syuichi, Miyamoto, Jun-ichi & Naoi, Wako. Second generation 'nanohybrid supercapacitor': Evolution of capacitive energy storage devices. *Energy Environ. Sci.* **5**, 9363–9373 (2012).

35. Miller, John R. & Burke, Andrew F. Electrochemical capacitors: Challenges and opportunities for real-world applications. *Electrochem. Soc. Interface* **17**, 53–57 (2008).

36. Kotz, R. & Carlen, M. Principles and applications of electrochemical capacitors. *Electrochim. Acta* **45**, 2483–2498 (2000).

37. Babakhani, Banafsheh & Ivey, Douglas G. Improved capacitive behavior of electrochemically synthesized Mn oxide/PEDOT electrodes utilized as electrochemical capacitors. *Electrochim. Acta* **55**, 4014–4024 (2010).

38. Sarangapani, S., Tilak, BV & Chen, C. P. Materials for Electrochemical Capacitors. *J. Electrochem. Soc.* **143**, 3791 (1996).

39. Zhang, Yong, Feng, Hui, Wu, Xingbing, Wang, Lizhen, Zhang, Aiqin, Xia, Tongchi, Dong, Huichao, Li, Xiaofeng & Zhang, Linsen. Progress of electrochemical capacitor electrode materials: A review. *Int. J. Hydrogen Energy* **34**, 4889–4899 (2009).

40. Augustyn, Veronica, Simon, Patrice & Dunn, Bruce. Pseudocapacitive oxide materials for high-rate electrochemical energy storage. *Energy Environ. Sci.* **7**, 1597–1614 (2014).

41. Yan, Jun, Wang, Qian, Wei, Tong & Fan, Zhuangjun. Recent advances in design and fabrication of electrochemical supercapacitors with high energy densities. *Adv. Energy Mater.* **4**, (2014).

42. Zhang, Li Li & Zhao, X. S. Carbon-based materials as supercapacitor electrodes. *Chem. Soc. Rev.* **38**, 2520–2531 (2009).

43. Zhong, Cheng, Deng, Yida, Hu, Wenbin, Qiao, Jinli, Zhang, Lei & Zhang, Jiujun. A review of electrolyte materials and compositions for electrochemical supercapacitors. *Chem. Soc. Rev.* **44**, 7484–7539 (2015).

44. Lee, Seung Woo, Gallant, Betar M., Byon, Hye Ryung, Hammond, Paula T. & Shao-Horn, Yang. Nanostructured carbon-based electrodes: Bridging the

gap between thin-film lithium-ion batteries and electrochemical capacitors. *Energy Environ. Sci.* **4**, 1972–1985 (2011).

45. Pandolfo, A. G. & Hollenkamp, A. F. Carbon properties and their role in supercapacitors. *J. Power Sources* **157**, 11–27 (2006).

46. Pan, Hui, Li, Jianyi & Feng, Yuan Ping. Carbon nanotubes for supercapacitor. *Nanoscale Res. Lett.* **5**, 654–668 (2010).

47. Burke, Andrew & Miller, Marshall. The power capability of ultracapacitors and lithium batteries for electric and hybrid vehicle applications. *J. Power Sources* **196**, 514–522 (2011).

48. Ue, Makoto, Ida, K. & Mori, S. Electrochemical Properties of Organic Liquid Electrolytes Based on Quaternary Onium Salts for Electrical Double-Layer Capacitors. *J. Electrochem. Soc.* **141**, 2989–2996 (1994).

49. Davies, Aaron & Yu, Aiping. Material advancements in supercapacitors: From activated carbon to carbon nanotube and graphene. *Can. J. Chem. Eng.* **89**, 1342–1357 (2011).

50. Xiong, Guoping, Meng, Chuizhou, Reifenberger, Ronald G., Irazoqui, Pedro P. & Fisher, Timothy S. A Review of Graphene-Based Electrochemical Microsupercapacitors. *Electroanalysis* **26**, 30–51 (2014).

51. Zuliani, Jocelyn E., Caguiat, Johnathon N., Kirk, Donald W. & Jia, Charles Q. Considerations for consistent characterization of electrochemical double-layer capacitor performance. *J. Power Sources* **290**, 136–143 (2015).

52. Fic, Krzysztof, Platek, Anetta, Piwek, Justyna & Frackowiak, Elzbieta. Sustainable materials for electrochemical capacitors. *Mater. Today* **21**, 437–454 (2018).

53. Saborío, Maricruz G. M. G., Svelic, Petra, Casanovas, Jordi, Ruano, Guillem, Pérez-Madrigal, Maria M. M., Franco, Lourdes, Torras, Juan, Estrany, Francesc, Alemán, Carlos, Pérez-Madrigal, Maria M. M., Franco, Lourdes, Torras, Juan, Estrany, Francesc & Alemán, Carlos. Hydrogels for flexible and compressible free standing cellulose supercapacitors. *Eur. Polym. J.* **118**, 347–357 (2019).

54. Ruano, Guillem, Díaz, Angélica, Tononi, Jordi, Torras, Juan, Puiggalí, Jordi & Alemán, Carlos. Biohydrogel from unsaturated polyesteramide: Synthesis, properties and utilization as electrolytic medium for

electrochemical supercapacitors. *Polym. Test.* **82**, (2020).

55. Stoller, Meryl D. & Ruoff, Rodney S. Best practice methods for determining an electrode material's performance for ultracapacitors. *Energy Environ. Sci.* **3**, 1294–1301 (2010).

56. Pérez-Madrigal, Maria M., Edo, Miquel G., Díaz, Angélica, Puiggalí, Jordi & Alemán, Carlos. Poly-γ-glutamic Acid Hydrogels as Electrolyte for Poly(3,4-ethylenedioxythiophene)-Based Supercapacitors. *J. Phys. Chem. C* **121**, 3182–3193 (2017).

57. Pérez-Madrigal, Maria M., Edo, Miquel G., Saborío, Maricruz G., Estrany, Francesc & Alemán, Carlos. Pastes and hydrogels from carboxymethyl cellulose sodium salt as supporting electrolyte of solid electrochemical supercapacitors. *Carbohydr. Polym.* **200**, 456–467 (2018).

58. Vol'fkovich, Yu. M. & Serdyuk, T. M. Electrochemical Capacitors. *Russ. J. Electrochem.* **38**, 935–959 (2002).

59. Kampouris, Dimitrios K., Ji, Xiaobo, Randviir, Edward P. & Banks, Craig E. A new approach for the improved interpretation of capacitance measurements for materials utilised in energy storage. *RSC Adv.* **5**, 12782–12791 (2015).

60. Lämmel, C., Schneider, M., Weiser, M. & Michaelis, A. Investigations of electrochemical double layer capacitor (EDLC) materials - A comparison of test methods. *Materwiss. Werksttech.* **44**, 641–649 (2013).

61. Frackowiak, Elzbieta, Abbas, Qamar & Béguin, François. Carbon/carbon supercapacitors. *J. Energy Chem.* **22**, 226–240 (2013).

62. Largeot, Celine, Portet, Cristelle, Chmiola, John, Taberna, Pierre-Louis, Gogotsi, Yury & Simon, Patrice. Relation between the Ion Size and Pore Size for an Electric Double-Layer Capacitor. *J. Am. Chem. Soc.* **130**, 2730–2731 (2008).

63. Yang, H., Yoshio, M., Isono, K. & Kuramoto, R. Improvement of Commercial Activated Carbon and Its Application in Electric Double Layer Capacitors. *Electrochem. Solid-State Lett.* **5**, A141 (2002).

64. Raymundo-Piñero, E., Kierzek, K., Machnikowski, J. & Béguin, F. Relationship between the nanoporous texture of activated carbons and their capacitance properties in different electrolytes. *Carbon N. Y.* **44**, 2498–2507

(2006).

65. Qu, Deyang & Shi, Hang. Studies of activated carbons used in double-layer capacitors. *J. Power Sources* **74**, 99–107 (1998).

66. Shiraishi, Soshi, Kurihara, Hideyuki, Okabe, Keiji, Hulicova, Denisa & Oya, Asao. Electric double layer capacitance of highly pure single-walled carbon nanotubes (HiPco^{TM}Buckytubes^{TM}) in propylene carbonate electrolytes. *Electrochem. commun.* **4**, 593–598 (2002).

67. Barisci, Joseph N., Wallace, Gordon G. & Baughman, Ray H. Electrochemical Characterization of Single-Walled Carbon Nanotube Electrodes. *J. Electrochem. Soc.* **147**, 4580 (2000).

68. Chen, Qiao, Li, Xinming, Zang, Xiaobei, Cao, Yachang, He, Yijia, Li, Peixu, Wang, Kunlin, Wei, Jinquan, Wu, Dehai & Zhu, Hongwei. Effect of different gel electrolytes on graphene-based solid-state supercapacitors. *RSC Adv.* **4**, 36253–36256 (2014).

69. Jin, Xuting, Sun, Guoqiang, Yang, Hongsheng, Zhang, Guofeng, Xiao, Yukun, Gao, Jian, Zhang, Zhipan & Qu, Liangti. A graphene oxide-mediated polyelectrolyte with high ion-conductivity for highly stretchable and self-healing all-solid-state supercapacitors. *J. Mater. Chem. A* **6**, 19463–19469 (2018).

70. Wang, Yan, Shi, Zhiqiang, Huang, Yi, Ma, Yanfeng, Wang, Chengyang, Chen, Mingming & Chen, Yongsheng. Supercapacitor Devices Based on Graphene Materials. *J. Phys. Chem. C* **113**, 13103–13107 (2009).

71. El-Kady, Maher F., Shao, Yuanlong & Kaner, Richard B. Graphene for batteries, supercapacitors and beyond. *Nat. Rev. Mater.* **1**, 16033 (2016).

72. Beidaghi, Majid & Gogotsi, Yury. Capacitive energy storage in micro-scale devices: recent advances in design and fabrication of micro-supercapacitors. *Energy Environ. Sci.* **7**, 867–884 (2014).

73. Huang, P., Lethien, C., Pinaud, S., Brousse, K., Laloo, R., Turq, V., Respaud, M., Demortière, A., Daffos, B., Taberna, P. L., Chaudret, B., Gogotsi, Y. & Simon, P. On-chip and freestanding elastic carbon films for micro-supercapacitors. *Science (80-.).* **351**, 691–695 (2016).

74. Xu, Bin, Wu, Feng, Chen, Renjie, Cao, Gaoping, Chen, Shi, Zhou, Zhiming & Yang, Yusheng. Highly mesoporous and high surface area carbon: A high

capacitance electrode material for EDLCs with various electrolytes. *Electrochem. commun.* **10**, 795–797 (2008).

75. Fang, Baizeng & Binder, Leo. A modified activated carbon aerogel for high-energy storage in electric double layer capacitors. *J. Power Sources* **163**, 616–622 (2006).

76. Morishita, T., Tsumura, T., Toyoda, M., Przepiórski, J., Morawski, A. W., Konno, H. & Inagaki, M. A review of the control of pore structure in MgO-templated nanoporous carbons. *Carbon N. Y.* **48**, 2690–2707 (2010).

77. Lee, J., Kim, J. & Hyeon, T. Recent Progress in the Synthesis of Porous Carbon Materials. *Adv. Mater.* **18**, 2073–2094 (2006).

78. Portet, C., Yang, Zhuxian, Korenblit, Y., Gogotsi, Yury, Mokaya, R. & Yushin, Gleb. Electrical Double-Layer Capacitance of Zeolite-Templated Carbon in Organic Electrolyte. *J. Electrochem. Soc.* **156**, A1–A6 (2009).

79. Fuertes, A. B., Lota, G., Centeno, T. A. & Frackowiak, E. Templated mesoporous carbons for supercapacitor application. *Electrochim. Acta* **50**, 2799–2805 (2005).

80. Inagaki, Michio, Konno, Hidetaka & Tanaike, Osamu. Carbon materials for electrochemical capacitors. *J. Power Sources* **195**, 7880–7903 (2010).

81. Qu, Deyang. Studies of the activated carbons used in double-layer supercapacitors. *J. Power Sources* **109**, 403–411 (2002).

82. Yu, Gui-Yan, Chen, Wei-Xiang, Zheng, Yi-Fan, Zhao, Jie, Li, Xiang & Xu, Zhu-De. Synthesis of Ru/carbon nanocomposites by polyol process for electrochemical supercapacitor electrodes. *Mater. Lett.* **60**, 2453–2456 (2006).

83. Arabale, Girish, Wagh, Deepali, Kulkarni, Mahesh, Mulla, I. S., Vernekar, S. P., Vijayamohanan, K. & Rao, A. M. Enhanced supercapacitance of multiwalled carbon nanotubes functionalized with ruthenium oxide. *Chem. Phys. Lett.* **376**, 207–213 (2003).

84. Maity, N. & Dawn, A. Conducting Polymer Grafting : Recent and key developments. *Polymers (Basel).* **12**, 709–732 (2020).

85. Fidanovski, Kristina & Mawad, Damia. Conjugated Polymers in Bioelectronics: Addressing the Interface Challenge. *Adv. Healthc. Mater.* **8**,

1–9 (2019).

86. Heeger, Alan J. Semiconducting and metallic polymers: The fourth generation of polymeric materials. *J. Phys. Chem. B* **105**, 8475–8491 (2001).

87. Sharma, Pawan & Bhatti, T. S. A review on electrochemical double-layer capacitors. *Energy Convers. Manag.* **51**, 2901–2912 (2010).

88. Ryu, Kwang Sun, Kim, Kwang Man, Park, Nam-Gyu, Park, Yong Joon & Chang, Soon Ho. Symmetric redox supercapacitor with conducting polyaniline electrodes. *J. Power Sources* **103**, 305–309 (2002).

89. Wang, Haixiao, Dai, Lixin, Chai, Danxia, Ding, Yi, Zhang, Hengbin & Tang, Jun. Recyclable and tear-resistant all-in-one supercapacitor with dynamic electrode/electrolyte interface. *J. Colloid Interface Sci.* **561**, 629–637 (2020).

90. Shi, Ye, Pan, Lijia, Liu, Borui, Wang, Yaqun, Cui, Yi, Bao, Zhenan & Yu, Guihua. Nanostructured conductive polypyrrole hydrogels as high-performance, flexible supercapacitor electrodes. *J. Mater. Chem. A* **2**, 6086–6091 (2014).

91. Hashmi, S. A. & Upadhyaya, H. M. Polypyrrole and poly(3-methyl thiophene)-based solid state redox supercapacitors using ion conducting polymer electrolyte. *Solid State Ionics* **152–153**, 883–889 (2002).

92. Yin, Bo Si, Zhang, Si Wen, Ke, Ke & Wang, Zhen Bo. Advanced deformable all-in-one hydrogel supercapacitor based on conducting polymer: Toward integrated mechanical and capacitive performance. *J. Alloys Compd.* (2019) doi:10.1016/j.jallcom.2019.07.144.

93. Fabregat, Georgina, Hodásová, L'udmila, del Valle, Luis J., Estrany, Francesc & Alemán, Carlos. Sustainable Solid-State Supercapacitors Made of 3D-Poly(3,4-ethylenedioxythiophene) and κ-Carrageenan Biohydrogel. *Adv. Eng. Mater.* **20**, 1–7 (2018).

94. Kishi, Ryoichi, Hiroki, Kazuaki, Tominaga, Taiki, Sano, Ken Ichi, Okuzaki, Hidenori, Martinez, Jose G., Otero, Toribio F. & Osada, Yoshihito. Electro-conductive double-network hydrogels. *J. Polym. Sci. Part B Polym. Phys.* **50**, 790–796 (2012).

95. Chen, Qing, Lu, Han, Chen, Fang, Chen, Lili, Zhang, Ning & Ma, Mingming. Supramolecular Hydrogels for High-Voltage and Neutral-pH Flexible

Supercapacitors. *ACS Appl. Energy Mater.* **1**, 4261–4268 (2018).

96. Yun, Tae Gwang, Park, Minkyu, Kim, Dong Ha, Kim, Donghyuk, Cheong, Jun Young, Bae, Jin Gook, Han, Seung Min & Kim, Il Doo. All-Transparent Stretchable Electrochromic Supercapacitor Wearable Patch Device. *ACS Nano* **13**, 3141–3150 (2019).

97. Rudge, Andy, Davey, John, Raistrick, Ian, Gottesfeld, Shimshon & Ferraris, John P. Conducting polymers as active materials in electrochemical capacitors. *J. Power Sources* **47**, 89–107 (1994).

98. Zhao, Dan-Dan, Bao, Shu-Juan, Zhou, Wen-Jia & Li, Hu-Lin. Preparation of hexagonal nanoporous nickel hydroxide film and its application for electrochemical capacitor. *Electrochem. commun.* **9**, 869–874 (2007).

99. Kim, Il-Hwan & Kim, Kwang-Bum. Electrochemical Characterization of Hydrous Ruthenium Oxide Thin-Film Electrodes for Electrochemical Capacitor Applications. *J. Electrochem. Soc.* **153**, A383 (2006).

100. Jia, Q. X., Song, S. G., Wu, X. D., Cho, J. H., Foltyn, S. R., Findikoglu, A. T. & Smith, J. L. Epitaxial growth of highly conductive RuO2 thin films on (100) Si. *Appl. Phys. Lett.* **68**, 1069–1071 (1996).

101. Sakiyama, Keizo. Deposition and Properties of Reactively Sputtered Ruthenium Dioxide Films. *J. Electrochem. Soc.* **140**, 834 (1993).

102. Wu, Nae-Lih, Kuo, Shin-Liang & Lee, Ming-Hsueh. Preparation and optimization of RuO2-impregnated SnO2 xerogel supercapacitor. *J. Power Sources* **104**, 62–65 (2002).

103. Sugimoto, Wataru, Yokoshima, Katsunori, Murakami, Yasushi & Takasu, Yoshio. Charge storage mechanism of nanostructured anhydrous and hydrous ruthenium-based oxides. *Electrochim. Acta* **52**, 1742–1748 (2006).

104. Takasu, Y. & Murakami, Y. Design of oxide electrodes with large surface area. *Electrochim. Acta* **45**, 4135–4141 (2000).

105. Xu, Kang. Nonaqueous Liquid Electrolytes for Lithium-Based Rechargeable Batteries. *Chem. Rev.* **104**, 4303–4418 (2004).

106. Gao, Qiang, Demarconnay, Laurent, Raymundo-Piñero, Encarnación & Béguin, François. Exploring the large voltage range of carbon/carbon supercapacitors in aqueous lithium sulfate electrolyte. *Energy Environ. Sci.*

5, 9611–9617 (2012).

107. Pal, Bhupender, Krishnan, Syam G., Vijayan, Bincy Lathakumary, Harilal, Midhun, Yang, Chun-Chen, Ezema, Fabian I., Yusoff, Mashitah Mohd & Jose, Rajan. In situ encapsulation of tin oxide and cobalt oxide composite in porous carbon for high-performance energy storage applications. *J. Electroanal. Chem.* **817**, 217–225 (2018).

108. Galiński, Maciej, Lewandowski, Andrzej, Stepniak, Izabela & Stępniak, Izabela. Ionic liquids as electrolytes. *Electrochim. Acta* **51**, 5567–5580 (2006).

109. Yu, A., Chabot, V. & Zhang, J. *Electrochemical Supercapacitors for energy storge and delivery: Fundamentals and applications*. (CRC Press, 2013).

110. Chen, Qing, Hu, Yue, Hu, Chuangang, Cheng, Huhu, Zhang, Zhipan, Shao, Huibo & Qu, Liangti. Graphene quantum dots–three-dimensional graphene composites for high-performance supercapacitors. *Phys. Chem. Chem. Phys.* **16**, 19307–19313 (2014).

111. Lang, Jun-wei, Yan, Xing-bin, Liu, Wen-wen, Wang, Ru-tao & Xue, Qun-ji. Influence of nitric acid modification of ordered mesoporous carbon materials on their capacitive performances in different aqueous electrolytes. *J. Power Sources* **204**, 220–229 (2012).

112. Demarconnay, L., Raymundo-Piñero, E. & Béguin, F. A symmetric carbon/carbon supercapacitor operating at 1.6V by using a neutral aqueous solution. *Electrochem. commun.* **12**, 1275–1278 (2010).

113. Iqbal, Javed, Numan, Arshid, Rafique, Saqib, Jafer, Rashida, Mohamad, Sharifah, Ramesh, K. & Ramesh, S. High performance supercapattery incorporating ternary nanocomposite of multiwalled carbon nanotubes decorated with Co3O4 nanograins and silver nanoparticles as electrode material. *Electrochim. Acta* **278**, 72–82 (2018).

114. Pal, Bhupender, Yang, Shengyuan, Ramesh, Subramaniam, Thangadurai, Venkataraman & Jose, Rajan. Electrolyte selection for supercapacitive devices: A critical review. *Nanoscale Adv.* **1**, 3807–3835 (2019).

115. Conway, B. E. *Electrochemical supercapacitors: Scientific fundamentals and technological applications*. (Kluwer Academic/Plenum, 1999).

116. Rogers, Robin D. & Voth, Gregory A. Ionic Liquids. *Acc. Chem. Res.* **40**,

1077–1078 (2007).

117. Armand, Michel, Endres, Frank, MacFarlane, Douglas R., Ohno, Hiroyuki & Scrosati, Bruno. Ionic-liquid materials for the electrochemical challenges of the future. *Nat. Mater.* **8**, 129–137 (2010).

118. Liew, Chiam-Wen, Arifin, K. H., Kawamura, J., Iwai, Y., Ramesh, S. & Arof, A. K. Effect of halide anions in ionic liquid added poly(vinyl alcohol)-based ion conductors for electrical double layer capacitors. *J. Non. Cryst. Solids* **458**, 97–106 (2017).

119. Brandt, A., Pohlmann, S., Varzi, A., Balducci, A. & Passerini, S. Ionic liquids in supercapacitors. *MRS Bull.* **38**, 554–559 (2013).

120. OHNO, Hiroyuki & FUKUMOTO, Kenta. Progress in Ionic Liquids for Electrochemical Reaction Matrices. *Electrochemistry* **76**, 16–23 (2008).

121. Snook, Graeme A., Kao, Pon & Best, Adam S. Conducting-polymer-based supercapacitor devices and electrodes. *J. Power Sources* **196**, 1–12 (2011).

122. Wasserscheid, P. & Welton, T. *Ionic Liquids in Synthesis*.

123. Bai, Hua, Li, Chun, Wang, Xiaolin & Shi, Gaoquan. A pH-sensitive graphene oxide composite hydrogel. *Chem. Commun.* **46**, 2376–2378 (2010).

124. Dou, Qingyun, Lian, Cheng, Lei, Shulai, Chen, Jiangtao, Liu, Honglai & Yan, Xingbin. Silica-grafted ionic liquid for maximizing the operational voltage of electrical double-layer capacitors. *Energy Storage Mater.* **18**, 253–259 (2019).

125. Garche, J., Dyer, CK, Moseley, PT, Ogumi, Z. & Rand, DAJ. *Encyclopedia of electrochemical power sources*. (Elsevier B.V, 2013).

126. Lewandowski, Andrzej & Galinski, Maciej. Practical and theoretical limits for electrochemical double-layer capacitors. *J. Power Sources* **173**, 822–828 (2007).

127. Huddleston, Jonathan G., Visser, Ann E., Reichert, W. Matthew, Willauer, Heather D., Broker, Grant A. & Rogers, Robin D. Characterization and comparison of hydrophilic and hydrophobic room temperature ionic liquids incorporating the imidazolium cation. *Green Chem.* **3**, 156–164 (2001).

128. Lewandowski, Andrzej, Olejniczak, Angelika, Galinski, Maciej & Stepniak, Izabela. Performance of carbon–carbon supercapacitors based on organic,

aqueous and ionic liquid electrolytes. *J. Power Sources* **195**, 5814–5819 (2010).

129. Chen, Yao, Zhang, Xiong, Zhang, Dacheng, Yu, Peng & Ma, Yanwei. High performance supercapacitors based on reduced graphene oxide in aqueous and ionic liquid electrolytes. *Carbon N. Y.* **49**, 573–580 (2011).

130. Merlet, Céline, Rotenberg, Benjamin, Madden, Paul A., Taberna, Pierre-Louis, Simon, Patrice, Gogotsi, Yury & Salanne, Mathieu. On the molecular origin of supercapacitance in nanoporous carbon electrodes. *Nat. Mater.* **11**, 306–310 (2012).

131. Feng, Guang, Huang, Jingsong, Sumpter, Bobby G., Meunier, Vincent & Qiao, Rui. A “counter-charge layer in generalized solvents” framework for electrical double layers in neat and hybrid ionic liquid electrolytes. *Phys. Chem. Chem. Phys.* **13**, 14723–14734 (2011).

132. Fedorov, Maxim V & Kornyshev, Alexei A. Ionic Liquids at Electrified Interfaces. *Chem. Rev.* **114**, 2978–3036 (2014).

133. Jiang, De-en & Wu, Jianzhong. Microscopic Insights into the Electrochemical Behavior of Nonaqueous Electrolytes in Electric Double-Layer Capacitors. *J. Phys. Chem. Lett.* **4**, 1260–1267 (2013).

134. Burt, Ryan, Birkett, Greg & Zhao, X. S. A review of molecular modelling of electric double layer capacitors. *Phys. Chem. Chem. Phys.* **16**, 6519–6538 (2014).

135. Baldelli, Steven. Surface Structure at the Ionic Liquid−Electrified Metal Interface. *Acc. Chem. Res.* **41**, 421–431 (2008).

136. Francisco, Brian E., Jones, Christina M., Lee, Se-Hee & Stoldt, Conrad R. Nanostructured all-solid-state supercapacitor based on Li2S-P2S5 glass-ceramic electrolyte. *Appl. Phys. Lett.* **100**, 103902 (2012).

137. Ulihin, A. S., Mateyshina, Yu. G. & Uvarov, N. F. All-solid-state asymmetric supercapacitors with solid composite electrolytes. *Solid State Ionics* **251**, 62–65 (2013).

138. Verma, Mohan L., Minakshi, Manickam & Singh, Nirbhay K. Synthesis and Characterization of Solid Polymer Electrolyte based on Activated Carbon for Solid State Capacitor. *Electrochim. Acta* **137**, 497–503 (2014).

139. Pal, Bhupender, Yasin, Amina, Kunwar, Ria, Yang, Shengyuan, Yusoff, Mashitah Mohd & Jose, Rajan. Polymer versus Cation of Gel Polymer Electrolytes in the Charge Storage of Asymmetric Supercapacitors. *Ind. Eng. Chem. Res.* **58**, 654–664 (2019).

140. Łatoszyńska, Anna A., Żukowska, Grażyna Zofia, Rutkowska, Iwona A., Taberna, Pierre-Louis, Simon, Patrice, Kulesza, Pawel J. & Wieczorek, Władysław. Non-aqueous gel polymer electrolyte with phosphoric acid ester and its application for quasi solid-state supercapacitors. *J. Power Sources* **274**, 1147–1154 (2015).

141. Fan, Le-Qing, Zhong, Ji, Wu, Ji-Huai, Lin, Jian-Ming & Huang, Yun-Fang. Improving the energy density of quasi-solid-state electric double-layer capacitors by introducing redox additives into gel polymer electrolytes. *J. Mater. Chem. A* **2**, 9011–9014 (2014).

142. Choudhury, N. A., Sampath, S. & Shukla, A. K. Hydrogel-polymer electrolytes for electrochemical capacitors: An overview. *Energy Environ. Sci.* **2**, 55–67 (2009).

143. Huang, Cheng-Wei, Wu, Ching-An, Hou, Sheng-Shu, Kuo, Ping-Lin, Hsieh, Chien-Te & Teng, Hsisheng. Gel Electrolyte Derived from Poly(ethylene glycol) Blending Poly(acrylonitrile) Applicable to Roll-to-Roll Assembly of Electric Double Layer Capacitors. *Adv. Funct. Mater.* **22**, 4677–4685 (2012).

144. Hsueh, Mei-Fang, Huang, Cheng-Wei, Wu, Ching-An, Kuo, Ping-Lin & Teng, Hsisheng. The Synergistic Effect of Nitrile and Ether Functionalities for Gel Electrolytes Used in Supercapacitors. *J. Phys. Chem. C* **117**, 16751–16758 (2013).

145. Duay, Jonathon, Gillette, Eleanor, Liu, Ran & Lee, Sang Bok. Highly flexible pseudocapacitor based on freestanding heterogeneous MnO2/conductive polymer nanowire arrays. *Phys. Chem. Chem. Phys.* **14**, 3329–3337 (2012).

146. Sudhakar, Y. N., Selvakumar, M. & Bhat, D. Krishna. LiClO4-doped plasticized chitosan and poly(ethylene glycol) blend as biodegradable polymer electrolyte for supercapacitors. *Ionics (Kiel).* **19**, 277–285 (2013).

147. Ramasamy, Chandrasekaran, Palma del vel, Jesús & Anderson, Marc. An activated carbon supercapacitor analysis by using a gel electrolyte of sodium salt-polyethylene oxide in an organic mixture solvent. *J. Solid State*

Electrochem. **18**, 2217–2223 (2014).

148. Wang, Shuang, Hsia, Ben, Carraro, Carlo & Maboudian, Roya. High-performance all solid-state micro-supercapacitor based on patterned photoresist-derived porous carbon electrodes and an ionogel electrolyte. *J. Mater. Chem. A* **2**, 7997–8002 (2014).

149. Pandey, G. P. & Hashmi, S. A. Ionic liquid 1-ethyl-3-methylimidazolium tetracyanoborate-based gel polymer electrolyte for electrochemical capacitors. *J. Mater. Chem. A* **1**, 3372–3378 (2013).

150. Murugan, Ramaswamy, Thangadurai, Venkataraman & Weppner, Werner. Fast Lithium Ion Conduction in Garnet-Type Li7La3Zr2O12. *Angew. Chemie Int. Ed.* **46**, 7778–7781 (2007).

151. Thangadurai, V. & Weppner, W. Recent progress in solid oxide and lithium ion conducting electrolytes research. *Ionics (Kiel).* **12**, 81–92 (2006).

152. Chong, Mee Yoke, Numan, Arshid, Liew, Chiam-Wen, Ng, H. M., Ramesh, K. & Ramesh, S. Enhancing the performance of green solid-state electric double-layer capacitor incorporated with fumed silica nanoparticles. *J. Phys. Chem. Solids* **117**, 194–203 (2018).

153. Ramzy, Adam & Thangadurai, Venkataraman. Tailor-Made Development of Fast Li Ion Conducting Garnet-Like Solid Electrolytes. *ACS Appl. Mater. Interfaces* **2**, 385–390 (2010).

154. Hu, Liangbing & Cui, Yi. Energy and environmental nanotechnology in conductive paper and textiles. *Energy Environ. Sci.* **5**, 6423–6435 (2012).

155. Jost, Kristy, Dion, Genevieve & Gogotsi, Yury. Textile energy storage in perspective. *J. Mater. Chem. A* **2**, 10776–10787 (2014).

156. El-Kady, Maher F. & Kaner, Richard B. Scalable fabrication of high-power graphene micro-supercapacitors for flexible and on-chip energy storage. *Nat. Commun.* **4**, 1475 (2013).

157. Sharifi, Farrokh, Ghobadian, Sasan, Cavalcanti, Flavia R. & Hashemi, Nastaran. Paper-based devices for energy applications. *Renew. Sustain. Energy Rev.* **52**, 1453–1472 (2015).

158. Ko, Yongmin, Kwon, Minseong, Bae, Wan Ki, Lee, Byeongyong, Lee, Seung Woo & Cho, Jinhan. Flexible supercapacitor electrodes based on real metal-

like cellulose papers. *Nat. Commun.* **8**, 536 (2017).

159. Li, Yingru, Sheng, Kaixuan, Yuan, Wenjing & Shi, Gaoquan. A high-performance flexible fibre-shaped electrochemical capacitor based on electrochemically reduced graphene oxide. *Chem. Commun.* **49**, 291–293 (2013).

160. Ambade, Rohan B., Ambade, Swapnil B., Salunkhe, Rahul R., Malgras, Victor, Jin, Sung-Ho, Yamauchi, Yusuke & Lee, Soo-Hyoung. Flexible-wire shaped all-solid-state supercapacitors based on facile electropolymerization of polythiophene with ultra-high energy density. *J. Mater. Chem. A* **4**, 7406–7415 (2016).

161. Shao, Yuanlong, El-Kady, Maher F., Wang, Lisa J., Zhang, Qinghong, Li, Yaogang, Wang, Hongzhi, Mousavi, Mir F. & Kaner, Richard B. Graphene-based materials for flexible supercapacitors. *Chem. Soc. Rev.* **44**, 3639–3665 (2015).

162. Puiggalí-Jou, Anna, Pérez-Madrigal, Maria M., del Valle, Luis J., Armelin, Elaine, Casas, María T., Michaux, Catherine, Perpète, Eric A., Estrany, Francesc & Alemán, Carlos. Confinement of a β-barrel protein in nanoperforated free-standing nanomembranes for ion transport. *Nanoscale* **8**, 16922–16935 (2016).

163. Zhao, Fan, Ma, Man Lung & Xu, Bing. Molecular hydrogels of therapeutic agents. *Chem. Soc. Rev.* **38**, 883–891 (2009).

164. Li, Jiayang, Kuang, Yi, Gao, Yuan, Du, Xuewen, Shi, Junfeng & Xu, Bing. d-Amino Acids Boost the Selectivity and Confer Supramolecular Hydrogels of a Nonsteroidal Anti-Inflammatory Drug (NSAID). *J. Am. Chem. Soc.* **135**, 542–545 (2013).

165. Vashist, Arti, Vashist, Atul, Gupta, Y. K. & Ahmad, Sharif. Recent advances in hydrogel based drug delivery systems for the human body. *J. Mater. Chem. B* **2**, 147–166 (2014).

166. Schneider, Hans-Jörg & Strongin, Robert M. Supramolecular Interactions in Chemomechanical Polymers. *Acc. Chem. Res.* **42**, 1489–1500 (2009).

167. Ionov, Leonid. Biomimetic Hydrogel-Based Actuating Systems. *Adv. Funct. Mater.* **23**, 4555–4570 (2013).

168. Molina, Brenda G., Cuesta, Sergi, Besharatloo, Hossein, Roa, Joan Josep,

Armelin, Elaine & Alemán, Carlos. Free-Standing Faradaic Motors Based on Biocompatible Nanoperforated Poly(lactic Acid) Layers and Electropolymerized Poly(3,4-ethylenedioxythiophene). *ACS Appl. Mater. Interfaces* **11**, 29427–29435 (2019).

169. Morales, Daniel, Palleau, Etienne, Dickey, Michael D. & Velev, Orlin D. Electro-actuated hydrogel walkers with dual responsive legs. *Soft Matter* **10**, 1337–1348 (2014).

170. Deligkaris, Kosmas, Tadele, Tadele Shiferaw, Olthuis, Wouter & den Berg], Albert [van. Hydrogel-based devices for biomedical applications. *Sensors Actuators B Chem.* **147**, 765–774 (2010).

171. Kopeček, Jindřich. Swell gels. *Nature* **417**, 389–391 (2002).

172. Peppas, N. A., Bures, P., Leobandung, W. & Ichikawa, H. Hydrogels in pharmaceutical formulations. *Eur. J. Pharm. Biopharm.* **50**, 27–46 (2000).

173. Zhang, Xi, Guan, Ying & Zhang, Yongjun. Ultrathin hydrogel films for rapid optical biosensing. *Biomacromolecules* **13**, 92–97 (2012).

174. Hoare, Todd R. & Kohane, Daniel S. Hydrogels in drug delivery: Progress and challenges. *Polymer (Guildf).* **49**, 1993–2007 (2008).

175. Peppas, N. A., Hilt, J. Z., Khademhosseini, A. & Langer, R. Hydrogels in Biology and Medicine: From Molecular Principles to Bionanotechnology. *Adv. Mater.* **18**, 1345–1360 (2006).

176. Seliktar, Dror. Designing Cell-Compatible Hydrogels. **336**, 1124–1129 (2012).

177. Chakrabarty, Rajesh, Mukherjee, Partha Sarathi & Stang, Peter J. Supramolecular Coordination: Self-Assembly of Finite Two- and Three-Dimensional Ensembles. *Chem. Rev.* **111**, 6810–6918 (2011).

178. Zhang, Qifeng, Uchaker, Evan, Candelaria, Stephanie L. & Cao, Guozhong. Nanomaterials for energy conversion and storage. *Chem. Soc. Rev.* **42**, 3127–3171 (2013).

179. Marcinek, M., Syzdek, J., Marczewski, M., Piszcz, M., Niedzicki, L., Kalita, M., Plewa-Marczewska, A., Bitner, A., Wieczorek, P., Trzeciak, T., Kasprzyk, M., P.Łężak, Zukowska, Z., Zalewska, A. & Wieczorek, W. Electrolytes for Li-ion transport – Review. *Solid State Ionics* **276**, 107–126

(2015).

180. Stephan], A. [Manuel. Review on gel polymer electrolytes for lithium batteries. *Eur. Polym. J.* **42**, 21–42 (2006).

181. Quartarone, Eliana & Mustarelli, Piercarlo. Electrolytes for solid-state lithium rechargeable batteries: recent advances and perspectives. *Chem. Soc. Rev.* **40**, 2525–2540 (2011).

182. Zhang, Tao & Zhou, Haoshen. From Li–O2 to Li–Air Batteries: Carbon Nanotubes/Ionic Liquid Gels with a Tricontinuous Passage of Electrons, Ions, and Oxygen. *Angew. Chemie Int. Ed.* **51**, 11062–11067 (2012).

183. Zhai, Wei, Zhu, Hua-jun, Wang, Long, Liu, Xiao-min & Yang, Hui. Study of PVDF-HFP/PMMA blended micro-porous gel polymer electrolyte incorporating ionic liquid [BMIM]BF4 for Lithium ion batteries. *Electrochim. Acta* **133**, 623–630 (2014).

184. Wang, Peng, Zakeeruddin, Shaik M., Moser, Jacques E., Nazeeruddin, Mohammad K., Sekiguchi, Takashi & Grätzel, Michael. A stable quasi-solid-state dye-sensitized solar cell with an amphiphilic ruthenium sensitizer and polymer gel electrolyte. *Nat. Mater.* **2**, 402–407 (2003).

185. Chen, Ching-Lun, Teng, Hsisheng & Lee, Yuh-Lang. In Situ Gelation of Electrolytes for Highly Efficient Gel-State Dye-Sensitized Solar Cells. *Adv. Mater.* **23**, 4199–4204 (2011).

186. Choudhury, Nurul A., Ma, Jia & Sahai, Yogeshwar. High performance and eco-friendly chitosan hydrogel membrane electrolytes for direct borohydride fuel cells. *J. Power Sources* **210**, 358–365 (2012).

187. Plumeré, Nicolas, Rüdiger, Olaf, Oughli, Alaa Alsheikh, Williams, Rhodri, Vivekananthan, Jeevanthi, Pöller, Sascha, Schuhmann, Wolfgang & Lubitz, Wolfgang. A redox hydrogel protects hydrogenase from high-potential deactivation and oxygen damage. *Nat. Chem.* **6**, 822–827 (2014).

188. Chen, Haisheng, Cong, Thang Ngoc, Yang, Wei, Tan, Chunqing, Li, Yongliang & Ding, Yulong. Progress in electrical energy storage system: A critical review. *Prog. Nat. Sci.* **19**, 291–312 (2009).

189. Zhang, Wei, Feng, Pan, Chen, Jian, Sun, Zhengming & Zhao, Boxin. Electrically conductive hydrogels for flexible energy storage systems. *Prog. Polym. Sci.* **88**, 220–240 (2019).

190. Pérez-Madrigal, Maria M., Edo, Miquel G. & Alemán, Carlos. Powering the future: Application of cellulose-based materials for supercapacitors. *Green Chem.* **18**, 5930–5956 (2016).

191. Pérez-Madrigal, Maria M., Estrany, Francesc, Armelin, Elaine, Díaz, David Díaz & Alemán, Carlos. Towards sustainable solid-state supercapacitors: Electroactive conducting polymers combined with biohydrogels. *J. Mater. Chem. A* **4**, 1792–1805 (2016).

192. Shi, Ye, Zhang, Jun, Pan, Lijia, Shi, Yi & Yu, Guihua. Energy gels: A bio-inspired material platform for advanced energy applications. *Nano Today* **11**, 738–762 (2016).

193. Chae, Ji Su, Park, Sul Ki, Roh, Kwang Chul & Park, Ho Seok. Electrode materials for biomedical patchable and implantable energy storage devices. *Energy Storage Mater.* **24**, 113–128 (2020).

194. Matsuda, Atsunori, Honjo, Hiroshi, Tatsumisago, Masahiro & Minami, Tsutomu. Electric double-layer capacitors using HClO4-doped silica gels as a solid electrolyte. *Solid State Ionics* (1998) doi:10.1016/s0167-2738(98)00280-x.

195. Gash, Alexander E., Tillotson, Thomas M., Satcher, Joe H., Hrubesh, Lawrence W. & Simpson, Randall L. New sol-gel synthetic route to transition and main-group metal oxide aerogels using inorganic salt precursors. *J. Non. Cryst. Solids* **285**, 22–28 (2001).

196. Li, Fengbin, Yao, Xueping, Wang, Zhaogen, Xing, Weihong, Jin, Wanqin, Huang, Jun & Wang, Yong. Highly porous metal oxide networks of interconnected nanotubes by atomic layer deposition. *Nano Lett.* **12**, 5033–5038 (2012).

197. Korhonen, Juuso T., Hiekkataipale, Panu, Malm, Jari, Karppinen, Maarit, Ikkala, Olli & Ras, Robin H. A. Inorganic hollow nanotube aerogels by atomic layer deposition onto native nanocellulose templates. *ACS Nano* **5**, 1967–1974 (2011).

198. Gao, Xiaonan, Esteves, Richard J., Luong, Thi Thu Hien, Jaini, Rajendra & Arachchige, Indika U. Oxidation-induced self-assembly of Ag nanoshells into transparent and opaque Ag hydrogels and aerogels. *J. Am. Chem. Soc.* **136**, 7993–8002 (2014).

199. Jung, Sung Mi, Jung, Hyun Young, Fang, Wenjing, Dresselhaus, Mildred S. & Kong, Jing. A facile methodology for the production of in situ inorganic nanowire hydrogels/aerogels. *Nano Lett.* **14**, 1810–1817 (2014).

200. Sayevich, Vladimir, Cai, Bin, Benad, Albrecht, Haubold, Danny, Sonntag, Luisa, Gaponik, Nikolai, Lesnyak, Vladimir & Eychmüller, Alexander. 3D assembly of all-inorganic colloidal nanocrystals into gels and aerogels. *Angew. Chemie - Int. Ed.* **55**, 6334–6338 (2016).

201. Vargas, R. A., Zapata, V. H., Matallana, E. & Vargas, M. A. More thermal studies on the PVOH/H3PO2/H2O solid proton conductor gels. *Electrochim. Acta* **46**, 1699–1702 (2001).

202. Rhim, Ji Won, Hwang, Ho Sang, Kim, Dae Sik, Park, Ho Bum, Lee, Chang Hyun, Lee, Young Moo, Moon, Go Young & Nam, Sang Yong. Aging effect of poly(vinyl alcohol) membranes crosslinked with poly(acrylic acid-co-maleic acid). *Macromol. Res.* **13**, 135–140 (2005).

203. Kang, Moon-Sung, Kim, Jong Hak, Won, Jongok, Moon, Seung-Hyeon & Kang, Yong Soo. Highly charged proton exchange membranes prepared by using water soluble polymer blends for fuel cells. *J. Memb. Sci.* **247**, 127–135 (2005).

204. Araujo, A. M., Neves, M. T., Azevedo, W. M., Oliveira, G. G., Ferreira, D. L., Coelho, R. A. L., Figueiredo, E. A. P. & Carvalho, L. B. Polyvinyl alcohol-glutaraldehyde network as a support for protein immobilisation. *Biotechnol. Tech.* **11**, 67–70 (1997).

205. Qiao, Jinli, Hamaya, Takeo & Okada, Tatsuhiro. New highly proton conductive polymer membranes poly(vinyl alcohol)–2-acrylamido-2-methyl-1-propanesulfonic acid (PVA–PAMPS). *J. Mater. Chem.* **15**, 4414–4423 (2005).

206. Fei, Haojie, Yang, Chongyang, Bao, Hua & Wang, Gengchao. Flexible all-solid-state supercapacitors based on graphene/carbon black nanoparticle film electrodes and cross-linked poly(vinyl alcohol)-H 2SO4 porous gel electrolytes. *J. Power Sources* **266**, 488–495 (2014).

207. Dasenbrock, Catherine O., Ridgway, Thomas H., Seliskar, Carl J. & Heineman, William R. Evaluation of the electrochemical characteristics of a poly(vinyl alcohol)/poly(acrylic acid) polymer blend. *Electrochim. Acta* **43**,

3497–3502 (1998).

208. Song, Bo, Li, Liyi, Zhu, Yuntong, Moon, Kyoung Sik & Wong, C. P. Miniaturized Integrated Micro-Supercapacitors as Efficient Power Sources for Wearable and Biocompatible Electronic Devices. *Proc. - Electron. Components Technol. Conf.* **2016**-**Augus**, 2046–2050 (2016).

209. Mangisetti, Sandhya Rani, Pari, Baraneedharan, Kamaraj, M. & Ramaprabhu, Sundara. Performance of Partially Exfoliated Nitrogen-Doped Carbon Nanotubes Wrapped with Hierarchical Porous Carbon in Electrolytes. *ChemSusChem* **11**, 1664–1677 (2018).

210. Pullanchiyodan, Abhilash, Manjakkal, Libu, Dervin, Saoirse, Shakthivel, Dhayalan & Dahiya, Ravinder. Metal Coated Conductive Fabrics with Graphite Electrodes and Biocompatible Gel Electrolyte for Wearable Supercapacitors. *Adv. Mater. Technol.* **5**, 1901107 (2020).

211. Elliott, Jeannine E., MacDonald, Mara, Nie, Jun & Bowman, Christopher N. Structure and swelling of poly(acrylic acid) hydrogels: Effect of pH, ionic strength, and dilution on the crosslinked polymer structure. *Polymer (Guildf).* **45**, 1503–1510 (2004).

212. Guo, Yunzhou, Zhou, Xiao, Tang, Qianqiu, Bao, Hua, Wang, Gengchao & Saha, Petr. A self-healable and easily recyclable supramolecular hydrogel electrolyte for flexible supercapacitors. *J. Mater. Chem. A* **4**, 8769–8776 (2016).

213. Kim, Kwang Man, Nam, Ji Hyun, Lee, Young Gi, Cho, Won Il & Ko, Jang Myoun. Supercapacitive properties of electrodeposited RuO2 electrode in acrylic gel polymer electrolytes. *Curr. Appl. Phys.* **13**, 1702–1706 (2013).

214. Feng, Enke, Gao, Wei, Li, Jingjing, Wei, Juanjuan, Yang, Qian, Li, Zhenliang, Ma, Xinxian, Zhang, Tiantian & Yang, Zhiming. Stretchable, Healable, Adhesive, and Redox-Active Multifunctional Supramolecular Hydrogel-Based Flexible Supercapacitor. *ACS Sustain. Chem. Eng.* (2020) doi:10.1021/acssuschemeng.9b07153.

215. Liao, Haiyang, Zhou, Fenglin, Zhang, Zhanzhan & Yang, Jia. A self-healable and mechanical toughness flexible supercapacitor based on polyacrylic acid hydrogel electrolyte. *Chem. Eng. J.* **357**, 428–434 (2019).

216. Jing, Xin, Mi, Hao Yang, Lin, Yu Jyun, Enriquez, Eduardo, Peng, Xiang Fang

& Turng, Lih Sheng. Highly Stretchable and Biocompatible Strain Sensors Based on Mussel-Inspired Super-Adhesive Self-Healing Hydrogels for Human Motion Monitoring. *ACS Appl. Mater. Interfaces* **10**, 20897–20909 (2018).

217. Fu, Rumin, Tu, Lingjie, Zhou, Yahong, Fan, Lei, Zhang, Fengmiao, Wang, Zhengao, Xing, Jun, Chen, Dafu, Deng, Chunlin, Tan, Guoxin, Yu, Peng, Zhou, Lei & Ning, Chengyun. A Tough and Self-Powered Hydrogel for Artificial Skin. *Chem. Mater.* **31**, 9850–9860 (2019).

218. Guarino, Vincenzo, Alvarez-Perez, Marco Antonio, Borriello, Anna, Napolitano, Teresa & Ambrosio, Luigi. Conductive PANi/PEGDA Macroporous Hydrogels For Nerve Regeneration. *Adv. Healthc. Mater.* **2**, 218–227 (2013).

219. Sivashanmugam, A., Arun Kumar, R., Vishnu Priya, M., Nair, Shantikumar V & Jayakumar, R. An overview of injectable polymeric hydrogels for tissue engineering. *Eur. Polym. J.* **72**, 543–565 (2015).

220. Hunt, John A., Chen, Rui, van Veen, Theun & Bryan, Nicholas. Hydrogels for tissue engineering and regenerative medicine. *J. Mater. Chem. B* **2**, 5319–5338 (2014).

221. Ionov, Leonid. Polymeric Actuators. *Langmuir* **31**, 5015–5024 (2015).

222. Wang, Xiangdong, Yu, Kexin, An, Ran, Han, Linglin, Zhang, Yulin, Shi, Lingying & Ran, Rong. Self-assembling GO/modified HEC hybrid stabilized pickering emulsions and template polymerization for biomedical hydrogels. *Carbohydr. Polym.* **207**, 694–703 (2019).

223. Peng, Zhiyuan, Zou, Yubo, Xu, Shiqi, Zhong, Wenbin & Yang, Wantai. High-Performance Biomass-Based Flexible Solid-State Supercapacitor Constructed of Pressure-Sensitive Lignin-Based and Cellulose Hydrogels. *ACS Appl. Mater. Interfaces* **10**, 22190–22200 (2018).

224. Deng, Lizhi & Zhang, Li Ming. Rheological characteristics of chitin/ionic liquid gels and electrochemical properties of regenerated chitin hydrogels. *Colloids Surfaces A Physicochem. Eng. Asp.* **586**, 124220 (2020).

225. de Oliveira, Ariel C., Sabino, Roberta M., Souza, Paulo R., Muniz, Edvani C., Popat, Ketul C., Kipper, Matt J., Zola, Rafael S. & Martins, Alessandro F. Chitosan/gellan gum ratio content into blends modulates the scaffolding

capacity of hydrogels on bone mesenchymal stem cells. *Mater. Sci. Eng. C* **106**, 110258 (2020).

226. Puckert, Christina, Tomaskovic-Crook, Eva, Gambhir, Sanjeev, Wallace, Gordon G., Crook, Jeremy M. & Higgins, Michael J. Electro-mechano responsive properties of gelatin methacrylate (GelMA) hydrogel on conducting polymer electrodes quantified using atomic force microscopy. *Soft Matter* **13**, 4761–4772 (2017).

227. Chen, Jinwei, Li, Enlong, Yan, Yujie, Yang, Qian, Cao, Shuguang, Zhong, Jianfeng, Chen, Huipeng & Guo, Tailiang. Flexible metal oxide synaptic transistors using biomass-based hydrogel as gate dielectric. *J. Phys. D. Appl. Phys.* **52**, (2019).

228. Moon, Won Gyun, Kim, Gil Pyo, Lee, Minzae, Song, Hyeon Don & Yi, Jongheop. A biodegradable gel electrolyte for use in high-performance flexible supercapacitors. *ACS Appl. Mater. Interfaces* **7**, 3503–3511 (2015).

229. Saborío, Mari Cruz G., Lanzalaco, Sonia, Fabregat, Georgina, Puiggalí, Jordi, Estrany, Francesc & Alemán, Carlos. Flexible Electrodes for Supercapacitors Based on the Supramolecular Assembly of Biohydrogel and Conducting Polymer. *J. Phys. Chem. C* **122**, 1078–1090 (2018).

230. Milroy, Craig A. & Manthiram, Arumugam. Bioelectronic Energy Storage: A Pseudocapacitive Hydrogel Composed of Endogenous Biomolecules. *ACS Energy Lett.* **1**, 672–677 (2016).

231. Zhao, Wen, Wei, Lu, Fu, Qiangang & Guo, Xin. High-performance, flexible, solid-state micro-supercapacitors based on printed asymmetric interdigital electrodes and bio-hydrogel for on-chip electronics. *J. Power Sources* **422**, 73–83 (2019).

232. Zeng, Juan, Wei, Lu & Guo, Xin. Bio-inspired high-performance solid-state supercapacitors with the electrolyte, separator, binder and electrodes entirely from: Kelp. *J. Mater. Chem. A* **5**, 25282–25292 (2017).

233. Wu, Xi Lin, Wen, Tao, Guo, Hong Li, Yang, Shubin, Wang, Xiangke & Xu, An Wu. Biomass-derived sponge-like carbonaceous hydrogels and aerogels for supercapacitors. *ACS Nano* **7**, 3589–3597 (2013).

234. Han, Jingquan, Ding, Qinqin, Mei, Changtong, Wu, Qinglin, Yue, Yiying & Xu, Xinwu. An intrinsically self-healing and biocompatible electroconductive

hydrogel based on nanostructured nanocellulose-polyaniline complexes embedded in a viscoelastic polymer network towards flexible conductors and electrodes. *Electrochim. Acta* **318**, 660–672 (2019).

235. Ding, Qinqin, Xu, Xinwu, Yue, Yiying, Mei, Changtong, Huang, Chaobo, Jiang, Shaohua, Wu, Qinglin & Han, Jingquan. Nanocellulose-Mediated Electroconductive Self-Healing Hydrogels with High Strength, Plasticity, Viscoelasticity, Stretchability, and Biocompatibility toward Multifunctional Applications. *ACS Appl. Mater. Interfaces* **10**, 27987–28002 (2018).

236. Saborío, M. G., Svelic, P., Casanovas, J., Ruano, G., Pérez-Madrigal, M. M., Franco, L., Torras, J., Estrany, F. & Alemán, C. Hydrogels for flexible and compressible free standing cellulose supercapacitors. *Eur. Polym. J.* **118**, (2019).

237. Liu, Limei, Wang, Binghao, Bai, Tong-chun & Dong, Bin. Thermal behavior and properties of chitosan fibers enhanced polysaccharide hydrogels. *Thermochim. Acta* **583**, 8–14 (2014).

238. Picone, Carolina Siqueira Franco & Cunha, Rosiane Lopes. Chitosan–gellan electrostatic complexes: Influence of preparation conditions and surfactant presence. *Carbohydr. Polym.* **94**, 695–703 (2013).

2. Objectives

This Thesis is divided in three independent parts, even though they have two common threads: 1) the development of components for energy storage devices, particularly electrochemical supercapacitors; and 2) the utilization of the biocompatible materials. In spite of such common facts, the specific objectives of each part are raised separately.

Part 1 is devoted to the development of a new biohydrogel and its utilization as solid electrolyte for electrochemical supercapacitors. Results of this part cover from chapter 3.1 and 3.3, whereas its specific objectives are:

1. Synthesize and characterize new biodegradable and biocompatible hydrogels by photo-crosslinking a known unsaturated polyestermide for the development of supporting electrolytes.
2. Examine the performance of the prepared polyesteramide hydrogels as novel and sustainable solid electrolytes for compact electrochemical supercapacitors manufactured with PEDOT electrodes.
3. Improve the performance as solid electrolyte of the polyesteramide hydrogels developed for objectives 1) and 2) using a synergistic strategy based on both computational molecular dynamics (MD) simulations and experimental approaches. More specifically, computer simulations have been conducted to investigate the effect of the pore structure in ions migration, looking for the optimization of the photo-polymerization time.
4. Compare the conductive and capacitive properties of polyesteramide hydrogels with those other biopolymeric hydrogels, which were previously developed to be used as solid electrolytes for electrochemical supercapacitors. For this purpose, properties of supercapacitors formed two conducting polymer electrodes sepatayed by κ-carrageenan, cellulose,

poly-γ-glutamic acid or polyesteramide hydrogels have been evaluated using electrochemical impedance spectroscopy (EIS).

Part 2 involves the fabrication of flexible, self-standing and conducting thin films as electrodes for biomedical applications that require shape-adapted electrochemical supercapacitors. Particular attention has been paid to the nano-structuration of such films. Results of this part correspond to chapters 3.4 and 3.5, whereas its specific objectives are:

5. Prepare multilayered polymeric films of submicrometric thickness with conducting and self-standing properties, using a strategy based on the alternation of insulating and conducting nanolayers.
6. Compare the performance as electrode material for electrochemical supercapacitor of multilayered films that differ in the number of layers and, therefore, in the chemical nature of the external layer (i.e. insulating polymer for and odd number of layers; conducting polymer for an even number of layers)..
7. Investigate the effect of oxidation and reduction on the structure and electronic properties of anodically polymerized PEDOT films similar to those used to prepare conducting layers in objective 6).

Finally, the design of conducting hydrogel is presented in the last part of this Thesis. In this case such hydrogel has been designed to be a multifunctional material that can be used not only as an electrode for electrochemical supercapacitors but also to manufacture sensitive pressure arrays and electro-regulated drug delivery systems. Accordingly, the specific objectives of this part are:

8. Synthesize and characterize an all-organic hydrogel forming an interpenetrated network between a CP and a biopolymer.
9. Test the performance of the hydrogel developed in objective 8 when it is used as a new flexible, self-healing, biocompatible and eco-friendly electrode for application in electrochemical capacitors.
10. Reformulate the hydrogel developed in objective 8 to fabricate a reusable pressure sensor array with capability for detecting both location and pressure of touches, and with good response time.
11. Reformulate the hydrogel developed in objective 8 to fabricate a carrier platform for electrically triggered drug delivery. The performance of the developed device will be tested using curcumin (CUR), a hydrophobic compound with a wide spectrum of biological and pharmacological activity, that is frequently employed as model drug.

3. Results

3.1 Biohydrogel from Unsaturated Polyesteramide: Synthesis, Properties and Utilization as Electrolytic Medium for Electrochemical Supercapacitors

3.1.1 Summary

The utilization of hydrogels derived from biopolymers as solid electrolyte (SE) of electrochemical supercapacitors (ESCs) is a topic of increasing interest because of their promising applications in biomedicine (*e.g.* for energy storage in autonomous implantable devices). In this work an unsaturated polyesteramide that contains phenylalanine, butenediol and fumarate as building blocks has been photo-crosslinked to obtain a hydrogel (UPEA-h). The structure of UPEA-h, which is characterized by a network of open interconnected pores surrounded by regions with compact morphology, favors ion transport, while the biodegradability and biocompatibility conferred by the α-amino acid unit and the ester group are appropriated for its usage in the biomedical field. Voltammetric and galvanostatic assays have been conducted to evaluate the behavior of UPEA-h when used as SE in ESCs with poly(3,4-ethylenedioxythiophene) (PEDOT) electrodes. Hence, PEDOT/UPEA-h devices displayed supercapacitor response of up 179 F/g and capacitance retention higher than 90%. Moreover, the long-term stability, leakage-current, and self-discharging response of PEDOT/UPEA-h ESCs reflect the great potential of UPEA-h as ion-conductive electrolyte. Indeed, the performance of PEDOT/UPEA-h is higher than found in analogous devices constructed using other biohydrogels as SE (*e.g.* κ-carrageenan, poly-γ-glutamic acid and cellulose hydrogels).

3.1.2 Introduction

The demand of flexible energy storage devices, including electrochemical supercapacitors (ESCs), increases with the development of flexible and wearable electronics [1–4]. Generally, the stretchable properties of energy storage devices are provided by elastic electrodes and/or electrolytes [5–7]. Within this context, cross-linked polymer hydrogels with high ionic conductivity and stretchable properties have been postulated as very promising electrolytes for multifunctional ESCs, even though not too much research has been carried out to address this issue yet [5,8–19]. The hierarchical porous structure of hydrogels makes them useful for other applications. Within this context, hydrogels from biopolymers (*i.e.* biohydrogels) are particularly attractive since, in addition of their demonstrated good performance as electrolytic media of ESCs [10,14–19], their biodegradability and biocompatibility are uniquely suitable for biological applications such as drug delivery vehicles and cell culture scaffolds. Consequently, such biohydrogels can be potentially used not only to power implantable medical devices (*e.g.* pacemakers) but also to fabrication multifunctional ESCs for biomedicine (*e.g.* self-powered drug release devices).

In recent years, the capabilities of some DNA [15,16], protein [17,18], and polysaccharide [17,19] biohydrogels as solid electrolytes (SEs) for multifunctional ESCs have been demonstrated. DNA biohydrogels made by enzymatic crosslinking of branched DNA monomers [20] were operative in cell culture media without exhibiting any cytotoxic effects. Accordingly, these devices showed potential interest as SEs for implantable energy storage devices able to operate in bioenvironments [15,16]. On the hand, the utilization as SE of gelatin biohydrogels, which were prepared using a mixture of water-soluble proteins, was hampered by their compact morphology [17]. In contrast, poly-γ-glutamic acid (γ-PGA) biohydrogels, which were obtained by crosslinking this polypeptide naturally

synthetized by a variety of members of the genus *Bacillus*, showed excellent properties not only as SE [18] but also as flexible electrode when combining with poly(3,4-ethylenedioxythiophene) (PEDOT) particles [7,21]. Regarding polysaccharides biohydrogels, the better response as SE was found for κ-carrageenan [17] and cellulose [19], whereas chitosan and alginate exhibited a poor behavior because of its poor mechanical integrity and water release, respectively [17].

In this work we explore a new strategy for the fabrication of biodegradable and biocompatible hydrogels as SEs for ESCs, using an unsaturated polyesteramide (UPEA) previously reported by Katsarava and co-workers [22]. This UPEA, which contains phenylalanine, butenediol and fumarate as building blocks, has been successfully photo-crosslinked to obtain a hydrogel (UPEA-h), as proved by FTIR and NMR characterizations. The α-amino acid unit and the ester group of the UPEA are expected to ensure the biodegradability and biocompatibility of the hydrogel. The work is organized as follows. After report on the synthesis of the UPEA and of the photo-crosslinking reaction used to produce the hydrogel, the morphological, topographical and thermal properties of UPEA-h are discussed. Then, the biodegradability and biocompatibility of the hydrogel are examined. Finally, the performance of UPEA-h as novel and sustainable SE for compact ESCs manufactured with PEDOT electrodes, hereafter denoted PEDOT/UPEA-h ESCs, has been analyzed. For this purpose, the electrochemical and electrical response of PEDOT/UPEA-h ESCs have been examined and compared with those previously obtained for ESCs prepared combining identical PEDOT electrodes with hydrogels derived from biopolymers as SEs.

3.1.3 Methods

3.1.3.1 Materials

All reagents were used as purchased without further purification. For the synthesis of the monomers and polymers, L-phenylalanine (reagent grade, 98%), *p*-toluenesulfonic acid monohydrate (ACS reagent, 98.5%), *cis*-2-butene-1,4-diol (97%), toluene (99.8%), fumaryl chloride (95%), acetone (HPLC, 99.9%), acryloyl chloride (97%), *N*,*N*-dimethylacetamide anhydrous (DMA), 1-butanol (ACS reagent, 99.4%), *n*-hexane (reagent grade) and 2-hydroxy-4'-(2-hydroxyethoxy)-2-methylpropiophenone (Irgacure) were purchased from Sigma-Aldrich and triethylamine, poly(ethylene glycol) (M_n= 10000 g/mol) and ethyl acetate were purchased from Fluka. Dimethyl sulfoxide (DMSO, Analytical reagent) was purchased from Fisher.

Acetonitrile (Reag. Ph. Eur. for analysis, ACS) was purchased from Panreac (Spain), while 3,4-ethylenedioxythiophene (EDOT, 97%) and $LiClO_4$ (ACS reagent, ≥ 95.0%; stored in an oven at 70 °C before use) were purchased from Sigma-Aldrich. NaCl salt sorting electrolyte for the electrochemical tests was purchased form Panreac. 3-(4,5-dimethylthiazol-2-yl)-2,5-diphenyl-2H-tetrazolium bromide (MTT), trypsin/EDTA, sodium phosphate buffer, sodium azide, Lipase *Rhizopus oryzae* and cell culture labware were purchased from Sigma-Aldrich (Spain).

3.1.3.2 Chemical characterization

Reaction products were analyzed using ^{1}H NMR and ^{13}C NMR spectra acquired with a Bruker Ascend 400 spectrometer operating at 400 MHz. Chemical shifts of all liquid state NMR were calibrated using tetramethylsilane as an internal standard. Deuterated chloroform and dimethyl sulfoxide-d_6 (DMSO-d_6) were used as solvent in the standard 5 mm NMR tubes. Solid state ^{13}C NMR spectra were

acquired with a solid standard bore cross polarization-magic angle spinning **CP-MAS probe** available for 300-950 MHz and 4 mm rotors. Experiments were carried out with freeze-dried samples at room temperature.

Infrared absorption spectra were recorded with a Fourier Transform FTIR 4100 Jasco spectrometer in the 4000–600 cm^{-1} range. A Specac Model MKII Golden Gate attenuated total reflection (ATR) cell with a heated Diamond ATR Top-Plate was used.

Molecular weight was estimated by gel permeation chromatography (GPC) using a liquid chromatograph (Shimadzu, model LC-8A, Tokyo, Japan) equipped with an Empower computer program (Waters). A PL HFIP gel column (Polymer Lab, Agilent Technologies Deutschland GmbH) and a refractive index detector (Shimadzu RID-10A) were employed. The polymer was dissolved and eluted in 1,1,1,3,3,3-hexafluoroisopropanol containing CF_3COONa (0.05 M). The flow rate was 1 mL/min, the injected volume 100 µL, and the sample concentration 2 mg/mL. Polymethyl methacrylate standards were used to determine the number and weight average molecular weights (M_n and M_w) and the polydispersion index (PDI)

3.1.3.3 Morphological, topographical, thermal and mechanical properties

The morphology of the photo-crosslinked synthetic unsaturated polyesteramide hydrogel (UPEA-h) was observed by scanning electron microscopy (SEM) using a Focused Ion Beam Zeiss Neon40 scanning electron microscope equipped with an energy dispersive X-ray (EDX) spectroscopy system and operating at 5 kV. All samples were sputter-coated with a thin carbon layer using a K950X Turbo Evaporator to prevent electron charging problems. Prior to SEM observation, samples were lyophilized. Thus, throughout the freeze-drying process, the capillary stress is avoided, preventing the collapse of the structure and minimizing the

shrinkage of the material. The size of pores was determined from the SEM images using the software SmartTIFF (v1.0.1.2.).

Atomic force microscopy (AFM) images were obtained with a Molecular Imaging PicoSPM using a NanoScope IV controller under ambient conditions. The tapping mode AFM was operated at constant deflection. The row scanning frequency was set to 1 Hz. AFM measurements were performed on various parts of the films, which provided reproducible images similar to those displayed in this work. The statistical application of the NanoScope Analysis software was used to determine the root mean square roughness (R_q), which is the average height deviation taken from the mean data plane.

Calorimetric data were obtained with a TA Instruments Q100 series equipped with a refrigerated cooling system (RCS). Experiments were conducted under a flow of dry nitrogen with a sample weight of approximately 3 mg, calibration being performed with indium. The T_{zero} calibration requested two experiments: the first was done without samples while the second one was performed with sapphire disks. The calorimetric analysis involved a heating run (20 ºC/min) of the as synthesized sample, a cooling run (20 ºC/min) after keeping the sample at 150 ºC from 2 minutes and finally a second heating run (20 ºC/min) of the cooled sample.

The thermal stability of the hydrogel was studied by thermal gravimetric analysis (TGA) at a heating rate of 20 ºC/min (sample weight *ca.* 5 mg) with a Q50 thermogravimetric analyser of TA Instruments and under a flow of dry nitrogen. Test temperatures ranged from 30 to 600 ºC.

The mechanical properties were evaluated using stress-strain assays with a Zwick Z2.5/TN1S testing machine. The deformation rate was 10 mm/min. Samples with a length of 10 mm, a width of 5 mm and a thickness of 1 mm were cut for stress-strain experiments. All the mechanical parameters reported in this work (*i.e.* Young modulus and tensile strength) correspond to the average of 8 independent measurements.

3.1.3.4 Enzymatic degradation studies.

Enzymatic degradation studies were carried out placing hydrogel samples (25 mg) in vials containing 0.1 mg/mL of lipase *Rhizopus oryzae* in a 5 mL of phosphate buffer saline (PBS) solution supplemented with 0.1 mg/mL of sodium azide to prevent contamination. Samples were incubated at 37 ºC in a shaking incubator set at 100 rpm for a total of three weeks. Vials were closed and sealed with parafilm to avoid loss of solution by evaporation, even though the PBS solution was replaced every 48 h. The variation of the weight loss against the exposure time was used to evaluate the enzymatic degradability from a quantitative point of view. For this purpose, samples (in triplicate) were removed every week from the solution, frozen, lyophilized and weighted. Degradation was quantitatively monitored as weight loss (WL, in %) of the hydrogels by applying the following:

$$WL=\frac{m_0-m_t}{m_0}\times 100 \qquad \text{(E.3.1.1)}$$

where m_0 is the weight of the hydrogel before the degradation assay and m_t is the weight of the film after exposure to the degradation medium. The influence of the enzymatic degradation on the morphology was evaluated by SEM, samples being sputter-coated with carbon before observation.

3.1.3.5 Cell adhesion and proliferation

Cellular assays were performed using Vero (green monkey kidney) and MDCK-SIAT1 (Canine Cocker Spaniel Kidney Sialic Acid Over Expression) cells, which exhibit epithelial morphology. These cells were selected due to their fast growth. Cells were cultured in DMEM high glucose buffered with 2.5 mM of 4-(2-hydroxyethyl)-1-piperazineethanesulfonic acid (HEPES), 10% fetal bovine serum (FBS), penicillin (100 units/mL), and streptomycin (100 µg/mL). The cultures were maintained in a humidified incubator with an atmosphere of 5% CO_2 and 95% O_2

at 37ºC. Culture media were changed every two days. When the cells reached 80-90% confluence, they were detached using 2 mL of trypsin (0.25% trypsin/EDTA) for 5 min at 37°C. Finally, cells were re-suspended in 5 mL of fresh medium and their concentration was determined by counting with a Neubauer camera using 0.4% trypan blue as a vital dye.

Tested hydrogel was placed in 24-well tissue culture polystyrene (TCPS) plates and sterilized using UV irradiation for 15 min in a laminar flux cabinet. Controls were simultaneously performed by culturing cells on wells without hydrogel. For adhesion and proliferation assays an aliquot of 40 μL with 2×10^4 cells and an aliquot of 90 μL with 5×10^4 cells, respectively, were deposited on the film of each well. Then, attachment of cells to the film surface was promoted by incubating under culture conditions for 30 min. Finally, 2 mL of the culture medium were added to each well. After 24 h, cellular adhesion was determined by quantifying the cells attached to the films or the control. Cellular proliferation was evaluated by quantifying the viable cells onto the evaluated materials after 7 days of culture.

Cellular viability was evaluated by the colorimetric MTT [3-(4,5-dimethylthiazol-2-yl)-2,5-diphenyltetrazolium bromide] assay. This assay measures the ability of the mitochondrial dehydrogenase enzyme of viable cells to cleave the tetrazolium rings of the MTT and form formazan crystals, which are impermeable to cell membranes and, therefore, are accumulated in healthy cells. This process is detected by a color change: the characteristic pale yellow of MTT transforms into the dark-blue of formazan crystals. Specifically, 50 μL of MTT solution (5 mg/mL in PBS) were added to each well. After 3 h of incubation, samples were washed twice with PBS and stored in clean wells. In order to dissolve formazan crystals, 1 mL of DMSO/methanol/water (70/20/10 % v/w) was added. Finally, the absorbance was measured in a plate reader at 570 nm. The viability results, derived from the

average of three replicates (*n*= 3) for each independent experiment, were normalized to the control, for relative percentages.

3.1.3.6 Electrochemical characterization

Before being used as supporting electrolyte (SE) in electrochemical supercapacitors (ESCs), washed UPEA-h hydrogels were loaded with a supporting electrolytic salt by immersion in a 0.5 M NaCl solution for 24 hours [19]. ESCs made of UPEA-h as novel and sustainable SE and poly(3,4-ethylenedioxythiophene) (PEDOT) electrodes, hereafter PEDOT/UPEA-h ESCs, were assembled in a two-step process. Firstly, UPEA-h pieces of rectangular shape, which were used as SE, were arranged separating two PEDOT electrodes at a distance of 1 mm, as illustrated in Figure 3.1.1. Finally, the external side of each PEDOT electrode was coated with another UPEA-h electrolyte piece. On the other hand, a supercapacitor configuration in which the UPEA-h based SE was replaced by a 0.5 M $NaHCO_3$ aqueous solution was used as control, hereafter denoted PEDOT/$NaHCO_3$.

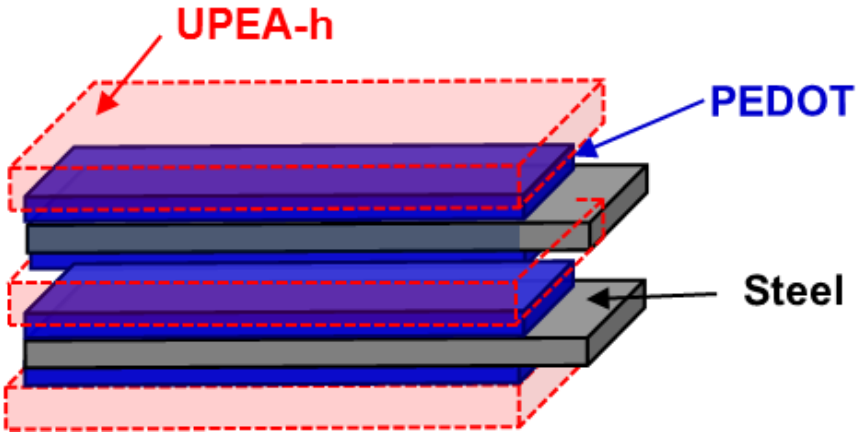

Figure 3.1.1. Scheme of the PEDOT/UPEA-h ESC.

The electrochemical response of PEDOT electrodes was studied in a two-electrode configuration by means of cyclic voltammetry (CV) and galvanostatic

charge/discharge (GCD) measurements. The specific capacitance (*SC*; in F/g) was expressed as:

$$SC = 4 \times \frac{C}{m} \qquad \text{(E.3.1.2)}$$

where *C* is the measured capacitance for the two-electrode cell and *m* the total mass of the active material in both electrodes. The multiplier 4 adjusts the capacitance of the cell and the combined mass of the two electrodes to the capacitance and mass of a single electrode.

GCD is the most commonly used procedure to determine the cell capacitance (*C*; in F) of a pseudocapacitor:

$$C = {I}\Big/{\left(\frac{dV}{dt}\right)} \qquad \text{(E.3.1.3)}$$

where *I* is the discharging current applied to the device and *dV/dt* should be calculated as $(V_{max} - ½V_{max})/(t_2 - t_1)$, where V_{max} corresponds to the highest voltage in the GCD curve after the voltage drop (V_{drop}) at the beginning of the discharging process. GCD curves between 0.0 and 0.8 V were run at different current densities (*i.e.* charge and discharge rates are specified in units of current per electrode mass): 0.30, 0.43, 0.61, 1.22 and 2.44 A/g, which corresponded to 0.35, 0.5, 0.7, 1.4 and 2.8 mA, respectively.

The coulombic efficiency (η, %) was evaluated as the ratio between the discharging and charging times (t_d and t_c, respectively) for the electrochemical window between 0.0 V and 0.8 V:

$$\eta = {t_d}/{t_c} \qquad \text{(E.3.1.4)}$$

Furthermore, CV measurements were also used to determine the cell capacitance, *C*, by applying Eqn E.3.1.3. In this case, *I* correspond to the average current during discharging (*i.e.* PEDOT reduction from 0.8 to 0.0 V), while *dV/dt* is the scan rate. Specifically, cyclic voltammograms were recorded from 0.0 V (initial and final potentials) to 0.8 V (reversal potential) at different scan rates: 10, 25, 50, 75, 100, 150 and 200 mV/s.

On the other hand, the cycling stability of the selected ESCs was tested by submitting the system to: *(i)* 1400 GCD cycles at a current density of 1.22 A/g from 0.0 V to 0.8 V; and *(ii)* 200 CV cycles at a scan rate of 50 mV/s from 0.0 V (initial and final potential) to 0.8 V (reversal potential). This potential interval was found to provide the highest capacitive response of PEDOT electrodes in devices with biopolymeric hydrogels as electrolytes [17]. Moreover, the evaluation of the self-discharging (SD) and leakage current (LC) curves of PEDOT/UPEA-h ESCs was carried out applying the following methodologies. In the first case, PEDOT/UPEA-h devices were charged to 0.8 V at 0.25 mA and kept at $1 \cdot 10^{-11}$ mA for 10 min (*i.e.* self-discharging). After that time, the device was discharged to 0 V at –1 mA. In the second case, after charging the device to 0.8 V at 0.25 mA, it was kept at 0.8 V for 300-600 seconds while recording the current data through the ESC (*i.e.* leakage current).

Electrochemical impedance spectroscopy (EIS) diagrams for PEDOT/UPEA-h ESCs were taken at open circuit (OCP) over the frequency range of 10^5 kHz to 10 Hz with potential amplitude of 0.05 V using an AUTOLAB-302N potentiostat/galvanostat. All experiments were performed at room temperature.

3.1.3.7 Synthesis of UPEA

The preparation of the di-*p*-toluenesulfonic acid salt of L-phenylalanine butene 1,4-diester (M1) and di-*p*-nitrophenyl fumarate (M2) monomers, as well as their solution polycondensation to produce the UPEA were adapted from Katsarava and co-workers [22].

Di-p-toluenesulfonic acid salt of L-phenylalanine butene 1,4-diester (M1). 0.03375 mol of L-phenylalanine (Phe), 0.03375 mol of *p*-toluenesulphonic acid monohydrate (TosOH) and 0.01687 mol of butenediol were dissolved in 90 mL of toluene. The solution was heated to 135 ºC and kept during at least 24 h in a Dean-

Stark trap until reaching the maximum volume of distilled water (*i.e.* 1.5 mL; 0.0669 mol) that the condensation makes. After this, the reaction mixture was cooling down and the obtained solid was filtered, dried and re-crystalized at least three times in dimethyl sulfoxide (DMSO). The obtained ^{1}H NMR and FTIR spectra are displayed in Figure 3.1.2.

Yield: 40 %. M.p.: 239 ºC. IR (cm^{-1}): 1737 (O=C), 1456 (=C–H).and 1191 (COO–). ^{1}H NMR (DMSO-d_6, ppm, δ): 8.41 (s, 3H, NH_3), 7.46, 7.09 (dd, 5H, arom), 7.31-7.22 (m,5H, Phe), 5.54 (t, 1H, CH), 4.66 (d, 2H, CH_2), 4.33 (t, 1H, CH), 3.07 (m, 4H, CH_2), 2.28 (s, 3H, CH_3).

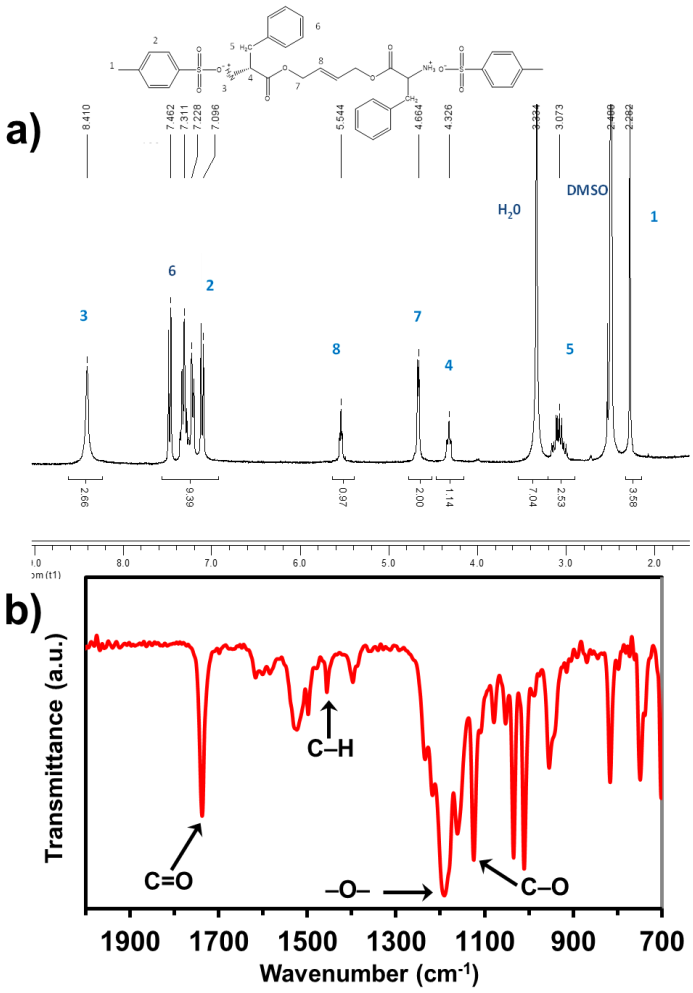

Figure 3.1.2. (a) ^{1}H-NMR and (b) FTIR spectra of di-p-toluenesulfonic acid salt of L-phenylalanine butene 1,4-diester (M1).

Di-p-nitrophenyl fumarate (M2). A 40 mL solution of fumaryl chloride (0.03 mol) in acetone was added dropwise to 100 mL of acetone with *p*-nitrophenol (0.06 mol) and triethylamine (0.06 mol) at –78 ºC using an acetone and dry ice bath. The system was kept under vigorous stirring at room temperature for 24 h. The resulting product was purified by recrystallization in acetonitrile. The obtained ^{1}H NMR and FTIR spectra are displayed in Figure 3.1.3.

Yield: 70 %. M.p.: 123 ºC. IR (cm^{-1}):3101 (C=CH–), 1734 (C=O), 1615, 957 (–CH=CH–CO–), 1519, 1345 (–NO_2), 1212 (COO–). ^{1}H NMR (DMSO-d_6, ppm, δ): 8.34 (d, 2H, arom), 7.59 (d, 2H, arom), 7.24 (s, 1H, =CH).

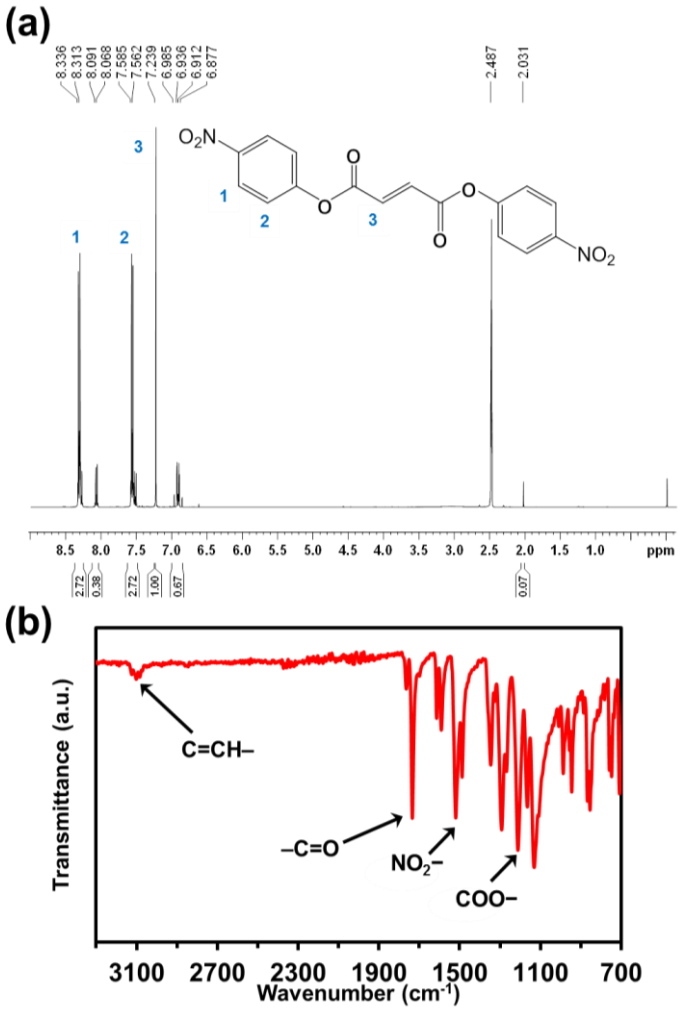

Figure 3.1.3. (a) ^{1}H-NMR and (b) FTIR spectra of di-*p*-nitrophenyl fumarate (M2).

UPEA. 1 mmol of M1 and 1 mmol of M2 were mixed in 4 mL of dry dimethylacetamide. Then, 2.2 mmol of trimethylamine were added dropwise and the solution was heated to 60 ºC with stirring for at least 96 h (*i.e.* until the complete dissolution of M1 and M2). The resulting solution was precipitated with cold ethyl acetate. The solid was filtered and extracted with ethyl acetate in a Soxhlet apparatus for 96 h, and finally dried. The obtained ^{1}H NMR and FTIR spectra are displayed in Figure 3.1.4.

Yield: 75 %. M.p.: 128 ºC. M_w: 60400 g/molPDI: 2.50. IR (cm^{-1}): 3315 (Amide A), 1736 (C=O), 1623 (Amide 1), 1530 (Amide 2), 1455 (=C–H, alkyl), 1170 (COO–). ^{1}H NMR (DMSO-d_6, ppm, δ): 8.93 (d,1H, NH), 7.22 (m, 5H, arom), 6.84 (s, 1H, CH), 5.58 (s, 1H, CH), 4.65 (s, 2H, CH_2), 4.58 (t, 1H, CH), 3.04 (m, 2H, CH_2).

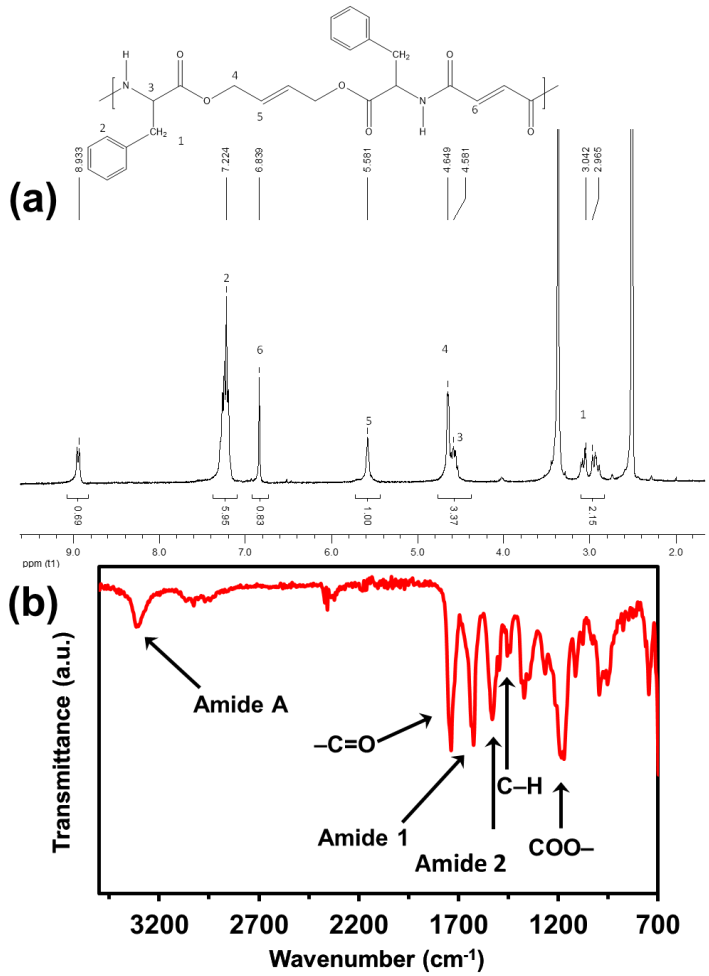

Figure 3.1.4. (a) ^{1}H-NMR and (b) FTIR spectra of UPEA.

3.1.4 Results and discussion

3.1.4.1 Synthesis of the UPEA-h

The preparation of the hydrogel involved three different steps: (a) the synthesis of the di-*p*-toluenesulfonic acid salt of L-phenylalanine butene 1,4-diester (M1) and di-*p*-nitrophenyl fumarate (M2) monomers (Schemes 3.1.1 and 3.1.2, respectively); (b) the solution polycondensation of M1 and M2 to produce UPEA chains with C=C double bonds in the backbone (Scheme 3.1.3); and (c) the photocrosslinking of the unsaturated bonds in UPEA. The synthesis of M1, M2 and UPEA (*i.e.* steps a and b), which were already described by Katsarava and co-workers [22], are reported in the Methods section.

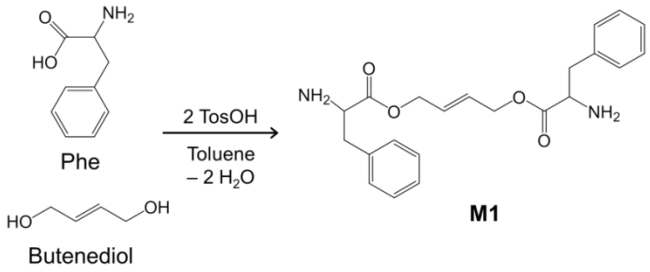

Scheme 3.1.1. Synthesis of the di-*p*-toluenesulfonic acid salt of L-phenylalanine butene 1,4-diester (M1).

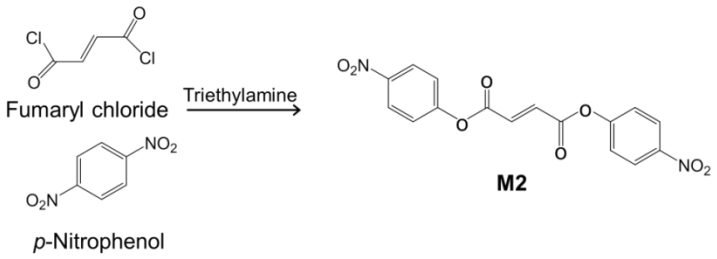

Scheme 3.1.2. Synthesis of di-*p*-nitrophenyl fumarate (M2).

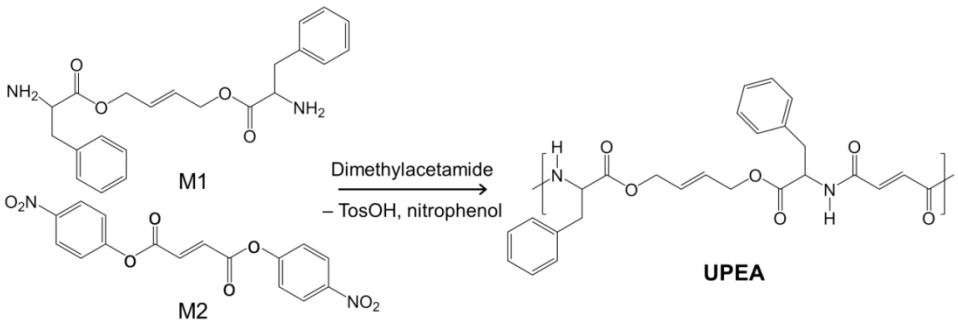

Scheme 3.1.3. Synthesis of the UPEA.

UPEA was used to produce UPEA-h using functionalized polyethylene glycol (*f*PEG) as cross-linker. The synthesis of *f*PEG (Scheme 3.1.4) and the hydrogel (Scheme 3.1.5), which was prepared to achieve the maximum cross-linking degree, are described below.

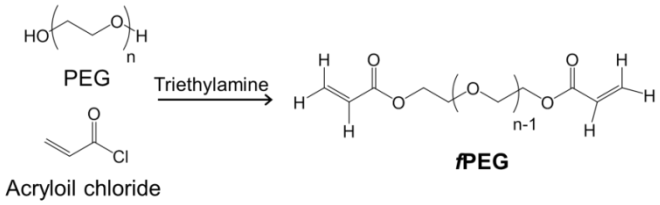

Scheme 3.1.4. Synthesis of the cross-linker (*f*PEG).

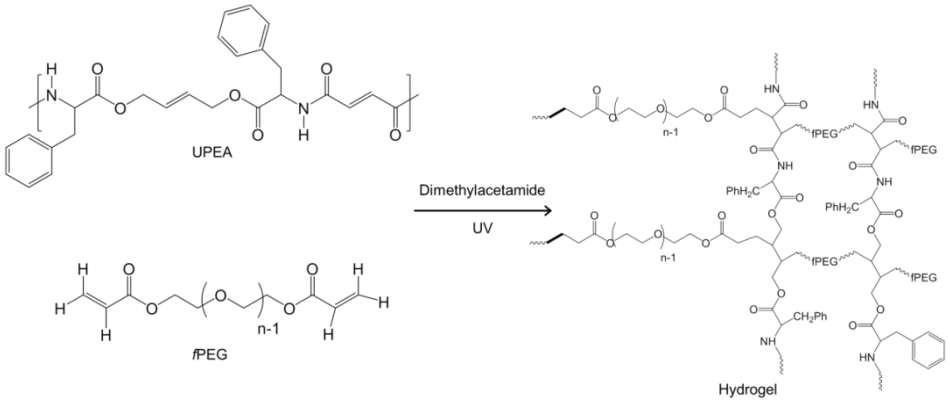

Scheme 3.1.5. Synthesis of the UPEA-h.

fPEG. 12 g (1.5 mmol) of PEG were dissolved in 150 mL of toluene at 45 ºC. The solution was cooled to room temperature and 1.67 (12.0 mmol) mL of

triethylamine were added. Then, 0.97 (12.0 mmol) mL of acryloil chloride were added dropwise. The mixture was heated to 80 ºC and kept for 3 h under nitrogen atmosphere. The obtained *f*PEG was precipitated in 700 mL of cold hexane (4 ºC), filtered and stored at 4 ºC. The obtained ^{1}H NMR and FTIR spectra are displayed in Figure 3.1.5.

Yield: 90 %. M_w= 32604 g/mol; PDI= 2.55. IR (cm^{-1}): 2885 (CH_2), 1724 (C=O), 1096 (C–O). ^{1}H NMR (DMSO-d_6, ppm, δ): 6.45, 5.82 (dd,1H,H_b), 6.37, 5.85 (dd,1H,H_a), 6.16 (m, 1H, CH), 4.31 (t, 2H, CH_2), 3.64 (t, CH_2).

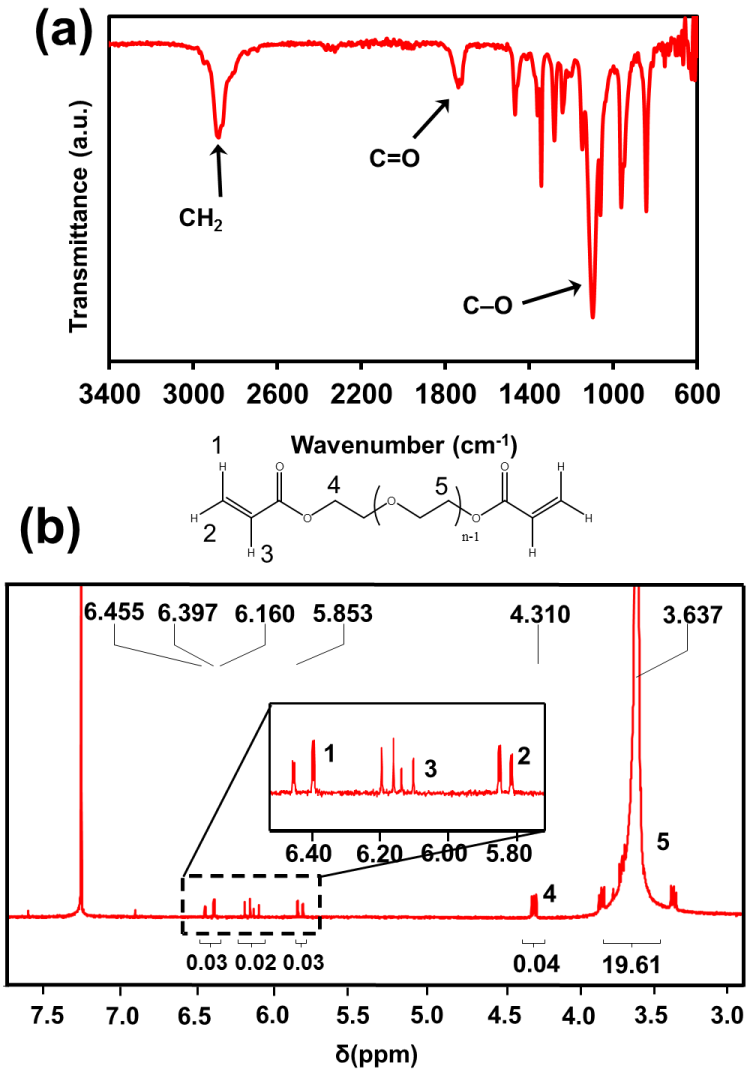

Figure 3.1.5. (a) FTIR and (b) ^{1}H-NMR spectra of the synthesized cross-linker, *f*PEG.

UPEA-h. 0.08 g of UPEA and 0.32 g of *f*PEG (*i.e.* 1/4 UPEA/*f*PEG w/w ratio) were dissolved in 2 mL of dimethylacetamide. The reticulation reaction was conducted by adding the photoinitiator irgacure 2959 (0.016 g, 5% wt. with respect to the total mass of the precursors). The solution was exposed to an UV lamp (230 V, 0.8 A) for 8 h at room temperature. The resulting gel was washed with distilled water, which was periodically replaced, during 3 days and afterwards lyophilized for its characterization. The obtained FTIR spectrum, a photograph of the hydrogel (hereafter denoted UPEA-h) and the ^{13}C CP/MAS spectrum are displayed in Figure 3.1.6.

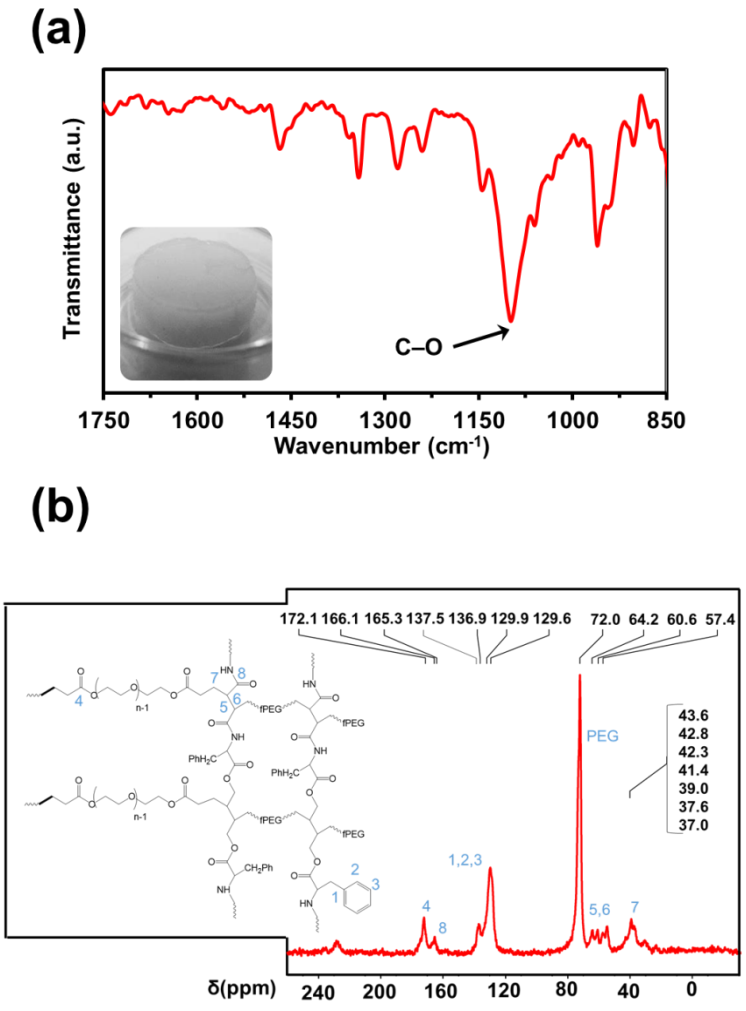

Figure 3.1.6. (a) FTIR and (b) ^{13}C-NMR spectra of the synthesized UPEA-h. A photograph of the hydrogel is displayed in (a).

Yield: 90 %. IR (cm^{-1}): 1096 (C–O). ^{13}C CP/MAS (100kHz, $\delta_{CP/MAS}$,ppm): 172.16 (COO), 166.10 (NH–C=O), 137.99, 129.93 (arom), 72.08 (polyethylene glycol; PEG), 64.25 (O=C–**C**H_2–N), 60.66 (O–CH_2), 57.40 (**C**H–CO–NH), 43-37 (CH_2).

3.1.4.2 Morphological, topographical, thermal and mechanical properties

As shown in Figure 3.1.7a, which displays scanning electron microscopy (SEM) micrographs, the lyophilized UPEA-h presents a homogeneous network structure with abundant pores. The size distribution of the pores, which tend to adopt an elliptic shape, is not uniform and ranges from 9 to 30 μm. This variability confers a relatively large standard deviation to the average diameter of pores, 17±7 μm. From the perspective of SE for ESCs, the structure of UPEA-h contains open interconnected pores surrounded by regions with compact morphology, which favors ion transport and provides mechanical stability and robustness to keep the electrodes at their positions.

Figure 3.1.7b displays a representative height atomic force microscopy (AFM) image and cross-sectional profiles of UPEA-h. The surface topography of the hydrogel is defined by the micrometric size of the pores that are separated by compact regions, which is fully consistent with SEM observations. The R_q determined for the hydrogel as a whole is 1.05±0.12 μm, this value decreasing to 119±29 nm when the pores are excluded from the measure and only the compact regions separating them are considered.

UPEA-h was a semicrystalline hydrogel due to the capability of the PEG segments (each one with more than 225 chemical repeat units) to crystallize. Thus, the differential scanning calorimetry (DSC) heating run of the as synthesized hydrogel showed a melting peak at 52.6 ºC and a small shoulder around 48.5 ºC (Figure 3.1.8a). The observed temperatures are in agreement with reported data

since they were between the reported temperature range between 63.0 ºC and 44.4 ºC that was determined for PEG homopolymers with molecular weights of 10,000 and 1,000 g/mol, respectively [23]. The corresponding melting enthalpy of UPEA-h gels was 96.9 J/g, which represents a crystallinity of 49.2 % by considering a melting enthalpy of 196.8 J/g for a 100% crystalline PEG [23]. This crystallinity increased to 61.5% when it was referred to the real PEG content (*i.e.* the presence of non crystallizable UPEA chains was not taken into account).

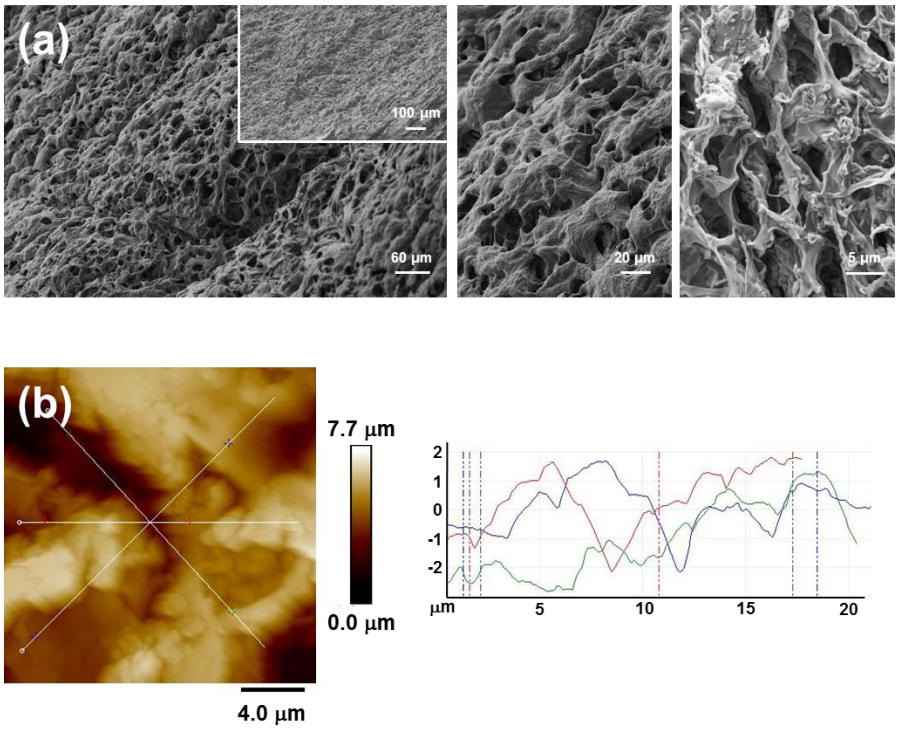

Figure 3.1.7. Representative (a) SEM micrographs at different magnifications and (b) AFM height image with the corresponding cross-section profiles of UPEA-h.

The PEG domains of the hydrogel were able to crystallize after being heated to 150 ºC. In fact, the enthalpy of the observed exothermic peak was comparable to that determined in the first heating run (*i.e.* 84.7 J/g with respect 96.9 J/g), a feature that suggest the capacity of preserving the basic mechanical properties after submitting the hydrogel to thermal treatments. The heating run obtained from a melt crystallized sample revealed also a small difference concerning the narrow melting peak that appeared at 52.8 ºC. In this case, the shoulder associated to

thinner lamellar crystals disappeared indicating that highly homogeneous crystalline domains could be obtained after the slow cooling process. Despite the significant crystallinity of the sample, a small glass transition signal could be observed around -52 ºC, being in good agreement with the values around -67 ºC and -52 ºC that are reported for PEG/polyethylene oxide (PEO) with higher molecular weights [24] (htt). Note that cross-linking did not play a significant effect on the mobility of PEG chains.

UPEA-h showed a high thermal stability (Figure 3.1.8b) since degradation started around 260 ºC. Decomposition took place according to two steps that appeared as a small shoulder and a peak at temperatures of 328 and 400 ºC, respectively. The main process involved a weight loss close to 80%, which is in concordance with the PEG content. The curves derived from the thermal gravimetric analysis (TGA) its derivative (DTGA) were in relative good agreement with the reported data for the degradation of PEG since a single decomposition step with a maximum DTGA peak at 426 ºC or 419 ºC was observed at a heating rate of 10 ºC/min with samples having molecular weights of 3,400 or 100,000 g/mol, respectively [24]. Note that peak temperature values should increase whit the heating rate and consequently thermal stability was clearly lower than observed for neat PEG. The DTGA shoulder observed at 328 ºC would probably be related to the decomposition of the UPEA main chain, enhancing the corresponding degradation products the decomposition of PEG segments. Finally, it should be indicated that a char yields close to 6% was determined at 600 ºC as consequence of the aromatic content of phenylalanine residues.

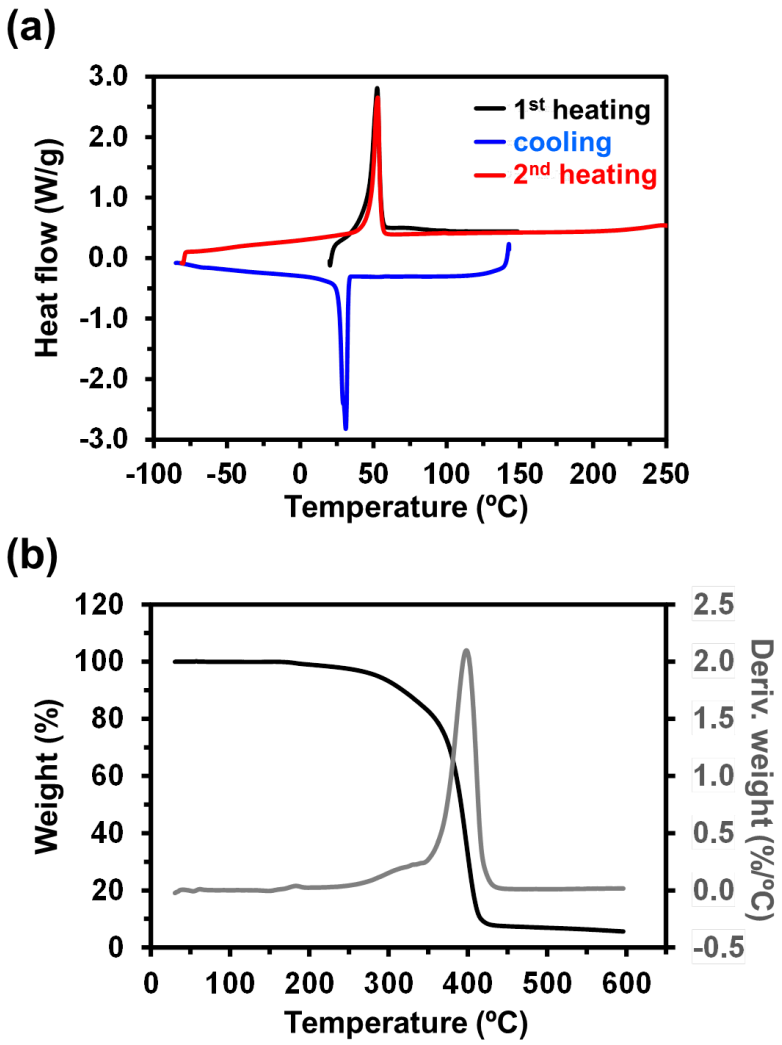

Figure 3.1.8. (a) Sequence of heating, cooling and reheating runs performed with the as synthesized UPEA-h sample. (b) TGA and DTGA curves of the UPEA-h sample.

The mechanical properties of UPEA-h, which have been determined by measuring stress-strain curves (Figure 3.1.9), reveals that the Young modulus and tensile strength are 2.3 ± 0.1 MPa and 66 ± 7 MPa, respectively. Unfortunately, it was not possible to evaluate the elongation at breakage since, in all cases, after reaching a certain elongation (*i.e.* from 24% to 29%, depending on the sample), the water leakage from the hydrogel caused the sliding of the jaws of the test machine and the consequent release of the sample. Obviously, this drawback also affects the numerical values of the Young modulus and tensile strength, which

should be considered as rough approximations only. In spite of this limitation, it should be remarked that the mechanical properties of UPEA-h are high. Thus, the modulus of most hydrogels is of the order of 0.1 MPa [25,26], which greatly limits their use. In recent years, a number of high modulus hydrogels have been developed, as for example, polyampholyte hydrogels ionically cross-linked (7.8 MPa) [27] and dual polyacrylamide–polyacrylic acid hydrogel with covalent and ionic cross-links (3.5 MPa) [28].

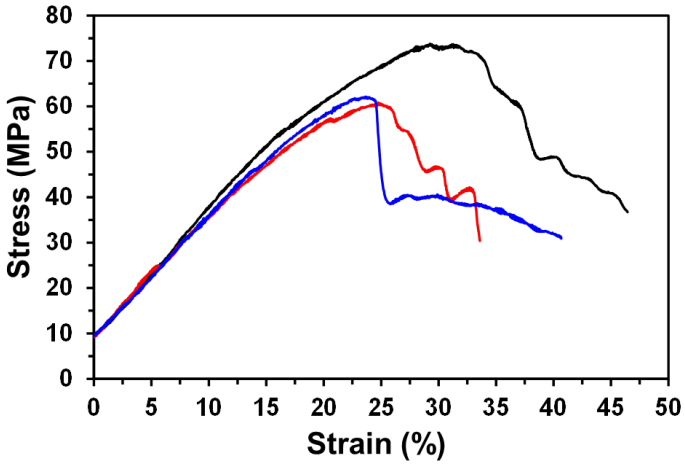

Figure 3.1.9. Three representative strain-stress curves of UPEA-h.

The swelling ratio (*SR*, %) of the UPEA-h was evaluated using the following Eqn E.3.1.5:

$$SR = \frac{w_W - w_D}{w_D} \qquad \text{(E.3.1.5)}$$

where w_W is the weight of the hydrogels as prepared (after the washing step) and w_D is the weight of the hydrogel after freeze-drying (dried hydrogel). The *SR* determined for the UPEA hydrogels is of 500% only, which is consistent with a high cross-linking degree. This value is comparable to that obtained for γ-PGA hydrogels with a high cross-linking degree (*i.e. SR* decreased from 4000% to 160% when the cross-linker : γ-PGA molar ratio increased from 1: 3.3 to 1:1) [18], but significantly lower than that achieved for sodium carboxymethyl cellulose

hydrogels (*i.e. SR* increased from 1064% to 2420% with the concentration of citric acid, which was the cross-linker) [19]. The low *SR* of UPEA hydrogels is expected to be very advantageous in terms of dimensional stability, which is crucial for the utilization of biohydrogels in the fabrication of energy storage devices [18,19,21].

3.1.4.3 Biodegradability and cell viability

Enzymatic degradation studies were conducted as is described in the Methods section, placing hydrogel samples in vials containing lipase *Rhizopus oryzae* in phosphate buffer saline (PBS). Samples were incubated at 37 ºC in a shaking incubator set at 100 rpm for a total of three weeks.

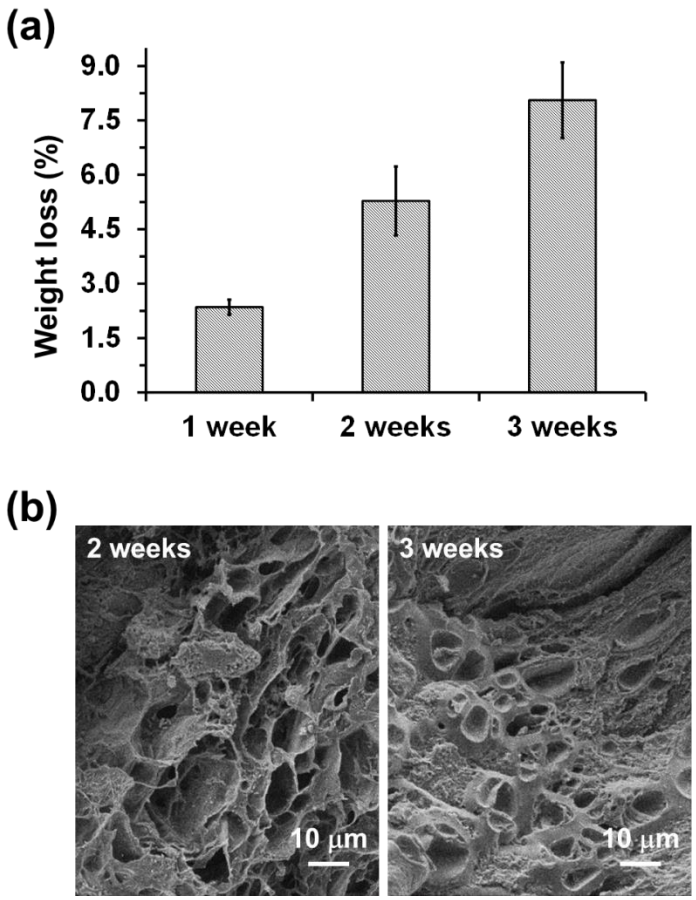

Figure 3.1.10. (a) Normalized weight loss (Eqn E.3.1.1) of UPEA-h after 1, 2 and 3 weeks of immersion in Lipase *Rhizopus oryzae*-containing PBS solution. (b) SEM micrograph of the UPEA-h after 2 and 3 weeks of immersion in above mentioned solution (left and right, respectively).

Figure 3.1.10a shows that weight loss (Eqn E.3.1.1) increases with the time of exposition to the degradation medium, reaching 8.1%±1.0% after 3 weeks. Weight loss has been attributed to the hydrolysis of the ester bonds, which is enzymatically catalyzed by the Lipase *Rhizopus oryzae*. Although the consistency of the hydrogel was apparently maintained during the whole 3 weeks period, the morphology of the hydrogel changed significantly. This is reflected in Figure 3.1.10b that compares SEM micrographs of the hydrogel after 2 and 3 weeks of exposition to the degradation medium. As it can be seen, the degraded fragments were retained in the surface of the hydrogel matrix, affecting the pores that were gradually occluded by the degraded material.

The response of the UPEA-h to cellular adhesion and proliferation has been compared with that of tissue culture polystyrene (TCPS), which consists on polystyrene exposed to a plasma gas in order to make it more hydrophilic and facilitate cell adhesion and growth *in vitro*. Assays were conducted using two cellular lines, Vero (green monkey kidney) and MDCK-SIAT (Canine Cocker Spaniel Kidney Sialic Acid Over Expression), which are epithelial-like cells. Quantitative results of cellular adhesion and proliferation assays are displayed in Figure 3.1.11a. Results indicate that UPEA-h does not promote cell adhesion with respect to the TCPS, differences being more marked for Vero cells than for MCDK-SIAT cells (*i.e.* the difference between the two substrates amounts to 55% and 23% for Vero and MDCK-SIAT, respectively). This behavior has been attributed to the surface roughness of the hydrogel (R_q= 1.05±0.12 μm), which is much higher and, therefore, less appropriated for cell attachment than that of the TCPS (R_q= 80 nm). Figure 3.1.11b displays micrographs recorded by SEM of Vero and MDCK-SIAT cells adhered onto UPEA-h.

Cell proliferation assays, which were performed by determining the cellular viability on the samples after seven days, reflect a significant enhancement in the

cellular colonization for UPEA-h. Evaluation of this increment with respect to the viability of adhered cells indicates that the preference of Vero and MDCK-SIAT cells is higher for the hydrogel than for the control (Figure 3.1.11a). Thus, although cell viabilities are still higher for the control than for the hydrogel, differences decreased to 25% and 8% for Vero and MDCK-SIAT cells, respectively. This growing in the cell viability evidences that the UPEA-h is biocompatible and can be considered as a potential candidate for biomedical applications.

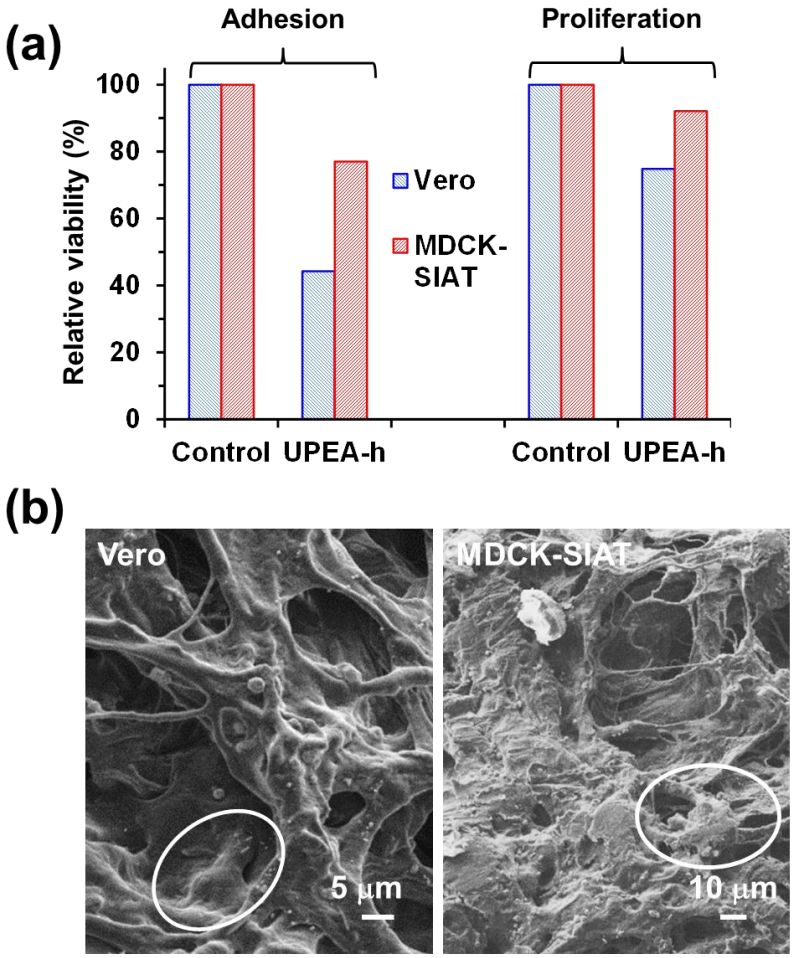

Figure 3.1.11. (a) Cellular adhesion and cellular proliferation on the surface of UPEA-h and TCPS plates (control). Vero and MDCK-SIAT cells were cultured during 24 h (adhesion assay) and 7 days (proliferation assay). The experiments were performed using three samples for each substrate. (b) SEM images of Vero and MDCK-SIAT cells adhered onto UPEA-h.

3.1.4.4. Electrochemical behavior of UPEA hydrogel as electrolyte

ESCs are electrochemical energy storage devices that operate on the simple mechanism of adsorption of ions from an electrolyte on a high-surface-area electrode. Thus, ESCs differ from ordinary capacitors in two important ways: (i) the electrodes have a much bigger area for the former than for latter; and (ii) the distance between the electrodes is much smaller for the former than for the latter. In an ordinary capacitor, the electrodes are separated by a relatively thick dielectric, as for example mica or plastic film. When the capacitor is charged, positive charges form on one electrode and negative charges on the other, creating an electric field between them. The field polarizes the dielectric, so its molecules line up in the opposite direction to the field and reduce its strength. In an ESC, there is no dielectric as such. Instead, both electrodes are soaked in an electrolyte, which can be liquid or solid. When the electrodes are charged up, charged ions from the electrolyte reorganize, and an electric double-layer is formed in the vicinity of the charged electrode surface (Scheme 3.1.6).

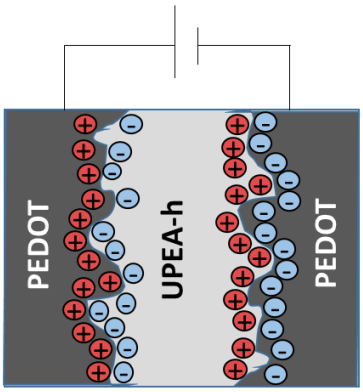

Scheme 3.1.6. Charging mechanism of ESCs.

In this work, the behavior of UPEA-h as solid electrolyte (SE) was evaluated in ESCs prepared using PEDOT electrodes, hereafter denoted PEDOT/UPEA-h. For this purpose, PEDOT films electropolymerized onto stainless steel sheets were carefully introduced into the UPEA-h hydrogel, which was previously loaded with

$NaHCO_3$ as supporting electrolytic salt (see Methods section), at a distance of 1 mm and fixed with tape to prevent movement during testing. Complete characterization of PEDOT electrodes was reported in previous work [17]. It is worth noting that PEDOT, which is an electrostable and biocompatible material [29–32], was also employed to prepare the electrodes of the ESCs used to investigate the performance of κ-carrageenan [17], γ-PGA [18], and cellulose [19] biohydrogels as SE. Accordingly, comparison of biohydrogels based on synthetic polyesteramides with those based on natural biopolymers is expected to provide information about the advantages of the former for energy storage applications (e.g. precise control of the photocrosslinking reaction to modulate the pore size and chemical design of the polymer to regulate the biodegradability). The electrochemical response of PEDOT/UPEA-h ESCs was investigated by cyclic voltammetry (CV) and galvanostatic charge/discharge (GCD) measurements using a two-electrode configuration to evaluate the performance of the whole cell.

Figure 3.1.12a compares the cyclic voltammograms recorded at different scan rates for PEDOT/UPEA-h ESCs. Cyclic voltammograms maintain an almost ideal rectangular shape for scan rates up to 100 mV/s, evidencing good capacitive behavior and small contact resistance. Moreover, the electrochemical activity of PEDOT electrodes, which corresponds to the similarity between the cathodic and anodic areas in the voltammograms, is very high, independently of the scan rate. Figure 3.1.12b displays the variation of the current density reached at the reversal potential (*i.e.* anodic current density), which measures the amount of oxidized molecules during the charging step, against the scan rate. The observed linear behavior (R^2= 0.9927) indicates that the electrochemical processes are not controlled by diffusion.

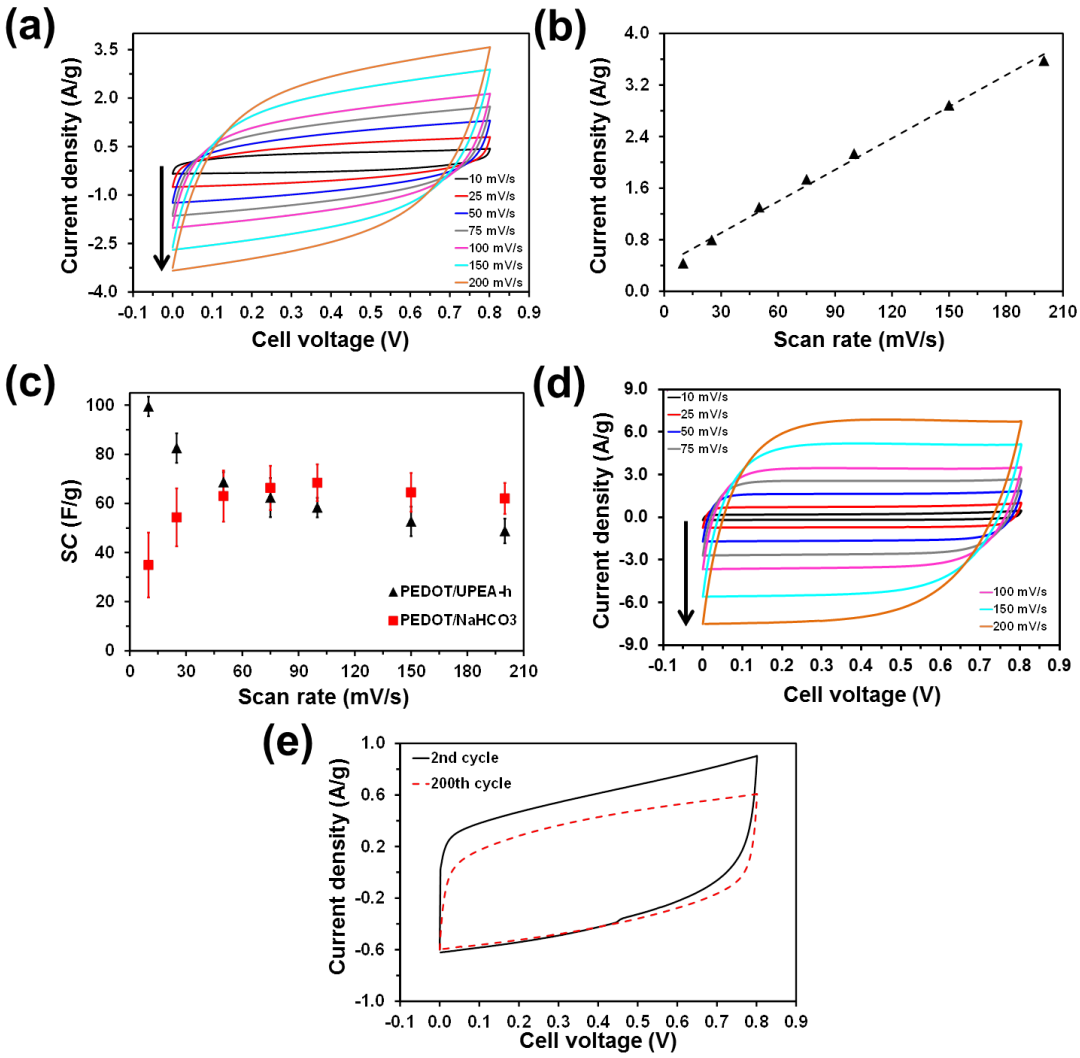

Figure 3.1.12. Characterization of PEDOT/UPEA-h and PEDOT/$NaHCO_3$ ESCs by CV. (a) Cyclic voltammograms (2^{nd} cycle shown) recorded from 0 to 0.8 V at scan rates of 10, 25, 50, 75, 100, 150 and 200 mV/s for PEDOT/UPEA-h. (b) Variation of the anodic current density against the scan rate for PEDOT/UPEA-h. (c) Variation of the *SC* against the scan rate for PEDOT/UPEA-h and PEDOT/$NaHCO_3$ ESCs. (d) Cyclic voltammograms (2^{nd} cycle shown) recorded from 0 to 0.8 V at scan rates of 10, 25, 50, 75, 100, 150 and 200 mV/s for PEDOT/$NaHCO_3$. (e) Comparison of the 2^{nd} and 200^{th} consecutive cyclic voltammograms recorded for PEDOT/UPEA-h (scan rate: 50 mV/s).

The specific capacitance (*SC*; in F/g) values obtained from CV measurements at different scan rates are displayed in Figure 3.1.12c. As it was expected, the *SC* decreases with increasing scan rate, which is fully consistent with the deviation

from the ideal rectangular shape of the voltammograms. Thus, *SC* decreases from 100±4 F/g to 49±5 F/g when the scan rate increases from 10 mV/s to 200 mV/s. For comparison, these results have been compared with those obtained for a control ESC device prepared using PEDOT electrodes and a $NaHCO_3$ (0.5 M) aqueous solution as electrolytic medium, denoted PEDOT/$NaHCO_3$. Cyclic voltammograms recorded PEDOT/$NaHCO_3$, which are shown Figure 3.1.12d, are more rectangular than those obtained for the same electrodes in UPEA hydrogel. However, the *SC* values obtained from CV measurements at low scan rates (*i.e.* below 75 mV/s) are higher for PEDOT/UPEA-h than for PEDOT/$NaHCO_3$ (*i.e.* the *SC* increases with the scan rate when the electrolyte is liquid). For scan rates from 75 to 200 mV/s, the *SC* values are slightly larger for the latter than for the former device (*i.e.* the largest difference is 13 F/g, which corresponds to less than 21%) (Figure 3.1.12c).

The PEDOT/UPEA-h ESC was submitted to 200 consecutive CV cycles from 0 to 0.8 V at a scan rate of 50 mV/s (Figure 3.1.12e). After such amount of cycles, the *SC* decreased from 68.7 F/g (2^{nd} cycle) to 67.4 F/g, which represents 98.1% of *SC* retention. Both PEDOT electrodes and hydrogel electrolyte underwent structural changes due to the swelling and shrinkage phenomena induced by the applied oxidation and reduction processes. However, in this case the access (oxidation) and escape (reduction) of dopant ions was only slightly reduced after 200 cycles, as observed from the voltammograms (Figure 3.1.12e). It is worth noting that, although voltammetric response of PEDOT/UPEA-h is similar to that reported for other ESCs prepared using PEDOT electrodes and biohydrogels from biopolymers as SE [17–19], the stability against consecutive redox cycles is higher for the device with UPEA-h.

Results from GCD measurements are displayed in Figure 3.1.13. Charging-discharging processes at different current densities led to symmetric GCD curves with a typical triangular shape and a V_{drop} at the beginning of the discharging.

Although the triangular shape of the GCD curves is better defined for PEDOT/$NaHCO_3$ than for PEDOT/UPEA-h, independently of the current density used, the *SC* values are systematically lower for the former than for the latter (Figures 3.1.13a-c). This is because discharging and charging times are about ~20% higher for PEDOT/UPEA-h ESCs than for PEDOT/$NaHCO_3$ ESCs, independently of the current density. The *SC* of the device with the hydrogel decreases from 179±12 to 114±7 F/g when current density increases from 0.30 to 2.43 A/g, while the *SC* values of the device with $NaHCO_3$ remain at around 65 F/g for all the examined current densities (Figure 3.1.13b). Moreover, PEDOT/UPEA-h ESCs were submitted to 1,400 GCD cycles at a current density of 0.43 A/g from 0 V to 0.8 V, which corresponds to t_c and t_d values of approximately 17-19 seconds (Figure 3.1.13d). After such amount of cycles, the *SC* decreased from 162 F/g to 149 F/g, which represents 92% of *SC* retention.

Comparison of the results obtained by GCD for PEDOT/UPEA-h with those achieved for ESCs prepared using identical PEDOT electrodes but κ-carrageenan [17], γ-PGA [18] or carboxymethyl cellulose [19] biohydrogels as SE (PEDOT/κ-car, PEDOT/γ-PGA and PEDOT/CMC, respectively) evidences that, in general, the former provides best response. The *SC* determined for PEDOT/κ-car, PEDOT/γ-PGA and PEDOT/CMC by GCD was 79[17], 159 [18] and 77 [19] F/g, respectively. This represents a reduction in the capacitive performance of more than 50% for the devices with κ-carrageenan and carboxymethyl cellulose hydrogels. Moreover, the retention of the *SC* after 1,400 consecutive GCD cycles was lower than 90% for PEDOT/κ-car and PEDOT/γ-PGA [17,19]. An exception to this behavior was found for PEDOT/CMC, which showed a self-stabilizing behavior. Thus, the *SC* of PEDOT/CMC ESC increased by 15% after 1400 charge-discharge cycles (*i.e.* from 76.8 to 88.7 F/g). In spite of this advantageous property, the *SC* of PEDOT/CMC was 40% lower than that of PEDO/UPEA-h after 1400 cycles.

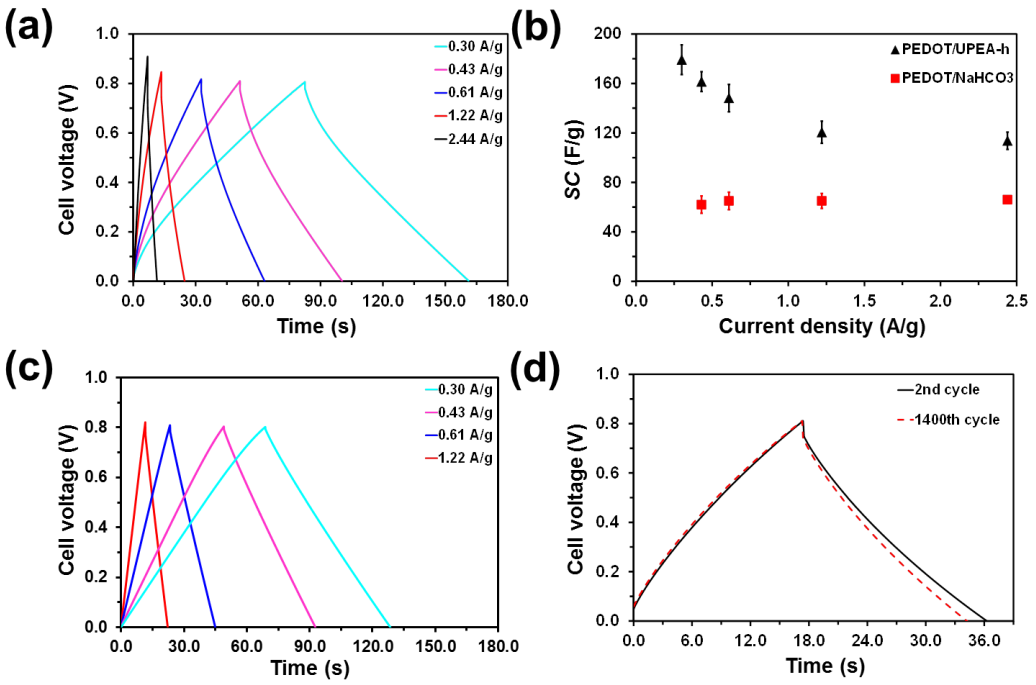

Figure 3.1.13. Characterization of PEDOT/UPEA-h and PEDOT/$NaHCO_3$ ESCs by GCD. (a) GCD curves recorded from 0 to 0.8 V at different current densities for the PEDOT/UPEA-h (2^{nd} cycle shown). (b) Variation of the *SC* against the current density for PEDOT/UPEA-h and PEDOT/$NaHCO_3$ ESCs. (c) GCD curves recorded from 0 to 0.8 V at different current densities for PEDOT/$NaHCO_3$ (2^{nd} cycle shown). (d) Comparison of the GCD curves recorded from 0 to 0.8 V at 0.43 A/g after 2 and 1400 consecutive cycles for PEDOT/UPEA-h.

Figure 3.1.14a shows the variation of the Coulombic efficiency (η) against the current density for PEDOT/UPEA-h. The Coulombic efficiency, which ranges from 0.92 to 0.78, decreases with the increasing V_{drop} and, therefore, with increasing current density (Figure 3.1.13a). However, the Coulombic efficiency remains higher than 0.90 for low current densities $\leq$ 0.61 A/g, indicating that these are the most appropriated charge-discharge conditions for the PEDOT/UPEA-h ESC.

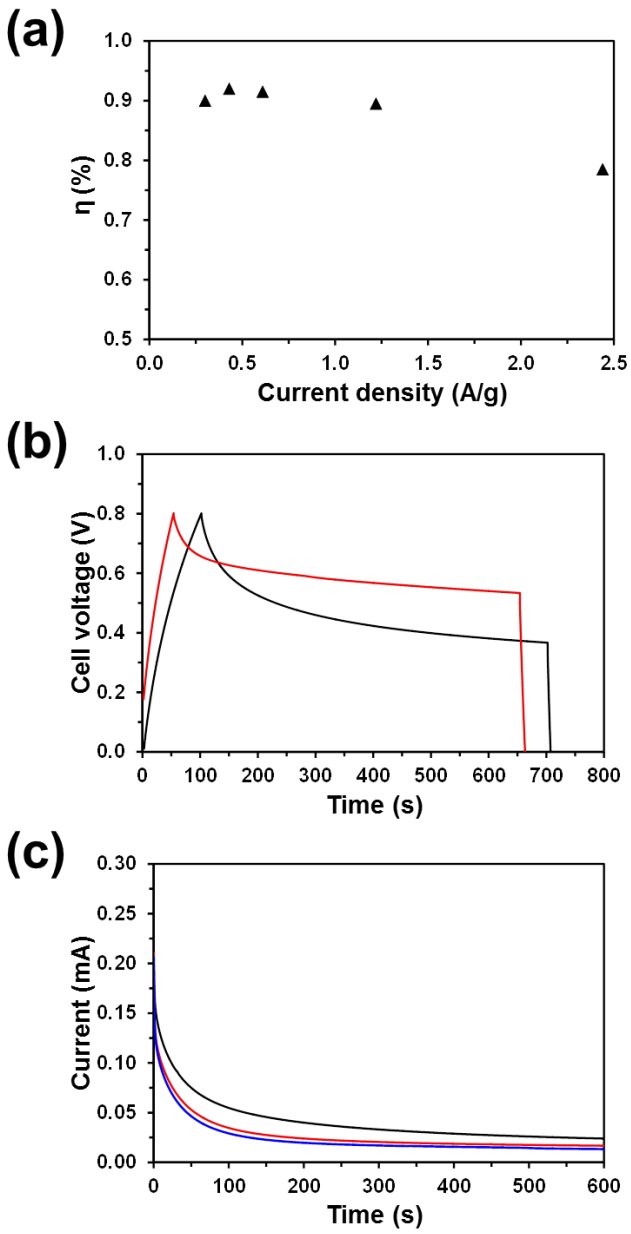

Figure 3.1.14. (a) Variation of the Coulombic efficiency (η) against the current density and both (b) self-discharge and (c) leakage current curves for PEDOT/UPEA-h ESCs.

Application of ESCs is mainly limited to short-term energy storage due to the self-discharge processes, which cause substantial voltage decay, leakage current and loss of stored energy. Self-discharge, which is typically defined as the voltage drop after a set period of time, affects the electrochemical response of the ESC by decreasing the power and energy densities. Self-discharge is influenced by the

chemistry and electrochemistry of the system, the purity of reagents and electrolyte, and the temperature [33,34]. In this work, the self-discharging (SD) was determined by charging the PEDOT/UPEA-h ESC to 0.8 V at 0.25 mA, keeping it at $1 \cdot 10^{-11}$ mA for 10 min (self-discharging), and discharging to 0.0 V at –1 mA. For most of the cases, the cell voltage ended at voltages comprised between 0.4 and 0.5 V after the set period of time (Figure 3.1.14b), which indicates that in the short term the self-discharging tendency of the PEDOT/UPEA-h device is very low.

Another self-discharging parameter is the leakage current, which represents the stable parasitic current expected when the capacitor is held indefinitely on charge at the rated voltage [35]. The leakage current was measured by charging the ESC to 0.8 V at 0.25 mA, keeping that potential for 5 or 10 minutes and, finally, recording the current data through the ESC. Figure 3.1.14c shows how the current quickly decreases to a value comprised between 13 and 24 μA that remained the rest of the time. This small leakage current is associated to a good stability of the PEDOT/UPEA-h ESC, which is crucial for energy storage applications.

The ionic conductivity of the UPEA-h was determined using electrochemical impedance spectroscopy (EIS). Accordingly, the impedance was measured for frequencies ranging from 10 to 10^5 Hz using a previously reported through-plane impedance cell [36]. Figure 3.1.15 displays the collected impedance (*Z*) data for three independent replicas as Nyquist plots. These consist in a capacitive semicircle in the high-frequency range and a straight ascending vertical line (almost 90º to the real axis) in the low-frequency range. This vertical line, which can be described as a "*capacitive spike*", is consistent with a double-layer porous capacitor and reflects the diffusion of the supporting $NaHCO_3$ ions.

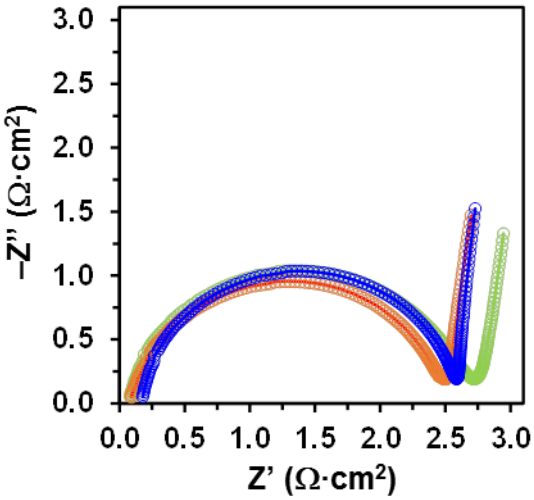

Figure 3.1.15. Nyquist plots recorded for UPEA-h.

The hydrogel conductivity (σ , in S/cm) was calculated from Eqn E.3.1.6:

$$\sigma = \frac{L}{R \cdot A} \qquad \text{(E.3.1.6)}$$

where L is the thickness of the SE (0.1 cm); A is the area of the electrode (1×1 cm^2), and R is the hydrogel resistance. The average conductivity determined for UPEA-h using three independent replicas is 0.039 ± 0.002 S/cm. Although this conductivity is smaller than the ones observed for hydrogels made of conducting polymers [37,38], which are able to exhibit electronic in addition to ionic conductivity, it is higher than that displayed by conventional gel polymer electrolytes (*ca.* 10^{-3} S/cm) under ambient conditions [39] and comparable to those of advanced biohydrogels (*e.g.* cellulose hydrogels prepared using ionic liquids, 0.040 S/cm) [40].

3.1.5 Conclusions

To conclude, we have reported the characterization of UPEA-h, which was synthesized by photo-crosslinking UPEA chains that contain phenylalanine, butenediol and fumarate as building blocks. The morphology of UPEA-h is appropriated for its utilization as SE in ESCs while the biocompatibility and

biodegradability confers applicability in the biomedical field. ESCs prepared using PEDOT as electrode material and UPEA-h as SE exhibit excellent performance: the *SC* obtained by CV and GCD extends from 100 to 49 F/g and 179 to 114 F/g, respectively, depending on the scan rate and the current density; high cyclic stability and Coulombic efficiency; low self-discharging tendency; and small leakage current. Our work shows that UPEA-h presents a better behavior as SE than biohydrogels derived from biopolymers, as for example natural and modified polysaccharides (κ-carrageenan and carboxymethyl cellulose, respectively) and polypeptides, without any detriment in the biocompatibility. Therefore, UPEA-h has great potential as SE material for the fabrication of flexible ESCs for self-powered biomedical implants and represents an excellent alternative to the biohydrogels derived from biopolymers typically used.

References

1. Wang, Xianfu, Lu, Xihong, Liu, Bin, Chen, Di, Tong, Yexiang & Shen, Guozhen. Flexible energy-storage devices: Design consideration and recent progress. *Adv. Mater.* **26**, 4763–4782 (2014).

2. El-Kady, Maher F. & Kaner, Richard B. Scalable fabrication of high-power graphene micro-supercapacitors for flexible and on-chip energy storage. *Nat. Commun.* **4**, 1475 (2013).

3. Zhao, Yu, Liu, Borui, Pan, Lijia & Yu, Guihua. 3D nanostructured conductive polymer hydrogels for high-performance electrochemical devices. *Energy Environ. Sci.* **6**, 2856–2870 (2013).

4. Li, Xinda, Liu, Li, Wang, Xianzong, Ok, Yong Sik, Elliott, Janet A. W., Chang, Scott X. & Chung, Hyun Joong. Flexible and Self-Healing Aqueous Supercapacitors for Low Temperature Applications: Polyampholyte Gel Electrolytes with Biochar Electrodes. *Sci. Rep.* **7**, 1–11 (2017).

5. Wang, Zhikui & Pan, Qinmin. An Omni-Healable Supercapacitor Integrated in Dynamically Cross-Linked Polymer Networks. *Adv. Funct. Mater.* **27**, 1–8 (2017).

6. Tang, Qianqiu, Chen, Mingming, Yang, Chongyang, Wang, Wenqiang, Bao, Hua & Wang, Gengchao. Enhancing the Energy Density of Asymmetric Stretchable Supercapacitor Based on Wrinkled CNT@MnO2 Cathode and CNT@polypyrrole Anode. *ACS Appl. Mater. Interfaces* **7**, 15303–15313 (2015).

7. Saborío, Mari Cruz G., Lanzalaco, Sonia, Fabregat, Georgina, Puiggalí, Jordi, Estrany, Francesc & Alemán, Carlos. Flexible Electrodes for Supercapacitors Based on the Supramolecular Assembly of Biohydrogel and Conducting Polymer. *J. Phys. Chem. C* **122**, 1078–1090 (2018).

8. Huang, Yan, Zhong, Ming, Huang, Yang, Zhu, Minshen, Pei, Zengxia, Wang, Zifeng, Xue, Qi, Xie, Xuming & Zhi, Chunyi. A self-healable and highly stretchable supercapacitor based on a dual crosslinked polyelectrolyte. *Nat. Commun.* **6**, (2015).

9. Chu, Xiang, Huang, Haichao, Zhang, Haitao, Zhang, Hepeng, Gu, Bingni, Su, Hai, Liu, Fangyan, Han, Yu, Wang, Zixing, Chen, Ningjun, Yan, Cheng, Deng, Wen, Deng, Weili & Yang, Weiqing. Electrochemically building three-

dimensional supramolecular polymer hydrogel for flexible solid-state micro-supercapacitors. *Electrochim. Acta* **301**, 136–144 (2019).

10. Armelin, Elaine, Pérez-Madrigal, Maria M., Alemán, Carlos & Díaz, David Díaz. Current status and challenges of biohydrogels for applications as supercapacitors and secondary batteries. *J. Mater. Chem. A* **4**, 8952–8968 (2016).

11. Tao, Feng, Qin, Liming, Wang, Zhikui & Pan, Qinmin. Self-Healable and Cold-Resistant Supercapacitor Based on a Multifunctional Hydrogel Electrolyte. *ACS Appl. Mater. Interfaces* **9**, 15541–15548 (2017).

12. Li, Huili, Lv, Tian, Sun, Huanhuan, Qian, Guiju, Li, Ning, Yao, Yao & Chen, Tao. Ultrastretchable and superior healable supercapacitors based on a double cross-linked hydrogel electrolyte. *Nat. Commun.* **10**, 1–8 (2019).

13. Rong, Qinfeng, Lei, Wenwei, Huang, Jin & Liu, Mingjie. Low Temperature Tolerant Organohydrogel Electrolytes for Flexible Solid-State Supercapacitors. *Adv. Energy Mater.* **8**, 1–7 (2018).

14. Pérez-Madrigal, Maria M., Edo, Miquel G. & Alemán, Carlos. Powering the future: Application of cellulose-based materials for supercapacitors. *Green Chem.* **18**, 5930–5956 (2016).

15. Hur, Jaehyun, Im, Kyuhyun, Kim, Sang Won, Kim, Un Jeong, Lee, Junho, Hwang, Sekyu, Song, Jaejung, Kim, Sungjee, Hwang, Sungwoo & Park, Nokyoung. DNA hydrogel templated carbon nanotube and polyaniline assembly and its applications for electrochemical energy storage devices. *J. Mater. Chem. A* **1**, 14460–14466 (2013).

16. Hur, Jaehyun, Im, Kyuhyun, Hwang, Sekyu, Choi, Byounglyong, Kim, Sungjee, Hwang, Sungwoo, Park, Nokyoung & Kim, Kinam. DNA hydrogel-based supercapacitors operating in physiological fluids. *Sci. Rep.* **3**, 1–7 (2013).

17. Pérez-Madrigal, Maria M., Estrany, Francesc, Armelin, Elaine, Díaz, David Díaz & Alemán, Carlos. Towards sustainable solid-state supercapacitors: Electroactive conducting polymers combined with biohydrogels. *J. Mater. Chem. A* **4**, 1792–1805 (2016).

18. Pérez-Madrigal, Maria M., Edo, Miquel G., Díaz, Angélica, Puiggalí, Jordi & Alemán, Carlos. Poly-γ-glutamic Acid Hydrogels as Electrolyte for Poly(3,4-

ethylenedioxythiophene)-Based Supercapacitors. *J. Phys. Chem. C* **121**, 3182–3193 (2017).

19. Pérez-Madrigal, Maria M., Edo, Miquel G., Saborío, Maricruz G., Estrany, Francesc & Alemán, Carlos. Pastes and hydrogels from carboxymethyl cellulose sodium salt as supporting electrolyte of solid electrochemical supercapacitors. *Carbohydr. Polym.* **200**, 456–467 (2018).

20. Um, Soong Ho, Lee, Jong Bum, Park, Nokyoung, Kwon, Sang Yeon, Umbach, Christopher C. & Luo, Dan. Enzyme-catalysed assembly of DNA hydrogel. *Nat. Mater.* **5**, 797–801 (2006).

21. Saborío, Maricruz G., Zukić, Šejla, Lanzalaco, Sonia, Casanovas, Jordi, Puiggalí, Jordi, Estrany, Francesc & Alemán, Carlos. Prototyping flexible supercapacitors produced with biohydrogel. *Mater. Today Commun.* **16**, 60–70 (2018).

22. Guo, Kai, Chu, C. C., Chkhaidze, E. & Katsarava, R. Synthesis and characterization of novel biodegradable unsaturated poly(ester amide)s. *J. Polym. Sci. Part A Polym. Chem.* **43**, 1463–1477 (2005).

23. Pielichowski, Krzysztof & Flejtuch, Kinga. Differential scanning calorimetry studies on poly(ethylene glycol) with different molecular weights for thermal energy storage materials. *Polym. Adv. Technol.* **13**, 690–696 (2002).

24. Vrandečić, Nataša Stipanelov, Erceg, Matko, Jakić, Miće & Klarić, Ivka. Kinetic analysis of thermal degradation of poly(ethylene glycol) and poly(ethylene oxide)s of different molecular weight. *Thermochim. Acta* **498**, 71–80 (2010).

25. Gao, Guorong, Du, Gaolai, Sun, Yuanna & Fu, Jun. Self-healable, tough, and ultrastretchable nanocomposite hydrogels based on reversible polyacrylamide/montmorillonite adsorption. *ACS Appl. Mater. Interfaces* **7**, 5029–5037 (2015).

26. Liu, Sijun & Li, Lin. Recoverable and Self-Healing Double Network Hydrogel Based on κ-Carrageenan. *ACS Appl. Mater. Interfaces* **8**, 29749–29758 (2016).

27. Sun, Tao Lin, Kurokawa, Takayuki, Kuroda, Shinya, Ihsan, Abu Bin, Akasaki, Taigo, Sato, Koshiro, Haque, Md Anamul, Nakajima, Tasuku & Gong, Jian Ping. Physical hydrogels composed of polyampholytes

demonstrate high toughness and viscoelasticity. *Nat. Mater.* **12**, 932–937 (2013).

28. Lin, Peng, Ma, Shuanhong, Wang, Xiaolong & Zhou, Feng. Molecularly engineered dual-crosslinked hydrogel with ultrahigh mechanical strength, toughness, and good self-recovery. *Adv. Mater.* **27**, 2054–2059 (2015).

29. Marzocchi, Marco, Gualandi, Isacco, Calienni, Maria, Zironi, Isabella, Scavetta, Erika, Castellani, Gastone & Fraboni, Beatrice. Physical and Electrochemical Properties of PEDOT:PSS as a Tool for Controlling Cell Growth. *ACS Appl. Mater. Interfaces* **7**, 17993–18003 (2015).

30. del Valle, Luis J., Estrany, Francesc, Armelin, Elaine, Oliver, Ramón & Alemán, Carlos. Cellular adhesion, proliferation and viability on conducting polymer substrates. *Macromol. Biosci.* **8**, 1144–1151 (2008).

31. Shi, Ye, Peng, Lele & Yu, Guihua. Nanostructured conducting polymer hydrogels for energy storage applications. *Nanoscale* **7**, 12796–12806 (2015).

32. Kirchmeyer, Stephan & Reuter, Knud. Scientific importance, properties and growing applications of poly(3,4-ethylenedioxythiophene). *J. Mater. Chem.* **15**, 2077–2088 (2005).

33. Andreas, Heather A. Self-Discharge in Electrochemical Capacitors: A Perspective Article. *J. Electrochem. Soc.* **162**, A5047–A5053 (2015).

34. Wang, Zixing, Chu, Xiang, Xu, Zhong, Su, Hai, Yan, Cheng, Liu, Fangyan, Gu, Bingni, Huang, Haichao, Xiong, Da, Zhang, Hepeng, Deng, Weili, Zhang, Haitao & Yang, Weiqing. Extremely low self-discharge solid-state supercapacitors: Via the confinement effect of ion transfer. *J. Mater. Chem. A* **7**, 8633–8640 (2019).

35. Xu, Yuxi, Lin, Zhaoyang, Huang, Xiaoqing, Liu, Yuan, Huang, Yu & Duan, Xiangfeng. Flexible solid-state supercapacitors based on three-dimensional graphene hydrogel films. *ACS Nano* **7**, 4042–4049 (2013).

36. Müller, Franciélli, Ferreira, Carlos A., Azambuja, Denise S., Alemán, Carlos & Armelin, Elaine. Measuring the proton conductivity of ion-exchange membranes using electrochemical impedance spectroscopy and through-plane cell. *J. Phys. Chem. B* **118**, 1102–1112 (2014).

37. Pan, Lijia, Yu, Guihua, Zhai, Dongyuan, Lee, Hye Ryoung, Zhao, Wenting,

Liu, Nian, Wang, Huiliang, Tee, Benjamin C. K., Shi, Yi, Cui, Yi & Bao, Zhenan. Hierarchical nanostructured conducting polymer hydrogel with high electrochemical activity. *Proc. Natl. Acad. Sci. U. S. A.* **109**, 9287–9292 (2012).

38. Mawad, Damia, Artzy-Schnirman, Arbel, Tonkin, Joanne, Ramos, Jose, Inal, Sahika, Mahat, Muzamir M., Darwish, Nadim, Zwi-Dantsis, Limor, Malliaras, George G., Gooding, J. Justin, Lauto, Antonio & Stevens, Molly M. Electroconductive Hydrogel Based on Functional Poly(Ethylenedioxy Thiophene). *Chem. Mater.* **28**, 6080–6088 (2016).

39. Choudhury, N. A., Sampath, S. & Shukla, A. K. Hydrogel-polymer electrolytes for electrochemical capacitors: An overview. *Energy Environ. Sci.* **2**, 55–67 (2009).

40. Kasprzak, Dawid, Stępniak, Izabela & Galiński, Maciej. Electrodes and hydrogel electrolytes based on cellulose: fabrication and characterization as EDLC components. *J. Solid State Electrochem.* **22**, 3035–3047 (2018).

3.2 Doped photo-crosslinked polyesteramide hydrogel as solid electrolyte for supercapacitors

3.2.1 Summary

High-performance hydrogels play a crucial role as solid electrolytes for flexible electrochemical supercapacitors (ESCs). More specifically, all solid-state ESCs based on renewable, biodegradable and/or biocompatible hydrogels doped with inorganic salts as electrolytes are attractive not only because of their contribution to reduce the resource consumption and/or the generation of electronic garbage, but also due to their potential applicability in the biomedical field. Here, computer simulations have been combined with experimental measurements to probe the outstanding capability as solid electrolyte of photo-crosslinked unsaturated polyesteramide hydrogels containing phenylalanine, butenediol and fumarate, and doped with NaCl (UPEA-Phe/NaCl). Atomistic molecular dynamics simulations have shown the influence of the hydrogel pore structure in Na^+ and Cl^- ions migration, suggesting that UPEA-Phe/NaCl hydrogels prepared without completing the photo-*crosslinking reaction* will exhibit better behavior as solid electrolyte. Theoretical predictions have been confirmed by potentiodynamic and galvanostatic studies on ESCs fabricated using poly(3,4-ethylenedioxythiophene) electrodes and UPEA-Phe/NaCl hydrogels, which were obtained using different times of exposure to UV radiation (*i.e.* 4 and 8 h for uncomplete and complete photo-crosslinking reaction). Moreover, the behavior as solid electrolyte of the UPEA-Phe/NaCl hydrogel prepared using a photo-polymerization time of 4 h has been found to be significantly superior to those exhibited by different polypeptide and polysaccharide hydrogels, which were analyzed using ESCs with identical electrodes and experimental conditions.

3.2.2 Introduction

Among modern flexible and wearable energy storage devices, compressible, stretchable and bendable electrochemical supercapacitors (ESCs) show great potential for practical applications because of its high power density, environmental friendliness, safety, fast rate of charging-discharging and long cycling lifetime [1–6]. Flexible ESCs require that all device components, the electrodes and the electrolyte, to be flexible. In the last few years a huge amount of work has been devoted to develop and characterize flexible electrodes [7–14]. Besides, polymeric hydrogels have attracted increasing attention as flexible electrolytes because of their minimum leakage compared to liquid electrolytes and relatively high ionic conductivity, especially when compared to solid polymers [15–21].

Polymer hydrogel electrolytes have been prepared using synthetic polymers, as for example polyvinyl alcohol [15–18] and polyacrylic acid [19,20]. However, in recent years the utilization of hydrogels based on biopolymers from biomass and/or synthetic biopolymers based on natural constituents is gaining more attention [21–35]. These bio-based solid electrolytes exhibit important advantages, for instance renewability, earth abundancy, low-cost, biodegradability, biocompatibility and/or environmental friendless. Thus, fabrication of bio-based electrolytes contributes to reduce not only the resource consumption but also the enormous electronic garbage after their service lifetime.

In the last few years we have been interested in the development of solid electrolytes for ESCs based on natural polysaccharides, such as κ-carrageenan [23,24] and cellulose [25], and on synthetic biopolymers, as for example poly-γ-glutamic acid [26] and phenylalanine-containing unsaturated polyesteramides (UPEAs) [27]. Interestingly, a photo-crosslinked UPEA hydrogel containing phenylalanine, butenediol and fumarate as building blocks and doped with NaCl (UPEA-Phe/NaCl), exhibited better behavior as supporting electrolyte than biohydrogels

derived from polysaccharides and polypeptides doped with same salt, without any detriment in the biodegradability and biocompatibility [27].

Studies on polysaccharides and polypeptides showed that the performance of biohydrogels as solid electrolytes is known to depend on the porous structure [25,26]. Thus, systems with large inter-connected pores were found to favor the transport of ions, exhibiting better response. Key in the control of the pore architecture and network structure is the synthesis of the hydrogel (*e.g.* regulating the concentration of polymer : crosslinker agent ratio or using templates). However, in the case of photo-crosslinked UPEAs this is expected to be done by adjusting the photo-polymerization time (*i.e.* the time of exposure to UV radiation). In this work we employ a synergistic strategy based on both computational molecular dynamics (MD) simulations and experimental approaches to optimize the properties of the UPEA-Phe/NaCl as solid electrolyte. More specifically, atomistic MD simulations have been conducted to investigate the effect of the pore structure in ions migration. Computational results have been used to reduce the photo-polymerization time from 8 h to 4 h, enhancing significantly the response of UPEA-Phe/NaCl as solid electrolyte, which has been proved by comparing key performance parameters. Our approach demonstrates that UPEA-Phe/NaCl hydrogel electrolyte could be used for manufacturing efficient flexible ESCs.

3.2.3 Methods

3.2.3.1 Computational methods

All simulations were performed using the Amber18 software package [36]. All parameters with exception of atomic charges (*i.e.* stretching, bending, torsional and van der Waals) were extrapolated from the General Amber Force Field (GAFF) [37,38]. Atomic charges were parametrized with the RED-III program [39,40] using the Restrained ElectroStatic Potential (RESP) strategy [41,42].

Periodic boundary conditions were applied using the nearest image convention and the atom pair cut-off distance used to compute the van der Waals interactions was set at 10.0 Å. Beyond cut-off distance, electrostatic interactions were calculated by using Particle Mesh of Ewald, with a points grid density of the reciprocal space of 1 $Å^3$ [43]. The Langevin thermostat [44] and the Berendsen barostat[45] were used to heat the system and to rapidly equilibrate its temperature and pressure at 298 K and 1 bar, respectively. The relaxation times used for the first and second heating cycles were 15 and 5 ps, respectively, while the relaxation time for pressure was 2 ps.

All constructed systems were submitted to 20000 steps of energy minimization (Newton–Raphson method) before any MD trajectory was run in order to relax conformational and structural tensions. The temperature, density and pressure of each model were equilibrated by three consecutive MD runs. First, the systems were heated at 50 K using a NVT MD for 10 ps. After that, the temperature was increased to 298 K by running a NVT MD for another 10 ps. The resulting atom velocities and coordinates were used as the starting point for a NPT-MD run (298 K, 1 bar pressure) that was enlarged until the variation of the density was lower than 1%. The end of this simulation was the starting point of the productive trajectories presented in this work (298 K, 1 bar pressure), which took 200 ns for each simulated system.

3.2.3.2 Synthesis of UPEA-Phe hydrogels

The synthesis of UPEA-Phe and its subsequent reticulation with functionalized PEG was exhaustively described in previous chapter and work [46,47].

3.2.3.3 Chemical and morphological characterization of hydrogels

Infrared absorption spectra were recorded with a Fourier Transform FTIR 4100 Jasco spectrometer in the 4000–600 cm^{-1} range. A Specac Model MKII Golden Gate attenuated total reflection (ATR) cell with a heated Diamond ATR Top-Plate was used.

The morphology of the photo-crosslinked UPEA-Phe hydrogels was observed by scanning electron microscopy (SEM) using a Focused Ion Beam Zeiss Neon40 scanning electron microscope equipped with an energy dispersive X-ray (EDX) spectroscopy system and operating at 5 kV. All samples were sputter-coated with a thin carbon layer using a K950X Turbo Evaporator to prevent electron charging problems. Prior to SEM observation, samples were lyophilized. Thus, throughout the freeze-drying process, the capillary stress is avoided, preventing the collapse of the structure and minimizing the shrinkage of the material. The size of pores was determined from the SEM images using the software SmartTIFF (v1.0.1.2.).

3.2.3.4 Synthesis and characterization of electrodes

Poly(3,4-ethylenedioxythiophene) electrodes were prepared by methods already described.[35] Briefly, PEDOT was obtained by anodic polymerization in acetonitrile at a constant potential of 1.25 V imposing a polymerization charge equal to 500 mC/cm^2 (at room temperature and nitrogen atmosphere). The mass of PEDOT deposited onto the WE (m_{pol}= 1.127 ± 0.203 mg) was determined as

the weight difference between coated and uncoated steel sheets (n = 20) using a CPA26P Sartorius analytical microbalance with a precision of 10^{-6} g. The electrical conductivity, average thickness and root-mean-square roughness of PEDOT films was 29 ± 1 S/cm, 4.1 ± 0.6 µm and 0.5 ± 0.1 µm, respectively.

3.2.3.5 Electrochemical characterization

The response of electrochemical supercapacitors (ESCs), which were prepared as is described in the main text using PEDOT electrodes and hydrogel solid electrolytes, was studied in a two-electrode configuration by means of cyclic voltammetry (CV) and galvanostatic charge-discharge (GCD) measurements.

The specific capacitance (*SC*; in F/g) is the capacitance per unit of mass for one electrode, is expressed as:

$$SC = 4 \times \frac{C}{m} \qquad \text{(E.3.2.1)}$$

where C is the measured capacitance for the two-electrode cell and m the total mass of the active material in both electrodes. The multiplier 4 adjusts the capacitance of the cell and the combined mass of the two electrodes to the capacitance and mass of a single electrode.

CV measurements were used to provide information regarding the cell capacitance (C, F) by applying Eq E.3.2.2

$$C = I \Big/ \left(\frac{dV}{dt}\right) \qquad \text{(E.3.2.2)}$$

where I corresponds to the average current during discharging and dV/dt is the scan rate. For the ESC devices studied in this work, CV curves were recorded from 0.0 V to 0.8 V at several scan rates: 10, 25, 50, 75, 100, 150 and 200 mV/s.

The cell capacitance was also determined using the GCD procedure and applying Eqn E.3.2.2. In this case, I is the discharging current applied to the device and dV/dt should be calculated as $(V_{max} - ½V_{max})/(t_2 - t_1)$, where V_{max} corresponds

to the highest voltage in the GCD curve after the voltage drop (V_{drop}) at the beginning of the discharging process. GCD curves were run at different current densities (*i.e.* charge and discharge rates are specified in units of current per electrode mass): 0.43, 0.61, 1.22 and 2.44 A/g, which corresponded to 0.5, 0.7, 1.4 and 2.8 mA, respectively.

The Coulombic efficiency (η, %) was evaluated as the ratio between the discharging and charging times (t_d and t_c, respectively) for the electrochemical window between 0.0 V and 0.8 V:

$$\eta = {}^{t_d}/_{t_c} \qquad \text{(E.3.2.3)}$$

On the other hand, the cycling stability of the selected ESCs was tested by submitting the system to: *(i)* 1400 GCD cycles at a current density of 1.22 A/g from 0.0 V to 0.8 V, which corresponds to t_c and t_d of approximately 40-60 seconds; and *(ii)* 200 CV cycles at a scan rate of 50 mV/s from 0.0 V (initial and final potential) to 0.8 V (reversal potential). Moreover, the self-discharging and the leakage current (LC) curves were evaluated by applying the following methodologies. In the first case, ESC devices were charged to 0.8 V at 0.25 mA and kept at $1 \cdot 10^{-11}$ mA for 10 min (*i.e.* self-discharging). After that time, the device was discharged to 0 V at –1 mA. In the second case, after charging the devices to 0.8 V at 0.25 mA, they were kept at 0.8 V for 300-600 s while recording the current data through the ESC (*i.e.* leakage current). Data were obtained from testing three independent samples for each device.

3.2.4 Results and Discussion

3.2.4.1 Computational modeling

UPEA-Phe hydrogel is synthesized by photo-crosslinking the unsaturated bonds of UPEA-Phe chains with poly(ethylene glycol) (PEG), which is previously functionalized with unsaturated bonds to act as crosslinker (Scheme 3.2.1) [46]:

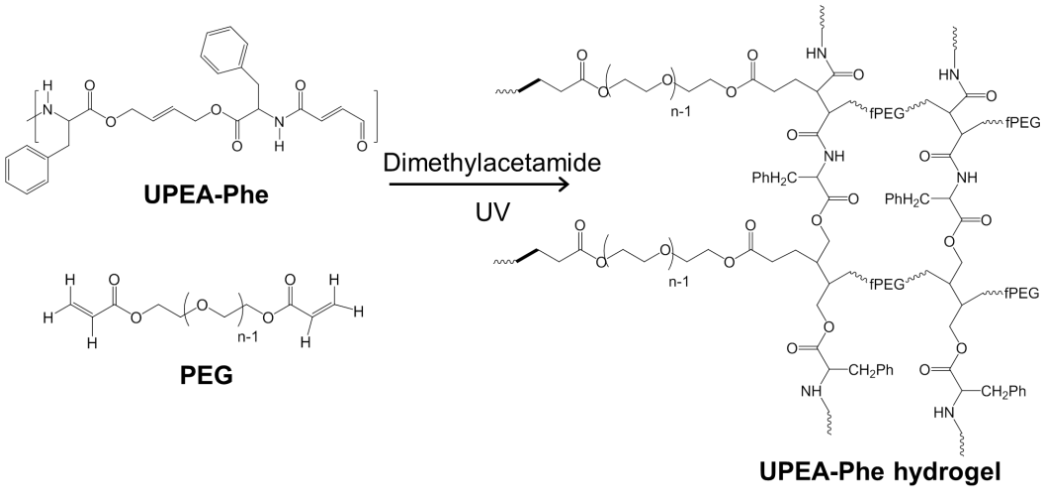

Scheme 3.2.1. Photopolymerization reaction to produce UPEA-Phe hydrogel

The pore size, which is controlled by the crosslinking degree (CLD) that in turn is regulated by the time of exposure to UV radiation, is expected to have a major effect on the properties of the hydrogel. In particular, its capacity to transport Na^+ and Cl^- ions when the doped UPEA-Phe/NaCl hydrogel is used as solid electrolyte in ESCs. In this section, the influence of the structure of the hydrogel on the diffusion of Na^+ and Cl^- ions in UPEA-Phe/NaCl has been studied using atomistic MD simulations. Three different variables have been considered for the simulations: the electric field (EF), the cross-linking degree CLD) and the hydration degree (HD).

Unfortunately, the construction of crosslinked polymeric models (*i.e.* starting configurations for MD) using conventional simulation techniques is very hard and inefficient because of the following adversity: a dense and heterogeneous

distribution of atoms with well-defined the connectivity for both the backbone and the crosslinks (*i.e.* bond lengths and bond angles).[48,49] In order to overcome such adversity, which involves severe restraints, the utilization of specifically designed approaches is necessary. Nonetheless, the length- and time-scales of polymer dynamics, which are unaffordable by such approaches, drastically restricts the efficacy of simulation algorithm that are subjected to strong geometric restrictions.[48,49] For example, UPEA-Phe and functionalized PEG require a photocrosslinking time of at least 6 h (see below) to reach a very high CLD. Thus, the dynamics of the system throughout this period allow all (or almost all) reactive sites to be close enough for photoreaction. This spatial coincidence cannot be achieved using current simulation algorithms and computational facilities, preserving the connectivity distribution (*i.e.* bond lengths and bond angles of both the main chain and crosslinks at the right values), due to the scale. These strong limitations can be solved by focusing the problem on the realistic representation of a single aspect of the system to be studied, and neglecting the rest of the aspects. In this work we focused simulations on the effect of the size of the pores in the transport ions, neglecting other aspects that depend on the dynamics of the polymer chains as for example the evolution of the hydrogel structure with the photocrosslinking time.

Three different hydrogel models were built using an early developed strategy that was engineered to construct reliable 3D molecular architectures of hydrated crosslinked materials.[50] More specifically, this methodology was designed to generate and relax molecular microstructures of crosslinked systems, respecting the connectivity of the molecular system (in the case of UPEA-Phe hydrogel is given by the formula displayed in Scheme 3.2.1) and imposing the CLD. In brief, this strategy consists on the following four-step algorithm:

1) The positions of the atoms of the first UPEA-Phe unit were generated within the simulation box using an algorithm that was designed to provide

conformations with minimum torsional strains and without repulsive non-bonded interactions.[51,52] Then, a Monte Carlo criterion was applied to choose one of the following three options: (i) the second UPEA-Phe repeat unit was generated at the left side of the first one; (ii) the second UPEA-Phe repeat unit was generated at the right side of the first one; and (iii) a PEG chain was generated to form a crosslink.

2) If option (i) or (ii) are selected in step 1), the second UPEA-Phe repeat unit is generated without steric overlaps. If option (iii) was chosen in the previous step, both a position of the first UPEA-Phe repeat unit and a position of the second UPEA-Phe repeat unit, are randomly chosen among those able to form crosslinks (*i.e.* those corresponding to unsaturated bonds) to generate the PEG chain. Then, a number of PEG repeat units, m_1, comprised between 25 and 50 is randomly chosen. The cross-link is considered as feasible when the atomic positions generated for the $(PEG)_{m1}$ chain do not overlap with previously generated atoms, whereas a new number of PEG repeat units, m_2 ($m_2 > m_1$) is randomly selected again if steric overlaps are detected. If after five trials, the generation of the crosslink fails, the algorithm comes back to step 1). Independently of the option, the positions of the atoms contained in the second UPEA-Phe repeat unit or the PEG crosslinker are obtained one-by-one.

3) The rest of the UPEA-Phe repeat units and PEG chains are generated one-by-one using the procedure. The following features are distinctive of this repetition process: (a) at the end of the generation process, the number of crosslinks is the whole system must be equal to the fixed CLD; and (b) the geometry of the connectivity (*i.e.* bond lengths and bond angles) must be respected in all cases.

Three models with 240 UPEA-Phe repeat units each and CLDs of 17%, 25% and 35%, which correspond to 40, 60 and 86 PEG chains, respectively, were generated using such strategy. The average number of repeat units per PEG crosslink in these systems was 42, 47 and 43, respectively. Models for CLD= 17%, 25% and 35% contained 27685, 36879 and 43677 explicit atoms, respectively. The homogeneous and relatively compact distribution of polymer chains found for the model without crosslinks transforms into a heterogeneous distribution due to the positional (functionalized PEG chains react with the double bonds of butenediol and fumarate units) and geometric (bond lengths and bond angles according to the connectivity) restraints introduced by the crosslinks. Thus, the crosslinks induced the formation of pores with ellipsoidal-like shapes, as is reflected in the models depicted in Figure 3.2.1. The pore size (PS) was determined by averaging at least 30 different diameters (including the major and the minor) at the surface of each pore and, subsequently, averaging the values found for the pores of 40 different stored snapshots separated by 2.5 ns intervals. The PS was 25±6, 39±11 and 58±14 Å for the model with a CLD of 17%, 25% and 35%, respectively, indicating that the size of the pores increases with the CLD. Obviously, this increasing effect is expected to occur until a threshold value of the CLD only, the dimensions of the pore decreasing when the number of crosslinks is very high because of the severe geometric constrictions. Unfortunately, reliable models with a CLD higher than 35-40% are not feasible using current computational strategies. Besides, inspection to the distributions of the measured diameters, which are included in Figure 3.2.1, reveals two peaks in all cases, which is fully consistent with the ellipsoidal-like geometry of the pores.

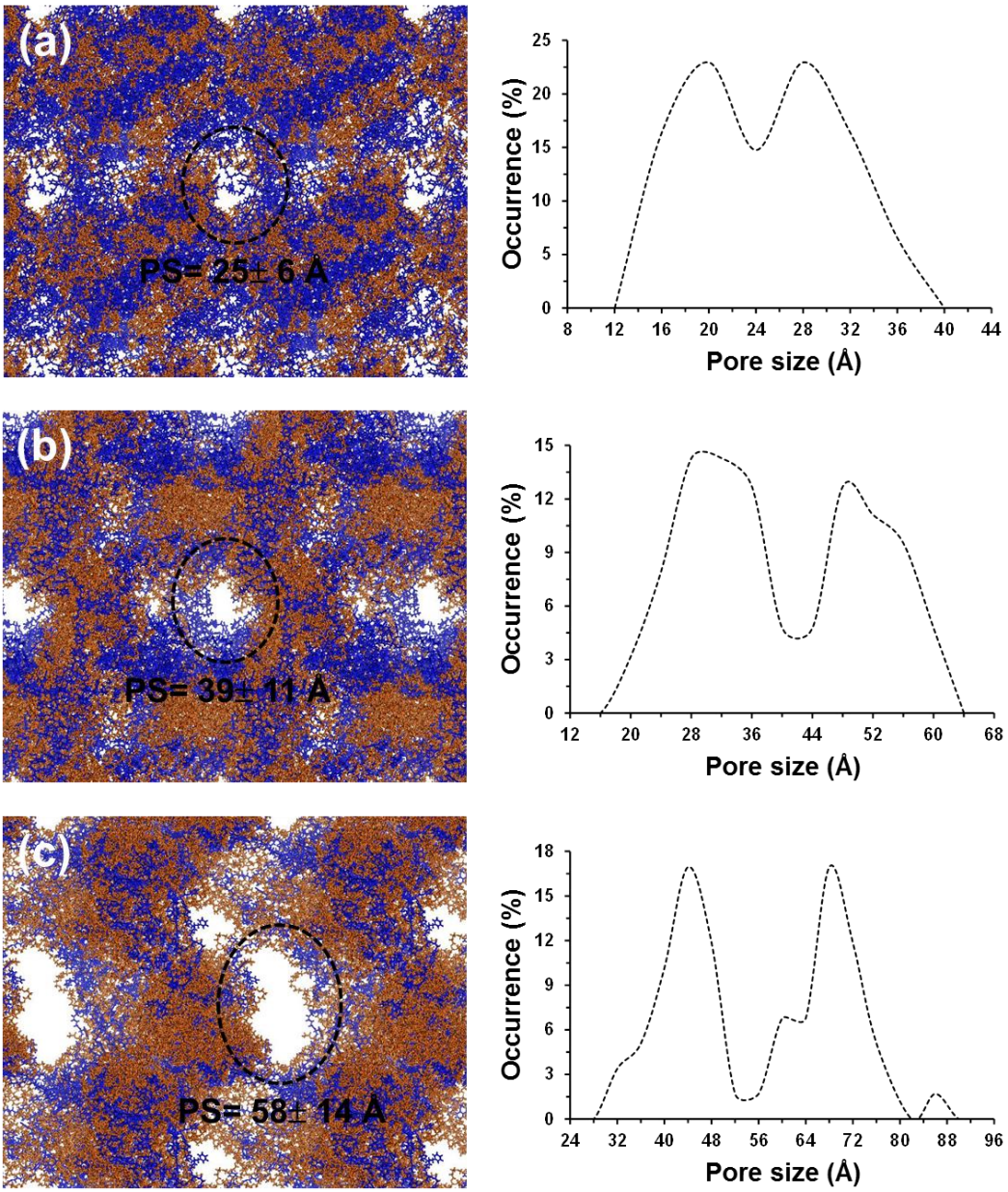

Figure 3.2.1. Models for UPEA-Phe hydrogel constructed with different CLDs: (a) 17%, (b) 25% and (c) 35%. Blue and orange chains correspond to the UPEA backbone and PEG cross-linkers, respectively. In order to provide a clearer visualization of the pores, parts of the neighboring periodic cells have been included in the images. The averaged value of the pore size (PS) is displayed for each model. The distribution of pore sizes as measured for 20 different stored snapshots separated by 5 ns intervals are displayed for each model (right).

Then, the three models were hydrated by introducing water molecules, which were randomly incorporated at positions not occupied by the polymer atoms.[50] For

each model, three different hydration degrees (HDs) were considered: 100% w/w, 300% w/w and 500% w/w. The exact number of explicit water molecules used for each model, which depends on the CLD, is provided in Table 3.2.1. Also, Na^+ and Cl^- ions were added to reach a 0.1 M NaCl concentration. The number of Na^+ and Cl^- ions added to each system is included in Table 3.2.1. Accordingly, the total number of explicit atoms for the nine simulated models (3 CLDs × 3 HDs with 0.1 M NaCl) ranged from 47,901 (CLD= 17%, HD= 100% w/w) to 285,399 (CLD= 35%, HD= 500% w/w).

Cross-linking degree	**Number of explicit water**		
	100% w/w	**300% w/w**	**500% w/w**
17%	6724 (12)	18155 (33)	30645 (55)
25%	8972 (16)	27584 (50)	45737 (82)
35%	16444 (29)	48136 (86)	80478 (144)

Table 3.2.1. Number of explicit water molecules considered for simulations of the UPEA-Phe hydrogel as a function of the cross-linking degree and the hydration. The number of NaCl molecules added to reach a 0.1 M NaCl concentration is displayed in parenthesis.

After their thermalization and equilibration using the protocol described in the method section, the nine constructed models were used as starting points for independent production MD simulations, which were conducted considering the following electric fields (EF): 0.0, 20, 40, 80 and 160 V/mm. The EF was fixed along the *z*-axis of the simulation box, the force on each atom, *i*, of the model ($\mathbf{F'}_i$) being defined by the following expression:

$$\mathbf{F'}_i = \mathbf{F}_i + q_i \cdot \mathbf{E}_z \qquad \text{(E.3.2.4)}$$

where $\mathbf{F}_i$ is the force defined by the potential force-field (*i.e.* the GAFF force-field[37,38] was used for this study), q_i is the charge of the atom *i*, and $\mathbf{E}_z$ is the EF. It is worth noting that the utilization of a fixed model, which successfully describes the transport of simple ions, allows a dramatic reduction in computational cost compared to polarizable models.[53,54] A total of 45 production MD runs (9 models × 5 EFs), each of 200 ns, were conducted, which represent a total simulation time of 9 μs.

All simulations were run using the Amber18 package,[36] computational details about the procedures being described in the methods section. The structure of the modeled hydrogels did not experience significant changes since they are considerably restrained by the crosslinks. For example, simulations using the largest electric field (EF= 160 V/mm) showed that the averaged pore size experienced a variation of 8%, 5% and 4% with respect to simulations without electric field for the systems with CLD= 17%, 25% and 35%, respectively.

The diffusion coefficient (*D*) of Na^+ and Cl^- ions was calculated using the Einstein relation:

$$D = \frac{1}{6n} \lim_{t\to\infty} \frac{d}{dt} MSD \qquad \text{(E.3.2.5)}$$

where *t* is time, *MSD* is the mean square displacement and *n* is the number of cations or anions. Eq (E.3.2.5) is only valid when the Einstein diffusive regimen is reached (*i.e.* the motion of the diffusing ions follows a random walk; in other words, their motion is not correlated with their motion at any previous time). Inspection of the temporal evolution of the *MSD* (see below) reflected an anomalous diffusion for a short period of time (ranging from ~30 ns to ~80 ns) before to reach the diffusive regime. This part of the trajectory was excluded from the diffusion analyses. Thus, after the anomalous diffusion period, the *MSD* of the diffusing particles increases linearly with time and the slope, *m*, of such curve is 1.0 (*i.e.*

accelerated and anomalous diffusive regimes exhibit $m < 1$ and $m > 1$, respectively [55]).

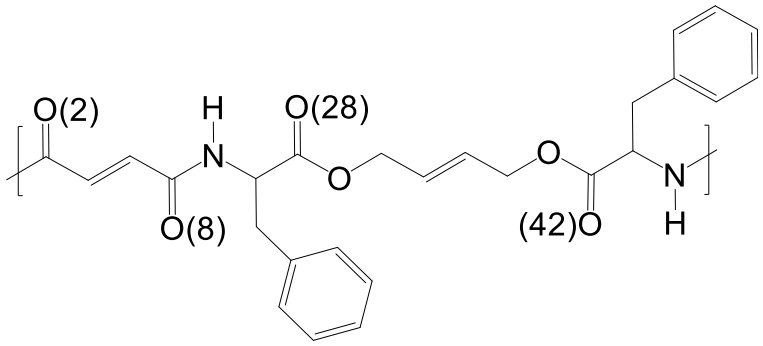

Scheme S1. Structure of the UPE-Phe displaying the labels used to identify the oxygen atoms for the analyses of MD trajectories.

Figures 3.2.3a and 3.2.3b represent the variation of D for Na^+ and Cl^- (D_{Na+} and D_{Cl-}, respectively) against the EF for UPEA-Phe/NaCl with CLD= 17%, 25% and 35% and HD= 100%, while Figure 3.2.2 shows the temporal evolution of MSD for a representative system (UPEA-Phe/NaCl with CLD= 17% and HD= 100%) using the different EFs. As is shown, the diffusion of the two ions does not follow any trend with respect to the EF variation in the studied range. Thus, the influence of the chemical structure of the hydrogel on D_{Na+} and D_{Cl-}, which range from $0.13 \cdot 10^{-5}$ (CLD= 17%) to $0.36 \cdot 10^{-5}$ cm^2/s (CLD= 35%) and from $0.20 \cdot 10^{-5}$ (CLD= 17%) and $0.49 \cdot 10^{-5}$ cm^2/s (CLD= 35%), respectively, is much higher than that of strength of the EF. Similarly, the effect of the EF on D_{Na+} and D_{Cl-} was practically inexistent for doped hydrogels with HD= 300% and 500% (Figure 3.2.4).

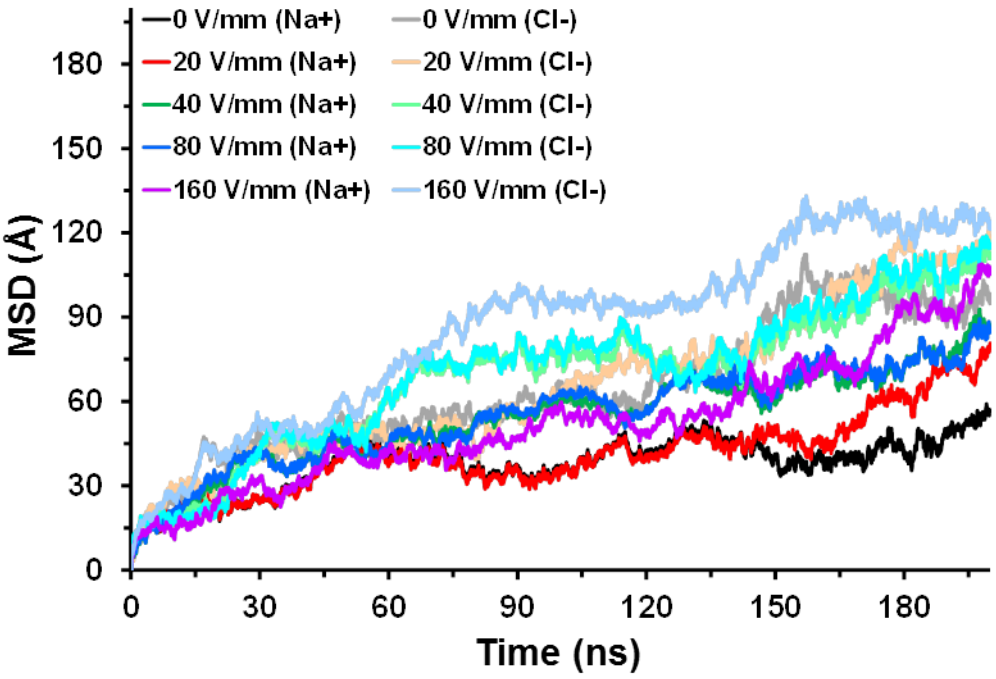

Figure 3.2.2. MSD for the system for UPEA-Phe/NaCl with CLD= 17% and HD= 100%.

On the other hand, Figures 3.2.3 and 3.2.4 show that D_{Cl-} is higher than D_{Na+} for all the studied CLDs and HDs. This has been attributed to the interaction between the Na^+ ions and the oxygen atoms from carbonyl groups of the UPEA-Phe backbone. The strength of this interaction is illustrated is Figure 3.2.5a, which displays the radial distribution functions (RDFs) for $Na^+\cdots$O2 atoms pair (O2 refers to the first oxygen atom of the fumarate unit, Scheme 3.2.2). The profiles obtained for hydrogels with CLD= 17%, 25% and 35% and HD=100% display a sharp and intense peak at a distance *r*= 2.3 Å. The intensity of this peak decreases with increasing CLD, reflecting that crosslinks hinder the access of Na^+ to the oxygen atoms of the fumarate units. Identical conclusions are reached by inspecting the RDFs involving the $Na^+\cdots$O8, $Na^+\cdots$O28 and $Na^+\cdots$O42 atom pairs (Figure 3.2.6), where O8, correspond to the oxygen atom of the second carbonyl of the fumarate unit and O28 and O42 refer to the oxygen atom of first and second Phe units (Scheme 3.2.1), respectively. Instead, no peak is observed in the RDFs involving Cl^- ions, explaining why their mobility is superior to that of Na^+ ions. This is

illustrated in Figure 3.2.5b, which displays the $Cl^{-}\cdots O2$ pair RDFs. Consistently, the profiles obtained for the other $Cl^{-}\cdots O\#$ pair RDFs (not shown) indicated that Cl^{-} ions do not interact with the carbonyl groups of the UPEA-Phe chains, independently of the CLD. It should be mentioned that, although the RDFs were displayed at short distances due to the inhomogeneity of the system, all them tend to converge to unity as expected, at $r = L/2$ (where L is the size of the simulation box).

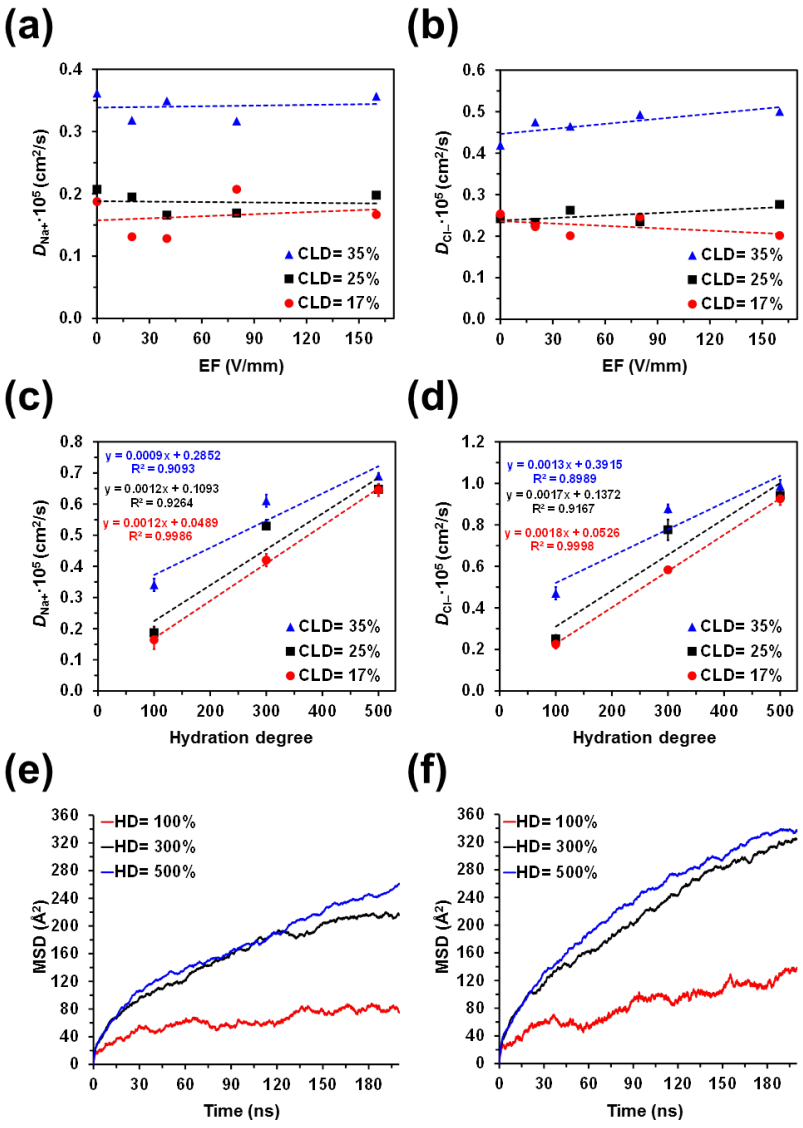

Figure 3.2.3. Variation of the diffusion coefficients of (a, c) Na^{+} and (b, d) Cl^{-} (D_{Na+} and D_{Cl-}, respectively) against: (a, b) the strength of the electric field for UPA-Phe hydrogels with HD= 100% (*i.e.* profiles for hydrogels with HD= 300% and 500% are shown in Figure 3.2.2.); and (c, d) the hydration degree. For hydrogels

displayed in (a)-(d), the plotted diffusion coefficients correspond to the averages of the values obtained using different electric fields, while the error bars are to the resulting standard deviations. Temporal evolution of the MSD for (e) Na^+ and (f) Cl^- ions in the hydrogel with CLD= 25% using EF= 20 V/mm (results for the systems with CLD= 17% and 35% are shown in Figure 3.2.7.).

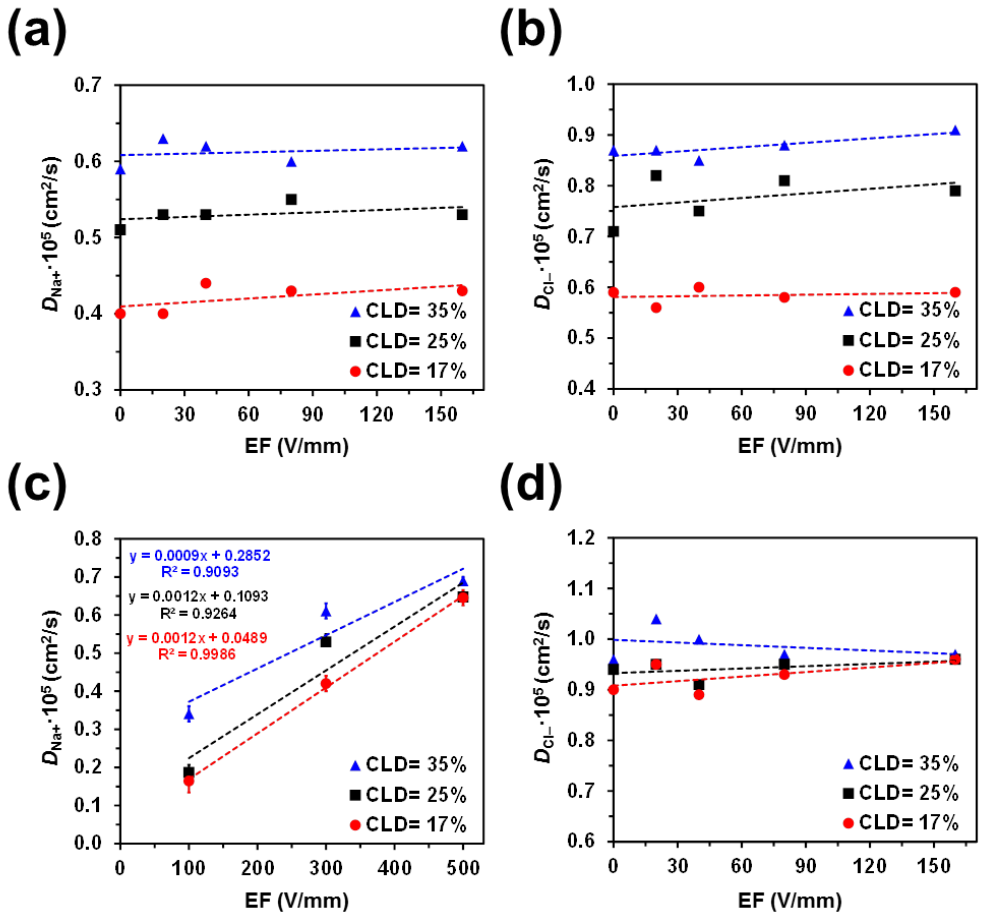

Figure 3.2.4. Variation of the diffusion coefficients of (a, c) Na^+ and (b, d) Cl^- (D_{Na+} and D_{Cl-}, respectively) against the strength of the electric field (EF) for UPA-Phe/NaCl hydrogels with (a, b) HD= 300% and (c, d) HD= 500% (*i.e.* profiles for hydrogels with HD= 100% are shown in Figures 3.2.3a and 3.2.3b).

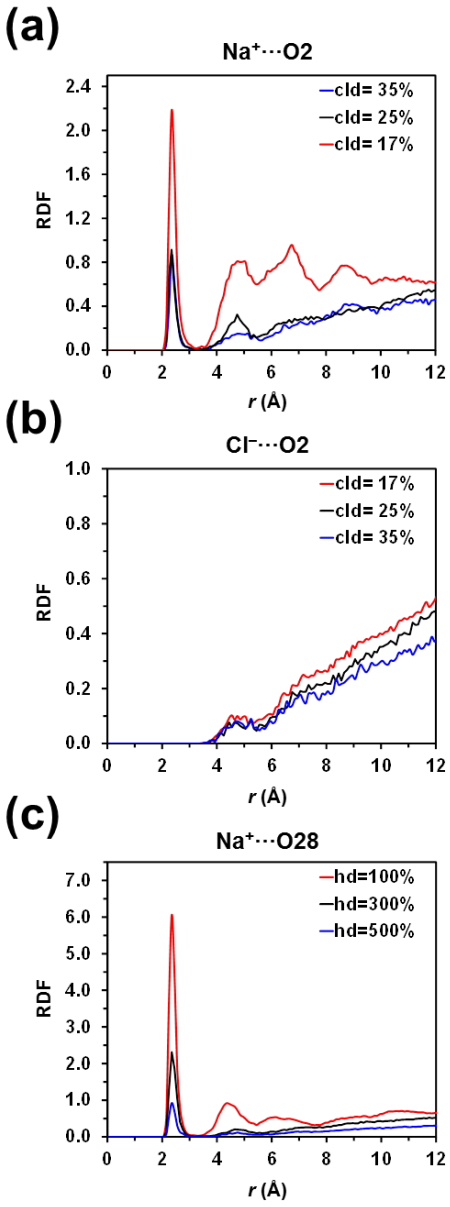

Figure 3.2.5. Radial distribution functions (RDF) for (a) $Na^+\cdots O2$ and (b) $Cl^-\cdots O2$ atom pairs, as determined from simulations of hydrogels with different cld and hb= 100%, and for (c) $Na^+\cdots O28$ atom pairs, as obtained from simulations of hydrogels with different hd and cld= 17%.

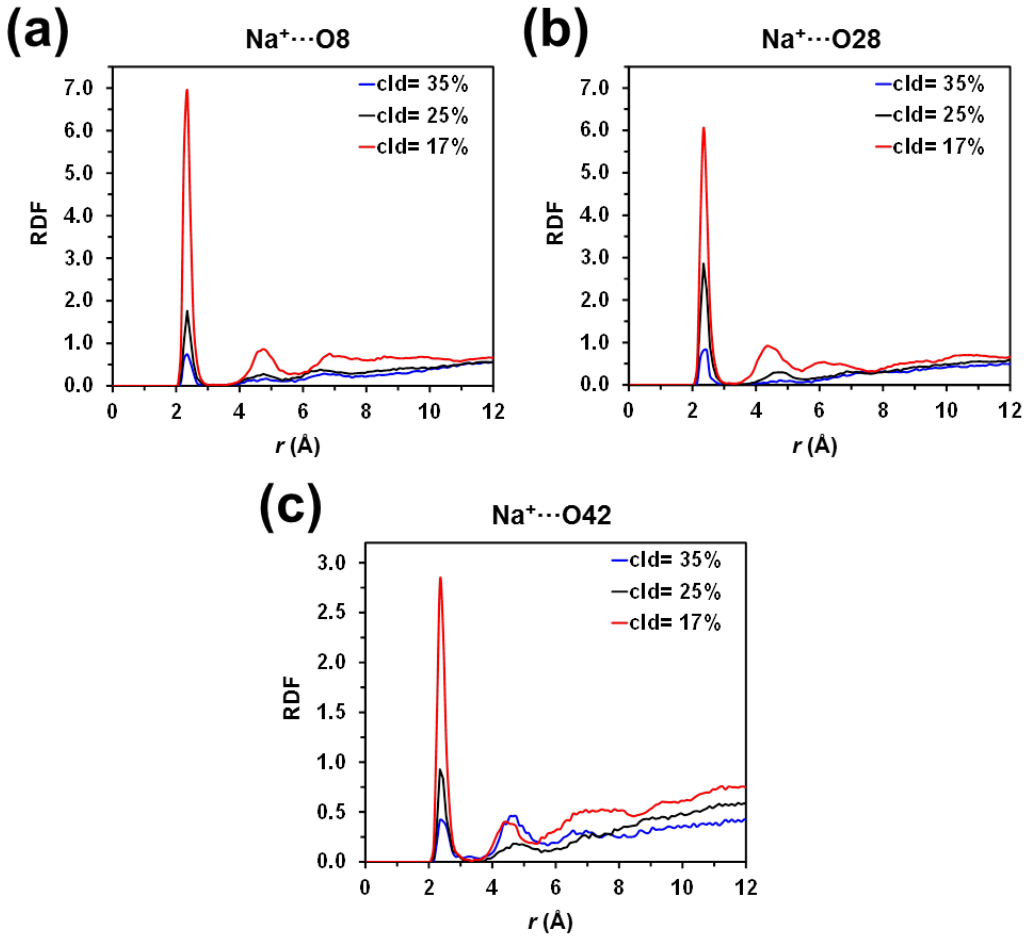

Figure 3.2.6. Radial distribution functions (RDF) for (a) $Na^+\cdots O8$, (b) $Na^+\cdots O28$ and (c) $Na^+\cdots O42$ atom pairs. Data correspond to simulations of hydrogels with different cld and hd= 100%.

Figure 3.2.3c-d plots the variation of D_{Na+} and D_{Cl-}, respectively, against the HD for the three hydrogels for EF= 20 V/mm. Both D_{Na+} and D_{Cl-} increase linearly with the HD, indicating that the mobility of the ions becomes easier with increasing water content. This effect is clearly illustrated in Figure 3.2.3e-f, which displays the temporal evolution of the MSD for representative simulations (EF= 20 V/mm) of systems with CLD= 25% (the temporal evolution of the MSD for the systems with CL= 17% and CLD= 35% are shown in Figure 3.2.7.). Thus, the amount of $Na^+\cdots$UPEA-Phe interactions and, therefore, the retention of Na^+ cations bound to the hydrogel matrix decreases with increasing HD. The linear increment of the

diffusion coefficients with the HD has been attributed to the fact that ion⋯polymer interactions are relatively weak and non-specific in comparison to ion⋯water interactions. This effect is illustrated in Figure 3.2.5c, which compares the RDFs involving the Na^+⋯O28 pair for the hydrogels with CLD= 17% and variable water contents, and supported by the RDFs shown in Figure 3.2.6 for Na^+⋯O2, Na^+⋯O8 and Na^+⋯O42 pairs. D_{Cl-} is higher than D_{Na+} for all the examined hydration degrees, which is due to the lack of specific interactions between Cl^- ions and UPEA-Phe atoms. It is worth noting that the chemical structure of hydrogels plays a crucial role in the diffusion coefficient for ions. For example, in ionene hydrogels (*i.e.* polyelectrolyte hydrogels in which a quaternary ammonium cation resides within the polymer backbone) the strong electrostatic interactions between the positively charged nitrogen atoms and ions dominate over the ion⋯water interactions.[56,57]

The growing diffusion of the ions with the HD becomes more pronounced with decreasing CLD. Thus, the ratio between the D_{Na+} values obtained for HD= 500% and 100%, D_{Na+}(HD= 500%) / D_{Na+}(HD=100%), is 3.9, 3.5 and 2.0 for CLD= 17%, 25% and 35%, respectively. Similarly, D_{Cl-}(HD= 500%) / D_{Cl-}(HD=100%) is 4.1, 3.8 and 2.1 for CLD= 17%, 25% and 35%, respectively. These results are consistent with the amount of specific interactions between Na^+ ions and UPEA-Phe atoms, which increase with decreasing CLD (Figures 3.2.5a and 3.2.6), and with the fact that the migration of Cl^- is faster than that of Na^+.

On the other hand, both D_{Na+} and D_{Cl-} increase with the CLD, as is reflected in Figure 3.2.8a-b, respectively. However, this tendency is less pronounced for systems with HD= 500% than for those with HD= 100% and 300%. Again this is consistent with the amount of Na^+⋯UPEA-Phe interactions, which is inversely proportional to the HD (Figures 3.2.5c and 3.2.4). The temporal evolution for the trajectories obtained using HD= 300% and 500% (EF= 20 V/mm) are shown in Figure 3.2.8c-d and 3.2.8e-f, respectively.

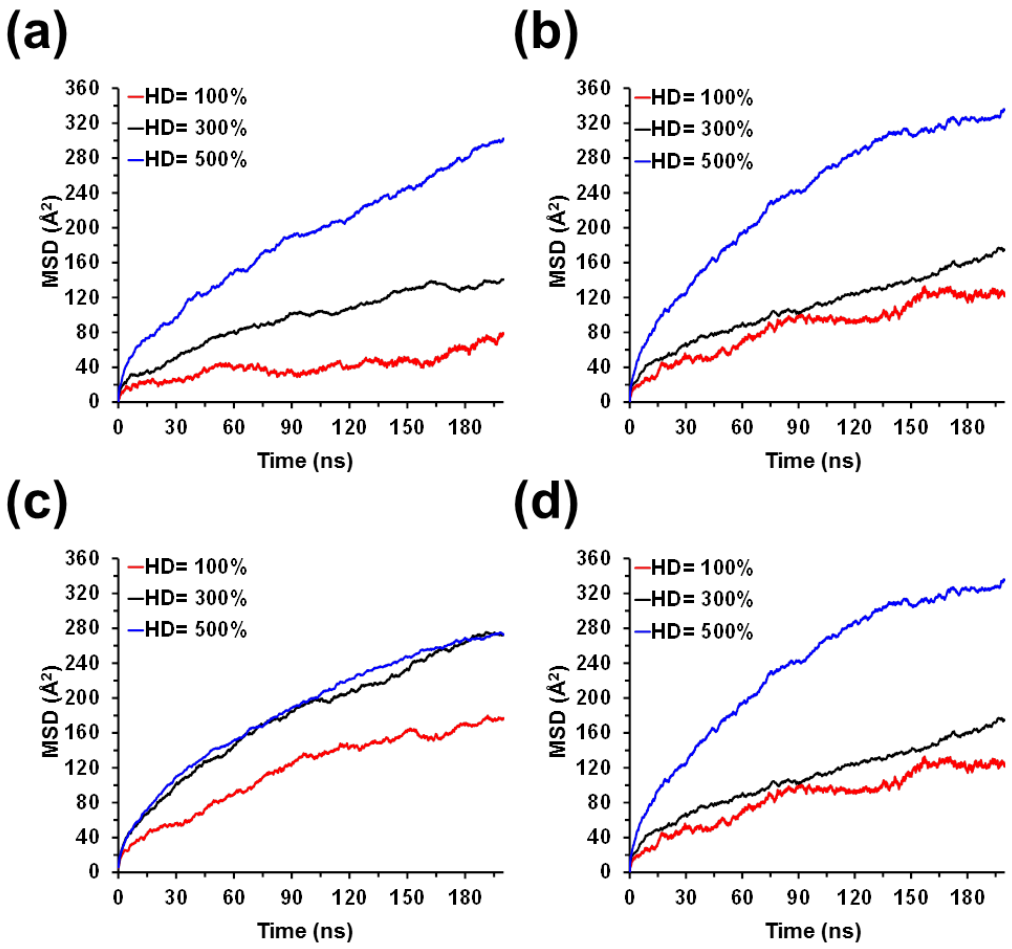

Figure 3.2.7. The temporal evolution of the MSD for (a, c) Na^+ and (b, d) Cl^- ions in doped hydrogels with (a, b) CLD= 17% and (c, d) CLD= 35% using EF= 20 V/mm (results for the system with CLD= 25% are shown in Figure 3.2.3e-f)

In summary, MD simulations show that Na^+ and Cl^- ions diffusion increases with the size of the pores, this structural parameter being indeed much more important than the strength of the electric field. This has inspired us to further improve the already outstanding properties of UPEA-Phe/NaCl as supporting electrolyte for ESCs, increasing the pore size. Because of the limitations typically found in the construction of crosslinked polymeric models, MD simulations were conducted using relatively low CLDs (*i.e.* CLD $\leq$ 35%), in which the pore size of modeled hydrogels increased with the CLD. However, in the laboratory, the size of the pore of real photo-crosslinked UPEA-Phe/NaCl hydrogels is expected to be increased

by reducing the time of exposure to UV radiation from 8 h, which ensured that the *crosslinking reaction* was *completed*, to 4 h. Experimental measures about the performance of UPhe-Phe/NaCl hydrogels prepared using such two photo-polymerization times are provided in the next section.

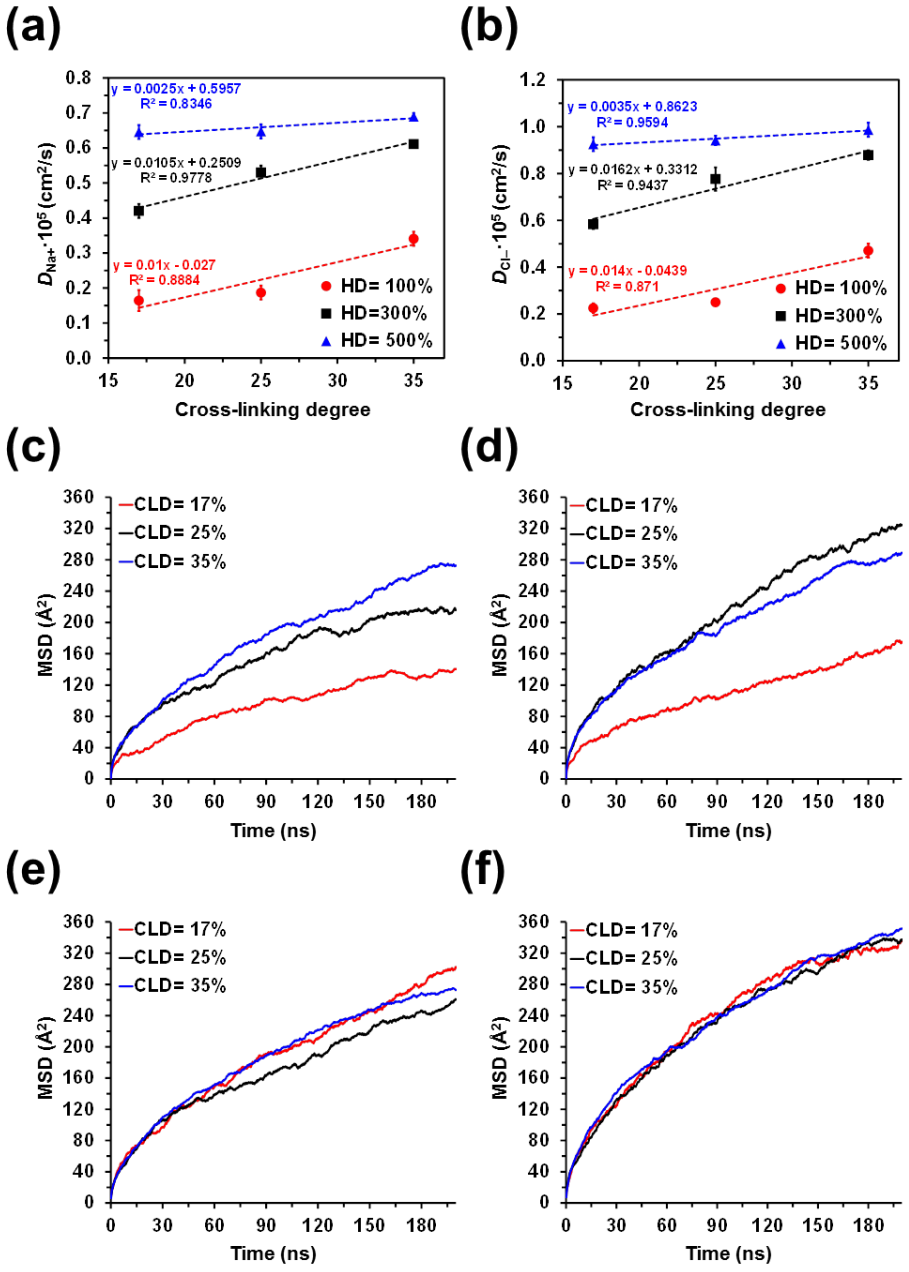

Figure 3.2.8. Variation of the diffusion coefficients of (a) Na^+ and (b) Cl^- (D_{Na+} and D_{Cl-}, respectively) against the cross-linking degree. The plotted diffusion coefficients correspond to the averages of the values obtained using different electric fields, while the error bars are to the resulting standard deviations. The

temporal evolution of the MSD for (c, e) Na^+ and (d, f) Cl^- ions in the hydrogels with (c, d) HD= 300% and (e, f) HD= 500% using EF= 20 V/mm.

3.2.4.2 Experimental characterization of UPEA-Phe/NaCl as solid electrolyte

UPEA-Phe hydrogels were prepared as described in previous work.[46] In brief, UPEA-Phe chains were obtained following the procedure reported by Katsarava and co-workers.[47] Then, UPEA-Phe chains were crosslinked using as reticulating agent a functionalized PEG (M_n= 10000 g/mol), which was obtained by reacting with 2-propenoyl chloride.[35] The crosslinking reaction between UPEA-Phe and the functionalized PEG was performed using the photo-initiator irgacure 2959 and exposing the reaction medium solution to an UV lamp (230 V, 0.8 A). Two photo-polymerization times (*i.e.* times of exposure to the UV radiation) were considered: 4 h and 8 h. The latter time ensured that the *crosslinking reaction* was *completed, as proved in previous work.[35] Therefore, the resulting hydrogel was used as a control. Instead, the choice of the shortest time was based on the computational results discussed in the previous section. Thus, such drastic reduction of photo-polymerization time (a factor of two) was expected to promote the formation of larger pores since the reticulation process was interrupted before it was completed.* Hydrogels obtained using times of 4 h and 8 h, hereafter named UPEA-Phe(4h) and UPEA-Phe(8h), were washed at room temperature with distilled water, which was changed every 12 h, during 48 h. Finally, the hydrogels were soaked a minimum of 24 h in a 0.1 M NaCl solution prepared with distilled water for doping. The doped hydrogels, UPEA-Phe(4h)/NaCl and UPEA-Phe(8h)/NaCl, were kept in such NaCl solution for future utilization or lyophilized by freeze-drying for further characterization. Figure 3.2.9a provides photographs of the UPEA-Phe(4h) hydrogel as prepared and after doping with NaCl.

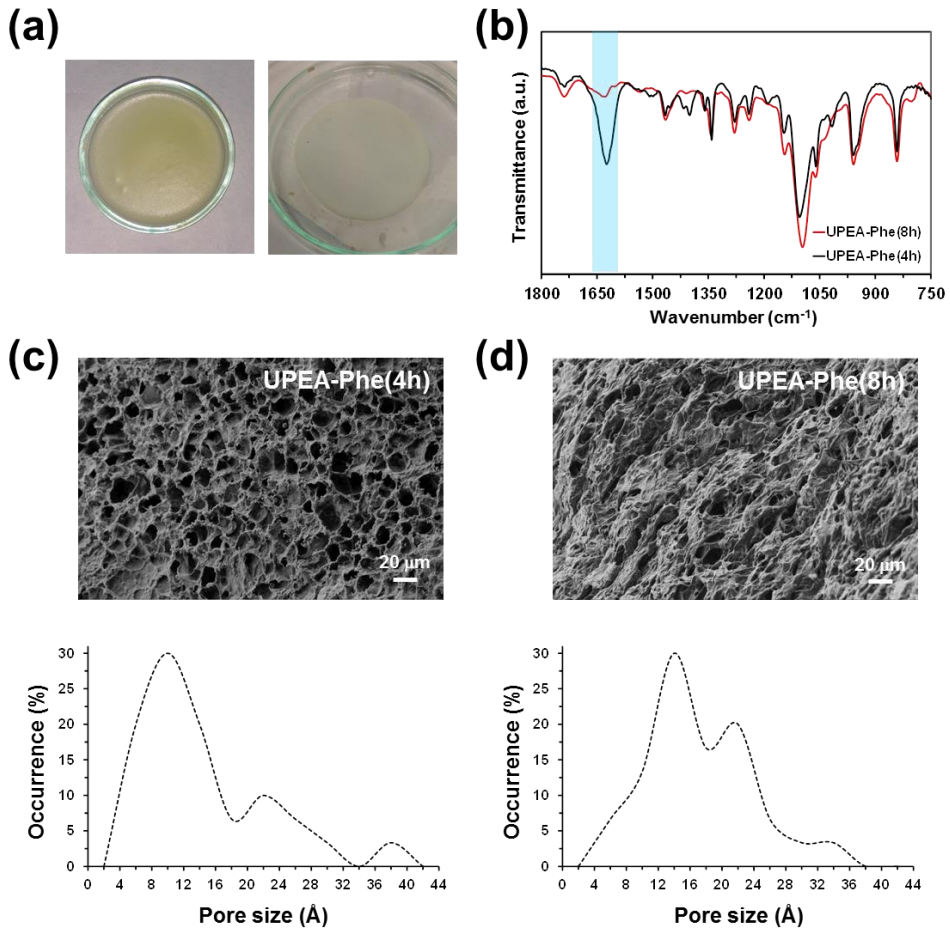

Figure 3.2.9. (a) Photographs of washed UPEA-Phe(4h) and doped UPEA-Phe(4h)/NaCl. (b) FTIR spectra of freeze-dried hydrogels. The band associated to the C=C stretching is marked in blue. Representative SEM micrographs and pore size distribution for freeze-dried (c) UPEA-Phe(4h) and (d) UPEA-Phe(8h) hydrogels.

The FTIR spectra of UPEA-Phe(4h) and UPEA-Phe(8h), which have been normalized using the most intense band at 1100 cm^{-1} (C–O stretching), are compared in Figure 3.2.9b. As expected, the main difference between the two compounds corresponds to the band at 1620 cm^{-1}, which is associated to the C=C stretching. The intensity of this band decreases with increasing CLD (*i.e.* with increasing photo-polymerization time). The rest of the FTIR bands, as well as the ^{1}H NMR spectra (not shown), are fully consistent with those described in previous work.[46]

On the other hand, representative SEM micrographs of freeze-dried UPEA-Phe(4h) and UPEA-Phe(8h) are shown in Figure 3.2.9c-d. Pores are much better defined in the former than in latter. In fact, UPEA-Phe(8h) shows some compact regions homogeneously distributed on the surface, in which the pores are totally or practically hindered. This effect has been attributed to the fact that the photo-polymerization reaction was complete after 8 h. Interestingly, the average size of the pores that remain open in UPEA-Phe(8h), 17±7 μm, is slightly higher than that of the UPEA-Phe(4h) pores, 14±10 μm, even though a higher dispersion of values is obtained for the latter. This observation, which is reflected in the distribution of sizes included in Figure 3.2.9c-d, indicates that the continuation of the photo-polymerization process for 4 additional hours mainly affects the smaller pores, suggesting that functionalized PEG tend to be grouped in micro/nanoclusters rather than homogeneously distributed in the reaction medium.

The swelling ratio (*SR*, %) of the two hydrogels was estimated using the weights of the hydrogels after washing and after freeze-drying (Methods section). The *SR* was 1501 % ± 342% and 500% ± 114 % for UPEA-Phe(4h) and UPEA-Phe(8h), respectively, reflecting that this parameter decreases with increasing CLD as was also observed for other polysaccharide- and polypeptide-based hydrogels.[25,26]

To compare the electrochemical achievements of UPEA-Phe(4h)/NaCl and UPEA-Phe(8h)/NaCl as solid electrolytes, ESCs devices were prototyped by assembling such doped hydrogels with poly(3,4-ethylenedioxythiophene) (PEDOT) electrodes, as is illustrated in Figure 3.2.10a. More specifically, a rectangular hydrogel piece was sandwiched between two PEDOT electrodes, separated at a distance of 1 mm. After this, the external side of each PEDOT electrodes was covered by another hydrogel piece. A photograph of the resulting ESC prototype is included in Figure 3.2.10a. It is worth noting that the choice of PEDOT electrodes, which consisted on steel sheets coated at the two sides by

anodically polymerized PEDOT (detailed description of the preparation and characterization of the electrodes is provided in the Methods section), and the two-electrodes configuration was done for consistency with previous studies in which other hydrogels were tested.[31-35] This has allowed us to stablish a rigorous comparison with hydrogels derived from biopolymers, showing the remarkable performance of UPEA-Phe(4h)/NaCl as solid and flexible electrolyte (see last sub-section).

Figure 3.2.10b shows the cyclic voltammetry (CV) curves of ESCs with UPEA-Phe(4h)/NaCl and UPEA-Phe(8h)/NaCl recorded at different scan rates (from 10 to 200 mV/s) and a working potential from 0.0 to 0.8 V. For each scan rate, the areas associated to the cathodic and anodic scans are significantly higher for UPEA-Phe(4h)/NaCl than for UPEA-Phe(8h)/NaCl, indicating that the reversible exchange of voltammetric charge is favored for the former hydrogel. Moreover, voltammograms at low scan rates exhibit a rectangular shape, reflecting the pseudo-capacitive behavior associated to the formation of the electrochemical double layer at the electrode/electrolyte interface. As the scan rate increases, voltammograms deviate from the rectangular shape for both ESCs. However, this effect is much less pronounced for UPEA-Phe(4h)/NaCl than for UPEA-Phe(8h)/NaCl, revealing better ionic diffusion for the former than for the latter.

Galvanostatic charge-discharge (GCD) curves at different current densities are displayed in Figure 3.2.10c. UPEA-Phe(4h)/NaCl-containing ESCs show lower voltage drop than those with UPEA-Phe(8h)/NaCl, independently of the current density, indicating that the internal resistance is lower for the former than for the latter. GCD triangular curves are more symmetric when more capacitive is the behavior due to symmetry in charge and discharge (*i.e.* coulombic efficiency close to one*)*. Compared with those of UPEA-Phe(8h)/NaCl, the shape of the GCD curves of UPEA-Phe(4h)/NaCl is closer to the ideal symmetric triangular profiles. This is consistent with the fact that electric double layer capacitive behavior is

better for ESCs containing the latter solid electrolyte, which is in agreement with CV results. Another important finding is that charge and discharge times are almost twice for the ESCs with UPEA-Phe(4h)/NaCl than for the ESC with UPEA-Phe(8h)/NaCl.

Figure 3.2.10d represents the specific capacitances (*SC*s) obtained from CV at various scan rates (from 10 to 200 mV/s) and from GCD at various current densities (from 0.43 to 2.44 A/g). In all cases, the *SC*s obtained for ESCs with UPEA-Phe(4h)/NaCl ESCs are higher than for those with UPEA-Phe(8h)/NaCl, reflecting again that the ionic diffusion is higher for the hydrogel with largest pores. Moreover, the difference between the specific capacitances of the two systems (*i.e.* $\Delta SC = SC_{\text{UPEA-Phe(4h)/NaCl}} - SC_{\text{UPEA-Phe(8h)/NaCl}}$) increases from 15.6 to 28.1 F/g when the scan rate increases from 10 to 200 mV/s, whereas ΔSC decreases from 19.8 to 2.9 F/g when the current density increases from 0.43 to 2.44 A/g. The latter observation indicates that the ions fully diffuse inside the electrodes at low current densities, this effect being enhanced for the hydrogel electrolyte with more available surface. As shown in Figure 3.2.10d, the *SC*s are higher for Phe(4)/NaCl hydrogel-containing ESCs than for control ESCs, which were prepared using PEDOT electrodes separated by a 0.5 M NaCl liquid solution, evidencing that the capacitive response was better for the former than for the latter.

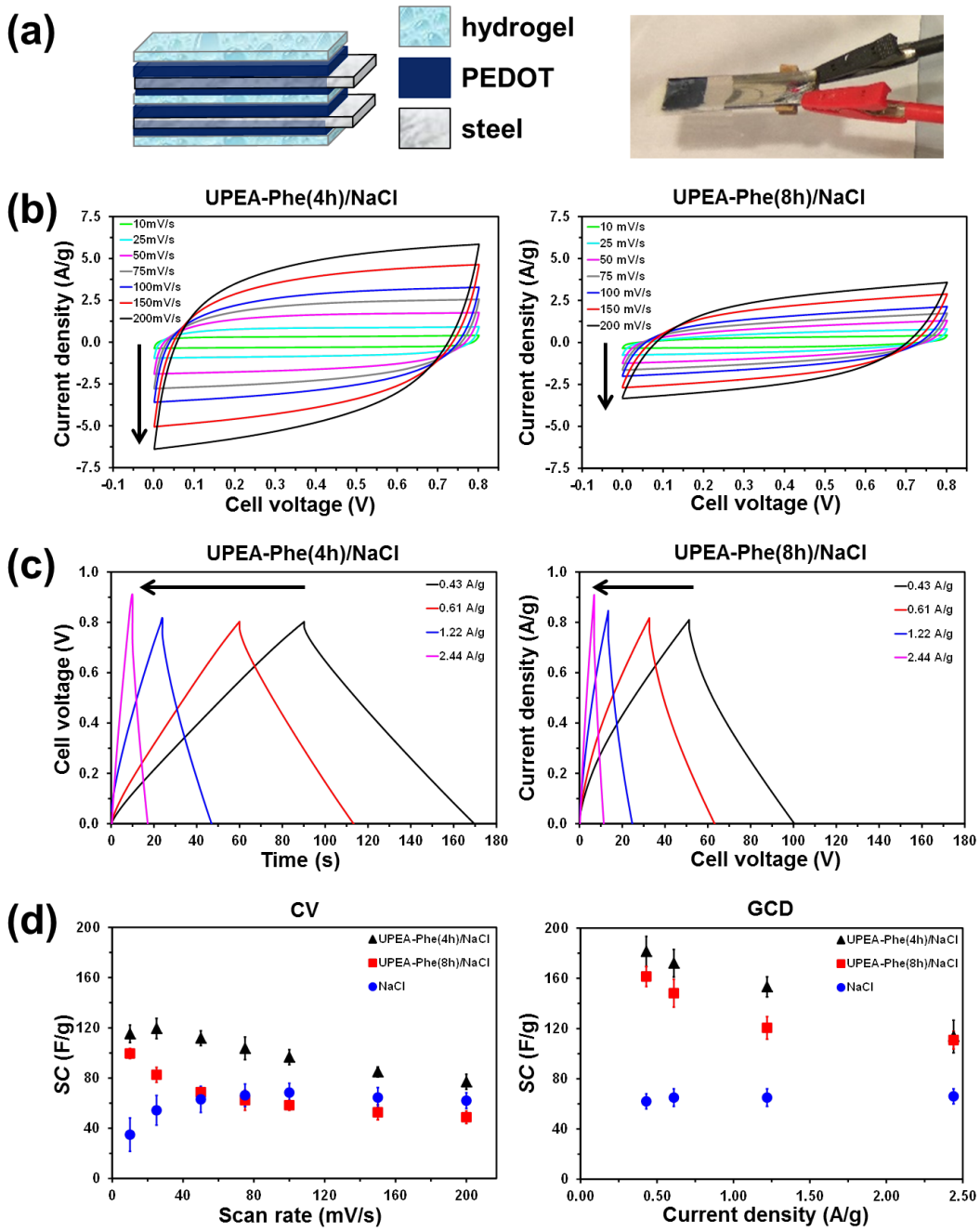

Figure 3.2.10. (a) Scheme and photograph of the ESC prepared in this work. For ESCs prepared using UPEA-Phe(4h)/NaCl and UPEA-Phe(8h)/NaCl: (b) Cyclic voltammograms recorded at different scan rates; (c) GCD curves recorded at different current densities; (d) *SC*s obtained by CV at different scan rates (left) and *SC*s obtained by GCD at different current densities. For comparison, *SC*s obtained using ESCs with a liquid electrolyte (0.5 M NaCl) are included in (d).

The UPEA-Phe(4h)/NaCl-containing ESC shows a Coulombic efficiency (η) that grows marginally, from 90% to 92%, when the current density increases from 0.43

to 2.44 A/g as compared with the more important reduction from 92% to 78% for the ESC with UPEA-Phe(8h)/NaCl (Figure 3.2.11a). These variations indicate that the 3D structure of the UPEA-Phe(4h) hydrogel is more appropriate to preserve the reversibility in ion diffusion processes than that of UPEA-Phe(8h) one. Indeed the low η obtained for the UPEA-Phe(8h)/NaCl-containing ESC at the highest current density (78%) should be attributed to the partial broken up of the diffusion paths for ions.

The self-discharge profiles, which represent the spontaneous voltage decay on a charged ESC after a set period of time, are compared in Figure 3.2.11b. For this assay, ESCs were charged to 0.80 V at 0.50 mA, maintained at $1 \cdot 10^{-1}$ mA for 10 min and, finally, discharged to 0.00 V at -1.00 mA. The end cell voltage, which was around 0.5 V, and the short-term self-discharging time was very similar for both UPEA-Phe(8h)/NaCl and UPEA-Phe(4h)/NaCl ESCs. Thus, the main difference occurs at the charging process that is faster for the former than for the latter, which is consistent with GCD assays (Figure 3.2.10c). In any case, the fact that both ESCs present a final voltage over 0.5 V, indicating a retention >60% in the short term, ensures specific practical applications.

On the other hand, the leakage current of the two devices, which are compared in Figure 3.2.11c show a significant dropping in the beginning followed by a gradual stabilization. For UPEA-Phe(4h)/NaCl-containing ESCs, the leakage current is of 99 and 93 μA after 150 and 600 s, respectively, whereas for ESCs with UPEA-Phe(8h)/NaCl is 23 and 13 μA after 150 and 600 s, respectively. Although such low values of leakage current, which are ascribed to the self-discharge course in the device, mean that shuttle reactions caused by the impurities at the electrode materials are very small, leakage is slightly prevented when the crosslinking is not complete.

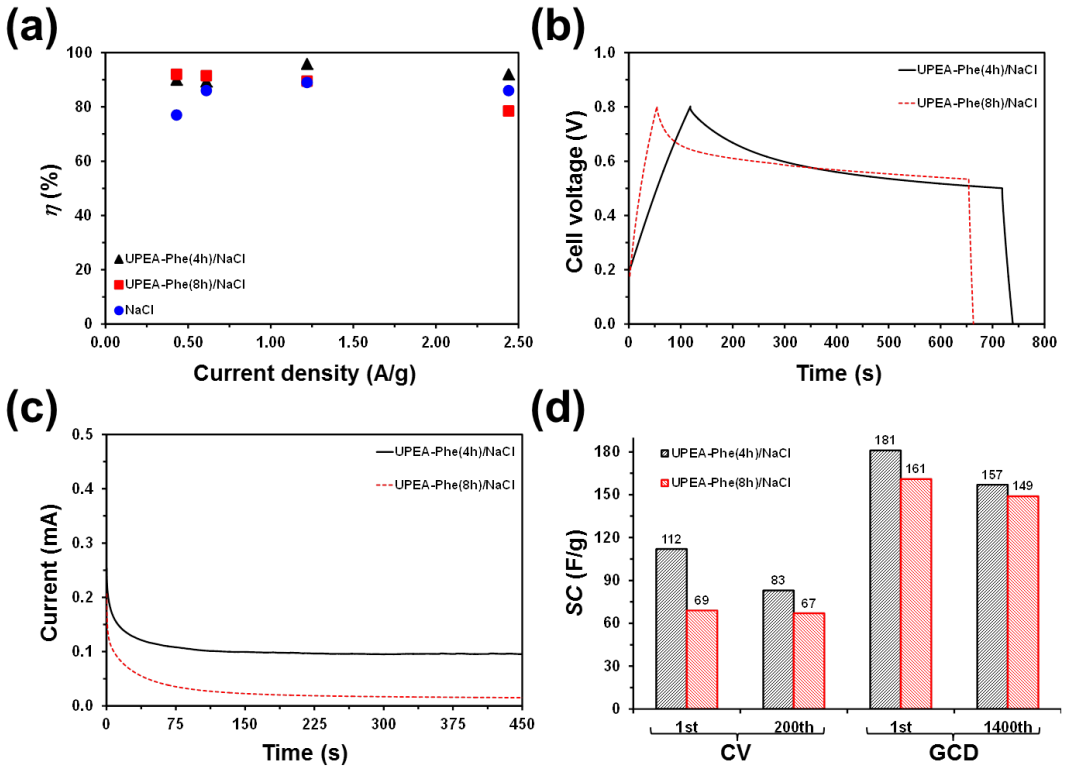

Figure 3.2.11. For ESCs with UPEA-Phe(4h)/NaCl and UPEA-Phe(8h)/NaCl: (a) Variation of the Coulombic efficiency (η) against the current density; (b) self-discharge; (c) leakage current curves; and (d) *SC*s after 200 consecutive CV cycles at 50 mV/s and after 1400 consecutive GCD cycles at 1.22 A/g. For comparison, the η values obtained using an ESC with a liquid electrolyte (0.5 M NaCl) are included in (a).

Cycling stability was evaluated considering 200 CV cycles at a scan rate of 50 mV/s and 1400 charge-discharge cycles at a current density of 1.22 A/g. The capacitance retention of two ESCs is compared in Figure 3.2.11d. The ESC with UPEA-Phe(8h)/NaCl exhibits higher capacitance retention (97% and 93% for CV and GCD, respectively) than the one with UPEA-Phe(4h)/NaCl (74% and 87% for CV and GCD, respectively). The relatively low capacitance retention of the latter has been attributed to some structural changes underwent by the hydrogel electrolyte, which make more difficult the access and escape of dopant ions. Thus, the structural integrity of the hydrogel increases with the time of exposure to UV radiation. In spite of this, it is worth noting that the *SC* of device with UPEA-

Phe(4h)/NaCl after 200 redox cycles and after 1400 charge-discharge cycles is higher than that of the ESC with pristine UPEA-Phe(8h)/NaCl (*i.e.* before starting the stability assays). This observation indicates that the lower of structural integrity in UPEA-Phe(4h) is compensated by higher available surface for ion diffusion.

It should be mentioned that UPEA-Phe hydrogels were also prepared using times of exposure to UV radiation of 2 and 6 h, named UPEA-Phe(2h) and UPEA-Phe(6h), respectively. The mechanical integrity of UPEA-Phe(2h) was very poor in comparison to that of UPEA-Phe(4h), requiring careful handling and, therefore, limiting its applicability as hydrogel electrolyte for ESCs. Instead, preliminary assays using ESCs constructed with UPEA-Phe(6h) showed a behavior close to those containing UPEA-Phe(8h), suggesting that, as expected, the photo-crosslinking reaction was very advanced after 6 h of exposure to UV radiation.

3.2.4.3 Comparison with other PEDOT-based ESCs

Figure 3.2.12. compares the performance of different ESCs devices that were all fabricated using PEDOT electrodes identical to the ones employed in the present work combined with different solid and liquid electrolytes. Accordingly, differences in their behaviors can be exclusively attributed to the electrolyte. Among solid electrolytes, UPEA-Phe(4h)/NaCl and UPEA-Phe(8h)/NaCl have been compared with the following doped hydrogels: *a)* poly-γ-glutamic acid hydrogel doped with $NaHCO_3$ in which polypeptide chains were covalently crosslinked using cystamine;[26] *b)* carboxymethyl cellulose hydrogel crosslinked with citric acid and doped with NaCl;[25] *c)* carboxymethyl cellulose sodium salt paste, which consists in an extremely high viscous polysaccharide aqueous solution, doped with NaCl;[25] and *d)* κ-carrageenan hydrogel, formed by adding KCl to a hot biopolymer aqueous solution, and doped with NaCl.[23] On the other hand, PEDOT-based ESCs with the following two liquid electrolytes were used for

comparison: *i)* a phosphate buffer saline (PBS) solution;[25] and *ii)* a 0.5 M NaCl aqueous solution.[23]

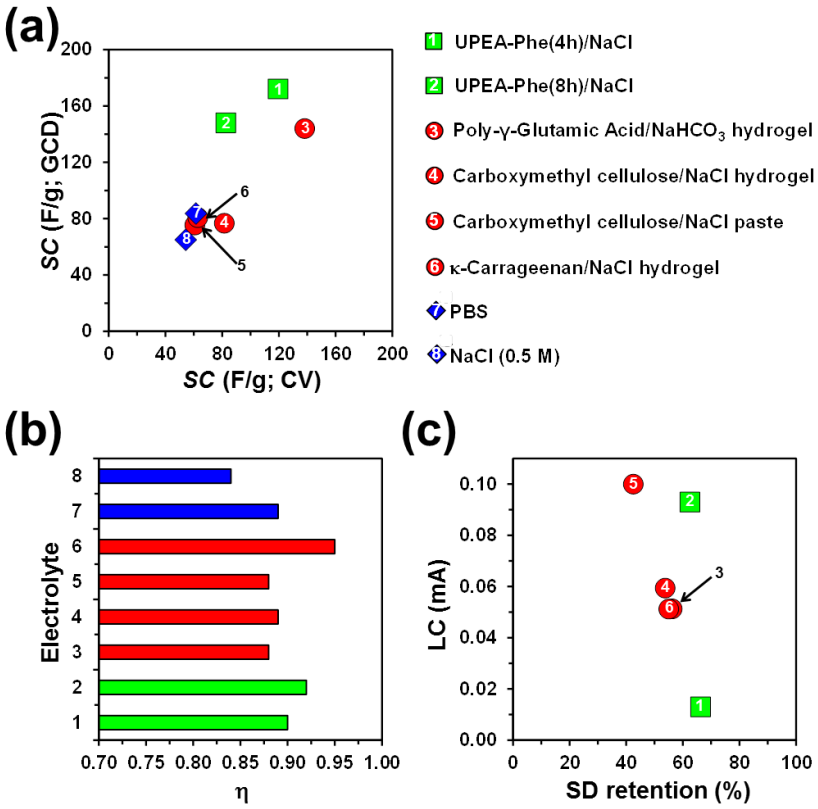

Figure 3.2.12. (a) *SC* map comparing the values obtained by CV (25 mV/s) and GCD (0.61 A/g) for different ESCs that only differ in the electrolyte (the number used to label the different solid and liquid electrolytes is displayed at the right). (b) Coulombic efficiency, as determined by GCD at 0.61 A/g, and (c) representation of the voltage retention (in %) by self-discharging against the leakage current for the same ESCs. The values compared in the different graphics were measured considering identical experimental set-ups and conditions for all ESCs.

Figure 3.2.12a shows the capacitive map of the different ESCs, in which the *SC*s obtained by CV at 25 mV/s are represented against the *SC*s by GCD at 0.61 A/g. The highest GCD value corresponds to the UPEA-Phe(4h)/NaCl-containing ESC, whereas CV value of the latter is only surpassed by the device with poly-γ-glutamic acid/$NaHCO_3$. Interestingly, the performance of UPEA-Phe(8h)/NaCl as solid electrolyte is much better than those of carboxymethyl cellulose/NaCl paste and both κ-carrageenan/NaCl and carboxymethyl cellulose/NaCl hydrogels, the

latter three exhibiting a *SC* values similar to that of liquid electrolytes. Figure 3.2.12b represents the Coulombic efficiencies, as determined by GCD at 0.61 A/g. The efficiencies of the two UPEA-Phe/NaCl hydrogels are only exceeded by the one of κ-carrageenan/NaCl. Indeed, the efficiency of carboxymethyl cellulose- and poly-γ-glutamic acid-containing devices is lower than that of the ESC with PBS as liquid electrolyte.

Figure 3.2.12c plots the voltage retention (in %) after applying a self-discharging test that was identical for all compared ESCs, against the leakage current. The highest end cell voltage retention is observed for the ESC with UPEA-Phe(4h)/NaCl. Moreover, the voltage retention of devices with the polypeptide/$NaHCO_3$ and carboxymethyl cellulose/NaCl is lower than the one of UPEA-Phe(8h)/NaCl by at least 6%. On the other hand, UPEA-Phe(4h)/NaCl presents the lowest leakage current, the parasitic current obtained for devices constructed with the other electrolytes being significantly higher. Because of its internal resistance, ESCs need a small current (the leakage current) to retain the cell voltage. Accordingly, Figure 3.2.12c allows us to conclude that the influence of the UPEA-Phe(4h)/NaCl electrolyte on the internal resistance of the whole ESC, which should be dominated by the two PEDOT electrodes, is much lower than those exerted by the other hydrogels.

3.2.5 Conclusions

In summary, molecular simulations of doped UPEA-Phe hydrogels have shown that the diffusion coefficients of Cl^- and, especially, of Na^+ increase linearly with the size of the pore. Moreover, this effect is also influenced by the hydration degree since the amount of $Na^+\cdots$UPEA-Phe interactions is inversely proportional to the hydration degree. Simulations indicate that a hydration degree of at least 300% is recommendable for the transport of the ions. Simulation results have been used to design doped UPEA-Phe hydrogels with higher pore size than those reported in previous work.[35] For this purpose, the exposure to UV radiation has been reduced from 8 h to 4 h. By taking advantage of the reduction of the pore size and structure, the ion migration improves considerably. More specifically, the *SC* determined by CV increases 54% in average (from 16% to 66%, depending on the scan rate), while the *SC* obtained by GCD increases 14% (from 3% to 27%, depending on the current density). Another parameter that experiences a drastic improvement is the leakage current, which decreases one order of magnitude with increasing pore size. As a result, the electrochemical parameters achieved by ESCs prepared using UPE-Phe(4h)/NaCl as electrolyte are outstanding not only with respect to liquid electrolytes, but also with respect to other biodegradable and biocompatible doped hydrogels based on polypeptides and polysaccharides, when identical electrodes and experimental conditions are compared. These results strongly that the UPEA-Phe(4h)/NaCl proposed here can be extended to the construction of a wide range of biocompatible, biodegradable and flexible energy-storage devices.

References

1. Dubal, Deepak P., Chodankar, Nilesh R., Kim, Do Heyoung & Gomez-Romero, Pedro. Towards flexible solid-state supercapacitors for smart and wearable electronics. *Chem. Soc. Rev.* **47**, 2065–2129 (2018).

2. Bao, Zhenan & Chen, Xiaodong. Flexible and Stretchable Devices. *Adv. Mater.* **28**, 4177–4179 (2016).

3. Pérez-Madrigal, Maria M., Edo, Miquel G. & Alemán, Carlos. Powering the future: Application of cellulose-based materials for supercapacitors. *Green Chem.* **18**, 5930–5956 (2016).

4. Xiao, Kang, Ding, Liang-Xin, Liu, Guoxue, Chen, Hongbin, Wang, Suqing & Wang, Haihui. Freestanding, Hydrophilic Nitrogen-Doped Carbon Foams for Highly Compressible All Solid-State Supercapacitors. *Adv. Mater.* **28**, 5997–6002 (2016).

5. Kou, Liang, Huang, Tieqi, Zheng, Bingna, Han, Yi, Zhao, Xiaoli, Gopalsamy, Karthikeyan, Sun, Haiyan & Gao, Chao. Coaxial wet-spun yarn supercapacitors for high-energy density and safe wearable electronics. *Nat. Commun.* **5**, 1–10 (2014).

6. Yang, Peihua & Mai, Wenjie. Flexible solid-state electrochemical supercapacitors. *Nano Energy* **8**, 274–290 (2014).

7. Zhang, Zhifang, Su, Xiaorui, Zhu, Yanyan, Chen, Zhonghui, Fang, Zebo & Luo, Xiaojing. Porous multishelled NiO hollow microspheres encapsulated within three-dimensional graphene as flexible free-standing electrodes for high-performance supercapacitors. *Nanoscale* **11**, 16071–16079 (2019).

8. Huang, Yunpeng, Cui, Fen, Bao, Jian, Zhao, Yan, Lian, Jiabiao, Liu, Tianxi & Li, Huaming. MnCo2S4/FeCo2S4 ‘lollipop’ arrays on a hollow N-doped carbon skeleton as flexible electrodes for hybrid supercapacitors. *J. Mater. Chem. A* **7**, 20778–20789 (2019).

9. Zhang, Yunhua, Shang, Zhen, Shen, Mengxia, Chowdhury, Susmita Paul, Ignaszak, Anna, Sun, Shuhui & Ni, Yonghao. Cellulose Nanofibers/Reduced Graphene Oxide/Polypyrrole Aerogel Electrodes for High-Capacitance Flexible All-Solid-State Supercapacitors. *ACS Sustain. Chem. Eng.* **7**, 11175–11185 (2019).

10. Lou, Gaobo, Wu, Yatao, Zhu, Xinqiang, Lu, Yingzhuo, Yu, Shuai, Yang, Chunhai, Chen, Hao, Guan, Cao, Li, Lu & Shen, Zhehong. Facile Activation of Commercial Carbon Felt as a Low-Cost Free-Standing Electrode for Flexible Supercapacitors. *ACS Appl. Mater. Interfaces* **10**, 42503–42512 (2018).

11. Sundriyal, Poonam & Bhattacharya, Shantanu. Inkjet-Printed Electrodes on A4 Paper Substrates for Low-Cost, Disposable, and Flexible Asymmetric Supercapacitors. *ACS Appl. Mater. Interfaces* **9**, 38507–38521 (2017).

12. Saborío, Mari Cruz G., Lanzalaco, Sonia, Fabregat, Georgina, Puiggalí, Jordi, Estrany, Francesc & Alemán, Carlos. Flexible Electrodes for Supercapacitors Based on the Supramolecular Assembly of Biohydrogel and Conducting Polymer. *J. Phys. Chem. C* **122**, 1078–1090 (2018).

13. Cai, Guofa, Darmawan, Peter, Cui, Mengqi, Wang, Jiangxin, Chen, Jingwei, Magdassi, Shlomo & Lee, Pooi See. Highly Stable Transparent Conductive Silver Grid/PEDOT:PSS Electrodes for Integrated Bifunctional Flexible Electrochromic Supercapacitors. *Adv. Energy Mater.* **6**, 1–8 (2016).

14. Wang, Gongkai, Sun, Xiang, Lu, Fengyuan, Sun, Hongtao, Yu, Mingpeng, Jiang, Weilin, Liu, Changsheng & Lian, Jie. Flexible pillared graphene-paper electrodes for high-performance electrochemical supercapacitors. *Small* **8**, 452–459 (2012).

15. Lu, Xihong, Yu, Minghao, Wang, Gongming, Tong, Yexiang & Li, Yat. Flexible solid-state supercapacitors: Design, fabrication and applications. *Energy Environ. Sci.* **7**, 2160–2181 (2014).

16. Yu, Jiali, Lu, Weibang, Pei, Shaopeng, Gong, Ke, Wang, Liyun, Meng, Linghui, Huang, Yudong, Smith, Joseph P., Booksh, Karl S., Li, Qingwen, Byun, Joon Hyung, Oh, Youngseok, Yan, Yushan & Chou, Tsu Wei. Omnidirectionally Stretchable High-Performance Supercapacitor Based on Isotropic Buckled Carbon Nanotube Films. *ACS Nano* **10**, 5204–5211 (2016).

17. Wang, Xianfu, Liu, Bin, Liu, Rong, Wang, Qiufan, Hou, Xiaojuan, Chen, Di, Wang, Rongming & Shen, Guozhen. Fiber-based flexible all-solid-state asymmetric supercapacitors for integrated photodetecting system. *Angew. Chemie - Int. Ed.* **53**, 1849–1853 (2014).

18. Li, Wanwan, Gao, Fengxian, Wang, Xiaoqian, Zhang, Ning & Ma, Mingming. Strong and Robust Polyaniline-Based Supramolecular Hydrogels for Flexible Supercapacitors. *Angew. Chemie - Int. Ed.* **55**, 9196–9201 (2016).

19. Guo, Yunzhou, Zhou, Xiao, Tang, Qianqiu, Bao, Hua, Wang, Gengchao & Saha, Petr. A self-healable and easily recyclable supramolecular hydrogel electrolyte for flexible supercapacitors. *J. Mater. Chem. A* **4**, 8769–8776 (2016).

20. Huang, Yan, Zhong, Ming, Huang, Yang, Zhu, Minshen, Pei, Zengxia, Wang, Zifeng, Xue, Qi, Xie, Xuming & Zhi, Chunyi. A self-healable and highly stretchable supercapacitor based on a dual crosslinked polyelectrolyte. *Nat. Commun.* **6**, (2015).

21. Liu, Xinhua, Wu, Dongbei, Wang, Huanlei & Wang, Qigang. Self-recovering tough gel electrolyte with adjustable supercapacitor performance. *Adv. Mater.* **26**, 4370–4375 (2014).

22. Xinhua Liu, Chengyao Yin, Jie Yang, Meiying Liang,Junjie Wei, Ziyang Zhang, Huanlei Wangand Qigang Wang. Controllable preparation of an eggshell membrane supported hydrogel electrolyte with thickness-dependent electrochemical performance. 13828–13841 (2016) doi:10.1039/c3ta12421e.

23. Pérez-Madrigal, Maria M., Estrany, Francesc, Armelin, Elaine, Díaz, David Díaz & Alemán, Carlos. Towards sustainable solid-state supercapacitors: Electroactive conducting polymers combined with biohydrogels. *J. Mater. Chem. A* **4**, 1792–1805 (2016).

24. Fabregat, Georgina, Hodásová, L'udmila, del Valle, Luis J., Estrany, Francesc & Alemán, Carlos. Sustainable Solid-State Supercapacitors Made of 3D-Poly(3,4-ethylenedioxythiophene) and κ-Carrageenan Biohydrogel. *Adv. Eng. Mater.* **20**, 1–7 (2018).

25. Pérez-Madrigal, Maria M., Edo, Miquel G., Saborío, Maricruz G., Estrany, Francesc & Alemán, Carlos. Pastes and hydrogels from carboxymethyl cellulose sodium salt as supporting electrolyte of solid electrochemical supercapacitors. *Carbohydr. Polym.* **200**, 456–467 (2018).

26. Pérez-Madrigal, Maria M., Edo, Miquel G., Díaz, Angélica, Puiggalí, Jordi & Alemán, Carlos. Poly-γ-glutamic Acid Hydrogels as Electrolyte for Poly(3,4-

ethylenedioxythiophene)-Based Supercapacitors. *J. Phys. Chem. C* **121**, 3182–3193 (2017).

27. Ruano, Guillem, Díaz, Angélica, Tononi, Jordi, Torras, Juan, Puiggalí, Jordi & Alemán, Carlos. Biohydrogel from unsaturated polyesteramide: Synthesis, properties and utilization as electrolytic medium for electrochemical supercapacitors. *Polym. Test.* **82**, (2020).

28. Yang, Hezhen, Liu, Ying, Kong, Lingbin, Kang, Long & Ran, Fen. Biopolymer-based carboxylated chitosan hydrogel film crosslinked by HCl as gel polymer electrolyte for all-solid-sate supercapacitors. *J. Power Sources* **426**, 47–54 (2019).

29. Sun, Zhuangzhi, Li, Fei, Zhang, Dan & Song, Wenlong. High-Performance All-Gel-State Nano-Biopolymer Artificial Muscles Enabled by Macromolecularly Interconnected Conductive Microporous Chitosan and Graphene Loaded Carbon Nanosheet Based Ionic Electrolyte Membrane. *J. Electrochem. Soc.* **165**, H820--H830 (2018).

30. Peng, Zhiyuan, Zou, Yubo, Xu, Shiqi, Zhong, Wenbin & Yang, Wantai. High-Performance Biomass-Based Flexible Solid-State Supercapacitor Constructed of Pressure-Sensitive Lignin-Based and Cellulose Hydrogels. *ACS Appl. Mater. Interfaces* **10**, 22190–22200 (2018).

31. Fu, Li, Wang, Aiwu, Lyu, Fucong, Lai, Guosong, Yu, Jinhong, Lin, Cheng Te, Liu, Zhong, Yu, Aimin & Su, Weitao. A solid-state electrochemical sensing platform based on a supramolecular hydrogel. *Sensors Actuators, B Chem.* **262**, 326–333 (2018).

32. Zhao, Jian, Chen, Yu, Yao, Ying, Tong, Zong Rui, Li, Pu Wang, Yang, Zi Ming & Jin, Shao Hua. Preparation of the polyelectrolyte complex hydrogel of biopolymers via a semi-dissolution acidification sol-gel transition method and its application in solid-state supercapacitors. *J. Power Sources* **378**, 603–609 (2018).

33. Cao, Lujie, Yang, Mingyang, Wu, Dong, Lyu, Fucong, Sun, Zhifang, Zhong, Xiongwei, Pan, Hui, Liu, Hongtao & Lu, Zhouguang. Biopolymer-chitosan based supramolecular hydrogels as solid state electrolytes for electrochemical energy storage. *Chem. Commun.* **53**, 1615–1618 (2017).

34. Kasturi, Palanisamy Rupa, Ramasamy, Harivignesh, Meyrick, Danielle,

Sung Lee, Yun & Kalai Selvan, Ramakrishnan. Preparation of starch-based porous carbon electrode and biopolymer electrolyte for all solid-state electric double layer capacitor. *J. Colloid Interface Sci.* **554**, 142–156 (2019).

35. Armelin, Elaine, Pérez-Madrigal, Maria M., Alemán, Carlos & Díaz, David Díaz. Current status and challenges of biohydrogels for applications as supercapacitors and secondary batteries. *J. Mater. Chem. A* **4**, 8952–8968 (2016).

36. D.A. Case, K. Belfon, I.Y. Ben-Shalom, S.R. Brozell, D.S. Cerutti, T.E. Cheatham, III, V.W.D. Cruzeiro, T.A. Darden, R.E. Duke, G. Giambasu, M.K. Gilson, H. Gohlke, A.W. Goetz, R. Harris, S. Izadi, S.A. Izmailov, K. Kasavajhala, A. Kovalenko, R. Krasny, T, D. M. York and P. A. Kollman. Amber 2018.

37. Wang, Junmei, Wang, Wei, Kollman, Peter A. & Case, David A. Automatic atom type and bond type perception in molecular mechanical calculations. *J. Mol. Graph. Model.* **25**, 247–260 (2006).

38. Wang, Junmei, Wolf, Romain M., Caldwell, James W., Kollman, Peter A. & Case, David A. Development and testing of a general Amber force field. *J. Comput. Chem.* **25**, 1157–1174 (2004).

39. A. Pigache, P. Cieplak &. F. Y. Dupradeau. Automatic and highly reproducible RESP and ESP charge derivation: Application to the development of programs RED and X RED. in (2004).

40. Dupradeau, Franois Yves, Pigache, Adrien, Zaffran, Thomas, Savineau, Corentin, Lelong, Rodolphe, Grivel, Nicolas, Lelong, Dimitri, Rosanski, Wilfried & Cieplak, Piotr. The R.E.D. tools: Advances in RESP and ESP charge derivation and force field library building. *Phys. Chem. Chem. Phys.* **12**, 7821–7839 (2010).

41. Bayly, Christopher I., Cieplak, Piotr, Cornell, Wendy & Kollman, Peter A. A well-behaved electrostatic potential based method using charge restraints for deriving atomic charges: the RESP model. *J. Phys. Chem.* **97**, 10269–10280 (1993).

42. Cieplak, Piotr, Cornell, Wendy D., Bayly, Christopher & Kollman, Peter A. Application of the multimolecule and multiconformational RESP methodology to biopolymers: Charge derivation for DNA, RNA, and

proteins. *J. Comput. Chem.* **16**, 1357–1377 (1995).

43. Darden, Tom, York, Darrin & Pedersen, Lee. Particle mesh Ewald: An N·log(N) method for Ewald sums in large systems. *J. Chem. Phys.* **98**, 10089–10092 (1993).

44. Davidchack, Ruslan L., Handel, Richard & Tretyakov, M. V. Langevin thermostat for rigid body dynamics. *J. Chem. Phys.* **130**, 234101 (2009).

45. Berendsen, H. J. C., Postma, J. P. M., van Gunsteren, W. F., DiNola, A. & Haak, J. R. Molecular dynamics with coupling to an external bath. *J. Chem. Phys.* **81**, 3684–3690 (1984).

46. Ruano, G., Díaz, A., Tononi, J., Torras, J., Puiggalí, J. & Alemán, C. Biohydrogel from unsaturated polyesteramide: Synthesis, properties and utilization as electrolytic medium for electrochemical supercapacitors. *Polym. Test.* **82**, (2020).

47. Guo, Kai, Chu, C. C., Chkhaidze, E. & Katsarava, R. Synthesis and characterization of novel biodegradable unsaturated poly(ester amide)s. *J. Polym. Sci. Part A Polym. Chem.* **43**, 1463–1477 (2005).

48. Leontidis, Epameinondas, Forrest, Bruce M., Widmann, Albert H. & Suter, Ulrich W. Monte Carlo algorithms for the atomistic simulation of condensed polymer phases. *J. Chem. Soc.{,} Faraday Trans.* **91**, 2355–2368 (1995).

49. Alemán, Carlos, Karayiannis, Nikos Ch, Curcó, David, Foteinopoulou, Katerina & Laso, Manuel. Computer simulations of amorphous polymers: From quantum mechanical calculations to mesoscopic models. *J. Mol. Struct. THEOCHEM* **898**, 62–72 (2009).

50. Bertran, Oscar, Curcó, David, Torras, Juan, Ferreira, Carlos A. & Alemán, Carlos. Field-induced transport in sulfonated poly(styrene-co-divinylbenzene) membranes. *Macromolecules* **43**, 10521–10527 (2010).

51. Curco, David & Aleman, Carlos. Performance of SuSi: A method for generating atomistic models of amorphous polymers based on a random search of energy minima. *J. Comput. Chem.* **25**, 790–798 (2004).

52. Curcó, David & Alemán, Carlos. Computational tool to model the packing of polycyclic chains: Structural analysis of amorphous polythiophene. *J. Comput. Chem.* **28**, 1743–1749 (2007).

53. Riniker, Sereina. Fixed-Charge Atomistic Force Fields for Molecular Dynamics Simulations in the Condensed Phase: An Overview. *J. Chem. Inf. Model.* **58**, 565–578 (2018).

54. English, Niall J. & Waldron, Conor J. Perspectives on external electric fields in molecular simulation: progress{,} prospects and challenges. *Phys. Chem. Chem. Phys.* **17**, 12407–12440 (2015).

55. Bae, J. M., Honma, I., Murata, M., Yamamoto, T., Rikukawa, M. & Ogata, N. Properties of selected sulfonated polymers as proton-conducting electrolytes for polymer electrolyte fuel cells. *Solid State Ionics* **147**, 189–194 (2002).

56. Bachl, Jürgen, Zanuy, David, Lõpez-Pérez, Daniel E., Revilla-Lõpez, Guillermo, Cativiela, Carlos, Alemán, Carlos & Díaz, David Díaz. Synergistic computational-experimental approach to improve ionene polymer-based functional hydrogels. *Adv. Funct. Mater.* **24**, 4893–4904 (2014).

57. Bachl, Jürgen, Bertran, Oscar, Mayr, Judith, Alemán, Carlos & Díaz Díaz, David. Aromatic ionene topology and counterion-tuned gelation of acidic aqueous solutions. *Soft Matter* **13**, 3031–3041 (2017).

3.3 Electrical and Capacitive Response of Hydrogel Solid-Like Electrolytes for Supercapacitors

3.3.1 Summary

Flexible hydrogels are attracting significant interest as solid-like electrolytes for energy storage devices, especially for supercapacitors, because of their lightweight and anti-deformation features. Here, we present a comparative study of four ionic conductive hydrogels derived from biopolymers and doped with 0.1 M NaCl. More specifically, such hydrogels are constituted by κ-carrageenan, carboxymethyl cellulose, poly-γ-glutamic acid or a phenylalanine-containing polyesteramide. After examining the morphology and the swelling ratio of the four hydrogels, their electrical and capacitive behaviors have been examined using electrochemical impedance spectroscopy. Measurements have been conducted on devices where a hydrogel film was sandwiched between two identical poly(3,4-ethylenedioxythiophene) electrodes. Overall, the polyesteramide hydrogel exhibits the most adequate properties (*i.e.* low electrical resistance, high capacitance and good interfacial contact with the electrode) to be used as semi-solid electrolyte for supercapacitors, which has been attributed to its distinctive structure based on the homogeneous and abundant distribution of both micro- and nano-pores. Indeed, the morphology of the polyestermide hydrogel reduces the hydrogel resistance, enhances the transport of ions, and results in a better interfacial contact between the electrodes and solid electrolyte. The correlation between the supercapacitor performance and the hydrogel porous morphology is presented as an important design feature for the next-generation of light and flexible energy storage devices for wearable electronics.

3.3.2 Introduction

In the last decade, organic electronics has been considered as a key technology for portable and wearable energy-storage devices, as for example batteries and supercapacitors, that require flexibility, lightweight and anti-deformation properties.[1-5] Although batteries can store a high amount of specific energy, they exhibit low power-handling capabilities, delivering electricity at low current densities.[6,7] Instead, supercapacitors provide high specific power and efficiency, as well as higher cyclic durability than batteries.[8,9]

In recent years, progress in the development of flexible supercapacitors has been mainly focused on the manufacture of flexible electrodes, which include not only flexible substrates coated with a thin layer of electrochemically active materials,[10,11] but also free-standing conducting carbon based materials, such as carbon nanotubes- and graphene-containing materials.[12-16] However, the combination of such electrodes with conventional liquid electrolytes presents serious limitations since the undesired leakage of harmful liquid and the dislocation of electrodes occur when the device is repeatedly bended or compressed. Furthermore, the incompressible behavior of liquid electrolytes hinders the mechanical integrity of the devices. In order to overcome those drawbacks, the substitution of liquid electrolytes by hydrogel solid-like electrolytes has appeared as a simple strategy able to prevent the above mentioned inconvenient under harsh mechanical conditions.

A hydrogel consists of a polymer network (*i.e.* with physical or chemical crosslinks) and an aqueous solution. The polymer makes the hydrogel an elastic solid, while the aqueous solution containing a salt (*e.g.* NaCl) makes it an ionic conductor. The mesh size of the polymer network is larger than the size of water molecules and ions coming from the salt, thus allowing water molecules in the hydrogel to maintain the same chemical and physical properties as in a liquid-state

solution.[17] Although at present time polyvinyl alcohol (PVA)-based gels are the most widely used electrolytes for solid-state supercapacitors,[1,18] biopolymer-derived systems are gaining increasing attention. For example, polysaccharides,[19-23] proteins and polypeptides,[24-27] and even synthetic polymers incorporating biological units, such as polyesteramides,[28,29] have been used to prepare hydrogels as solid-like electrolytes for manufacturing bioinspired supercapacitors. Indeed, their electrochemical response has been well-studied by cyclic voltammetry and galvanostatic charge-discharge cycles;[1,18-29] however, their ionic conductivity and capacitive properties remain unknown in many cases. It is worth noting that materials to be applied as an electrolyte must exhibit high ionic conductivity, in the order of ~10^{-3} S/cm at room temperature.[30] Although this condition is fulfilled by synthetic hydrogels, as for example polyethylene oxide (PEO)-based hydrogel electrolytes with 30% wt. KOH (~10^{-3} S/cm),[31] PVA blended with PEO (~10^{-2} S/cm),[32] and potassium polyacrylate (PAAK; ~0.3 S/cm),[33] the ionic conductivity of many biopolymeric hydrogels is yet to be determined.

Hence, in this work, we investigate the conductive and capacitive properties of different biopolymeric hydrogels using electrochemical impedance spectroscopy (EIS). More specifically, hydrogels from the following four biopolymers have been prepared: 1) κ-carrageenan (κC);[23] 2) carboxymethyl cellulose sodium salt (CMC);[22] 3) poly-γ-glutamic acid (PGGA);[27] and 4) polyesteramide containing phenylalanine, butenediol and fumarate (PEA).[29] By applying EIS, we aim to obtain additional information on their supercapacitor performance and, thus, fully characterize these hydrogel-based systems to act as solid-like electrolytes. To that end, all prepared hydrogels were doped with 0.1 M NaCl. After evaluating their morphology and swelling ratio, data derived from EIS studies, including the electrical equivalent circuits (EECs) have been obtained and discussed. Overall, the suitability of these biopolymer-derived systems in organic electronics is

confirmed. Concretely, the PEA hydrogel, which contains biological units, exhibits the most adequate properties - in terms of electrical resistance, capacitance and interfacial contact - to be used as semi-solid electrolyte for supercapacitors.

3.3.3 Methods

3.3.3.1 Materials

All reagents were used as purchased without further purification. κC sulfated plant polysaccharide (22048, 5-25 mPa.s, 0.3% in H_2O (25 ºC)), NaCMC with high viscosity (1500-3000 cP, 1 % in H_2O at 25 °C), cystamine dihydrochloride (≥98.0%), 1-[3-(dimethylamino)propyl]-3-ethylcarbodiimide methiodide (EDC methiodine), citric acid (99%), sodium azide (NaN_3 ≥99.5%), L-phenylalanine (reagent grade, 98%), *p*-toluenesulfonic acid monohydrate (ACS reagent, 98.5%), *cis*-2-butene-1,4-diol (97%), toluene (99.8%), fumaryl chloride (95%), acetone (HPLC, 99.9%), acryloyl chloride (97%), *N*,*N*-dimethylacetamide anhydrous, 1-butanol (ACS reagent, 99.4%), *n*-hexane (reagent grade) and 2-hydroxy-4'-(2-hydroxyethoxy)-2-methylpropiophenone (Irgacure) were purchased from Sigma-Aldrich. Free-acid PGGA (from *Bacillus subtilis*) with average molecular weight (M_w) of 350,000 was purchased from Wako Chemicals GmbH (Neuss, Germany). Poly(ethylene glycol) (M_n= 10000 g/mol) and ethyl acetate were purchased from Fluka. Dimethyl sulfoxide (DMSO, Analytical reagent) was purchased from Fisher.

3.3.3.2 Synthesis

The synthesis of the four studied hydrogels was already reported[28,34-37] and, therefore, a brief description of the employed procedures is only provided.

κ-Carrageenan (κC) hydrogel. κC has one ester sulfate group in the repeating unit, which forms strong and rigid gels in the presence of K^+. In this work, κC was dissolved in water at 2% w/v at *ca.* 75-80 °C. Then, the corresponding volume of 1 M KCl (10% v/v) was added, and the solution stirred vigorously. Finally, the hydrogel was obtained by cooling the hot κC aqueous solution to room temperature for several hours, enabling a 3D network in which polymeric segments form

junction points cross-linked by K^+.[34] The κC hydrogel was washed with distilled water three times.

Carboxymethyl cellulose sodium salt (CMC) hydrogel. CMC (10 % wt.) was mixed with water using, firstly, a high speeded magnet mixer and later, as the viscosity increased, manually with a glass rod. Then, the resulting CMC paste was processed in small pieces with a hydraulic press (10 Pa, 1 min), which were kept at 4 °C prior to the formation of the hydrogel. CMC polymeric chains were cross-linked by immersing the pieces into 1.5 M citric acid solution for 24 hours at room temperature under slight shaking (80 rpm).[35] The excess of citric acid was removed by washing the pieces four times with distilled water.

Poly-γ-glutamic acid (PGGA) hydrogel. PGGA hydrogel (1 mL) was prepared by dissolving PGGA and EDC in 750 µL of sodium hydrogen carbonate solution (0.5 M) at 4 °C under magnetic stirring. Then, cystamine dihydrochloride, previously dissolved in 0.25 mL sodium hydrogen carbonate solution (0.5 M), was added to the solution and mixed during 2-3 minutes. The PGGA / EDC / cystamine molar ratio was 5 / 5 / 2.5. The final solution was mixed with a magnetic stirrer, and then poured into glass molds. The solution was let to gel at room temperature for one hour.[36] In order to remove any compound in excess, the resulting hydrogel was washed with distilled water three times.

Polyesteramide (PEA) hydrogel. The synthesis of the di-*p*-toluenesulfonic acid salt of L-phenylalanine butene 1,4-diester and di-*p*-nitrophenyl fumarate monomers, as well as their polycondensation to produce UPEA chains with C=C double bonds in the backbone, were conducted using the procedure described by Katsarava and co-workers.[37] Functionalized polyethylene glycol, which was used as crosslinker, was prepared using triethylamine and acryloil chloride, as reported in recent work.[28] Then, a 1:4 UPEA:crosslinker (w/w) mixture was dissolved in dimethylacetamide for the reticulation reaction, which was conducted by adding the photoinitiator irgacure 2959 (5% wt.) and exposing the solution to an UV lamp

(230 V, 0.8 A) for 4 h at room temperature. The resulting hydrogel was washed with distilled water, which was periodically replaced, during 3 days.

3.3.3.3 Characterization

Infrared absorption spectra were recorded with a Fourier Transform FTIR 4100 Jasco spectrometer equipped with a Specac Model MKII Golden Gate attenuated total reflection (ATR) cell and a heated Diamond ATR.

Scanning electron microscopy (SEM) studies were performed using a Focused Ion Beam Zeiss Neon40 scanning electron microscope equipped with an energy dispersive X-ray (EDX) spectroscopy system and operating at 5 kV. Prior to SEM observation, samples were lyophilized. All samples were sputter-coated with a thin carbon layer using a K950X Turbo Evaporator to prevent electron charging problems. Pore size was determined from the SEM images using the software SmartTIFF (v1.0.1.2.).

The swelling ratio (SR, %) of the prepared hydrogels was determined according to:

$$SR = \frac{w_W - w_D}{w_D} \qquad \text{(E.3.3.1)}$$

where w_W is the weight of the hydrogels as prepared (after the washing step) and w_D is the weight of the hydrogel after freeze-drying (dried hydrogel).

Electrochemical impedance spectroscopy (EIS) diagrams were taken at open circuit (OCP) over the frequency range of 100 kHz to 10 Hz with potential amplitude of 0.05 V using an AUTOLAB-302N potentiostat/galvanostat. All experiments were performed at room temperature using a hydrogel as solid electrolyte sandwiched between two poly(3,4-ethylenedioythiophene) (PEDOT) electrodes.

PEDOT electrodes were prepared by chronoamperometry (CA) using a constant potential of 1.40 V under nitrogen atmosphere and at room temperature.

A three-electrode one-compartment cell was filled with 50 mL of acetonitrile containing EDOT monomer (10 mM) and $LiClO_4$ (0.1 M) as supporting electrolyte. Stainless Steel AISI 316 sheets with an area of 6 cm^2 were employed as working and counter electrodes. The reference electrode was an Ag|AgCl electrode containing a KCl saturated aqueous solution (E^0 = 0.222 V *vs.* standard hydrogen electrode at 25 °C). The polymerization time (θ) was adjusted to obtain PEDOT electrodes with a polymerization charge of 2.67 C (445 mC/cm^2).

After data collection, EIS results were then processed and fitted to an electrical equivalent circuit (EEC). The percentage error associated with each circuit element was acceptably low (see next section).

3.3.4 Results and Discussion

The successful preparation of the κC, CMC, PGGA and PEA hydrogels was confirmed by FTIR. The chemical structures derived from the recorded spectra (not shown) were fully consistent with those reported in previous works.[22,23,27,29] Before running EIS analyses, the morphology (Figure 3.3.1) and SR (Eq E.3.3.1, Table 3.3.1) of the four hydrogels were examined.

SEM characterization was conducted to determine the morphology of the hydrogel networks and understand the correlation between pore size and the supercapacitor performance. Representative low and high magnification SEM micrographs of the four studied hydrogels are shown in Figure 3.3.1. In spite of their morphological differences, pores can be easily identified in the low magnification micrographs of all samples. Although κC, CMC and PGGA hydrogels present well-defined pores with average size of 26 ± 9, 52 ± 14 and 19 ± 8 μm, respectively, the structure of κC is clearly less open than those of CMC and PGGA. Thus, the latter hydrogels show micropores similar to those typically found in honey-comb structures, whereas κC exhibits more compact and less interconnected microporous. In addition to such micrometric pores, representative high magnification micrographs reveal the existence of regions with nanometric pores, which are heterogeneously distributed and are expected to participate in the ion diffusion process. On the other hand, although PEA hydrogel exhibits a more compact structure, micrometric pores with an average size 14 ± 10 μm are clearly identified. Another remarkable difference between PEA and the other three hydrogels is the existence of nanometric pores homogeneously distributed throughout the whole surface, which is evidenced in the high resolution SEM micrograph. Therefore, both κC and PEA hydrogels display a more densely packed network, which is expected to affect the conductive and capacitive features of the resulting device.

Swelling measurements gave us additional information about the porous structure of the hydrogels. Indeed, high SR values indicate that the swellable hydrogels are able to hold large amounts of water. In general, the amount of swelling depends on several factors, such as chemical structure, composition, crosslinking density, solvent, among others. Hence, although a porous structure was observed for the four systems, the different nature of the hydrogels could influence the swelling response. The SR of the four studied hydrogels varies as follows: PGGA < κC << PEA << CMC. It is worth noting that CMC shows the largest micropores (Table 3.3.1), which explains the very high SR of this hydrogel (SR = 2356% ± 241%). Instead, the average size of the micropores in PEA is comparable to that of PGGA, its high SR (SR = 1416% ± 297%) being attributed to the homogeneous and abundant distribution of nanopores on the whole surface.

Table 3.3.1. Diameter of the micropores (D), swelling ratio (SR) and resistance (R_p) of the four studied hydrogels.

Hydrogel	D (μm)	SR (%)	R_P (Ω)
κC	26 ± 9,	1070 ± 122	2.89
CMC	52 ± 14	2356 ± 241	5.57
PGGA	19 ± 8	483 ± 39	2.49
PEA	17 ± 7	1416 ± 297	2.17

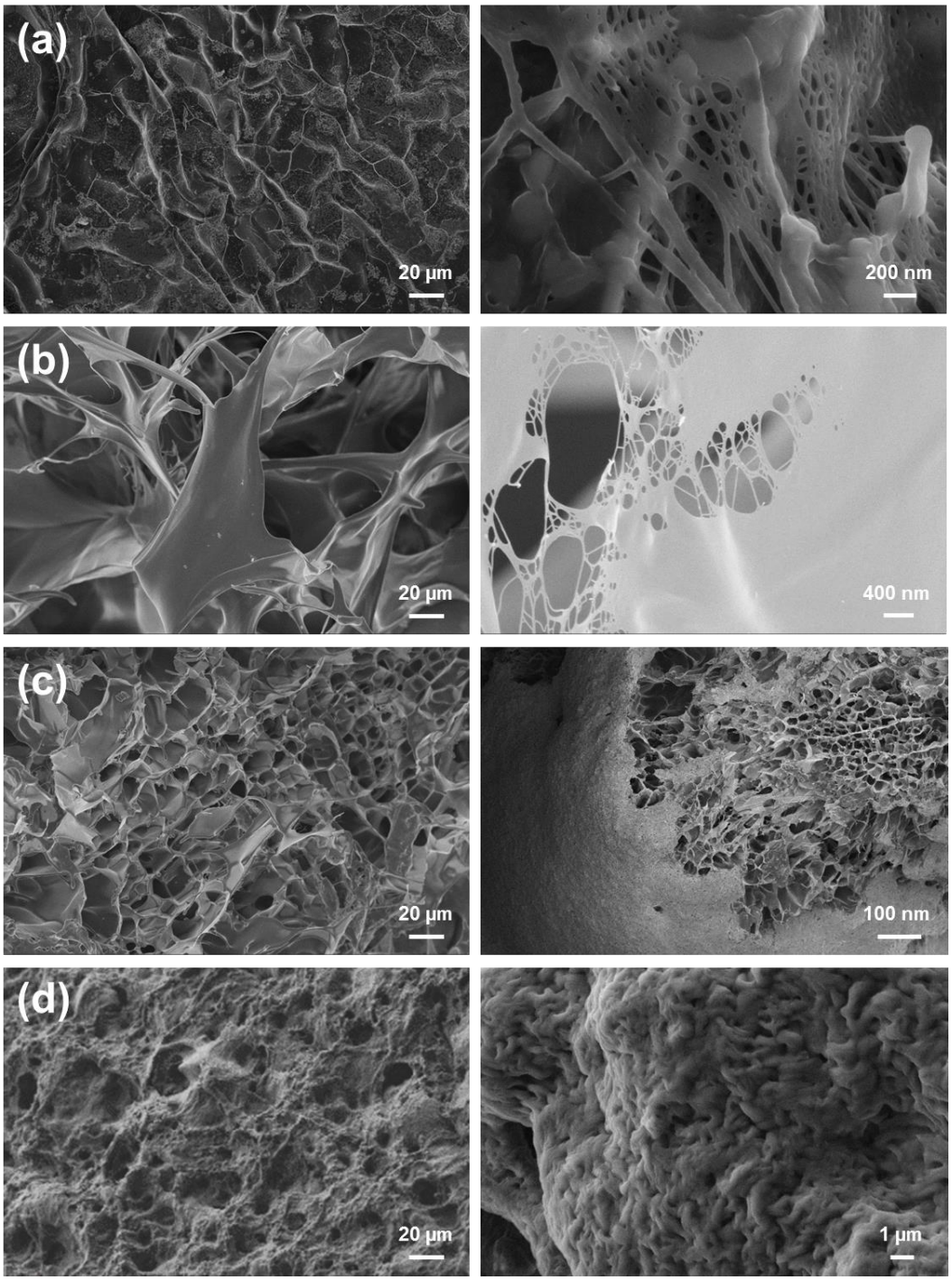

Figure 3.3.1. SEM micrographs of (a) κC, (b) CMC, (c) PGGA and (d) PEA hydrogels: General view (low magnification images, left) and details (high magnification images, right).

EIS was employed to investigate the electrical and capacitive performance of κC, CMC, PGGA and PEA hydrogels, which were previously doped by soaking them in 0.1 M NaCl solution prepared with distilled water for 24 h. Then, hydrogels

were cut in pieces of rectangular shape of dimensions 0.5 × 0.5 × 0.1 cm^3. EIS measurements were conducted at room temperature using a sandwiched configuration, in which each hydrogel piece was arranged separating two PEDOT electrodes at a distance of 0.1 cm (Figure 3.3.2). PEDOT electrodes were prepared as described in the Methods section.

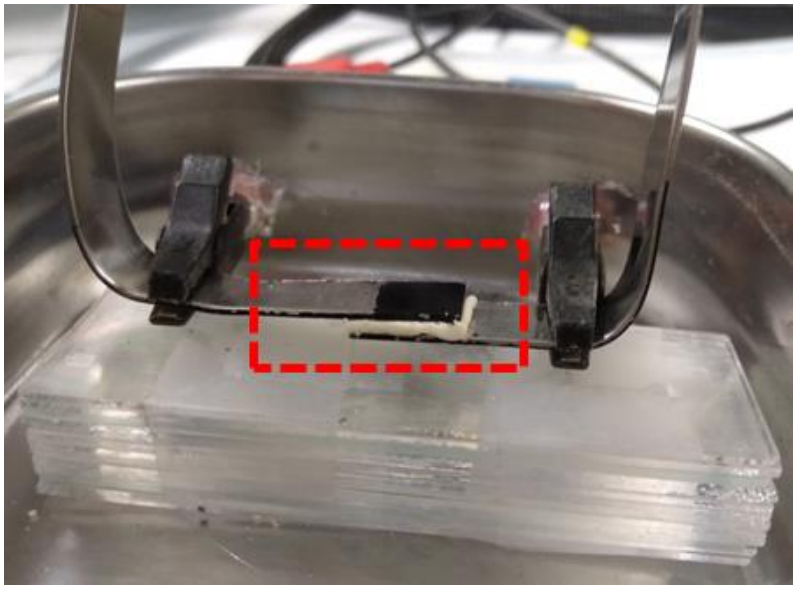

Figure 3.3.2. Sandwiched configuration used to perform EIS measurements on κC, CMC, PGGA and PEA hydrogels. The hydrogel separating the two PEDOT electrodes are marked by the read box.

The Nyquist and Bode plots, as well as the electric equivalent circuit (EEC) derived from such diagrams, are displayed in Figures 3.3.3-3.3.6. The quality of the experimental data fitted to the EEC was evaluated to estimate the percentage error associated with each circuit element, being comprised between 0.1% and 6.2% for κC, 0.3% and 7.1% for CMC, 0.3% and 5.2% for PGGA, and 0.3% and 5.1% for PEA. The EEC obtained for CMC, PGGA and PEA are identical (Figures 3.3.4-3.3.6), while κC exhibits a more complex ECC with two additional elements (Figure 3.3.3), which we ascribe to its particularly compact structure (see below).

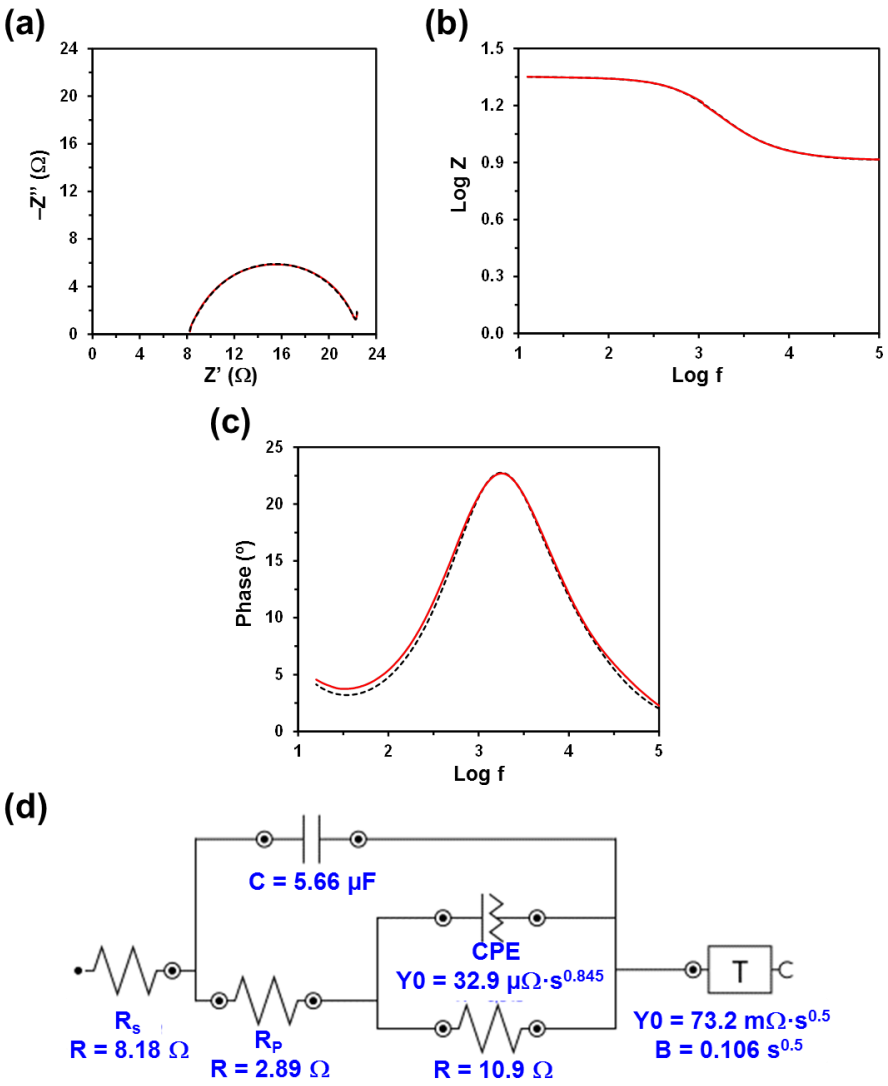

Figure 3.3.3. Measured and fitted EIS spectra (solid red line and dashed black line, respectively) for the κC hydrogel sandwiched between two PEDOT electrodes: (a) Nyquist plot; (b) impedance Bode plot; and (c) phase Bode plot. (d) EEC model used for numerical fitting of the EIS data. Numerical results from fitting the spectra are displayed for all the elements of the EEC.

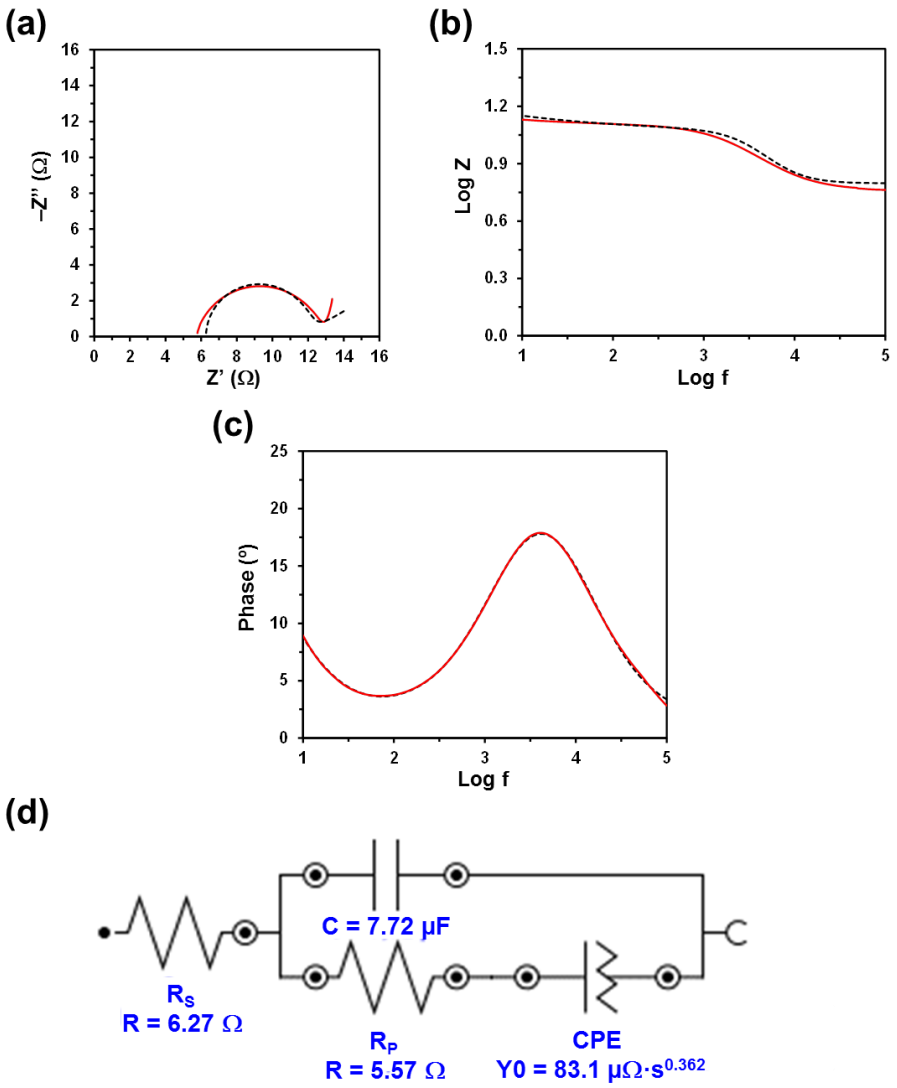

Figure 3.3.4. Measured and fitted EIS spectra (solid red line and dashed black line, respectively) for the CMC hydrogel sandwiched between two PEDOT electrodes: (a) Nyquist plot; (b) impedance Bode plot; and (c) phase Bode plot. (d) EEC model used for numerical fitting of the EIS data. Numerical results from fitting the spectra are displayed for all the elements of the EEC.

The measured Nyquist plots, in which the real part of the impedance (Z) is plotted against the imaginary part (Z'), show a semicircle in all cases. The starting point of each curve (*i.e.* the intercept of the curve with the real Z-axis in the high frequency region) indicates the electrolyte resistance (R_S), that is the resistance of the doping solution inside the hydrogel pore. R_S only depends on the ionic concentration, type of ions, temperature and the geometry of the area in which the

current is carried (*i.e.* hydrogel mesh size). Considering that in this work all hydrogels were soaked in a 0.1 M NaCl electrolytic solution and that the temperature was very similar in all experiments, the small variation expected among the different analyzed systems should be attributed to the different concentration of NaCl inside the hydrogels (*i.e.* the doping capacity of the hydrogels) and the morphology of the hydrogel (*i.e.* mesh size). Thus, the lower the concentration and the ion mobility (*i.e.* more restricted by the morphology) in the hydrogel, the higher the R_S value will be.

Although the R_S values displayed in Figures 3.3.3-3.3.6 are of the same order of magnitude, they increase as follows: PEA (3.11 Ω) < PGGA (5.92 Ω) < CMC (6.27 Ω) < κC (8.18 Ω). κC exhibited the most compact structure (Figure 3.3.1a) and, therefore, the largest area, which affected negatively the entrance of ions. Instead, PEA displays a homogeneous network of nanometric pores (Figure 3.3.1d), facilitating the access of Na^+ and Cl^- ions and their mobility inside the hydrogel. Both CMC and PGGA exhibit pseudo-honey-comb structures with very similar R_S values, which are intermediate between those of κC and PEA. Overall, the resistivity of the doped hydrogel increases with R_S. Thus, when the solution resistance increases, it means that the resistivity of the electrolyte solution increases and the pore area (solid phase area) decreases.

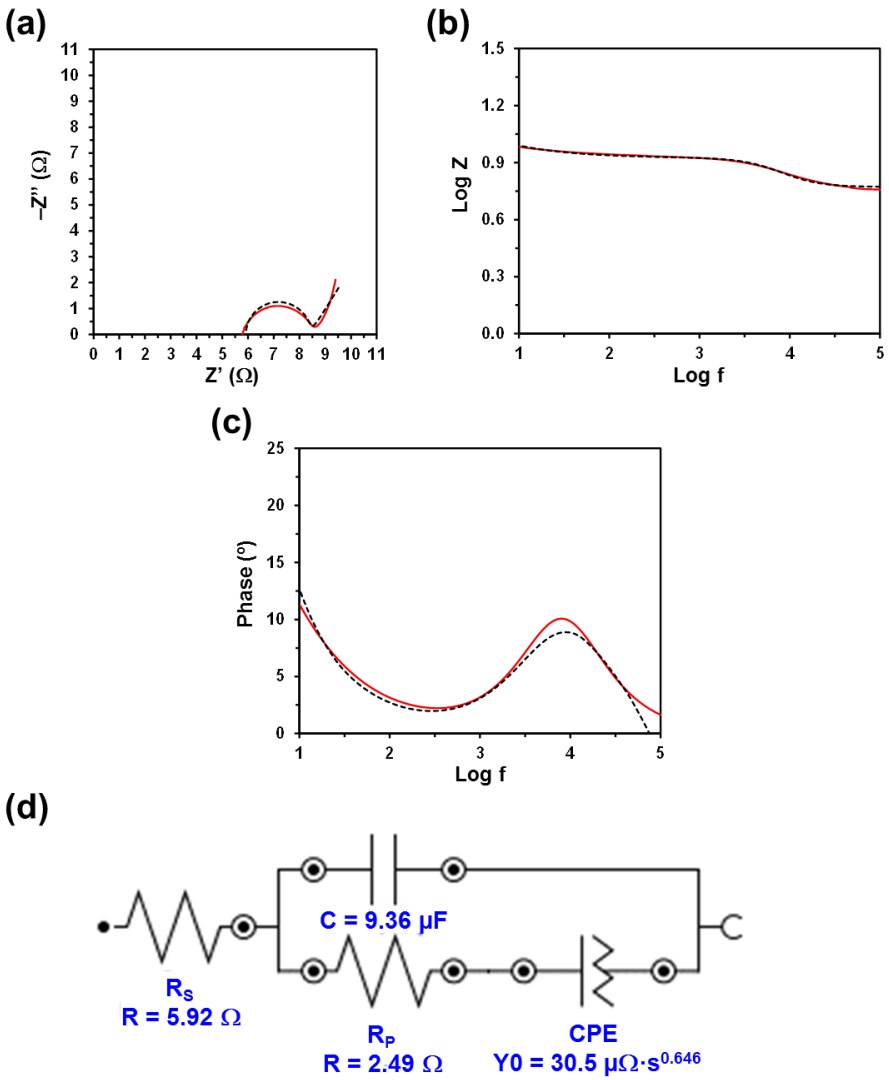

Figure 3.3.5. Measured and fitted EIS spectra (solid red line and dashed black line, respectively) for the PGGA hydrogel sandwiched between two PEDOT electrodes: (a) Nyquist plot; (b) impedance Bode plot; and (c) phase Bode plot. (d) EEC model used for numerical fitting of the EIS data. Numerical results from fitting the spectra are displayed for all the elements of the EEC.

The diameter of the semicircle corresponds to the charge transfer resistance (R_P) at the PEDOT electrode / hydrogel interface, also known as the interface reaction resistance. In all the cases, the R_P, which includes the resistance of the hydrogel and the PEDOT electrodes, is slightly lower than the R_S. The values R_P obtained for κC, PGGA and PEA are similar (*i.e.* 2.89, 2.49 and 2.17 Ω, respectively) and lower than that of CMC (5.57 Ω), which indicates that the former

hydrogels present better interfacial contact between the electrodes and the solid electrolyte. Indeed, the better the interfacial contact, the faster the ion transport and the lower the interfacial resistance.

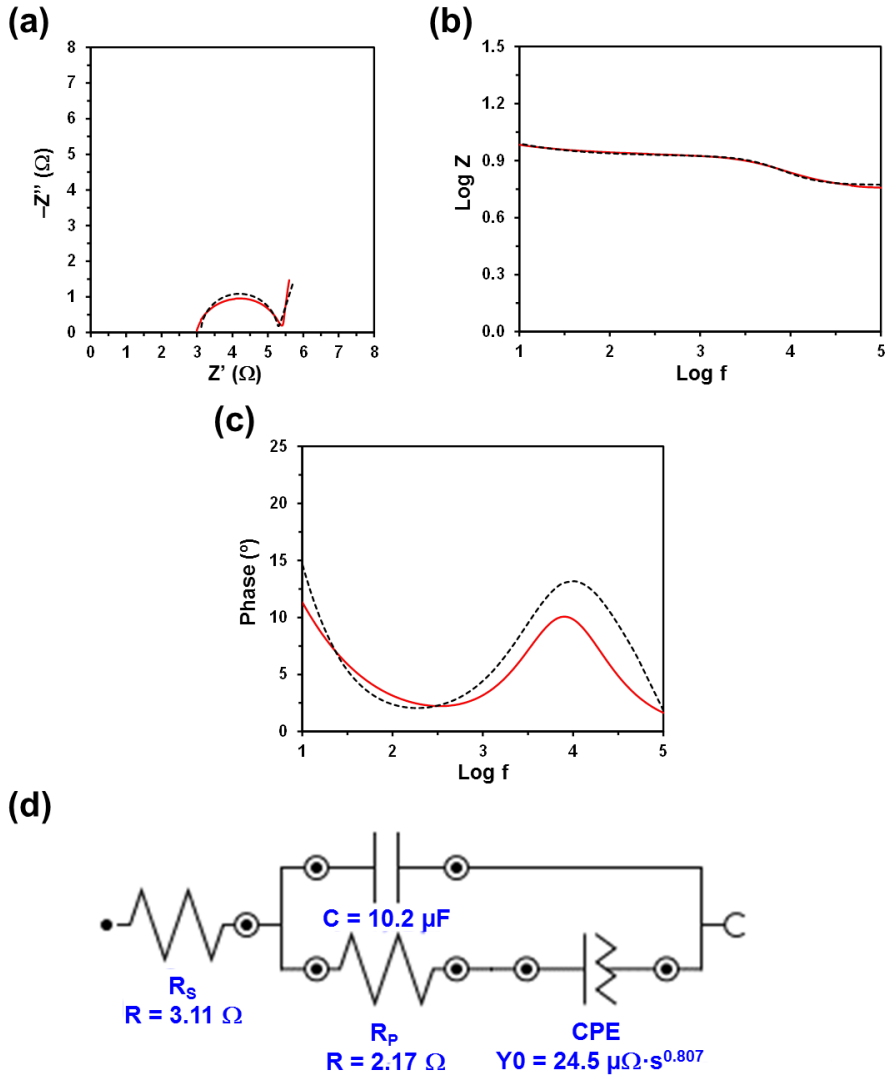

Figure 3.3.6. Measured and fitted EIS spectra (solid red line and dashed black line, respectively) for the PEA hydrogel sandwiched between two PEDOT electrodes: (a) Nyquist plot; (b) impedance Bode plot; and (c) phase Bode plot. (d) EEC model used for numerical fitting of the EIS data. Numerical results from fitting the spectra are displayed for all the elements of the EEC.

The Bode diagrams, which represent the frequency response of impedance (Figure 3.3.3b-3.3.6b) and phase angle (Figure 3.3.3c-3.3.6c), display two time constants. The first is below 10^1 Hz and is related to the hydrogel, whereas the second is around $10^{3.2}$, $10^{3.6}$, $10^{3.9}$ and $10^{4.0}$ Hz for κC, CMC, PGGA and PEA hydrogels, respectively. The second time constant has been associated with the interface between the PEDOT electrode and the hydrogel.

The sum of the electrolyte resistance (R_S) and the interfacial resistance (R_P) can be interpreted as the internal resistance ($R_b = R_S + R_P$), which corresponds to the bulk resistance of the whole device, as was recently demonstrated.[37,38] The values of R_b increase as follows: PEA (5.28 Ω) < PGGA (8.41 Ω) < κC (11.07 Ω) < CMC (11.84 Ω). Overall, the conductive properties of PGGA and, especially, PEA are superior to those of κC and CMC, which we ascribe to their better interfacial contact and the hydrogel structure.

The bulk conductivity (σ) of the prepared doped hydrogels is 76, 48, 36 and 34 mS/cm for PEA, PGGA, κC and CMC, respectively. It is worth noting that the conductivity of these biohydrogels is comparable to those reported for PVA-containing hydrogels; for instance, PVA doped with H_3PO_4 or H_2SO_4 (11.6 or 7.1 mS/cm, respectively),[39,40] PVA doped with H_3PO_4 and 2-mercaptopyridine (22.6 mS/cm),[41] PVA doped with H_2SO_4 and indigo carmine or alizarin red S (20.3 or 33.1 mS/cm, respectively),[42] chemically crosslinked PVA-poly(ethylene glycol) (67.1 mS/cm)[43] and KCl doped boron cross-linked PVA (38 mS/cm).[44] Besides, the ionic conductivity of a 0.1 M NaCl aqueous solution is ~20 mS/cm, a concentration of 1 M NaCl being required to obtain a value comparable to that of doped PEA hydrogel.[45] This feature evidences the important role of the hydrogel structure in the mobility of ions.

The EEC used to fit the experimental EIS results for CMC, PGGA and PEA corresponds to the Randles-type electrical equivalent circuit.[46] Besides R_S and R_P,

the diagram shows two additional elements: 1) the capacitance C of the hydrogel in parallel with R_P; and 2) the constant phase element (CPE), which is associated with the capacitance of the electrical double layer (C_{dl}) on the electrode surface, in series with R_P. In the case of κC, the CPE is in parallel with a resistance and, in addition, it shows a tangent hyperbolic diffusion element (T), also named bounded Warburg, which is common for porous electrodes.

The perfect semicircle obtained in the Nyquist plot for all the studied systems indicates that the four doped hydrogels behave as ideal capacitors. Accordingly, the capacitance C, which is in parallel with R_P, reflects their ability to store charge. The C values obtained for κC, CMC, PGGA and PEA are 5.56, 7.72. 9.36 and 10.2 μF, respectively. Thus, the amount of accumulated charge increases with decreasing R_S, which evidences that the capacitance improves with the mobility and transport of ionic charge.

The C_{dl} is associated with the separation of charges at the electrode/electrolyte interface. The double layer capacitance was represented with a CPE, which describes a non-ideal capacitor when the phase angle is different from –90º, to model the heterogeneity of the samples. The CPE impedance is attributed to the distributed surface reactivity, surface heterogeneity, and roughness of the current and potential distribution, which in turn are related to the electrode geometry and the electrode porosity.[47] The CPE impedance has been expressed as:

$$Z_{CPE} = [Y_0(j \cdot \omega)^n]^{-1} \quad (1)$$

where Y_0 is the admittance of an ideal capacitance and *n* is an empirical constant, ranging from 0 to 1. When *n* = 1, the CPE behaves as a pure capacitor and Y_0= 1/C, while the CPE behaves a pure resistor and Y_0= 1/R when *n* = 0. Furthermore, when *n* = 0.5, the CPE is associated with a diffusion process, being the equivalent of the so-called Warburg element (W) and Y_0= √2/W. The *n* values obtained for κC

and PEA (*n* = 0.845 and 0.807, respectively) are close to 1, while those of CMC and PGGA (*n* = 0.362 and 0.646, respectively) are close to 0.5.

The T diffusion element found in the EEC of κC, which is characteristic of films that contain a fixed amount of electroactive material,[48,49] in this case PEDOT, appears when the electroactive material cannot be replenished once it has been consumed. The T element is characterized by two parameters, an "admittance" parameter, Y_0, and a time constant parameter, B (units: $sec^{½}$):

$$Z_T \frac{1}{Y_0\sqrt{j\cdot\omega}}\coth(B\cdot\sqrt{j\cdot\omega}) \qquad (2)$$

The parameter Y_0 is related to the diffusion coefficient for the mobile species within the film. In this case, the T element has been associated with the counter ions confined into the PEDOT film situated between the metal substrate and the κC solid electrolyte. This confinement, which may be due to the compact structure of the hydrogel, is also responsible for the apparition of a resistance element linked to the electrode.

Hydrogels based on biopolymer-derived networks have emerged as a green energy approach to produce solid-like electrolytes. The four polymeric systems studied, which have been successfully applied as supercapacitors, are presented as technology options for energy storage devices. From a fundamental aspect, the characterization by EIS of the ionic and capacitive properties allowed us to choose the most suitable option. Most importantly, the correlation between such performance and the hydrogel porous morphology can be used as a design tool for the next-generation innovative systems.

3.3.5 Conclusions

In summary, the doped polyesteramide hydrogel, which displays a homogeneous distribution of micro- and nanopores, presents better properties as a solid-like electrolyte than doped biohydrogels with pseudo-honey-comb and compact heterogeneous structures. Indeed, the polyesteramide hydrogel shows low electrical resistance, high capacitance and good interfacial contact with the electrode, thus meeting the electrical requirements of solid-like electrolytes for supercapacitors. The full characterization of the hydrogel solid-like electrolytes by EIS provides additional valuable data (*i.e.* ionic and capacitive properties) to select the most adequate system. In addition, the hydrogel morphology, which has a significant effect on the device performance, is required to be highly porous and open. The correct optimization of these parameters would improve the application of biopolymer-derived hydrogels in light and wearable flexible devices.

References

1. D. P. Dubal, N. R. Chodankar, D.-H. Kim, P. Gomez-Romero. Towards flexible solid-state supercapacitors for smart and wearable electronics. *Chem. Soc. Rev.* **2018**, *47*, 2065-2129.
2. L. Li, Z. Lou, D. Chen, K. Jiang, W. Han, G. Shen. Recent advances in flexible/stretchable supercapacitors for wearable electronics. *Small* **2018**, *14*, 1702829.
3. Y. Liu, K. He, G. Chen, W. R. Leow, X. Chen. Nature-inspired structural materials for flexible electronic devices. *Chem. Rev.* **2017**, *117*, 12893-12941.
4. W. Weng, P. Chen, S. He, X. Sun, H. Peng. Smart electronic textiles. *Angew. Chem., Int. Ed.* **2016**, *55*, 6140-6169.
5. W. Zeng, L. Shu, Q. Li, S. Chen, F. Wang, X. M. Tao. Fiber-based wearable electronics: a review of materials, fabrication, devices, and applications. *Adv. Mater.* **2014**,*26*, 5310-5336.
6. B. Evanko, S. W. Boettcher, S. J. Yoo, G. D. Stucky. Redox-enhanced electrochemical capacitors: Status, opportunity, and best practices for performance evaluation. *ACS Energy Lett.* **2017**, *2*, 2581-2590.
7. A. Mukhopadhyay, B. W. Sheldon. Deformation and stress in electrode materials for Li-ion batteries. *Prog. Mater. Sci.* **2014**, *63*, 58-116.
8. L. Xia, L. Yu, D. Hu, G. Z. Chen. Electrolytes for electrochemical energy storage. *Mater. Chem. Front.* **2017**, *1*, 584-618.
9. L. L. Zhang, R. Zhou, X. S. Zhao. Graphene-based materials as supercapacitor electrodes. *J. Mater. Chem.* **2010**, *20*, 5983-5992.
10. X. Wang, J. Gao, Z. Cheng, N. Chen, L. Qu. A responsive battery with controlled energy release. *Angew. Chem.* **2016**, *128*, 14863-14867.
11. M. G. Saborio, S. Lanzalaco, G. Fabregat, J. Puiggalí, F. Estrany, C. Alemán. Flexible electrodes for supercapacitors based on the supramolecular assembly of biohydrogel and conducting polymer. J. Phys. Chem. C **2018**, *122,* 2, 1078–1090
12. M. Q. Zhao, C. E. Ren, Z. Ling, M. R. Lukatskaya, C. Zhang,K. L. Van Aken, M. W. Barsoum, Y. Gogotsi. Flexible Mxene/carbon nanotube composite paper with high volumetric capacitance. *Adv. Mater.* **2015**, *27*, 339-345.
13. L. T. Le, M. H. Ervin, H. Qiu, B. E. Fuchs, W. Y. Lee, Graphene supercapacitor electrodes fabricated by inkjet printing and thermal reduction of graphene oxide. *Electrochem. Commun.* **2011**, *13*, 355-358.

14. A. Lamberti, F. Clerici, M. Fontana, L. Scaltrito, A highly stretchable supercapacitor using laser-induced graphene electrodes onto elastomeric substrate. *Adv. Energy Mater.* **2016**, *6*, 1600050.
15. K. G. Laelabadi, R. Moradian, I. Manouchhri. One-step fabrication of flexible, cost/time effective, and high energy storage reduced graphene oxide@PANI supercapacitor. *ACS Appl. Energ. Mater.* **2020**, *3*, 5301-5312.
16. S. Chen, L. Qiu, H.-M. Ling. Carbon-based fibers for advanced electrochemical energy storage devices. *Chem. Rev.* **2020**, *120*, 2811-2878.
17. C. Yang, Z. Suo. Hydrogel Ionotronics. *Nat. Rev. Mater.* **2018**, *3*, 125-142.
18. E. Feng, W. Gao, J. Li, J. Wei, Q. Yang, Z. Li, X. Ma, T. Zhang, Z. Yang. Stretchable, healable, adhesive, and redox-active multifunctional supramolecular hydrogel-based flexible supercapacitor. *ACS Sustainable Chem. Eng.* **2020**, *8*, 3311-3320.
19. R. P. Tong, G. X. Chen, D. H. Pan, J. F. Tian, H. S. Qi, R. A. Li, F. C. Lu, M. H. He. Ultrastretchable and antifreezing double-cross-linked cellulose ionic hydrogels with high strain sensitivity under a broad range of temperature. *ACS Sustainable Chem. Eng.* **2019**, *7*, 14256-14265.
20. J. Zeng, L. Wei, X. Guo. Bio-inspired high-performance solid-state supercapacitors with the electrolyte, separator, binder and electrodes entirely from kelp. *J. Mater. Chem. A* **2017**, *5*, 25282-25292.
21. Y. N. Sudhakar, D. K. Bhat, M. Selvakumar. Ionic conductivity and dielectric studies of acid doped cellulose acetate propionate solid electrolyte for supercapacitor. *Polym. Eng. Sci.* **2016**, *56*, 196-203.
22. M. M. Pérez-Madrigal, M. G. Edo, M. G. Saborio, F. Estrany, C. Alemán. Pastes and hydrogels from carboxymethyl cellulose sodium salt as supporting electrolyte of solid electrochemical supercapacitors. *Carbohydr. Polym.* **2018**, *200*, 456-467.
23. E. Armelin, M. M. Perez-Madrigal, C. Alemán, D. Díaz-Díaz. Current status and challenges of biohydrogels for applications as supercapacitors and secondary batteries. *J. Mater. Chem. A* **2016**, *4*, 8952–8968.
24. J. Y. Nan, G. T. Zhang, T. Y. Zhu, Z. K. Wang, L. J. Wang, H. S. Wang, F. X. Chu, C. P. Wang, C. B. Tang. A highly elastic and fatigue-resistant natural protein-reinforced hydrogel electrolyte for reversible-compressible quasi-solid-state supercapacitors. *Adv. Sci.* **2020,** 2000587.
25. Z. Y. Xun, S. P. Ni, Z. H. Gao, Y. H. Zhang, J. Y. Gu, P. F. Huo. Construction of polymer electrolyte based on soybean protein isolate and hydroxyethyl cellulose for a flexible solid-state supercapacitor. Polymers **2019**, *11*, 1895.

26. P. F. Huo, S. P. Ni, P. Hou, Z. Y. Xun, Y. Liu, J. Y. Gu. A crosslinked soybean protein isolate gel polymer electrolyte based on neutral aqueous electrolyte for a high-energy-density supercapacitor. Polymers 2019, 11, 863.
27. M. M. Pérez-Madrigal, M. G. Edo, A. Díaz, J. Puiggalí, C. Alemán. Poly-γ-glutamic acid hydrogels as electrolyte for poly(3,4-ethylenedioxythiophene)-based supercapacitors. J. Phys. Chem. C **2017**, 121, 6, 3182-3193.
28. G. Ruano, A. Díaz, J. Tononi, J. Torras, J. Puiggalí, C. Alemán. Biohydrogel from unsaturated polyesteramide: Synthesis, properties and utilization as electrolytic medium for electrochemical supercapacitors. *Polym. Test.* **2020**, *82*, 106300.
29. G. Ruano, J. Tononi, D. Curcó, J. Puiggali, J. Torras, C. Alemán. Doped photo-crosslinked polyesteramide hydrogels as solid electrolytes for supercapacitors. *Soft Matter* **2020**, *16*, 8033-8046.
30. N. A. Choudhury, S. Sampathb, A. K. Shukla. Hydrogel-polymer electrolytes for electrochemical capacitors: an overview. *Energy Environ. Sci.* **2009**, *2*, 55-67.
31. H. Inoue, S. Okuda, E. Higuchi, S. Nohara. Inorganic hydrogel electrolyte with liquidlike ionic conductivity. *Electrochem. Solid-State Lett.* **2009**, *12*, A58.
32. A. Yuan, J. Zhao. Composite alkaline polymer electrolytes and its application to nickel–metal hydride batteries. *Electrochim. Acta* **2006**, *51*, 2454-2462.
33. S. Nohara, H. Wada, N. Furukawa, H. Inoue, M. Morita, C. Iwakura. Electrochemical characterization of new electric double layer capacitor with polymer hydrogel electrolyte. *Electrochim. Acta* **2003**, *48*, 749-753.
34. C. Rochas, M. Rinaudo. Mechanism of gel formation in κ-carrageenan. *Biopolymers* **1984**, *23*, 735-745.
35. W. Jiang, J. Gao, Z. Wei, J. Zhou, Y. Mei. Facile fabrication of self-healing carboxymethyl cellulose hydrogels. *Eur. Polym. J.* **2015**, *72*, 514-522.
36. M. Matsusaki, H. Yoshida, M. Akashi. The construction of 3D-engineered tissues composed of cells and extracellular matrices by hydrogel template approach. *Biomaterials* **2007**, *28*, 2729-2737.
37. B.-A. Mei, O. Munteshari, J. Lau, B. Dunn, L. Pilon. Physical interpretations of Nyquist plots for EDLC electrodes and devices. *J. Phys. Chem. C* **2018**, *122*, 194-206.
38. i. Yang, S.-G. Kim, S. H. Kwon, M.-S. Kim, J. C. Jung, Relationships between pore size and charge transfer resistance of carbon aerogels for organic electric double-layer capacitor electrodes. *Electrochim. Acta* **2017**, *223*, 21-30.

39. K. Sun, M. Dong, E. Feng, H. Peng, G. Ma, G. Zhao, Z. Lei. High performance solid state supercapacitor based on a 2-mercaptopyridine redox-mediated gel polymer. *RSC Adv.* **2015**, *5*, 22419-22425
40. S. Mallakpour, A. Abdolmaleki, S. Borandeh. Surface functionalization of GO, preparation and characterization of PVA/TRIS-GO nanocomposites. *Polymer* **2015**, *81*, 140-150.
41. K. Sun, M. Dong, E. Feng, H. Peng, G. Ma, G. Zhao, Z. Lei. High performance solid state supercapacitor based on a 2-mercaptopyridine redox-mediated gel polymer. *RSC Adv.* 2015, **5**, 22419-22425.
42. G. Ma, M. Dong, K. Sun, E. Feng, H. Peng, Z. Lei. A redox mediator doped gel polymer as an electrolyte and separator for a high performance solid state supercapacitor. *J. Mater. Chem. A* **2015**, *3,* 4035-4041.
43. L. Guo, W.-B. Ma, Y. Wang, X.-Z. Sing, J. Ma, X.-D. Han, X.-Y. Tao, L.-T. Guo, H.-L. Fan, Z.-S. Liu, Y.-B. Zhu, X.-Y. Wei, A chemically crosslinked hydrogel electrolyte based all-in-one flexible supercapacitor with superior performance *J. Alloys Compd.* **2020**, *843*, 155895.
44. K. Sun, E. Feng, G. Zhao, H. Peng, G. Wei, Y. Ly, G. Ma. A Single robust hydrogel film based integrated flexible supercapacitor. ACS Sustainable Chem. Eng. **2019**, *7,* 165-173.
45. C. S. Widodo, H. Sela, D. R. Santos. The effect of NaCl concentration on the ionic NaCl solutions electrical impedancevalue using electrochemical impedancespectroscopy methods. *AIP Conf. Proc.* **2021**, 050003.
46. R. N. Vyas, B. Wang. Electrochemical analysis of conducting polymer thin films. *Int. J. Mol. Sci.* **2010**, *11*, 1956-1972.
47. J.-B. Jorcin, M. E. Orazen, N. Pébère, B. Tribollet, CPE analysis by local electrochemical impedance spectroscopy. *Electrochim. Acta* **2006**, *51*, 14731479.
48. N. A. Zubair, N. A. Rahman, H. N. Lim, Y. Sulaiman. Production of conductive PEDOT-coatedPVA-GO composite nanofibers. *Nanoscale Res.Lett.* **2017**, *12*, 113.
49. P. M. Dziewonski, M. Grzeszczuk, Towards TiO2-conducting polymer hybrid materials for lithium ion batteries. *Electrochim. Acta* **2010**, *55*, 3336-3347.

3.4 Free-standing, flexible nanofeatured polymeric films as electrodes for supercapacitors

3.4.1 Abstract

Flexible and self-standing multilayered films made of nanoperforated poly(lactic acid) (PLA) layers separated by anodically polymerized poly(3,4-ethylenedioxythiophene) (PEDOT) conducting layers have been prepared and used as electrodes for supercapacitors. The influence of the external layer has been evaluated by comparing the charge storage capacity of 4- and 5-layered films, in which the external layer is made of PEDOT (PLA/PEDOT/PLA/PEDOT) and nanoperforated PLA (PLA/PEDOT/PLA/PEDOT/PLA), respectively. In spite of the amount of conducting polymer is the same for both 4- and 5-films, they exhibit significant differences. The electrochemical response in terms of electroactivity, areal specific capacitance, stability and coulombic efficiency was greater for the 4-layered electrodes than for the 5-layered ones. Also, the response in terms of leakage current and self-discharge was significantly better for the former electrodes than for the latter ones.

3.4.2 Introduction

Among energy storage devices, electrochemical supercapacitors (SCs) have gained increasing attention during recent years [1-5]. SCs exhibit higher power density and energy density than batteries and conventional capacitors, respectively. In ESCs, electrodes are separated by an ion transport layer through which electrolyte ions shuttle to the electrode surfaces during the charging and discharging processes. Based on their different energy storage mechanisms, SCs are divided into several types: electrochemical double layer capacitors (EDLCs), pseudo-capacitors and hybrid capacitors [6-7]. For EDLCs, the electrical energy is stored by electrostatic accumulation of charges, while the energy storage in pseudo-capacitors is achieved through reversible and fast redox reactions. Hybrid capacitors are combinations of an EDLC or pseudo-capacitor electrode and a battery electrode in one SC.

Independently of the energy storage mechanism, electrodes have a critical impact on the electrochemical performance of SCs and, therefore, their study deserves special attention. Within this context, a wide variety of electrode materials have been developed. For example, graphene [8-10], carbon nanotubes [11-13], and carbon nanofibers [14-16] are typical EDLC electrode materials, whereas metal oxides [17-19] and conducting polymers [20-23] (CPs) are pseudo-capacitor electrode materials. In general pseudo-capacitor electrodes exhibit higher capacitance and energy density than EDLC electrodes. Instead, pseudo-capacitor electrodes show lower power density and rate capability than EDLC electrode materials.

In recent years, flexible, lightweight and environmentally friendly electrodes for SCs have attracted increasing attention since they meet the needs for portable (*e.g.* foldable phones) and wearable (*e.g.* smart textiles) electronics [24-27]. In these devices, which exhibit high specific energy and power densities and long life cycles, all components, including the electrodes, are flexible. In general, it is well-

accepted that polymeric gel electrolytes fulfill the practical conditions required by the electrolyte layers of flexible SCs, especially in terms of electrochemical performance, excellent compressive/tensile properties, simple manufacturing properties, satisfactory tolerance over a wide temperature range [28-31]. However, the most suitable format for the electrodes in flexible SCs is still controversial and highly dependent on the final application of the device. Within this context, nanostructured conducting electrodes based on hydrogels [32-34], films [35-37], and fibers [38-40] have been reported for flexible SCs designed for different final applications.

In this work, we develop conducting and self-standing films of submicrometric thickness as flexible electrodes for SCs. These electrodes were obtained by alternating nanofeatured layers of an insulating polymer, which provided mechanical strength, and a CP that supplied electrochemical properties. Nanoperforations created in the insulating polymer layers were used to let the interpenetration of the CP layers, allowing the entire self-assembled film to be electrochemically active. Moreover, the two materials chosen for this device, polylactic acid (PLA) and poly(3,4-ethylenedioxythiophene) (PEDOT), are biocompatible, suggesting that flexible SCs prepared using such electrode are specially appropriated for biomedical applications. For example, the voltage and power consumption required by pressure sensors, radio transmitters, wearable sensor for biomolecules, pacemakers and surface electromyography, are relatively low (*i.e.* typically < 100 mV and < 20 µW) and, therefore, could be supplied by flexible SCs. Furthermore, the combination of planarity, thinness and flexibility provided by the electrodes reported in this work is particularly appropriated for applications requiring shape-adapted SCs.

Two different types of electrodes, which differ in the number of layers and, therefore, in the chemical nature of the external layer that can be of PLA (odd number of layers) or PEDOT (even number of layers), were prepared. More

specifically, the system with an odd number of layers was obtained by self-assembling 3 PLA and 2 PEDOT layers alternatively (*i.e.* PLA/PEDOT/PLA/PEDOT/PLA), whereas the one with an even number of layer only contained 2 PLA layers (*i.e.* PLA/PEDOT/PLA/PEDOT). It should be remarked that the amount of electrochemically active CP is the same for the two electrodes, hereafter denoted 3PLA/2PEDOT and 2PLA/2PEDOT, respectively. Therefore, differences between them have been attributed to the effect of the external PLA layer that, although it was found to be beneficious for electromechanical (*i.e.* faradaic motors) [41] and tissue engineering applications [42], has a detrimental effect for energy storage applications.

3.4.3 Methods

3.4.3.1 Materials

PEDOT: PSS 1.3 wt. % dispersion in water, 3,4-ethylenedioxythiophene (EDOT) monomer, PVA 87-89% hydrolysed and lithium perchlorate ($LiClO_4$) were purchased from Sigma-Aldrich (USA). $LiClO_4$ was stored at 80 °C before its use. PLA 2002D pellets were supplied by Nupik International (Polinyà, Spain). Acetonitrile and HFIP were purchased from Panreac Quimica S.A.U. (Spain).

3.4.3.2 Preparation of the films

Multilayered films were prepared by combining the spin-coating and the anodic polymerization techniques, following a recently reported procedure. In brief, a steel sheet (AISI 304) of 0.50×0.25 cm^2 was coated with a sacrificial layer of PEDOT:PSS by spin-coating deposition (1200 rpm for 60 s). Then, a PLA:PVA layer was generated onto the sacrificial layer by spin-coating (1200 rpm for 60 s) a 90:10 v/v mixture of PLA (10 mg/mL) and PVA (10 mg/mL) HFIP solutions. The nanoperforated PLA layer was obtained by removing the PVA domains via water etching. The resulting PEDOT:PSS/PLA bilayer was used as working electrode for the anodic polymerization of PEDOT doped with ClO_4^- (PEDOT:ClO_4^-), as described below. Afterwards, the following nanoperforated PLA or PEDOT layers were obtained by iterating this procedure. Then, 5-and 4-layered films of composition PLA/PEDOT/PLA/PEDOT/PLA (3PLA/2PEDOT) and PLA/PEDOT/PLA/PEDOT (2PLA/2PEDOT), still supported onto the PEDOT:PSS-coated steel substrate, were achieved. These supported films were detached from the metallic substrate by selective elimination of the PEDOT:PSS sacrificial layer. This was achieved by submerging the supported films into milli-Q water for 12 h. Finally, films were completely detached from the steel substrate with the help of

tweezers, and converted into self-standing multi-layered films. The spin-coating steps were performed using a WS-400BZ-6NPP/A1/AR1 (Laurell Technologies Corporation) spin-coater.

PEDOT was prepared by anodic polymerization using an Autolab PGSTAT302N controlled by the NOVA software. Polymerizations were carried out by chronoamperometry in a three-electrode cell filled with a 0.1 M $LiClO_4$ acetonitrile solution containing 10 mM EDOT. In both cases, a constant potential of +1.40 V was applied and the polymerization charge was adjusted to 270 mC. The reference electrode was an Ag|AgCl electrode containing a KCl-saturated aqueous solution (E°= 0.222 V at 25°C), while the counter electrode was a bare steel AISI 316L sheet.

3.4.3.3 Characterization

The morphology of the different samples was studied by scanning electron microscopy (SEM). Micrographs were acquired in a Focused Ion Beam Zeiss Neon 40 equipped with an EDX spectroscopy system, operating at 5 kV, depending on the sensitivity to beam degradation of the studied systems.

Film thickness and roughness measurements were carried out using a Dektak 150 stylus profilometer (Veeco, Plainview, NY). Conducted using the following settings: tip radius = 2.5 μm; stylus force = 3 mg; scan length = 1000 μm; speed = 33 μm s^{-1}.

All electrochemical measurements were performed using a microcomputer-controlled potentiostat/galvanostat Autolab with PGSTAT101 equipment and Nova software. A conventional Ag|AgCl 3 M KCl electrode and a platinum electrode were used as reference electrode and counter electrode, respectively.

The electrochemical response of 3PLA/2PLA and 2PEDOT/2PLA free standing films (0.50 × 0.25 cm^2) as electrodes was studied in a three-electrode configuration

by means of cyclic voltammetry (CV) and galvanostatic charge/discharge (GCD) measurements. The areal capacitance (*AC*) was calculated from CV cycles recorded in a three-electrode system (E 3.4.1):

$$AC = {I}/{A \cdot \left(\frac{dV}{dt}\right)} \qquad \text{(E.3.4.1)}$$

where *I* is the average discharge intensity, *A* is the surface area (0.125 cm^2) and $\frac{dV}{dt}$ is the scan rate (100mV/s). Furthermore, GCD measurements were also used to determine the cell capacitance, *AC*, by applying Eq 3.4.2

$$C = {I \cdot t_d}/{A \cdot \Delta V} \qquad \text{(E.3.4.2)}$$

where *I* is the applied current ($5 \cdot 10^{-5}$ A), t_d is the discharge time, ΔV is the potential window (from 0.0 to 0.8V). The cycling stability of was tested by submitting the studied systems to: *(i)* 3000 GCD cycles at a current density of 0.05 mA from 0.0 V to 0.8 V; and *(ii)* 1000 CV cycles at a scan rate of 100 mV/s from 0.0 V (initial and final potential) to 0.8 V (reversal potential). A 0.1 M NaCl solution was used as electrolyte in all cases.

The evaluation of the self-discharging (SD) and leakage current (LC) curves of SCs was carried out applying the following methodologies. In the first case, the SCs were charged to 0.8 V at 0.015 mA and kept at $1 \cdot 10^{-11}$ mA for 10 min (*i.e.* self-discharging). After that time, the device was discharged to 0 V at –1 mA. In the second case, after charging the device to 0.8 V at 0.015 mA, it was kept at 0.8 V for 600 seconds while recording the current data through the SC (*i.e.* leakage current).

3.4.4 Results and discussion

The procedure used for the preparation of multilayered films formed by alternated layers of PLA and PEDOT was reported in previous work [41] and is schematically summarized in Figure 3.4.1. In brief, after spin-coating a sacrificial electroactive layer of PEDOT doped with polystyrene sulfonate (PEDOT:PSS) on a steel sheet (AISI 304) of 0.50×0.25 cm^2, the rest of the process consisted in the sequential combination of three different steps. The first (steps "1" in Figure 3.4.1) was the spin-coating of a 90:10 v/v mixture of PLA and poly(vinyl alcohol) (PVA) solutions (both 10 mg/mL) in 1,1,1,3,3,3-hexafluoro-2-propanol (HFIP). After this, the second step involved the elimination of the nanospherical PVA domains by water-etching (steps "2" in Figure 3.4.1). It is worth noting that the diameter of such PVA nanofeatures, which were induced by the phase segregation between immiscible PLA and PVA during the spin-coating process, was adjusted to the thickness of the layer by selecting appropriated operational parameters (*i.e.* spinning speed, spinning time and both concentration and solvent for the polymer solutions) [41,42]. Consequently, the electroactive material under the PLA layer became accessible through the nanoperforations obtained by removing PVA. Finally, the third step consisted in the electrochemical polymerization of PEDOT doped with ClO_4^- anions (steps "3" in Figure 3.4.1).

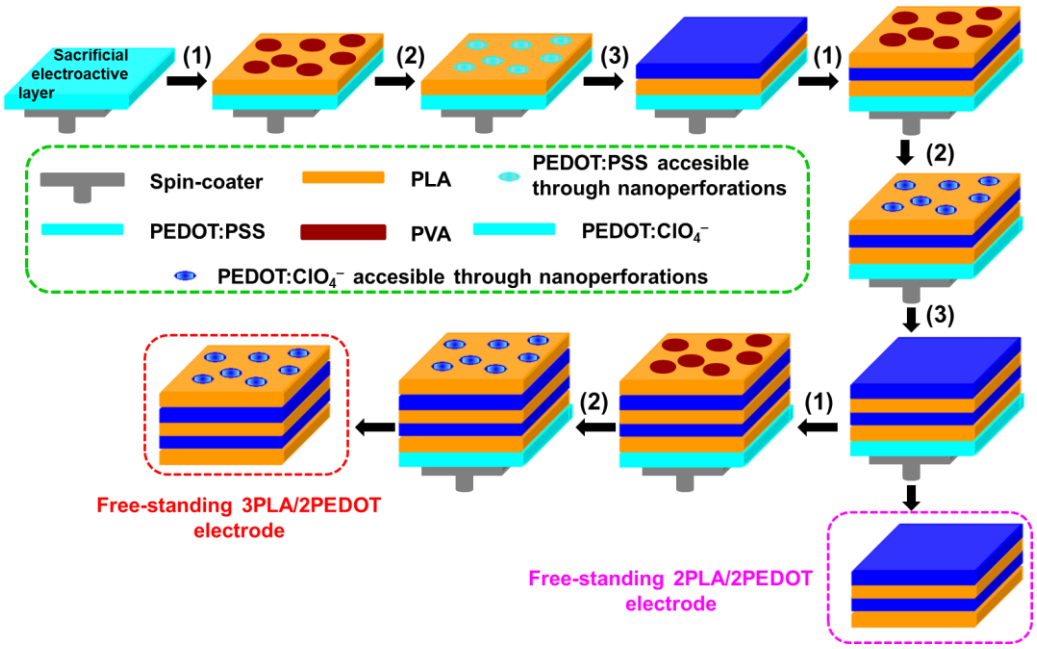

Figure 3.4.1. (a) Descriptive scheme of the procedure used to prepare self-standing 3PLA/PEDOT and 2PLA/2PEDOT films.

The formation of the PEDOT:ClO_4^- layer was promoted by the electroactive material accessible through nanoperformations. For the fabrication of 3PLA/2PEDOT and 2PLA/2PEDOT films, steps “1” and “2” were repeated three and two times, respectively, while step “3” was repeated two times in both cases. Finally, the supported multilayered films were detached from the steel substrate by removing the PEDOT:PSS sacrificial layer, which was accomplished by submerging the supported membranes into milli-Q water for 12 h. The 5- and 4-layered films were completely detached from the steel with the help of tweezers, converting them into self-standing.

Figure 3.4.2 shows photographs of self-supported 2PLA/2PEDOT films, which cannot be macroscopically distinguished from 3PLA/2PEDOT films. These self-standing films are very flexible and robust. This is evidenced in Figure 3.4.2, which show digital camera images of how the film floating in water folds on itself, experiencing a complete loss the shape when it exposed to air. However, the original shape is fully restored after the film is dropped back into the water. The

thickness of the layers, as determined by perfilometry, was: 45 nm (1st PLA), 259 nm (1st PEDOT), 94 nm (2nd PLA), 199 nm (2nd PEDOT) and 113 nm (3rd PLA).

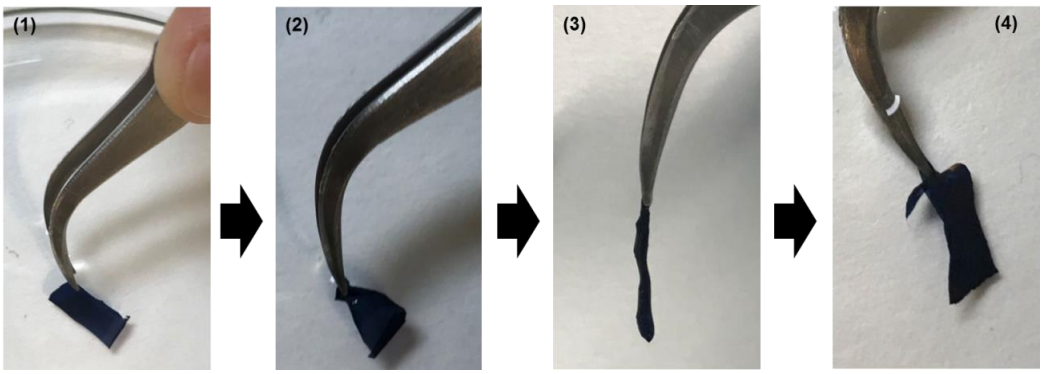

Figure 3.4.2. Digital camera photographs of a free-standing 2PLA/2PEDOT film: (1) floating on water; (2) clamped with tweezers while remains floating on water; (3) clamped out of water (in air); (4) introduced again on water.

The surface morphology of 2PLA/2PEDOT and 3PLA/2PLA films, which was studied by scanning electron microscopy (SEM), is displayed in Figure 3.4.3. 2PLA/2PEDOT surface is very similar to that previously described for single layered PEDOT films and can be described as a very homogeneous distribution of small aggregates, which are associated with the linear growing of polymer chains (Figure 3.4.3a) [20,45]. A completely different morphology was observed for 3PLA/2PEDOT (Figure 3.4.3b). Although low magnification SEM images suggests a compact, homogeneous and flat surface, as is illustrated in the micrograph displayed in the inset, high magnification images evidences the presence of nanoperforations of 156 ± 23 nm in diameter. Moreover, the templating effect of the internal PEDOT layer on the external PLA layer is also reflected in the highest magnification micrograph (Figure 3.4.3b, right). Detailed description of the morphology and topography of 3PLA/2PLA films was provided in previous work [41,42], in which the effect of each layer was analyzed one-by-one.

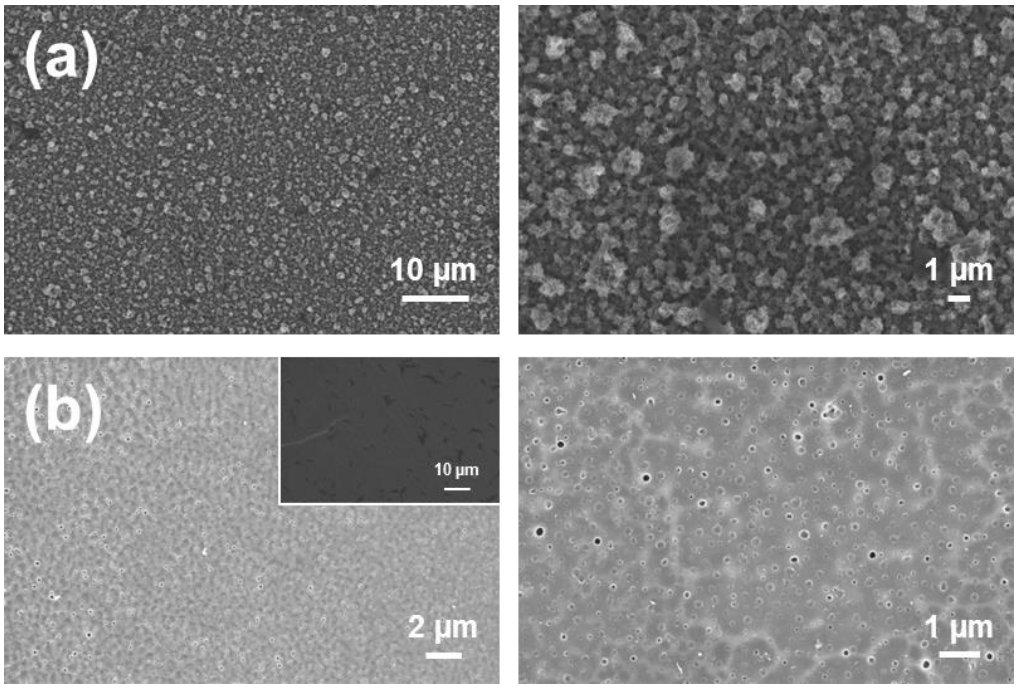

Figure 3.4.3 SEM micrographs of (a) 2PLA/2PEDOT and (b) 3PLA/2PEDOT.

Figure 3.4.4a compares the cyclic voltammetry (CV) control curves recorded of free-standing 2PLA/2PEDOT and 3PLA/2PEDOT electrodes in a 0.1 M NaCl solution. From a qualitative point of view, the non-quasi rectangular and symmetric shape of the two voltammograms is similar, indicating pseudocapacitive behaviour and good reversibility, respectively [43,44]. The redox shoulders at 0.25021 and 0.30023 V are consistent with the high pseudocapacitive behavior. Another important characteristic of the voltammograms recorded for the two electrodes is the deviation from ideal horizontal voltammetric curves, which has been attributed to the presence of external and internal PLA layers in the films. From a quantitative point of view, the anodic and cathodic areas of the voltammograms are significantly larger for 2PLA/2PEDOT than for 3PLA/2PEDOT, indicating that the electrochemical activity (electroactivity) of the former is higher. Indeed, comparison of the total voltammetric charges, which are the sum of anodic and cathodic charge

densities, indicates that the electroactivity is 61% higher for 2PLA/2PEDOT than for 3PLA/2PEDOT.

In order to evaluate the electrochemical stability of the electrodes, 1000 consecutive oxidation-reduction cycles were applied to both 2PLA/2PEDOT and 3PLA/2PEDOT using the same interval of potentials and scan rate. The voltammograms recorded after such 1000 CV cycles, which are included in Figure 3.4.4a, exhibit the same shape (*i.e.* non-quasi rectangular and symmetrical) that the control ones. However, the area varies, this feature being more evident for 3PLA/2PEDOT than for 2PLA/2PEDOT. This result suggests that the external layer of PLA is the most affected by the applied redox processes.

Figure 3.4.4b represents the evolution of the loss of electrochemical activity (LEA; in %) against the number of CV cycles. The LEA was expressed as:

$$\mathrm{LEA} = \frac{Q_i - Q_1}{Q_1} \cdot 100 \qquad \text{(E.3.4.3)}$$

where Q_i is the difference of voltammetric charge (in C) obtained for cycle *i* and Q_1 is the voltammetric charge corresponding to the first cycle. For 3PLA/2EDOT the electrochemical activity decreases rapidly with increasing number of cycles. Thus, the LEA increases to 10% after only 100 cycles and, after that, the value progressively grows around 1% every 100 cycles. Conversely, the LEA of 2PLA/2PEDOT decreases up to –2.5% during the first 600 CV cycles, evidencing a self-stabilizing process. After that, the LEA increases by around 1% every 100 cycles. Comparison of the LEA profiles obtained for 3PLA/2EDOT and 2PLA/2EDOT confirms the previous hypothesis according to which the lower electrochemical stability of the former electrode is due to the damage induced by the potential scan in the last PLA layer.

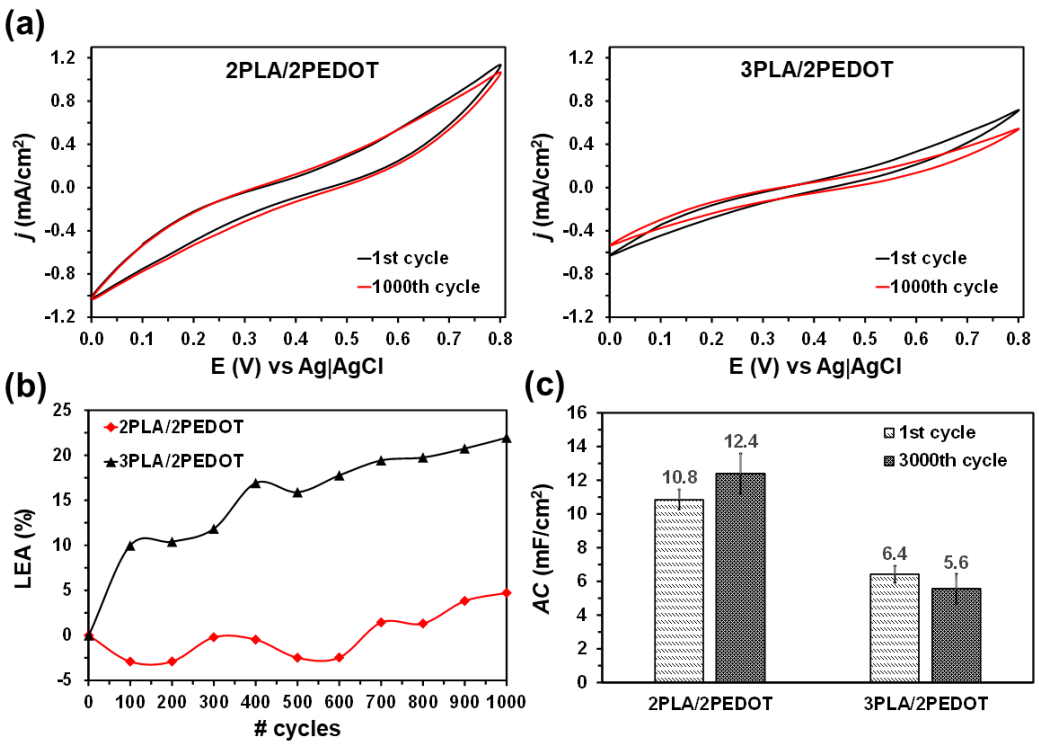

Figure 3.4.4. (a) Cyclic voltammograms of free standing (left) 2PLA/2PEDOT and (right) 3PLA/2PEDOT films using a 0.1 M NaCl electrolytic solution. Cyclic curves correspond to the 1st and 1000th cycles. Initial and final potential: 0.0 V; reversal potential: 0.8 V. Scan rate: 100 mV/s. (b) Evolution of the loss of electrochemical activity (LEA) with the number of redox cycles. (c) *AC* determined for 2PLA/2PEDOT and 3PLA/2PEDOT electrodes after the 1st and 1000th voltammetric cycles.

The areal specific capacitance (*AC*; in mF/cm^2) was determined using the following expression:

$$AC = \frac{Q}{\Delta V \cdot A} \qquad \text{(E.3.4.4)}$$

where *Q* is voltammetric charge determined by integrating the oxidative or the reductive parts of the cyclic voltammogram curve, *ΔV* is the potential window (in V), and *A* is the area of the electrode (in cm^2). Results are compared in Figure 3.4.4c. The *AC* of 2PLA/2PEDOT electrode increases 15% after 1000 CV cycles (from 10.8 to 12.4 mF/cm^2), which is consistent with the previously mentioned self-

stabilizing effect, whereas that of 3PLA/2PLA decreases the same amount (from 6.4 to 5.6 mF/cm^2).

Energy storage ability of pseudocapacitive electrodes is typically related with the access and scape of the electrolyte into them. This diffusion-controlled process depends on the potential scan rate. Cyclic voltammograms of 2PLA/2PEDOT and 3PLA/2PEDOT films supported on ITO at different scan rates are shown in Figure 3.4.5. The deviation from the horizontal of the voltammograms increases with the scan rate. This loss of ideality indicates that the number of ions that successfully reaches the films decreases with increasing scan rate, since diffusion is limited. On the other hand, the unfavorable contribution of PLA layers to the electrical conductivity of the films explains the loss of the ideal rectangular shape, which is more evident for 3PLA/2PEDOT than for 2PLA/2PEDOT. All curves, with exception of that obtained for 3PLA/2PEDOT at the lowest scan rate, are symmetric, indicating good reversibility even at the higher rates.

Figure 3.4.6a-b shows the curve voltage versus time for galvanostatic charge-discharge (GCD) measurements performed at a 0.80 V window for a current density of 0.40 mA/cm^2. Comparison of the triangle-like shaped GCD curves obtained for 2PLA/2PEDOT and 3PLA/2PEDOT indicates that charge and discharge times (t_d and t_c, respectively) are longer for the former (t_c = 9.5 s and t_d =9.5 s) than for the latter (t_c = 8.2 s and t_d = 7.5 s). Indeed, a t_d shorter than t_c, as observed for 3PLA/2PEDOT, indicates low coulombic efficiency (η). This parameter, defined as the ratio between t_d and t_c, was of η = 1.0 and 0.9 for 2PLA/2PEDOT and 3PLA/2PEDOT, respectively.

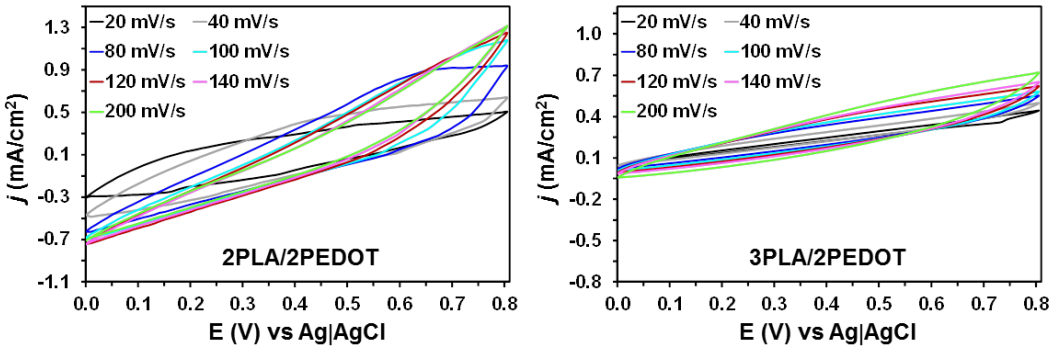

Figure 3.4.5. Cyclic voltammograms of (left) 2PLA/2PEDOT and (right) 3PLA/2PEDOT films supported on ITO using a 0.1 M NaCl electrolytic solution. Cyclic curves were determined using different scan rates, which range from 20 to 200 mV/s. Initial and final potential: 0.0 V; reversal potential: 0.8 V.

After 3000 GCD cycles (Figure 3.4.6a-b), the value of t_c increases to 10.5 and 13.5 s for 2PLA/2PEDOT and 3PLA/2PEDOT, respectively, while the t_d increases to 10.5 s for the former and decreases to 6.0 s for the latter. Accordingly, after 3000 GCD cycles, η remains at 1.0 for 2PLA/2PEDOT and decreases to 0.4 for 3PLA/2PEDOT. Consistently, the potential drop (Figure 3.4.6a-b) is twice for 3PLA/2PEDOT than for 2PLA/2PEDOT (*i.e.* 0.2 V vs 0.1 V), indicating that the electrical conductivity is higher for the latter than for the former. Moreover, the potential drop of 2PLA/2PEDOT becomes almost inappreciable (*i.e.* < 0.03 V) after 3000 GCD cycles. These results, which are fully consistent with CV observations, are corroborated by the *AC* (Figure 3.4.6c), which was 33% higher for 2PLA/2PEDOT than for 3PLA/2PEDOT after the first cycle, this difference increasing to 127% after 3000 GCD cycles. It should be noted that GCD cycles are much less aggressive than CV cycles. Thus, previous studies showed that potentiostatic redox cycles alter drastically the structure of polymers [46,47]. This feature explains that *AC* values derived from GCD measures are, in general, higher than those obtained using CV, as shown in Figures 3.4.4c and 3.4.6c.

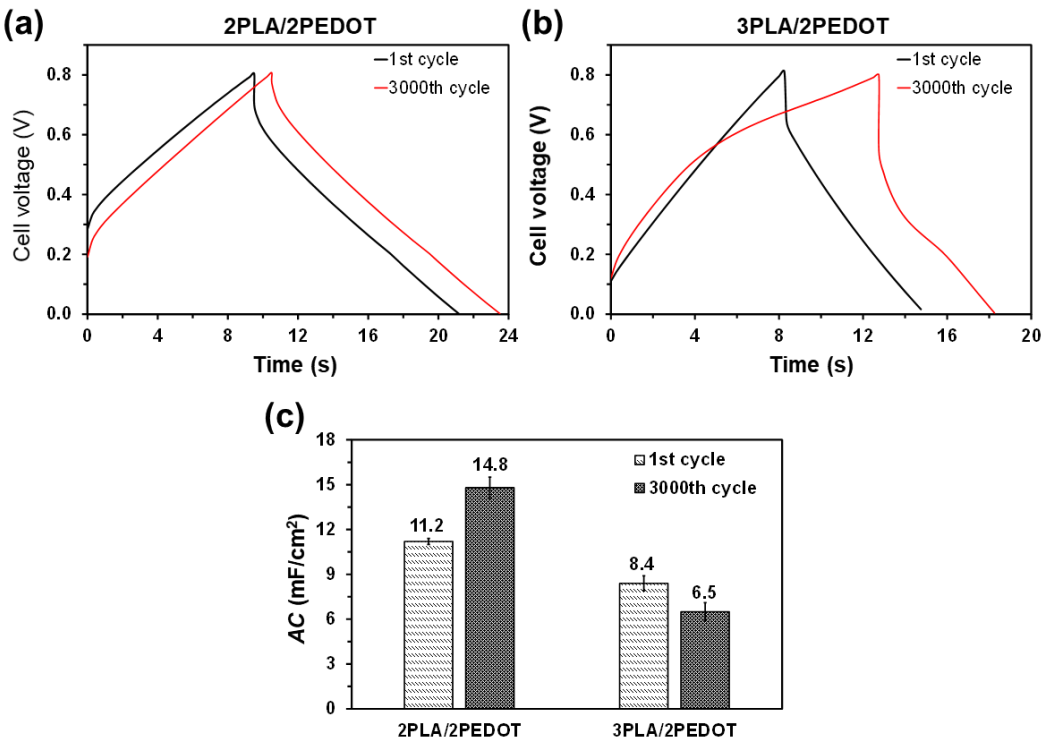

Figure 3.4.6. GCD cycles of free standing (a) 2PLA/2PEDOT and (b) 3PLA/2PEDOT films using a 0.1 M NaCl electrolytic solution. Curves correspond to the 1st and 3000th cycles. (c) *AC* determined for 2PLA/2PEDOT and 3PLA/2PEDOT electrodes after the 1st and 3000th GCD cycles.

Overall, CV and GCD assays indicate that the connection between the two PEDOT layers increases with the number of cycles for 2PLA/2PEDOT, which has been attributed to the degradation of the internal PLA layer. Thus, the cleavage PLA chains at such internal layer probably results in charged species, giving place to additional parasitic electrochemical reactions and explaining the increment of the *SC* and the t_d, as well as the practical elimination of the potential drop, with the increasing number of cycles. On the contrary, the two external layers of PLA plug the internal layers of PEDOT (with the exception of nanoperforations) in 3PLA/2PEDOT, making electrochemical processes more difficult and, therefore, protecting the PLA chains of the internal layer from degradative oxidation and reduction processes.

Figure 3.4.7a compares the leakage current of 2PLA/2PEDOT and 3PLA/2PEDOT after charging to 0.8 V at 0.1 mA. As it can be seen, the discharge is not only faster for the former than for the latter but also the current stabilizes at a higher value for the former than for the latter. These feature indicate that 2PLA/2PEDOT electrodes provide better stability than 3PLA/2PEDOT ones. Figure 3.4.7b shows the voltage drop of charged systems. Such representative self-discharging curves indicate that the voltage of 2PLA/2PEDOT is systematically higher than that of 3PLA/2PEDOT. The rate of current leakage self-discharge is influenced by different factors, such as the chemistry and electrochemistry of the system, the purity of reagents and electrolyte and the temperature [48]. Considering that both types of electrodes were manufactured using identical chemical components (*i.e.* PLA, PEDOT) and the experimental conditions, the lower self-discharging tendency of 2PLA/2PEDOT reflects higher capacity to store energy electrochemically.

3.4.5 Conclusions

The performance as electrodes for SCs of multilayered films made of alternated nanometric layers of nanofeatured PLA and electrochemically polymerized PEDOT, has been evaluated. Both 4- and 5-layered films, which differ in the chemical nature of the external layer, which is PEDOT and nanoperforated PLA, respectively, have been prepared and characterized. In spite of the amount of conducting PEDOT is the same for both 4- and 5-layered films, electrochemical assays indicate that their performance as electrodes for energy storage devices is very different. Both CV and GCD assays show that the voltammetric charge and the stability of 4-layered films is significantly higher than that of 5-layered ones. Indeed, the *AC* is 69% and 33% higher for the former than for the latter as determined by CV and GCD, respectively. Moreover, 4-layered films exhibit a self-stabilizing behavior with increasing number of cycles that is not detected in 5-layered films. Indeed, the latter experiences a progressive loss of electroactivity with increasing number of cycles. Also, 4-layered electrodes exhibited the best performance in terms of current leakage and the self-discharging. In summary, results obtained for self-standing and flexible 2PLA/2PEDOT electrodes open new perspectives for their technological application in the biomedical and textile fields.

References

1. L. Miao, Z. Song, D. Zhu, L. Li, L. Gan, M. Liu, Recent advances in carbon-based supercapacitors. *Mater. Adv.* 1 **2020** 945–966.
2. E. Pomerantseva, F. Bonaccorso, X. Feng, Y. Cui, Y. Gogotsi, Energy storage: The future enabled by nanomaterials, *Science* **2019** *366* 82-85
3. C. Cao, Y. Chu, Y. Zhou, C. Zhang, S. Qu, Recent advances in stretchable supercapacitors enabled by low-dimensional nanomaterials, *Small* **2018** 14 39-76.
4. C. Lu, X. Chen, Latest advances in flexible symmetric supercapacitors: From material engineering to wearable applications, *Acc Chem Res*. 18 **2020** 1468–1477.
5. E. Armelin, M. M. Pérez-Madrigal, C. Alemán, D. D. Díaz, Current status and challenges of biohydrogels for applications as supercapacitors and secondary batteries, *J. Mater. Chem. A* **2016**, 4 8952–8968.
6. K. Jost, G. Dion, Y. Gogotsi, Textile energy storage in perspective, *J. Mater. Chem. A* **2014** 2 10776–10787.
7. F. Béguin, V. Presser, A. Balducci, E. Frackowiak, Carbons and Electrolytes for Advanced Supercapacitors, *Adv. Mater*. **2014**, 26, 2219–2251.
8. J. Ji, J. Liu, X. Zhao, Y. Zhen, J. Lin, Y. Zhu, H. Ji, L. L. Zhang, R. Ruoff, In situ activation of nitrogen-doped graphene anchored on graphite foam for a high-capacity anode, *ACS Nano* **2015** 9 8609–8616,
9. X. Y. Xu, J. D. Yang, X. F. Zhou, S. Q. Jiang, W. Chen, Z. P. Liu, Highly crumpled graphene-like material as compression-resistant electrode material for high energy -power density supercapacitor, *Chem. Eng. J.* **2020** 397 125525.
10. F. Guo, P. Xiao, B. Y. Yan, M. Hahn, Y. Y. Kong, W. Zhang, Y. Z. Piao, G. W. Diao, One-pot synthesis of hydrazide-pillar[5]arene functionalized reduced graphene oxide for supercapacitor electrode. *Chem. Eng. J*. **2020** 391 123511.
11. Y. Zhou, X. X. Wang, L. Acauan, E. Kalfon-Cohen, X. C. Ni, Y. Stein, K. K. Gleason, B. L. Wardle, Ultrahigh-areal-capacitance flexible supercapacitor electrodes enabled by conformal P3MT on horizontally aligned carbon-nanotube arrays, *Adv. Mater*. **2019** 31 1901916.
12. Y. Chen, C. Xu, J. Zhao, J. D. Juang, H. Xu, G. J. Gou, Creating a new electrode material of supercapacitors from the waste multi-walled carbon nanotubes, *Electrochim. Acta* **2020** 330 135237.

13. T. Yeo, J. Lee, D. Shin, S. Park, H. Hwang, W. Choi, One-step fabrication of silver nanosphere-wetted carbon nanotube electrodes via electric-field-driven combustion waves for high-performance flexible supercapacitors. *J. Mater. Chem. A* **2019** 7 9004–9018.
14. J. H. Zhu, Q. Zhang, H. P. Zhang, H. P. Chen, R. Y. Zhang, L. F. Liu, J. Y. Yu, Setaria viridis-inspired electrode with polyaniline decorated on porous heteroatom-doped carbon nanofibers for flexible supercapacitors, *ACS Appl. Mater. Interfaces* **2020** 12 43634–43645.
15. R. Zhang, L. Wang, J. Zhao, S. W. Guo, Effects of sodium alginate on the composition, morphology, and electrochemical properties of electrospun carbon nanofibers as electrodes for supercapacitors, *ACS Sust. Chem. Eng.* **2019** 7 632–640.
16. A. Gopalakrishan, P. Sahatiya, S. Badhulika, Template-assisted electrospinning of bubbled carbon nanofibers as binder-free electrodes for high-performance supercapacitors, *Chem. Electro.Chem*. **2018** 5 531–539.
17. K. Q. Qu, Y. You, H. J. Qi, C. Shi, Z. Sun, Z. H. Huang, B. N. Yuan, Z. H. Guo, Fungus bran-derived porous n-doped carbon-zinc manganese oxide nanocomposite positive electrodes toward high-performance asymmetric supercapacitors, *J. Phys. Chem. C* **2020** 124 15713–15722.
18. S. Biswas, V. Sharma, D. Mandal, A. Chowdhurry, M. Chalravarty, S. Priva, P. De, I. Singh, A. Chandra, C. C. Gowda, Hollow nanostructures of metal oxides as emerging electrode materials for high performance supercapacitors, *CrystEngComm*.**2020** 22 1633–1644.
19. Y. Guo, C. H. Wu, N. W. Li, S. Yuan, L. Yu, Formation of Co-Mn mixed oxide double-shelled hollow spheres as advanced electrodes for hybrid supercapacitors, *J. Mater. Chem. A* **2019** 7 25247–25253.
20. D. Aradilla, F. Estrany, C. Aleman, Ultraporous poly (3, 4-ethylenedioxythiophene) for nanometric electrochemical supercapacitor, Thin Solid Films **2012** 520 4402–4409.
21. M. M. Pérez-Madrigal, F. Estrany, E. Armelin, D. D. Díaz, C. Alemán, Towards sustainable solid-state supercapacitors: electroactive conducting polymers combined with biohydrogels, *J. Mater. Chem. A* **2016** 4 1792–1805.
22. K. Li, X. H. Wang, S. Li, P. Urbankowski, J. M. Li, Y. X. Xu, Y. Gogotsi, An ultrafast conducting polymer@MXene positive electrode with high volumetric capacitance for advanced asymmetric supercapacitors, *Small* **2020** 4 1906851.

23. C. Xia, W. Chen, X. B. Wang, M. N. Hedhili, N. N. Wei, H. N. Alshareef, Highly stable supercapacitors with conducting polymer core-shell electrodes for energy storage applications, *Adv. Energy Mater.* **2015** 5 1401805.
24. L. Kang, M. Y. Zhang, J. Zhang, S. D. Liu, N. Zhang, W. J. Yao, Y. Ye, C. Luo, Z. W. Gong, C. L. Wang, X. F. Zhou, X. Wu, S. C. Jun, Dual-defect surface engineering of bimetallic sulfide nanotubes towards flexible asymmetric solid-state supercapacitors, *J. Mater. Chem. A* **2020** 8 24053–24064.
25. W. W. Zhao, M. Y. Jiang, W. K. Wang, S. J. Liu, W. Huang, Q. Zhao, Flexible transparent supercapacitors: Materials and devices, *Adv. Funct. Mater*. **2020** 31 2009136.
26. Q. F. Liu, J. H. Qiu, C. Yang, L. M. Zang, G. H. Zhang, E. Sakai, High-performance PVA/PEDOT:PSS hydrogel electrode for all-gel-state flexible supercapacitors, *Adv. Mater. Technol*. **2021** 6 2000919.
27. W. Y. Chen, T. T. Wei, L. E. Mo, S. G. Wu, Z. Q. Li, S. H. Chen, X. X. Zhang, L. H. Hu, CoS2 nanosheets on carbon cloth for flexible all-solid-state supercapacitors, *Chem. Eng. J.* **2020** 400 125856.
28. H. M. Yu, N. Rouelle, A. D. Qiu, J. A. Oh, D. M. Kempajah, J. D. Whittle, M. Aakyiir, W. J. Xing, J. Ma. Hydrogen bonding-reinforced hydrogel electrolyte for flexible, robust, and all-in-one supercapacitor with excellent low-temperature tolerance*, ACS Appl. Mater. Interfaces* **2020** 12 37977–37985.
29. G. Ruano, J. Tononi, D. Curcó, J. Puiggalí, J. Torras, C. Alemán, Doped photo-crosslinked polyesteramide hydrogels as solid electrolytes for supercapacitors*, Soft Matter* **2020** 16 8033–8046.
30. H. Y. Liao, F. L. Zhou, Z. Z. Zhang, J. Yang, A self-healable and mechanical toughness flexible supercapacitor based on polyacrylic acid hydrogel electrolyte*, Chem. Eng*. J. **2019** 357 428–434.
31. M. M. Pérez-Madrigal, M. Edo, M. G. Saborío, F. Estrany, C. Aleman, Pastes and hydrogels from carboxymethyl cellulose sodium salt as supporting electrolyte of solid electrochemical supercapacitors, *Carbohydr. Polymm* **2018** 200 456–467.
32. A. Gupta, S. Sardana, J. Dalal, S. Lather, A. S. Maan, R. Tripathi, R. Punia, K. Singh, A. Ohlan, Nanostructured polyaniline/graphene/Fe_2O_3 composites hydrogel as a high-performance flexible supercapacitor electrode material, *ACS Appl. Energy Mater*. **2020** 3 6434–6446.
33. M. G. Saborío, S. Lanzalaco, G. Fabregat, J. Puiggalí, F. Estrany, C. Alemán, Flexible electrodes for supercapacitors based on the supramolecular

assembly of biohydrogel and conducting polymer, *J. Phys. Chem*. **2018** 122 1078–1090.

34. W. Zhang, P. Feng, J. Chen, Z. M. Sun, B. X. Zhao, Electrically conductive hydrogels for flexible energy storage systems*, Prog. Polym. Sci*. **2019** 88 220–240.
35. Z. R. Ying, Y. Z. Zhang, X. M. Lin, S. J. Hui, Y. X. Wang, Y. B. Yang, Y. C. Li, A biomass-derived super-flexible hierarchically porous carbon film electrode prepared via environment-friendly ice-microcrystal pore-forming for supercapacitors, *Chem. Commun*. **2020** 5610730–10733.
36. P. Zhang, Q. Z. Zhu, R. A. Soomro, S. Y. He, N. Sun, N. Qiao, B. Xu, In situ ice template approach to fabricate 3D flexible MXene film-based electrode for high performance supercapacitors, *Adv. Funct. Mater*. **2020** 30 2000922.
37. Q. F. Wang, Y. Ma, X. Liang, D. H. Zhang, M. H. Miao, Flexible supercapacitors based on carbon nanotube-MnO_2 nanocomposite film electrode, *Chem. Eng. J*. **2019** 371 145–153.
38. C. S. Kwak, T. H. Ko, J. H. Lee, H. Y. Kim, B. S. Kim, Flexible transparent symmetric solid-state supercapacitors based on NiO-decorated nanofiber-based composite electrodes with excellent mechanical flexibility and cyclability, *ACS Appl. Energy Mater*. **2020** 3 2394–2403.
39. E. Samuel, B. Joshi, M. W. Kim, Y. I. Kim, M. T. swithart, S. S. Yoon, Hierarchical zeolitic imidazolate framework-derived manganese-doped zinc oxide decorated carbon nanofiber electrodes for high performance flexible supercapacitors, *Chem. Eng. J.* **2019** 371 657–665.
40. J. H. Park, H. H. Rana, J. Y. Lee, H. S. Park, Renewable flexible supercapacitors based on all-lignin-based hydrogel electrolytes and nanofiber electrodes, *J. Mater. Chem. A* **2019** 7 16962–16968.
41. B. G. Molina, S. Cuesta, H. Besharatloo, J. J. Roa, E. Armelin, C. Alemán, Free-standing faradaic motors based on biocompatible nanoperforated poly(lactic acid) layers and electropolymerized poly(3,4-ethylenedioxythiophene), *ACS Appl. Mater. Interfaces* **2019** 11 29427–29435.
42. B. Molina, S. Cuesta, A. Puiggalí-Jou, L. J. del Valle, E. Armelin, C. Alemán, Perforated polyester nanomebranes as templates of electroactive and robust free-standing films*, Eur. Polym. J.* **2019** 114 213–222.
43. P. Simon, Y. Gogotsi, Materials for electrochemical capacitors*, Nat. Mater.* **2008** 7 845–854.
44. J. Garcia-Torres, C. Crean, Multilayered flexible fibers with high performance for wearable supercapacitor applications, *Adv. Sustain. Syst.* **2018** 7

1700143−1700152.

45. D. Aradilla, F. Estrany, F. Casellas, J. I. Iribarren, C. Aleman, All-polythiophene rechargeable batteries, *Org. Electron.* **2012** 15, 40−46.
46. M. Ujvári, M. Takács, S. Vesztergom, F. Bazsó, F. Ujhelyi, G. G. Láng, G. G. Monitoring of the electrochemical degradation of PEDOT films on gold using the bending beam method*, J. Solid State Electrochem*. **2011** 15 2341–2349.
47. M. C. G. Saborío, F. Estrany, C. Alemán, Properties of in situ polymerized poly(3,4-ethylenedioxythiophene)/alumina composites for energy storage applications, *J. Polym. Sci., Part B: Polym*. Phys. **2017** 55 1131–1141,
48. H. A. Andreas, Self-discharge in electrochemical capacitors: A perspective, *J. Electrochem. Soc*. **2015** 16 A5047.

3.5 Study on the Control of Porosity in Films of Polythiophene Derivatives

3.5.1 Summary

Conducting polymers typically exhibit different oxidation states, which are easily interchangeable among them by means of the application of an electrical potential. In this work, we present a theoretical and experimental study to regulate the pore size of poly(3,4-ethylenedioxythiophene) (PEDOT) films doped with ClO_4^- ions by controlling their oxidation state. More specifically, different bulk and surface PEDOT models have been evaluated applying 2D- and 3-D periodic boundary conditions to density functional theory calculations. In highly oxidized PEDOT films, calculations predict that the incorporation of dopant ions increases the separation between neighboring chains, causing a structural re-organization. Thus, the calculated average pore size, which has been modeled as a structural defect in 2D surface models, increases by 15.1%. This increment is consistent with experimental measures of the nanopore size in PEDOT films with enhanced porosity, which reflect a difference of 25.2% between the oxidized and reduced forms. This superficial phenomenon could easily be used to retain and release controlled drugs through the application of different electric potentials.

3.5.2 Introduction

The ability to create controlled interfaces, such as nonporous and nanoperforated membranes, has been an important topic of study during the last decade, particularly in the biomedical field.[1–4] Among them, polymeric free-standing nanomembranes (from 1 up to 100 nm thick) have emerged as versatile elements for biomedical applications such as overlapping therapy, burn wound infection treatment, antimicrobial platforms, scaffolds for tissue engineering, drug-loading and delivery systems, biosensors, etc.[5–7] Moreover, the utilization of electrically conducting materials and devices for biomedical and biotechnological applications has become an interesting topic to the community due their potential applications. [8–10] In fact, intrinsically conducting polymers (ICPs) are perceived as suitable candidates for these biomedical devices because of both their luminescence properties,[11] electrical [12,13] behavior and biocompatibility.[14,15] These interesting properties were previously exploited on the use of ICP as electro-chemo-mechanical actuators that can be envisaged as artificial muscles.[16–21]

Recently, new nanomembranes were created for biomedical and biotechnological applications using ICPs based on poly(thiophene) and its derivatives.[22] Moreover, a novel methodology was developed to create nanoperforated nanomembranes [23] to fix biological material in a well-defined nano-holes, thus, increasing the potential applicability of those nanomembranes.[4] Taking into account the state-of-the-art, an interesting application can be envisaged for nanoporous ICP ultra-thin membranes as a potential drugs releaser by controlling the nanopore size. More specifically, the release of drugs immobilized inside the nanopores could be regulated by changing the nanopore size through the electro-chemo-mechanical properties of ICPs. In some circumstances, ICP films can be considered as motors driven by reversible electrochemical reactions (Faradaic motors).[24,25] Thus, electrons are extracted from or injected to polymeric chains

during the reactions generating positive or negative chains, respectively, while hydrated counterions (*i.e.* anions or cations accompanied with water molecules) are exchanged between the polymeric matrix and the electrolyte to keep the charge balance inside the film (Fig. 3.5.1a). Such electronic and ionic charge transport processes cause conformational movements in the polymer chains that, together with the compositional variation inside the polymeric matrix (*i.e.* entrance and scape of hydrated ions), guarantee film volume variations during reversible oxidation and reduction reactions (swelling and shrinking, respectively). Within this context, it should be mentioned that this electrochemically induced actuation mechanism was recently used to regulate the drug delivery from polyester microfibres loaded with poly(3,4-ethylenedioxythiophene) (PEDOT) nanoparticles, which exhibited a volume variation of ~17% upon the application of electric pulses, increasing the porosity of the microfibers.[26]

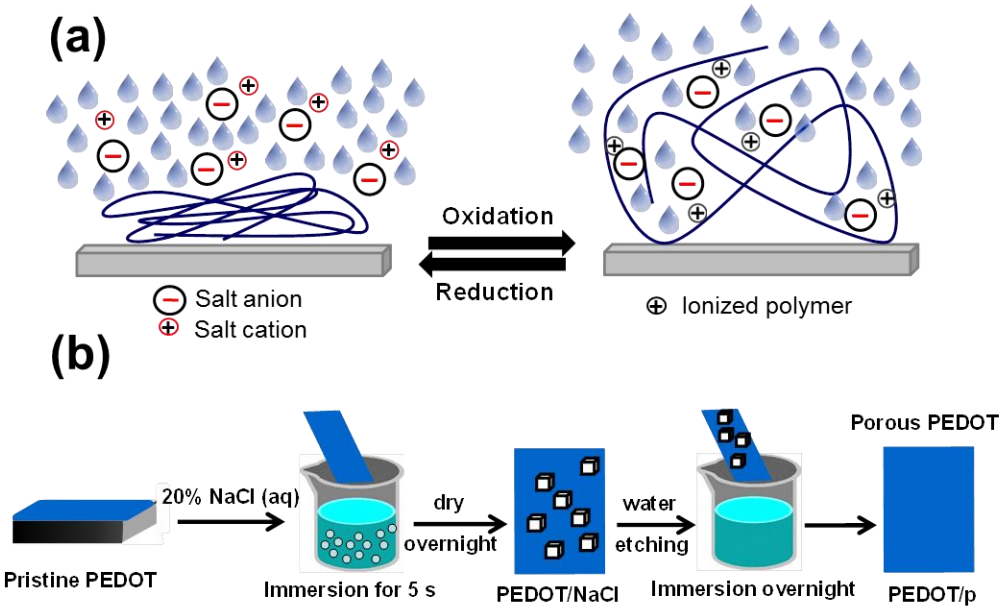

Figure 3.5.1. (a) Reaction induced swelling/shrinking of an ICP film. (b) Preparation of porous PEDOT growing NaCl crystals on the surface of the film and etching them with water.

Concepts relating the volume variation of macroscopic ICP films with oxidation and reduction reactions (*i.e.* with the doping level) can be extrapolated to

microscopic nanopores and nanoperforations for regulating the transport of medium size molecules in drug delivery applications. Indeed, chemical and physical properties of ICPs are, in general, intimately related with their doping level.[27] For example, experimental and theoretical studies on oxidized (doped) and reduced (dedoped) PEDOT showed important structural differences (*e.g.* the inter-chain distance was shorter for the latter than for the former).[28,29] Moreover, the cohesion between polymer chains was found to increase when dopant ions are intercalated among them.[30] Within the context of structure-electronic properties relationships, theoretical calculations on ICPs are usually conducted using either oligomers with a growing number of repetitive units or applying periodic boundary conditions (PBC) along the direction of growth of the polymer chain (1D-PBC),[31–34] while more complex solid state calculations with 2D- or 3D-PBC approaches have been scarcely reported.[35,36] The main goal of this work is to evaluate the influence of the doping level on the pore size of ICP films combining advanced theoretical approaches based on 3D-PBC models and experimental measures.

In this work, we use full 2D- and 3D-PBC density functional theory (DFT) calculations to conduct a differential investigation on the structural and electronic changes induced by the doping level. Furthermore, the influence of the doping level on the micro-pore size of porous anodically polymerized PEDOT has been experimentally characterized by scanning electron microscopy (SEM). Results, which have allowed us to check the viability on the pore-size control, are expected to assist for regulating the release of drugs immobilized inside the pores by controlling their diameter through the doping level.

3.5.3 Methods

3.5.3.1 Materials

3,4-ethylenedioxythiophene (EDOT) and acetonitrile of analytical reagent grade were purchased from Sigma-Aldrich and used as received, without further purification. Anhydrous $LiClO_4$, analytical reagent grade from Aldrich, was stored in an oven at 70 °C before use in electrochemical experiments. Milli-Q water grade (0.055 S/cm) was used in all synthetic processes.

3.5.3.2 Synthesis of porous PEDOT films.

PEDOT films were prepared by chronoamperometry under a constant potential of 1.40 V and adjusting the polymerization charge to 0.55 C. Electrolytic cells made of three-electrode one-compartment were used for all polymerizations under nitrogen atmosphere (99.995% in purity) at 25 ºC. Stainless steel AISI 316 sheets of 1.0×1.5 cm^2 were used as working and counter electrodes in combination with a reference electrode of Ag|AgCl containing a KBr saturated aqueous solution (E^o = 0.222 V *vs.* standard hydrogen electrode at 25 ºC). To avoid interferences during the electrochemical analyses, before each trial the working and counter electrodes were cleaned with ethanol, after that with acetone, and dried in an air-flow.

The electrolytic cell was filled with 40 mL of a 10 mM acetonitrile solution of EDOT monomer with 0.1 M $LiClO_4$ as doping electrolyte. The experimental set-up for this anodic polymerization was described in previous work.[37] PEDOT porous film were achieved by the growing and etching stages of NaCl crystals on the surface of the previously obtained PEDOT film using a simple methodology, which is sketched in Fig. 3.5.1b. First, NaCl crystals were grown by plunging the prepared films in a 20% w/v salt aqueous solution during 5 s and, subsequently, dried in a desiccator overnight. After this, the porous surface was obtained by removing the

grown salt crystals from PEDOT/NaCl films by plunging in water overnight and drying in a desiccator for at least 24 h. Hereafter, the resulting porous PEDOT films are denoted PEDOT/p.

3.5.3.3 Chemical characterization of oxidized-reduced PEDOT/p films.

FTIR spectra of PEDOT/p films were recorded on a FTIR Jasco 4100 spectrophotometer. Attenuated total reflection accessory with a diamond crystal (Specac model MKII Golden Gate Heated Single Reflection Diamond ATR) were used to place the samples. A total of 64 scans were performed between 4000 and 600 cm-1 (4 cm-1 of resolution) for each sample.

Raman spectra of PEDOT films were recorded using a Renishaw inVia Qontor confocal Raman microscope with 785 nm laser excitation and a nominal 300mW output power directed through a microscope (specially adapted Leica DM2700 M microscope) to the sample. The scattered light is collected and directed to a spectrometer with a 1200 lines·mm-1 grating. The laser power was adjusted to 1% of its nominal output power with an exposure time of 10 s. Each spectrum was collected with 3 accumulations.

3.5.3.4 Surface characterization of oxidized-reduced PEDOT/p films.

Two different oxidation states were obtained by applying two different potentials to the porous PEDOT/p film. Specifically, chronoamperometries (CA) were conducted applying a constant potential of +1.1 (oxidation) and –1.1 (reduction) V for 10 s to PEDOT/p films to obtain oxidized and reduced porous PEDOT films (hereafter PEDOT/p^{oxd} and PEDOT/p^{red} respectively). These experiments were made in cells of three electrodes under a nitrogen atmosphere at 25 ºC.

The doping Level (*dl*) of oxidized and reduced PEDOT/p layers were determined by cyclic voltammetry (CV) using an aqueous solution of 0.1 M $LiClO_4$. The initial and final potential were –0.5 V, while the reversal potential was +1.1 V. The scan rate was set to 100 mV s^{-1}. Electrochemical estimation of the doping level (dl) was carried out using the following equation:[38]

$$dl = \frac{2\,Q_{ox}}{Q_{pol} - Q_{ox}} \qquad \text{(E.3.5.1)}$$

where Q_{ox} is the charge associated to the oxidation process derived from the latter CV, and Q_{pol} is the total charge used for the PEDOT film deposition at the generation time.

Film thickness measurements were carried out using a Dektak 150 stylus profilometer (Vecco, Plainview). Several scratches were intentionally caused on the films to allow the film thickness measurement. Imaging of the film was conducted using the following optimized setting: tip radius = 2.5 µm, stylus force = 1.5 mg scan length = 3 mm and a scan resolution of 0.33 µm. Two different measures were obtained: (a) the vertical distances (***I***), which is the difference between the polymer and substrate height without any average; (ii) the surface roughness (***Ra***) as the arithmetical mean deviation of the assessed profile. The density of both reduced and oxidized polymers was determined by the flotation method from CCl_4 + C_2H_5I mixtures.

The X-ray diffraction (XRD) experiments were performed by using Bruker D8 Advance X-ray diffractometer with a monochromatic Cu radiation (λ = 1.5406 Å). Polymer powders were deposited in a silicon wafer and then were fixed by vacuum grease. Finally the fixed PEDOT powder was used in powder XRD measurement.

Scanning electron microscopy (SEM) studies were performed to examine the surface morphology of the prepared films. Dried samples were placed in a Focused Ion Beam Zeis Neon 40 scanning electron microscope operating at 5 kV, equipped with an energy dispersive X-ray (EDX) spectroscopy system. The average pore

size of each system was obtained statistically from a set of 200 measures distributed among 20 SEM pictures of a total of 3 different samples each.

3.5.3.5 Theoretical calculations.

Surface nanopore expansion/constriction associated to the reversible transition between dedoped and doped PEDOT systems have been examined by means of six different models covering the three possible states (*i.e.* bulk, raw surface and nanopored surface). Firstly, two bulk structures were simulated. These consisted of eight EDOT repeated units distributed in two chains, which grew along the lattice vector ***c*** using a 3D-PBC approach. In one of them, four ClO_4^- anions were introduced in order to simulate the doped bulk at an ideal doping level of 0.5. Initial coordinates were obtained from a previous crystallographic study using 1D-PBC approach. [30] The other four systems were used to model PEDOT surfaces, which were build starting from the previous optimized bulk system but adding a vacuum region of 45 Å along lattice vector b. In this case, two of the models simulated the raw surface while the other two simulated the porous nanomembrane. This was achieved building four different supercells: the two simulating the raw surface were based on two repeating bulk units along c-direction (doped and dedoped), and the other two were made of two repeating units along c-direction while only one along a-direction, thus leaving an empty space replicating the porous surface (doped and dedoped)

All calculations were based on the DFT in the standard Kohn−Sham formalism, as implemented in the SIESTA package[39] with PBC. The generalized gradient approximation (GGA) was used on the calculation of exchange-correlation energy employing the Perdew−Burke−Ernzerhof (PBE) functional.[40] All atoms were represented by the Troullier-Martins norm-conserving pseudopotentials[41] and a numerical double-ζ basis set with polarization function. Initial structures were

allowed to relax under PBC by means of conjugate gradient minimization. Thus, the atom coordinates were optimized until the forces acting on each atom were smaller than 0.04 eV/Å, using a mesh cutoff of 350 Ry. Sampling of the irreducible Brillouin zone was performed according to the scheme proposed by Monkhorst and Pack[42] with a k-points mesh made of 6×4×4 and 6×1×4 for the bulk and surface models, respectively.

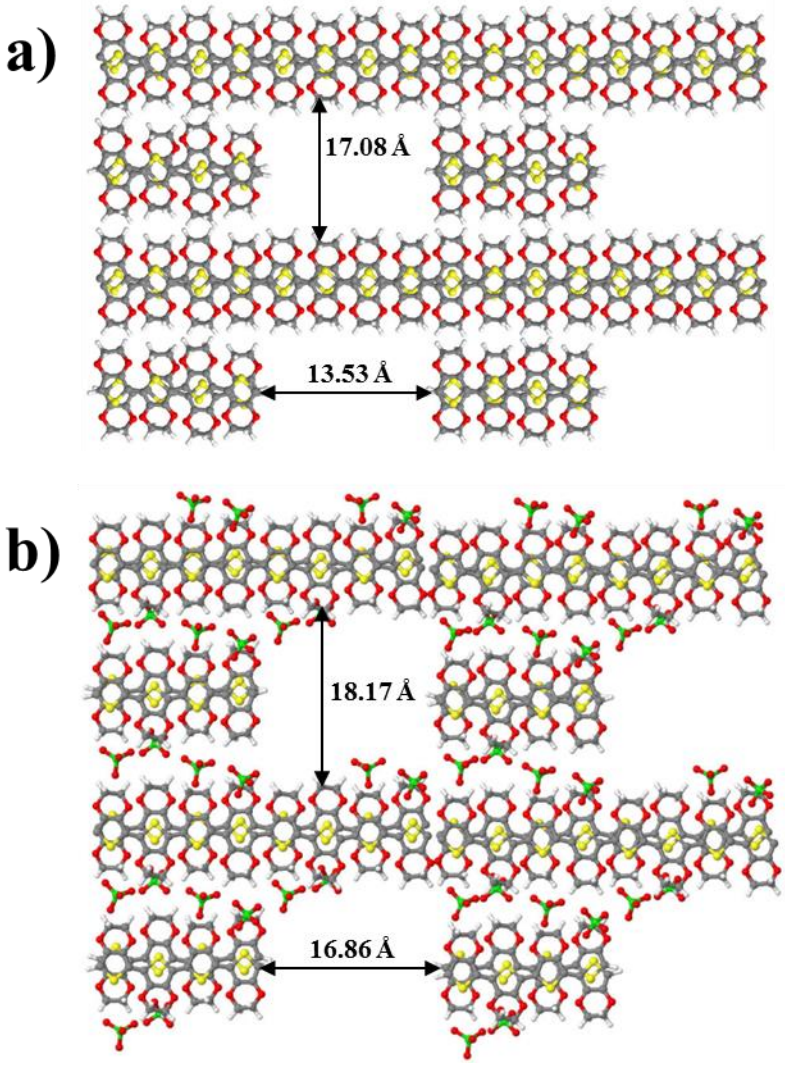

Figure 3.5.2. Pore dimensions on a 2x2 supercell of (a) *np*-dedoped and *np*-doped systems.

3.5.4 Results and Discussion

3.5.4.1 Dedoped and doped bulk structures.

Fig. 3.5.3 compares the structures obtained for the dedoped and ClO_4^- doped bulk PEDOT models (hereafter named *b*-dedoped and *b*-doped model, respectively) after optimization using the 3D-PBC DFT approach. Since the unit cell angles were freely optimized, all resulting systems present a triclinic symmetry. However, some angles show very close values to higher crystal symmetry. In those cases, the crystal unit cell will be denoted as *quasi*- the closest symmetry. Table 3.5.1 compares the structural parameters for both systems with experimental values. Although the calculated *b*-dedoped model presents a *quasi*-monoclinic unitary cell (γ = 81.9º) with α = 89.7º and β = 90.0º, the obtained interlayer and interchain distances can be easily compared with the experimental orthorhombic unitary cell presented by Tran-Van *et al*. [43] In that work, the two most intense diffraction peaks at 7.87 and 10.52 Å of a dedoped PEDOT film were assigned to the distances of periodic structure along lattice vector ***c*** (*i.e.* polymer repeat distance along the chain) and ***a*** (*i.e.* parallel interchain distance, d_R), respectively. Those values are in very good agreement with the theoretical parameters of 7.90 and 10.28 Å obtained for the *b*-dedoped system in this work, respectively (Table 3.5.1). Furthermore, the inter-chain stacking distance (minimum distance between two adjacent chain planes of thiophene rings, d_H) obtained in this work for the simulated model of dedoped PEDOT was 3.44 Å, while the 020 reflection plane (***b***/2) was 3.68 Å. The latter distance can be associated to the third most intense peak of the X-ray diffractogram of Tran-Van *et al*. [43] with an angle of 25.9º and 3.43 Å. This value is also pretty similar to the stacking distance reported for the tosylated-doped PEDOT in a orthorhombic crystal[28]. Also, the torsion between lattice direction ***a*** and the plane of PEDOT chain due to interactions between adjacent PEDOT layers reported in the literature with values of 8.1º[29] and 10º,[44]

are similar to the value calculated for the *b*-dedoped model of 14.7º. As in general the concordance between the calculated and experimental values is very good for the bulk models, the 2D-PBC approach described in the Methods section is expected to represent satisfactorily the PEDOT surface.

Table 3.5.1. Calculated Values of the Crystal Structures, Supercell Volume (V), Inter-chain Stacking Distance (d_H) and theParallel Interchain Distance (d_R) of Dedoped and Doped PEDOT. The meaning of d_H and d_R is sketched in Fig. 3.5.3.

	Supercell (Å)	**Angles (º)**	**V (Å³)**	**Unit cell (Å)**	**d_H (Å)**	**d_R (Å)**
			b-dedoped			
DFT	a =10.28 b = 7.37 c =15.80	α = 89.7 β = 90.0 γ = 81.9	1185.2	a =10.28 b =7.37 c =7.90	3.44	10.28
exp.[43]				a =10.52 b =6.86 c =7.86	3.43	10.52
			b-doped			
DFT	a =12.64 b =6.59 c =15.48	α = 86.3 β = 88.3 γ = 66.6	1183.5	a =12,54 b =6.59 c =7.74	3.14	12.64
exp.[a,28]				a =14.0 b =6.8	3.4	14.0

	c =7.8

[a] Tosylate-doped PEDOT.

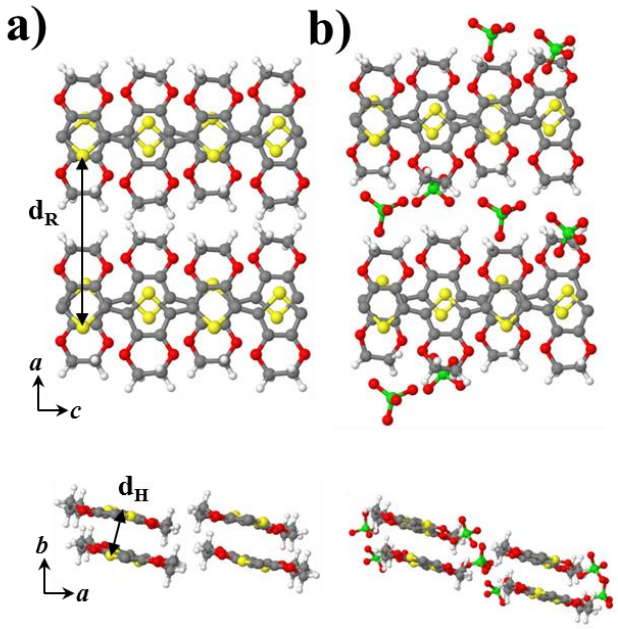

Figure 3.5.3. Top and Side Views of the Optimized (a) Dedoped and (b) Doped PEDOT Bulk Models as Derived from 3D-PBC DFT Calculations. d_H and d_R chain distance are also shown.

From the theoretical and experimental parameters reported in Table 3.5.1, comparison of PEDOT's dedoped and doped structures reflects a compactness in the stacking distance of 0.3 Å, but also a significant increase in PEDOT inter-chains distances of 2.36 Å. The latter is clearly due to the disposition of the dopant perchlorate anions. Moreover, it is also observed a small elongation of 0.16 Å along the axis of growth on the doped polymer.

3.5.4.2 Dedoped and doped surface structures.

Optimized structures of two multilayers with a large buffer along the lattice vector ***b*** to model a polymer surface were obtained using the 2D-PBC DFT approach.

Table 3.5.2 lists the structural parameters of dedoped PEDOT and ClO_4^- doped PEDOT surface systems (hereafter *s*-dedoped and *s*-doped, respectively). An expected small contraction, which is due to the loss of periodicity in one of the crystallographic lattice direction, is observed. Furthermore, there is an important crystal restructuring with a change in the main angles of the unitary cell. Indeed, we can see how the *quasi*-monoclinic dedoped bulk crystal becomes almost a *quasi*-orthorhombic system on the calculated surface model, the γ angle increasing from 81.9º to 86.8º, meanwhile the other two unit cell angles remains close to 90º. In contrast, in the *s*-doped system γ increases from 66.6º to 73.2º while the cells maintains the triclinic geometry.

Table 3.5.2. Calculated Values on the Optimized Surface Structures of the Supercell's Vectors (Distances and Angles in Å and º, respectively), Volume (V; in Å^3), Inter-chain Stacking Distance (d_H; in Å) and Parallel Interchain Distance (d_R; in Å) of Dedoped and Doped PEDOT of Raw Surface Models (*s*-) and Nanopored (*np*-) Surface Models.

Surface	**Slab**[a]			**Angles**			**V**	**d_H**	**d_R**
	a	***b***	***c***	α	β	γ			
s-dedoped	20.40	6.48	15.67	91.1	89.9	86.8	2069	3.24	10.20
s-doped	24.51	6.44	15.44	85.0	87.1	73.2	2325	3.22	12.26
np-dedoped[b]	20.50	6.54	15.67	90.4	89.8	92.0	2096	3.27	10.18[d]
np-doped[b]	23.38	6.54	15.43	85.6	87.1	74.6	2362	3.27	12.18[d]

[a] Only the slab surface dimensions are considered. There is a buffer of about 45 Å along ***b*** lattice vector in all systems. [b] The slab supercell distances along ***c*** lattice vector is divided by two to be compared with the *s*- models, which are holding only 4 EDOT units along ***c*** lattice vector. [d] Averaged d_R distances.

Overall, a reduction on the interchain distances is observed when comparing bulk and surface models, which is mainly due to the periodicity reduction. Indeed, *s*-dedoped presents a large reduction (−5.8%) on the d_H interchain distance (perpendicular to the surface), whereas on the other lattice direction (d_R) the reduction on the interchain distances is slightly lower (−2.4%). Furthermore, *s*-doped presents different figures than *s*-dedoped when is compared with the *b*-doped crystal. Specifically, the d_H interchain distance increases about +2.5% meanwhile d_R is compacted on about −3% when is compared with *b*-doped model.

The doping effect on the surface models leads to a supercell volume increase of 12.4%. The slab volume was calculated following the general unit cell volume formula ($V= \boldsymbol{a}\times\boldsymbol{b}\times\boldsymbol{c}$) but considering the ***b*** lattice vector as the double of the interchain d_H distance. This figure comes from the necessary distance increase between parallel PEDOT chains (d_R) to accommodate the perchlorate dopant ions into such interchain space with a Δd_R=2.06 Å, which represents an increment of 20%. Similar figures were obtained when comparing *b*-dedoped and *b*-doped models with Δd_R = 2.19 Å (21 % increase).

3.5.4.3 Nanopored surface structure.

Fig. 3.5.4 shows the optimized structure of dedoped and ClO_4^- doped nanopored polymer surface models (hereafter *np*-dedoped and *np*-doped, respectively), which were obtained using a 2D-PBC DFT approach. The two models are made of two nanopored multilayered systems with a large buffer along ***b*** lattice vector and a crystal defect induced by 4 EDOT units missing in both layers. In order to accommodate the defect we doubled the supercell along ***c*** lattice direction (8 EDOT units) compared with the *s*-dedoped and *s*-doped surface models (4 EDOT units). Table 3.5.2 lists the structural parameters of both nanopored structures. The

supercell dimension has been normalized to be compared with the *s*-surface models holding only 4 EDOT units along ***c*** lattice vector.

As it can be seen, there are not much structural differences in the slab surface dimensions due to the presence of a nano-pore defect in the surface. It is observed a slight increment on the ***b*** lattice vector (~1%) when the *np*-models are compared with the corresponding *s*-models and, in addition, a short contraction along ***a*** lattice vector is detected for the *np*-doped system. Consequently, a very similar volume increment is observed for both *s*- and *np*-doped systems (12.4 % and 12.7 %, respectively) with respect to the *s*- and *np*-dedoped models.

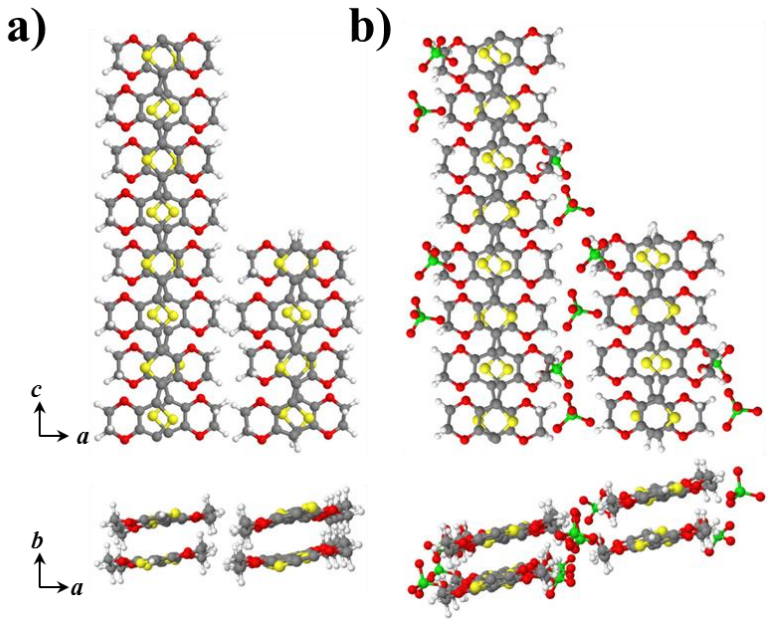

Figure 3.5.4. Top and Side Views of the Optimized Nanopored (a) Dedoped (*np*-Dedoped) and (b) Doped (*np*-Doped) PEDOT Surface Models as Derived from 2D-PBC DFT Calculations.

Table 3.5.3. Averaged Inter-Ring Dihedral Angle (θ; º), Intrachain S···S Distance (d_{S-S}^{intra}; Å), Interchain S···S Distances (d_{S-S}^{inter}; Å), and Shortest Cl···Cl distances ($d_{Cl\text{-}Cl}$; Å) for the Optimized Bulk (*b*-), Raw Surface (*s*-) and Nanopored Surface (*np*-) Models of Dedoped and Doped PEDOT.

Surface	$\boldsymbol{\theta}$	$\boldsymbol{d_{S-S}^{intra}}$		$\boldsymbol{d_{S-S}^{inter}}$		$\boldsymbol{d_{Cl-Cl}}$		
b-dedoped	177.1±1.2	4.47±0.00	3.56±0.00	4.78±0.00	-	-	-	

b-doped	176.7±1.4	4.45±0.00	3.38±0.04	4.47±0.05	5.21±0.00	4.93±0.00	5.33±0.00
s-dedoped	174.2±3.3	4.44±0.00	3.40±0.00	4.80±0.00	-	-	-
s-doped	175.3±3.2	4.46±0.00	3.38±0.00	4.96±0.04	5.09±0.00	4.65±0.00	5.38±0.00
np-dedoped	170.0±2.7	4.44±0.00	3.53±0.01	4.70±0.06	-	-	-
np-doped	174.7±3.5	4.44±0.00	3.41±0.01	4.89±0.01	5.05±0.13	4.69±0.02	4.57±0.28

On the other hand, the pore dimensions are much more affected on the surface model because of the distribution of the dopant anions. Fig. 3.5.2 (see methods section) shows the surface pore reconstruction in a supercell of 2×2 slabs and the pore dimension for both *np*-models. Despite of a short contraction of the pore along the ***a*** lattice vector (~1.1 Å) there is a large increment of 3.3 Å along ***c*** lattice vector, which leads to 32.5 % of the pore-surface increment after *np*-dedoped system doping (i.e., 15.1 % of circular pore-diameter increment). This large surface increment would allow to release potentially immobilized drugs inside the surface of dedoped PEDOT after doping, enabling the control on drug release by regulating the doping level.

3.5.4.4. Structural differences among models.

Table 3.5.3 compares selected structural parameters for all the calculated dedoped and doped PEDOT models. Interestingly, notable distortions from planarity are observed on the inter-ring dihedral angles (θ) of PEDOT chains, which are defined by the S–C–C–S sequence. More specifically, the averaged inter-ring dihedral angle is getting further away from the ideal *anti* conformation (θ = 180º) as the model is losing periodicity (*i.e.* θ = 177.1º, 174.2º, and 170.0º for the *b*-, *s*- and *np*-dedoped models, respectively). Similar behavior is observed on doped models with averaged inter-ring dihedral angles of θ= 176.7º, 175.3º and 174.7º for the *b*-, *s*- and *np*-systems, respectively.

Fig. 3.5.5 shows intra- and intermolecular distances measured between sulphur and chlorine atoms within the supercell. Intramolecular S···S distances present close values among all optimized systems (d_{S-S}^{intra} = 4.45 ± 0.05 Å), differences being attributed to the planarity degree of the polymer chain previously discussed. On the other hand, comparison of the intermolecular S···S distances for *b*- and *s*-dedoped models reveals a short reduction of both $d_{S-S,1}^{inter}$ and $d_{S-S,2}^{inter}$ (see Fig. 3.5.5). This observation is consistent with a compaction effect, which was previously discussed. Similarly, some reorganization is observed for *np*-doped, in which the S···S distances take larger values, especially on the $d_{S-S,2}^{inter}$ distance, due to the distortions induced by the periodicity break along chain axis and the subsequent reorganization of the repetitive units closest to the crystallographic defect. Nevertheless, the obtained inter-chain S···S distances are significantly lower than those previously reported from 1D-PBC DFT calculations on PEDOT doped with ClO_4^- ions (d_{S-S}^{inter}= 5.89 Å).[30] Thus, the present study indicates that compaction effect is larger than reported in previous works.

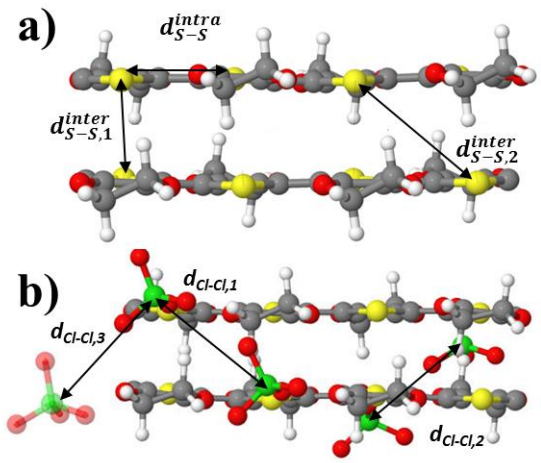

Figure 3.5.5. Detail of (a) S···S Distances and (b) Cl···Cl Distances on the Side View of (a) *b*-Dedoped and (b) *b*-Doped Models of PEDOT. Glassy ClO_4^- Represents the Closest Virtual Image.

Table 3.5.3 lists the three closest Cl···Cl distances among pairs of ClO_4^- ions for the doped PEDOT models, while Fig. 3.5.5 shows their location within unit cell. It is observed that compaction effect on parallel chains also leads to the reorganization of the dopant ions, which is reflected by differences in their Cl···Cl distances. Specifically, $d_{Cl\text{-}Cl,1}$ and $d_{Cl\text{-}Cl,2}$ (see Fig. 3.5.5) present some reduction when the periodicity of the surface is lost. However, the distance involving one virtual dopant ion ($d_{Cl\text{-}Cl,3}$), which corresponds to the closest periodic image, presents a major reorganization. This has been attributed to the pore surface defect, with a reduction of about 0.76 Å when is compared with the *b*-doped model.

Table 3.5.4. HOMA Aromaticity Index for All Dedoped and Doped PEDOT systems.

System	***b*-dedoped**	***b*-doped**	***s*-dedoped**	***s*-doped**	***np*-dedoped**	***np*-doped**
HOMA	0.607	0.550	0.696	0.558	0.711	0.576
$HOMA_c$[a]	-	-	-	-	0.710	0.573
$HOMA_p$[b]	-	-	-	-	0.713	0.588

[a] PEDOT chains without any crystallographic defect; [b] PEDOT chains that have been shortened because of the surface pore modelling.

Table 3.5.4 lists the averaged Harmonic Oscillator Model of Aromaticity (HOMA index) for all systems under study. HOMA[45] index allows to quickly and easily assign the aromatic character of any system based on the C–C and C–S bond length alternation pattern along the π-system. This methodology has been previously used to study the aromaticity of different thiophene based polymers.[46] Within this context, the HOMA index is equal to zero for a Kekulé structure formed by a typical aromatic system with single and double bonds arranged alternatively, whereas it is equal to 1 for systems with all bonds equal to the optimal aromatic values. The inspection of the HOMA indexes shows an increase on the aromaticity

values as the models loss the periodicity, and less interaction with their virtual images is observed. Also, a general loss of aromaticity is shown on all doped models when they are compared with the corresponding dedoped models.

It is known that dopant molecules induce important changes on the single and double bond alternation pattern favoring the Kekulé structure, exhibiting a transition from aromatic to quinoid-like structure, and thus, reducing the HOMA aromaticity index.[29,36] Similarly, the HOMA index is affected by the pore defect when the aromaticity index of the two different PEDOT chains contained in the *np*-models, are compared. These correspond to the indexes calculated considering independently the chains that are next to the pore ($HOMA_p$ in Table 3.5.4) and the chains that are out of the pore ($HOMA_c$ in Table 3.5.4). Although it is observed a minimum loss of aromaticity for the *np*-dedoped model, this effect becomes more pronounced for the *np*-doped model with an increase of 2.6 % on the HOMA value.

3.5.4.5 Surface morphological study.

Theoretical calculations discussed in previous sub-sections show important changes in the volume and in the surface area of the nanopores when dedoped (reduced) PEDOT coverts into doped (oxidized). In order to measure experimentally the variation on the porous size with the doping level (*i.e.* oxidation state) a morphological comparison between PEDOT/p^{red} and PEDOT/p^{oxd} films was conducted. Doping level values (*dl*) were obtained by CV on both PEDOT/p^{red} and PEDOT/p^{oxd} films. PEDOT/p^{oxd} film presents a *dl* value of 0.42, close to those observed in most of the polythiophene derivatives,[27] whereas the reduced film shows a *dl* value of 0.06, low enough to be helpful on the pore size comparison among both polymers.

In order to obtain the two films at different *dl*, several steps had to be performed. Initially, a PEDOT sample was obtained by anodic polymerization. Fig. 3.5.7a,

which displays a representative SEM micrograph of such pristine PEDOT film, shows small aggregates connected by dense networks of thin fiber-like structures. Thus, the as prepared PEDOT surface presents a porous morphology, facilitating the dopant ions movement during oxidation and reduction processes. In order to facilitate the measurement of the pore size, the surface porosity was enhanced by immersing the pristine PEDOT film in a NaCl aqueous solution (Fig. 3.5.1b), which resulted in the formation micrometric salt crystals on the film surface. Fig. 3.5.7b shows a representative SEM micrograph of the resulting PEDOT/NaCl film. As it can be seen, NaCl crystals with a regular and parallelepiped-shape grew among already existing conducting polymer clusters, enhancing the size of the surface cavities. Indeed, the porosity enhanced by this methodology only affects the film surface. Further characterization of PEDOT/NaCl films is provided in Fig. 3.5.6, which shows SEM micrographs and EDX spectra of two specific surface film points that allow perfectly differentiating between the salt crystals and the polymer matrix. Although the PEDOT surface initially acts as a template, the crystal growing process causes structural distortions.

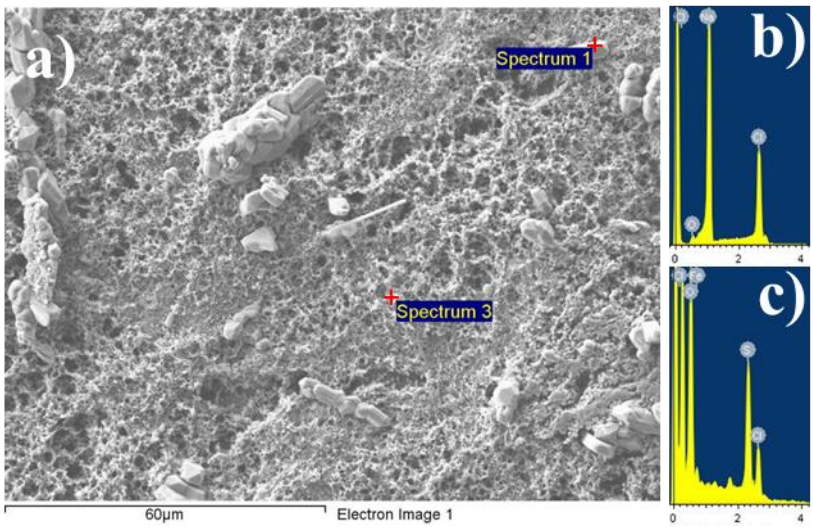

Figure 3.5.6. SEM micrographs of (a) PEDOT/NaCl film, and the energy-dispersive X-ray (EDX) spectra on two different surface points with (b) NaCl crystal predominance and (c) PEDOT predominance.

Microcrystals were rinsed from the surface with water whilst their induced cavity remains (Fig. 3.5.1b), resulting in a bolstered porous PEDOT/p film. Thus, pores from pristine PEDOT converts into a set of larger pores once the NaCl crystals are removed from the surface. The surface porosity enhancement will facilitate doping and dedoping processes. The new pores obtained from rinsed NaCl crystals are located on the surface of PEDOT film with an observed size on the macropore length-scale (Fig. 3.5.7). Since this process is previous to doping level adjustment of each sample, initial film macroporosity won't interfere on the experimental measurement of the final nanopore size that will be done at a lower length-scale.

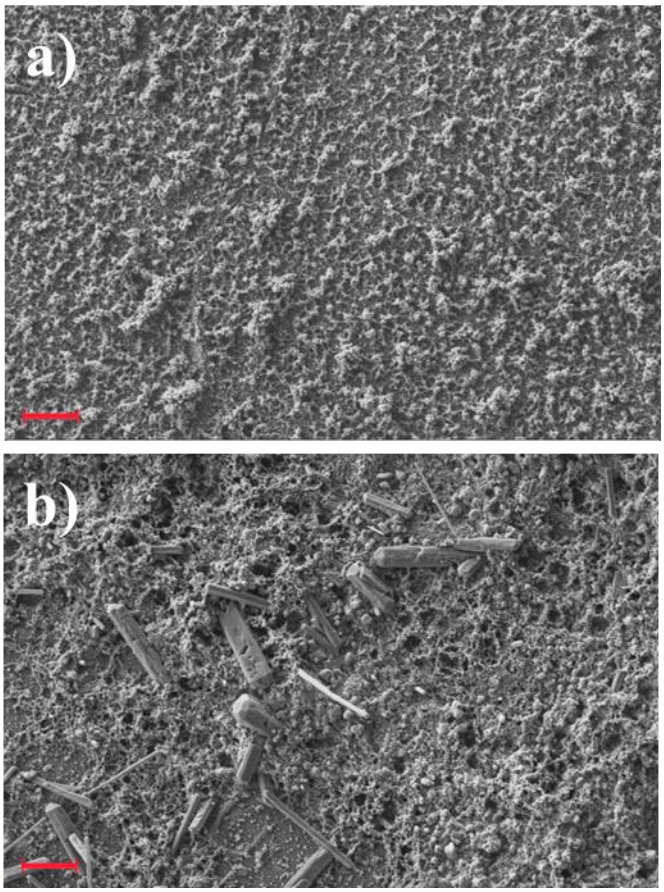

Figure 3.5.7. Representative SEM micrographs of (a) pristine PEDOT and (b) PEDOT/NaCl films (scale bar: 10 μm).

The enhanced porous PEDOT/p film was reduced and oxidized by chronoamperometry at a constant potential of –1.1 and 1.1 V, respectively, to

obtain the PEDOT/p^{red} (dl = 0.06) and PEDOT/p^{oxd} (dl = 0.42) films. Representative SEM micrographs of PEDOT/p^{red} and PEDOT/p^{oxd} films with a magnification of 200,000 are displayed in Figs. 3.5.8a, and 3.5.8b, respectively. Clusters of similar globular structures are observed in both films, even though the pore size is apparently larger for PEDOT/p^{oxd} than for PEDOT/p^{red}. The enhanced porosity of the precursor PEDOT/p film allows faster movements for the dopant ions during the both reduction and oxidation steps. The scape of the ClO_4^- ions from the PEDOT matrix in the reduction process leads to a more compact porous structure than its oxidized form, in which the dopant ions enter into the polymer matrix. The thicknesses and roughness of PEDOT/p^{red} and PEDOT/p^{oxd} has been determined by contact profilometry. The thicknesses of dedoped and doped films are $l \approx 4.8$ and $l \approx 6.3$ μm, respectively, whereas the roughnesses are $R_a \approx 1.0$ and $R_a \approx 2.1$ μm, respectively. It is observed a similar film thickness in both films, although we can still see a different roughness that might show a higher micro-porosity on doped film.

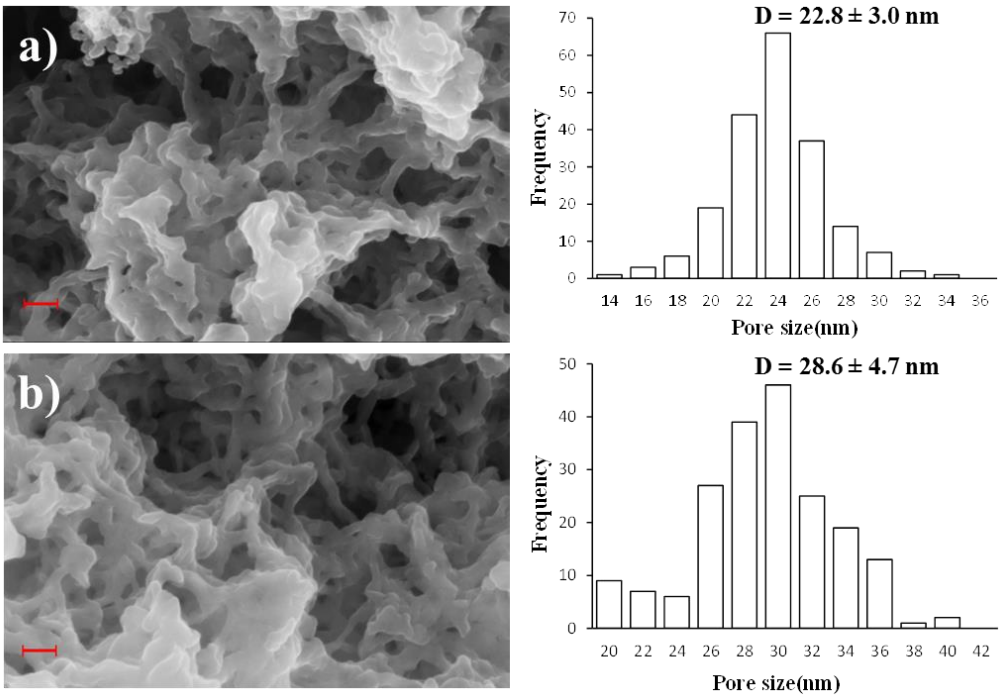

Figure 3.5.8 Representative SEM micrographs (left, magnification: 200k, scale bar: 100 nm) and nanopores size histogram derived from SEM measurements (right) of (a) PEDOT/p^{red} and (b) PEDOT/p^{oxd} films.

FTIR spectra of both PEDOT/p^{oxd} and PEDOT/p^{red} are shown in Fig. 3.5.9a. The comparative analysis presents an IR band at 985 cm^{-1}, which is assigned to C–S bond vibration[47], and the 1420 cm^{-1} band that is assigned to the symmetric stretching of the C=C bond. Within the oxyethylene ring the IR bands at approximately 1087 and 1215 cm^{-1} corresponds to the C–O–C bond stretching[47,48], meanwhile the band at 1369 cm^{-1} is assigned to the CH_2 bending[43]. Furthermore, Raman spectra were taken from both PEDOT/p^{oxd} and PEDOT/p^{red} films (Fig. 3.5.9b). The Raman bands located at approximately 576, 698, 857, 991, and 1561 cm^{-1} are assigned to the C-O-C, C-S-C, O-C-C, oxyethylene ring deformations and CH_2 bending, respectively. Moreover, the band at 1368 and 1434 cm^{-1} are assigned to the C_α-C_β stretching and the C_α=C_β symmetrical bond stretching of the thiophene ring, respectively[49]. Interestingly, a red shift of about 20 and 4 cm^{-1} on the C_α-C_α inter-ring stretching (1271 cm^{-1}) and C_α=C_β antisymmetric stretching (1517 cm^{-1}) of PEDOT/p^{red} are observed, when it is doped. This is due to the PEDOT ability to

change from aromatic-like structure to quinoid-like structure when doped with ClO_4. The π-electrons becomes more delocalized in the quinoid-like structure due to the increase of planarity between two consecutive PEDOT rings, and thus with an increase of the system conductivity [48].

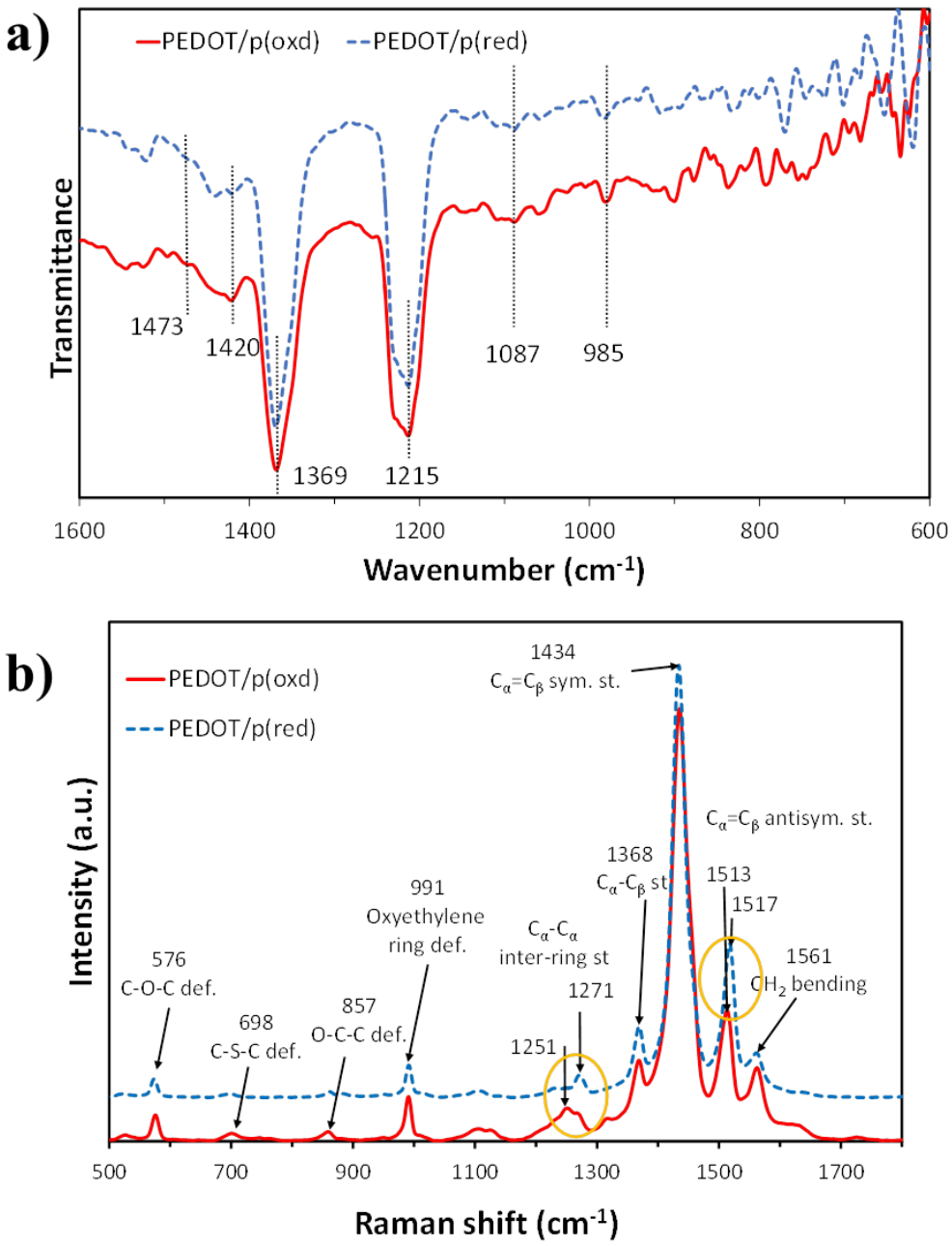

Figure 3.5.9. FTIR spectra (a) and RAMAN spectra (b) of PEDOT/p^{oxd} (red line) and PEDOT/p^{red} (blue dashed line) films.

X-ray diffraction (XRD) patterns of PEDOT powder at different doping levels are shown in Fig. 3.5.10. The diffraction peak at scattering angles (2θ) of 6.20º and 6.14º can be ascribed to the (100) planes of the PEDOT/p^{red} and PEDOT/p^{oxd}, respectively[28]. Thus, the parallel interchain distances (along ***a*** crystal axis, $\boldsymbol{d_R}$) of both samples are very close with values of 14.2 and 14.4 Å, respectively. Comparing with the value of 12.64 Å derived from the theoretical model used in this work (Table 3.5.1) it appears to underestimate the theoretical $\boldsymbol{d_R}$ distances in ~10%, which may lead to a lower threshold on the nanoporous size estimation. The diffraction hump centered about 2θ ≈ 12º corresponds to the Si wafer and the vacuum grease used mounting the XRD samples. From the diffraction patterns, it is observed that both dedoped and doped samples presents a very low crystallinity of ~ 5% that can be evaluated by the relationship between the crystalline peaks area and the total area under the diffraction pattern[50].

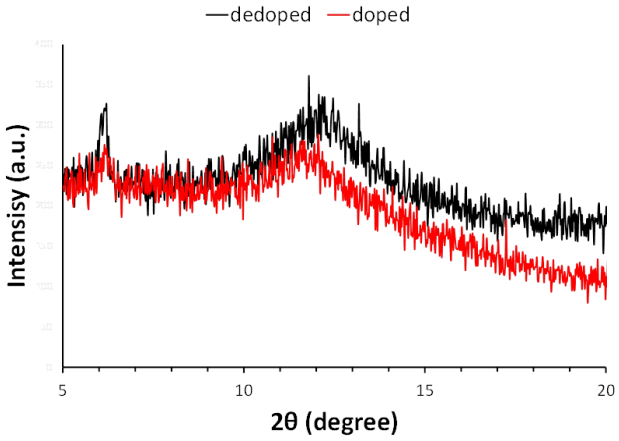

Figure 3.5.10. XRD patterns of PEDOT/p^{red} (dedoped, black line) and PEDOT/p^{oxd} (doped, red line) films.

The density of PEDOT/p^{red} and PEDOT/p^{oxd} has been obtained by means of the flotation method with values of 1.69 and 1.73 g/cm^3, respectively. The PEDOT/p^{red} density is close to the theoretical density calculated by the *b*-dedoped crystal (d=1.57 g/cm^3), however, the PEDOT/p^{oxd} system present a much lower density than that on the *b*-doped theoretical crystal (d=2.13 g/cm^3). Still, before a direct

comparison among theoretical and experimental density values some considerations have to be taken. Synthetized reduced and oxidized PEDOT films are semicrystalline polymers with a low degree of crystallinity (~5%, see above), and consequently, with a higher percentage of amorphous domains. The density of the crystalline domain is typically larger than that on the amorphous domain since the polymer chains are more tightly packed than the amorphous region[51]. Thus, the measured density of PEDOT will be expected to be an intermediate value between both domains. On the other hand, synthetized films present some different doping level that is not equal to the idealized theoretical system. So, after correcting the amount of dopant ions (dl=0.06) the density of *b*-dedoped system is 1.64 g/cm^3, in good agreement with the experimental value. However, the high density value obtained by the *b*-doped system can be explained not only by its doping level difference with the synthetized film (dl = 0.42 instead of 0.50) but for the 10% of error in the length of parameter ***a*** on the crystal unit cell (see above). After correcting both points a theoretical density of ~1.80 g/cm^3 is obtained, which is close to the experimental value.

Three different samples of PEDOT/p^{red} and PEDOT/p^{oxd} were used to measure the average pore size, which was 22.8 ± 3.0 and 28.6 ± 4.7 nm, respectively. Although both theoretical and experimental values points qualitatively to an increment of the pore surface upon oxidation, there is a clear quantitative difference. Thus, the increment of the pore size observed experimentally is 25.2% (56.9% of pore-surface increment) while that derived from theoretical calculations is 15.1% (32.5% of pore-surface increment). Obviously, this difference has been attributed to the different length-scales of theoretical calculations (~ 1.5 nm) and experimental measures (~ 30.0 nm) but also due to the ~10% of error evaluating $\boldsymbol{d_R}$ of *np*-doped system, which after correction will lead to close values (~21% of pore size increment) to those experimentally observed.

Material properties may change dramatically when are reduced to nanoscale dimensions. In fact, from roughly about 100 nm and below, materials break a size barrier below which the quantum effects and electronic energy becomes relevant. Thus, materials on nanoscale can show very different properties compared to what they show on a macroscale. In this work, experimental pores were found and measured on the nanoscale, where the dimension of the nanofibers is similar to the observed nanopores (Fig. 3.5.8) and below 100 nm. Thus, it is expected that quantum effects will have a noticeable importance on the material organization and nanopores formation among the nanochains of PEDOT. Even though there is a factor of ~20 between the theoretical simulated nanopores size and its experimental measurement, theoretical model (at quantum level of calculation) used to study the PEDOT surface chains organization due to the presence of a nano-void becomes a good model to capture all the quantum interactions. However, important phenomena happening during the oxidation-reduction steps, such as the surface-clustering of EDOT fibers, changes in the crystallographic system of the surface, and the ion diffusion in and out from the EDOT-matrix, might influence on the magnification of the porosity observed when the oxidized and reduced surface films are compared at the nanometric scale with the simulated values.

3.5.5 Conclusions

The influence of the oxidation state on the pores size has been studied in PEDOT films using theoretical calculations and experimental measures. *b*-, *s*- and *np*-dedoped and doped models have been simulated under periodical boundary conditions at the DFT level. The *quasi*-monoclicic structure obtained for *b*-dedoped PEDOT evolves towards a triclinic system after doping with ClO_4^- anions. Although the *s*-models of PEDOT keep structures similar to those *b*-models, the volume of *s*-doped is 12.5% higher than that of *s*-dedoped. Besides, *np*-models maintain structural similarities with *s*-models, the incorporation of ClO_4^- dopant anions causing important changes in the supercell dimensions. Moreover, the size of the pore created as a structural defect in the *np*-dedoped model increases by 15.1% in the *np*-doped one (~21 % after a cell parameter correction). The structural tendencies predicted by theoretical calculations have been confirmed by experimental observation. More specifically, the average pore size of PEDOT porous films has been compared after chronoamperometric reduction and oxidation. The averaged pore size of PEDOT/p^{oxd} is 25.2 % larger than that of PEDOT/p^{red}. This important change on the surface porosity of the PEDOT matrix under different oxidation states allows foreseeing important potential applications on the load and release of drugs controlled by the oxidation state of the polymeric matrix.

References

1. Desai, Tejal A., Hansford, Derek J., Kulinsky, Lawrence, Nashat, Amir H., Rasi, Guido, Tu, Jay, Wang, Yuchun, Zhang, Miqin & Ferrari, Mauro. Nanopore Technology for Biomedical Applications. *Biomed. Microdevices* **2**, 11–40 (1999).

2. Hou, Xu. Smart Gating Multi-Scale Pore/Channel-Based Membranes. *Adv. Mater.* **28**, 7049–7064 (2016).

3. Zhang, Huacheng, Tian, Ye & Jiang, Lei. Fundamental studies and practical applications of bio-inspired smart solid-state nanopores and nanochannels. *Nano Today* **11**, 61–81 (2016).

4. Puiggalí-Jou, Anna, Pérez-Madrigal, Maria M., del Valle, Luis J., Armelin, Elaine, Casas, María T., Michaux, Catherine, Perpète, Eric A., Estrany, Francesc & Alemán, Carlos. Confinement of a β-barrel protein in nanoperforated free-standing nanomembranes for ion transport. *Nanoscale* **8**, 16922–16935 (2016).

5. Pérez-Madrigal, Maria M., Armelin, Elaine, Puiggalí, Jordi & Alemán, Carlos. Insulating and semiconducting polymeric free-standing nanomembranes with biomedical applications. *J. Mater. Chem. B* **3**, 5904–5932 (2015).

6. Komachi, Takuya, Sumiyoshi, Hideaki, Inagaki, Yutaka, Takeoka, Shinji, Nagase, Yu & Okamura, Yosuke. Adhesive and robust multilayered poly(lactic acid) nanosheets for hemostatic dressing in liver injury model. *J. Biomed. Mater. Res. B. Appl. Biomater.* **105**, 1747–1757 (2017).

7. Park, Sang Min, Kim, HyeMi, Song, Kwang Hoon, Eom, Seongsu, Park, HyoungJun, Doh, Junsang & Kim, Dong Sung. Ultra-thin, aligned, free-standing nanofiber membranes to recapitulate multi-layered blood vessel/tissue interface for leukocyte infiltration study. *Biomaterials* **169**, 22–34 (2018).

8. Wallace, G. G., Higgins, M. J., Moulton, S. E. & Wang, C. Nanobionics: the impact of nanotechnology on implantable medical bionic devices. *Nanoscale* **4**, 4327–4347 (2012).

9. Guo, Baolin & Ma, Peter X. Conducting Polymers for Tissue Engineering. *Biomacromolecules* **19**, 1764–1782 (2018).

10. Kenry & Liu, Bin. Recent Advances in Biodegradable Conducting Polymers and Their Biomedical Applications. *Biomacromolecules* **19**, 1783–1803 (2018).

11. Lu, Fang-Hsien, Mohamed, Mohamed Gamal, Liu, Tzeng-Feng, Chao, Chuen-Guang & Kuo, Shiao-Wei. A facile cosolvent/chelation method for the preparation of semi-crystalline CuCl2(ethylene glycol)/poly(3-hexylthiophene) complexes displaying specific luminescence properties. *RSC Adv.* **5**, 87723–87729 (2015).

12. Long, Yun-Ze, Li, Meng-Meng, Gu, Changzhi, Wan, Meixiang, Duvail, Jean-Luc, Liu, Zongwen & Fan, Zhiyong. Recent advances in synthesis, physical properties and applications of conducting polymer nanotubes and nanofibers. *Prog. Polym. Sci.* **36**, 1415–1442 (2011).

13. Lu, Fang-Hsien, Chang, Feng-Chih, Mohamed, Mohamed-Gamal, Liu, Tzeng-Feng, Chao, Chuen-Guang & Kuo, Shiao-Wei. Conducting Ag/oligothiophene complex pastes through a simple quenching/chelation method. *J. Mater. Chem. C* **2**, 6111–6118 (2014).

14. Balint, Richard, Cassidy, Nigel J. & Cartmell, Sarah H. Conductive polymers: Towards a smart biomaterial for tissue engineering. *Acta Biomater.* **10**, 2341–2353 (2014).

15. Mohamed, Mohamed Gamal, Cheng, Chih-Chia, Lin, Yung-Chih, Huang, Cheng-Wei, Lu, Fang-Hsien, Chang, Feng-Chih & Kuo, Shiao-Wei. Synthesis and self-assembly of water-soluble polythiophene-graft-poly(ethylene oxide) copolymers. *RSC Adv.* **4**, 21830–21839 (2014).

16. Casanovas, Jordi, Zanuy, David & Alemán, Carlos. Conducting Polymer Actuator Mechanism Based on the Conformational Flexibility of Calix[4]arene. *Angew. Chemie Int. Ed.* **45**, 1103–1105 (2006).

17. Zanuy, David & Alemán, Carlos. Contraction Process of an Electroactive Actuator Based on a One Microsecond Atomistic Molecular Dynamics Simulation. *Chem. – A Eur. J.* **13**, 2695–2700 (2007).

18. Valero, L., Arias-Pardilla, J., Cauich-Rodríguez, J., Smit, M. A. & Otero, T. F. Characterization of the movement of polypyrrole–dodecylbenzenesulfonate–perchlorate/tape artificial muscles. Faradaic control of reactive artificial molecular motors and muscles. *Electrochim. Acta*

56, 3721–3726 (2011).

19. Beregoi, Mihaela, Evanghelidis, Alexandru, Diculescu, Victor C., Iovu, Horia & Enculescu, Ionut. Polypyrrole Actuator Based on Electrospun Microribbons. *ACS Appl. Mater. Interfaces* **9**, 38068–38075 (2017).

20. Jager, E. W., Smela, E. & Inganäs, O. Microfabricating conjugated polymer actuators. *Science* **290**, 1540–1545 (2000).

21. Fuchiwaki, Masaki, Martinez, Jose G. & Otero, Toribio F. Polypyrrole Asymmetric Bilayer Artificial Muscle: Driven Reactions, Cooperative Actuation, and Osmotic Effects. *Adv. Funct. Mater.* **25**, 1535–1541 (2015).

22. Pérez-Madrigal, Maria M., Giannotti, Marina I., del Valle, Luis J., Franco, Lourdes, Armelin, Elaine, Puiggalí, Jordi, Sanz, Fausto & Alemán, Carlos. Thermoplastic Polyurethane:Polythiophene Nanomembranes for Biomedical and Biotechnological Applications. *ACS Appl. Mater. Interfaces* **6**, 9719–9732 (2014).

23. Puiggalí-Jou, Anna, Medina, Judith, del Valle, Luis J. & Alemán, Carlos. Nanoperforations in poly(lactic acid) free-standing nanomembranes to promote interactions with cell filopodia. *Eur. Polym. J.* **75**, 552–564 (2016).

24. Otero, T. F., Martinez, J. G. & Arias-Pardilla, J. Biomimetic electrochemistry from conducting polymers. A review: Artificial muscles, smart membranes, smart drug delivery and computer/neuron interfaces. *Electrochim. Acta* **84**, 112–128 (2012).

25. Otero, Toribio F. Coulovoltammetric and Dynamovoltammetric Responses from Conducting Polymers and Bilayer Muscles as Tools to Identify Reaction-driven Structural Changes. A review. *Electrochim. Acta* **212**, 440–457 (2016).

26. Puiggalí-Jou, Anna, Cejudo, Alberto, del Valle, Luis J. & Alemán, Carlos. Smart Drug Delivery from Electrospun Fibers through Electroresponsive Polymeric Nanoparticles. *ACS Appl. Bio Mater.* **1**, 1594–1605 (2018).

27. Roncali, Jean. Conjugated poly(thiophenes): synthesis, functionalization, and applications. *Chem. Rev.* **92**, 711–738 (1992).

28. Aasmundtveit, K. E., Samuelsen, E. J., Pettersson, L. A. A., Inganäs, O., Johansson, T. & Feidenhans'l, R. Structure of thin films of poly(3,4-ethylenedioxythiophene). *Synth. Met.* **101**, 561–564 (1999).

29. Kim, Eung-Gun & Brédas, Jean-Luc. Electronic Evolution of Poly(3,4-ethylenedioxythiophene) (PEDOT): From the Isolated Chain to the Pristine and Heavily Doped Crystals. *J. Am. Chem. Soc.* **130**, 16880–16889 (2008).

30. Casanovas, Jordi, Zanuy, David & Alemán, Carlos. Distribution of dopant ions around poly(3{,}4-ethylenedioxythiophene) chains: a theoretical study. *Phys. Chem. Chem. Phys.* **19**, 9889–9899 (2017).

31. Bartha, F., Howard, I. A., Geerlings, P., Van Alsenoy, C., Vanderzande, D., Cleij, T. J. & Bogár, F. Density functional crystal orbital study of cyano-substituted poly(para-phenylene-vinylene) and poly(quinoxaline-vinylene). *Int. J. Quantum Chem.* **106**, 1912–1923 (2006).

32. Janesko, Benjamin G. Comparing modern density functionals for conjugated polymer band structures: Screened hybrid, Minnesota, and Rung 3.5 approximations. *J. Chem. Phys.* **134**, (2011).

33. Zade, Sanjio S. & Bendikov, Michael. Twisting of Conjugated Oligomers and Polymers: Case Study of Oligo- and Polythiophene. *Chem. – A Eur. J.* **13**, 3688–3700 (2007).

34. Wong, Bryan M. & Cordaro, Joseph G. Electronic Properties of Vinylene-Linked Heterocyclic Conducting Polymers: Predictive Design and Rational Guidance from DFT Calculations. *J. Phys. Chem. C* **115**, 18333–18341 (2011).

35. Kaloni, Thaneshwor P., Giesbrecht, Patrick K., Schreckenbach, Georg & Freund, Michael S. Polythiophene: From Fundamental Perspectives to Applications. *Chem. Mater.* **29**, 10248–10283 (2017).

36. Shi, Wen, Zhao, Tianqi, Xi, Jinyang, Wang, Dong & Shuai, Zhigang. Unravelling Doping Effects on PEDOT at the Molecular Level: From Geometry to Thermoelectric Transport Properties. *J. Am. Chem. Soc.* **137**, 12929–12938 (2015).

37. Ocampo, Cintia, Oliver, Ramon, Armelin, Elaine, Alemán, Carlos & Estrany, Francesc. Electrochemical Synthesis of Poly(3,4-ethylenedioxythiophene) on Steel Electrodes: Properties and Characterization. *J. Polym. Res.* **13**, 193–200 (2006).

38. Randriamahazaka, H., Noël, V. & Chevrot, C. Nucleation and growth of poly(3,4-ethylenedioxythiophene) in acetonitrile on platinum under

potentiostatic conditions. *J. Electroanal. Chem.* **472**, 103–111 (1999).

39. Soler, José M., Artacho, Emilio, Gale, Julian D., Garc\'\ia, Alberto, Junquera, Javier, Ordejón, Pablo & Sánchez-Portal, Daniel. The {SIESTA} method forab initioorder-Nmaterials simulation. *J. Phys. Condens. Matter* **14**, 2745–2779 (2002).

40. Perdew, John P., Burke, Kieron & Ernzerhof, Matthias. Generalized Gradient Approximation Made Simple. *Phys. Rev. Lett.* **77**, 3865–3868 (1996).

41. Troullier, N. & Martins, José Lu\'\is. Efficient pseudopotentials for plane-wave calculations. *Phys. Rev. B* **43**, 1993–2006 (1991).

42. Monkhorst, Hendrik J. & Pack, James D. Special points for Brillouin-zone integrations. *Phys. Rev. B* **13**, 5188–5192 (1976).

43. Tran-Van, François, Garreau, Sébastien, Louarn, Guy, Froyer, Gérard & Chevrot, Claude. Fully undoped and soluble oligo(3{,}4-ethylenedioxythiophene)s: spectroscopic study and electrochemical characterization. *J. Mater. Chem.* **11**, 1378–1382 (2001).

44. Zhang, Biao, Wang, Kan, Li, Dongde & Cui, Xudong. Doping effects on the thermoelectric properties of pristine poly(3{,}4-ethylenedioxythiophene). *RSC Adv.* **5**, 33885–33891 (2015).

45. Krygowski, Tadeusz Marek. Crystallographic studies of inter- and intramolecular interactions reflected in aromatic character of .pi.-electron systems. *J. Chem. Inf. Comput. Sci.* **33**, 70–78 (1993).

46. Torras, Juan, Bertran, Oscar & Alemán, Carlos. Structural and Electronic Properties of Poly(thiaheterohelicene)s. *J. Phys. Chem. B* **113**, 15196–15203 (2009).

47. Zhao, Qin, Jamal, Ruxangul, Zhang, Li, Wang, Minchao & Abdiryim, Tursun. The structure and properties of PEDOT synthesized by template-free solution method. *Nanoscale Res. Lett.* **9**, 557 (2014).

48. Chutia, P. & Kumar, A. Charge-carrier relaxation dynamics and ac conductivity scaling of poly(3,4-ethylenedioxythiophene) nanoparticles. *Phys. status solidi* **212**, 2727–2737 (2015).

49. Chiu, William W., Travaš-Sejdić, Jadranka, Cooney, Ralph P. &

Bowmaker, Graham A. Studies of dopant effects in poly(3,4-ethylenedi-oxythiophene) using Raman spectroscopy. *J. Raman Spectrosc.* **37**, 1354–1361 (2006).

50. Chandra, Subhash, Annapoorni, S., Singh, Fouran, Sonkawade, R. G., Rana, J. M. S. & Ramola, R. C. Low temperature resistivity study of nanostructured polypyrrole films under electronic excitations. *Nucl. Instruments Methods Phys. Res. Sect. B Beam Interact. with Mater. Atoms* **268**, 62–66 (2010).

51. Kholodovych, V. & Welsh, W. J. Densities Of Amorphous And Crystalline Polymers. in *Physical Properties Of Polymers Handbook* (ed. Mark, J. E.) 612–617 (Springer New York, 2007).

3.6 Self-Healable and Eco-Friendly Hydrogels for Flexible Supercapacitors

3.6.1 Summary

One limitation of wearable electronics, and at the same time a challenge, is the lack of energy storage devices with multiple functionalities produced using clean and environmental-friendly strategies. Here, a multifunctional conductive hydrogel containing poly(3,4-ethylenedioxythiophene) (PEDOT) and alginate was fabricated, to be used as electrodes in supercapacitors, by applying water-mediated self-assembly and polymerization processes at room temperature. The interpenetration of both polymers allowed combining flexibility and self-healing properties within the same hydrogel together with the intrinsic biocompatibility and sustainability of such materials. Initially, PEDOT: polystyrene sulfonate and alginate aqueous solutions were mixed in two different proportions (1:1 and 1:3) and ionically cross-linked with $CaCl_2$. Subsequently, re-interpenetration of poly(hydroxymethyl-3,4-ethylenedioxythiophene) (PHMeDOT) by anodic polymerization in $CaCl_2$ aqueous solution was achieved. Re-interpenetrated 1:3 PEDOT/alginate hydrogels showed excellent capacitance values (35 mF/cm^2) and good capacitance retention. On the other hand, the electrochemical properties were not significantly changed after many cutting/self-healing cycles as was observed by cyclic voltammetry. Therefore, this sustainably produced hydrogel shows promising properties as wearable energy storage devices.

3.6.2 Introduction

Electrochemical capacitors (ECs) are currently considered as advanced devices for applications in electrical vehicles and renewable energy due to their high power density, high rate capability, exceptional durability and reversibility compared to conventional capacitors and Li-ion batteries.[1–6] ECs are classified into two groups: (*i*) electrical double layer capacitors (EDLCs), which store the electric charge using reversible adsorption of ions from the electrolyte onto the electrode surface and (*ii*) redox or pseudo-capacitors, which utilize fast and reversible faradaic reactions occurring at the electrode-electrolyte interface. ECs are commonly fabricated using inorganic/organic hybrid materials, such as metal nanoparticles/nanowires (*e.g.* Ag, Cu), metal oxides (*e.g.* MnO_2, RuO_2), carbon materials (CNT, graphene) dispersed in conductive or non-conductive polymers.[7–11]

On the other hand, in recent years, ECs have become important elements for flexible and wearable electronic devices, which are playing important roles in fields like health monitoring, artificial intelligence, sensory skin or soft robotics. To date, many wearable devices have been successfully developed to monitor, for example, heart beat rate, glucose content in sweat or body temperature,[12–14] all them requiring soft, flexible, lightweight and comfortable energy storage systems. Within this context, ECs based on polymeric systems are particularly attractive since, in addition of the above mentioned properties, polymers can also incorporate new functionalities, such as being biocompatible, conformable, self-healing and sustainable, to fulfil special demands.[15–18] Conducting polymer (CP)-based hydrogels are ideal candidates for use in flexible ECs due to their unique properties such as good electronic properties, tuneable mechanical flexibility, and ease of processing.[19,20] In addition, hydrogel materials may have remarkable biological

characteristics (*e.g.* self-adhesive and anti-microbial activity) for biomedical applications.[21]

While many works are available in the literature about combining conducting and synthetic polymers to form hydrogels for energy storage devices, studies related to the synergistic effect between CPs and biopolymers are scarce yet. For example, lightweight hydrogels based on the macromolecular assembly of CPs with poly-γ-glutamic acid,[15] lignin,[16] or bacterial cellulose [22] have been fabricated. Although these studies only reported on the flexibility, electrochemical properties and energy storage performance of the ECs, no other functionality, such the self-healing capacity, was developed.

In this work, we have developed an all-organic hydrogel forming an interpenetrated network between a CP and a biopolymer to be used as a new flexible, self-healing, biocompatible and eco-friendly electrode for application in ECs. More specifically, we have combined the properties of poly(3,4-ethylenedioxythiophene) (PEDOT) and alginate to prepare hydrogels using a two-step simple and green procedure. Among CPs, PEDOT is an ideal candidate for bioelectronics because of its high ionic and electrical conductivity, environmental and chemical stability (even in biological media), fast doping-dedoping capacity, and good biocompatibility and electrochemical properties.[22–26] Furthermore, the combination of PEDOT with natural polymers, such as polysaccharides, can improve biocompatibility and electrochemical stability in physiological media and confer 3D structural support to the electroactive material.[26–28] Moreover, they form hydrogels in water, reducing the stiffness of the hybrid material to values similar to those in biological tissues. Among the employed polysaccharides, alginate presents special interest because of its processability, biocompatibility, and reversible and easy hydrogel formation by divalent cations. Furthermore, the conductive hydrogel, which has been prepared through a physical crosslink followed by an anodic polymerization both in $CaCl_2$ aqueous solution, avoids the

utilization of organic solvents and chemical cross-linkers that could damage the environment. The self-healing property of the resulting conductive hydrogel is essential for extending the life and durability of the EC, enabling to repair the mechanical damage that it can suffer during use.

3.6.3 Methods

3.6.3.1 Materials

Sodium alginate (Molecular weight, Mw= 240 kDa), PEDOT: PSS suspension (1.3 wt.%), and HMeDOT (95%) were obtained from Sigma Aldrich. Calcium chloride (CaCl2) was purchased from Scharlab. Milli-Q water grade (0.055 S/cm) was used in all solutions and synthetic processes.

3.6.3.2 Synthesis of PEDOT/Alginate and PEDOT/Alginate/PHMeDOT hydrogels

PEDOT/Alginate (PA) hydrogels are rapidly fabricated in a very simple one step process by mixing commercial PEDOT: PSS and sodium alginate and further cross-linking with $CaCl_2$. Thus, suspensions with different PEDOT: PSS/Alginate ratios (1:1 and 1:3) were first prepared by mixing a PEDOT: PSS suspension (1.3 wt.%) with an alginate solution (either 1.3 wt.% or 3.9 wt.%). The dispersion was magnetically stirred during 20 minutes at room temperature to assure a complete homogenization between both components. The dispersions were poured into silicone moulds of $2\times0.4\times$ 0.5 cm^3. After that, the moulds were immersed in a $CaCl_2$ solution (3 wt.%) to cross-link the alginate. The dispersion was let to gel during 24h at room temperature. The resulting hydrogel was washed three times with milli-Q water to remove unreacted compounds.

In order to improve the electrochemical activity of PA hydrogels, PHMeDOT was interpenetrated inside the previously synthesized hydrogel using an anodic polymerization process. For this purpose, three-electrode system was used. Ag|AgCl| 3 $mol\cdot dm^{-3}$ KCl and platinum wire were used as reference and counter electrodes respectively. A PA hydrogel placed onto the ITO (indium thin oxide) side of an ITO-coated polyethylene terephthalate (PET) film was used as working

electrode. The three electrode system was immersed in a 10 mM HMeDOT aqueous solution containing 0.1 M $CaCl_2$ overnight and the solution was magnetically stirred to assure diffusion of the electrolyte within the PA hydrogel. After that, the anodic polymerization of HMeDOT monomer was performed by chronoamperometry at a constant potential (*E*=1.1 V) and different electropolymerization times (30, 60, 90 and 120 min) at room temperature. The resulting PEDOT/Alginate/PHMeDOT has been denoted PAP.

Alginate and PEDOT: PSS hydrogels were also prepared for comparison purposes. Alginate hydrogels were prepared following the protocol previously described for PA hydrogels but without PEDOT: PSS. On the other hand, PEDOT: PSS hydrogels were obtained following the work from Yao *et al.* [29] Briefly, a PEDOT:PSS suspension (1.3 wt.%, Sigma Aldrich) containing 0.1 M H_2SO_4 was placed in the mould and kept at 90ºC for 3h. The resulting hydrogel was further purified by repeatedly washing with deionized water.

3.6.3.3 Morphological, spectroscopic and swelling characterization

Hydrogel surface morphology was evaluated using a Zeiss Neon 40 Analytical Field Emission Scanning Electron Microscope. Samples were first lyophilized and then mounted on a stainless-steel stub. The applied voltage for observation was 5 kV. The diameter of the pores was estimated from SEM images (300 measures) using the software SmartTIFF. The surface porosity was estimated from the threshold black areas of the SEM images (pores) using the software ImageJ. Before image processing, the contrast was adjusted to get strong differences between the pores and the rest of the surface. EDS was performed with the same scanning electron microscope to study the distribution of both PEDOT and alginate polymers within the hydrogel.

Attenuated total reflectance Fourier transform infrared spectroscopy (ATR-FTIR) spectra were obtained with a FTIR 4100 spectrophotometer, equipped with a diamond crystal (Specac model MKII Golden Gate Heated Single Reflection Diamond ATR). The samples were evaluated using spectra manager software. For each sample 3 scans were performed between 4000 and 600 cm^{-1} with a resolution of 4 cm^{-1} at room temperature.

The swelling ratio (SR, in %), which is a good indicative of hydrogel cross-linking degree, will be determined according to Equation E.3.6.1:

$$SR = \frac{W_w - W_d}{W_d} \times 100 \qquad \text{(E.3.6.1)}$$

where W_w is the weight of the hydrogel after being immersed in distilled water for 24 hours and W_d is the weight of the dried hydrogel (*i.e.* after freeze-drying). Three different samples were used to check for reproducibility.

3.6.3.4 Electrochemical characterization

CV and GCD measurements were performed using a microcomputer-controlled potentiostat/galvanostat Autolab with PGSTAT101 equipment and Nova software. A conventional three-electrode cell was used with the conducting hydrogel supported onto an ITO-coated PET sheet as working electrode, Ag|AgCl (KCl, 3M) reference electrode and platinum wire as counter electrode. The electrolyte employed was a 0.1 M $CaCl_2$ solution.

In all CV experiments potential was scanned from 0 to 0.8 V with various scan rates (5-100 mV/s) at room temperature. For GCD experiments, current density was varied from 2 to 20 µA/cm^2. The areal capacitance was calculated from GCD curves recorded in a three-electrode system (Equation E.3.6.2):

$$C = \frac{I\, t_d}{A\, \Delta V} \qquad \text{(E.3.6.2)}$$

where I, is the applied current, t_d is the discharge time, ΔV is the potential window and A the surface area (geometric area) of the hydrogel. Moreover, the coulombic efficiency (η, in %) was also evaluated as the ratio between the charge (t_c) and discharge times (t_d) (Equation E.3.6.3):

$$\eta = \frac{t_d}{t_c} \qquad \text{(E.3.6.3)}$$

EIS diagrams were taken at open circuit (OCP) over the frequency range of 10^4 kHz to 0.1 Hz with potential amplitude of 0.05 V using an AUTOLAB-302N potentiostat/galvanostat. All experiments were performed at room temperature.

3.6.4 Results and discussion

3.6.4.1 Preparation of PEDOT/Alginate (PA) hydrogels

In this study, we have developed flexible and self-healable hydrogels for supercapacitor applications. The hydrogel is formed by the electrostatic interaction of PEDOT with alginate chains following cross-linking of alginate with $CaCl_2$. During this process, the polystyrene sulfonate (PSS) polyanions that stabilized PEDOT molecules in PEDOT:PSS are replaced by alginate chains. Density Functional Theory (DFT) calculations (results not shown) indicate that the PEDOT⋯alginate interaction is favoured over the PEDOT⋯PSS one. The overall procedure for the preparation of the conductive hydrogel-based electrodes is illustrated in Figure 3.6.1. First, PEDOT:PSS/alginate suspensions with two different ratios (1:1 and 1:3) were prepared by mixing a PEDOT:PSS suspension (1.3 wt.%) with a sodium alginate solution (either 1.3 wt.% or 3.9 wt.%). After complete homogenization between both components the dispersions were poured into silicon molds and subsequently immersed in a $CaCl_2$ solution (3 wt.%) to cross-link the alginate and form PEDOT/Alginate (PA) hydrogels. After 24 h gelling, the hydrogels were thoroughly washed to remove the excess of alginate and the leaving PSS chains. In a second step, poly(hydroxymethyl-3,4-ethylenedioxythiophene) (PHMeDOT) was interpenetrated into the previous PA hydrogels, by *in situ* electropolymerization of hydroxymethyl-3,4-ethylenedioxythiophene (HMeDOT) was electropolymerized into the previous PA hydrogels, to prepare the PEDOT/Alginate/ PHMeDOT (PAP) hydrogels.

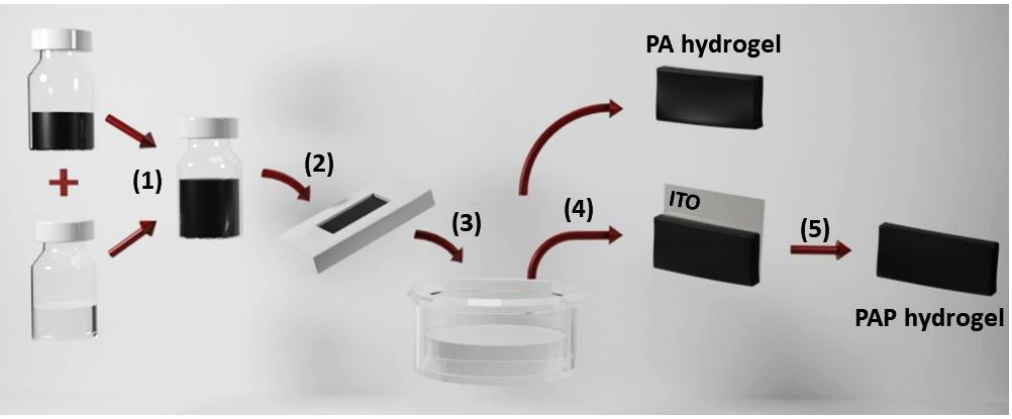

Figure 3.6.1. Scheme of the synthesis steps to fabricate PA and PAP hydrogels. (1) Mixing PEDOT:PSS and sodium alginate solutions. (2) Pouring the solution in a silicone mould. (3) Cross-linking the mixture in $CaCl_2$ solution. (4) Placement of PA hydrogels onto ITO (indium thin oxide)-coated PET electrodes. (5) Electropolymerization of HMeDOT to get PAP hydrogels.

3.6.4.2 Morphological and spectroscopic analysis. Swelling ratio.

Representative scanning electron microscopy (SEM) cross-section micrographs of lyophilized 1:1 and 1:3 PA hydrogels, which are shown Figure 3.6.2a-3.6.2b, prove the development of open and interconnected porous structures. This open structure is expected to be beneficial for the studied application, enabling the fast movement and easy access of the electrolyte to the hydrogel surface, favoring charge-discharge processes and, therefore, higher energy storage capability. Moreover, the hydrogels appear to be homogeneous along the cross-section, which suggests a good entanglement and dispersion between both polymers. Energy dispersive spectroscopy (EDS) analyses allowed corroborating the homogeneous distribution of PEDOT and alginate as signals from both polymers (sulfur for PEDOT and calcium for alginate) are detected along the hydrogel cross-section.

However, one remarkable difference between 1:1 and 1:3 PA hydrogels is the pore size. As observed in the SEM images, larger pores evolved as alginate content in the hydrogel was increased. The pore size for the 1:1 and 1:3 hydrogels showed a unimodal distribution (Figure 3.6.2a-3.6.2b), the average value being 10

± 3 µm and 70 ± 11 µm, respectively. Such increase has been attributed to the higher content of alginate within the hydrogel. Thus, the higher the alginate content, the higher the cross-linking degree and therefore a higher rigidity is obtained hindering a compact folding of the polymeric chains. The result is a bigger pore size in the 1:3 PA hydrogel. The surface porosity, which was estimated using image processing, was larger for the 1:1 PA than for the 1:3 PA (*i.e.* 60% vs 43%).

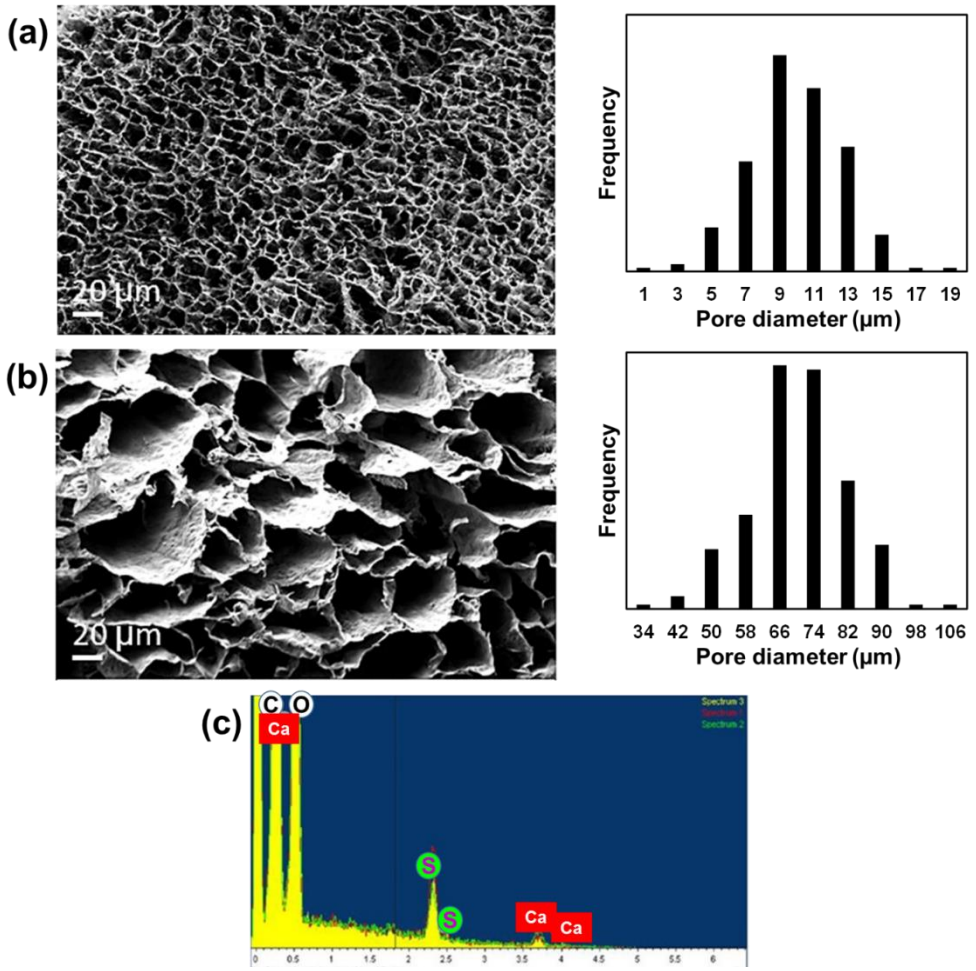

Figure 3.6.2. Cross-section SEM images of (a) 1:1 and (b) 1:3 PA hydrogels. The pore size distribution is displayed at the right. (c) EDS spectrum of the hydrogels showing S and Ca peaks for PEDOT:PSS and alginate, respectively.

The swelling ratio (SR%) of the 1:1 and 1:3 PA hydrogels was also determined as a good indication of the cross-linking degree. We observed that the SR% of 1:1 hydrogel (6405 ± 132 %) was significantly higher than that for the 1:3 hydrogel (3708 ± 107 %) which is attributed to the different content of alginate. Again, the

higher the alginate content, the higher the cross-linking degree and, therefore, the higher the stiffness resulting in a lower amount of absorbed water. Such structural characteristics may have an impact on the electrochemical properties of the hydrogel, as the pore size but also the swelling ratio may vary the surface area available for energy storage. Based on the pore size results, we could hypothesize that the 1:1 PA hydrogel will have better electrochemical energy storage capabilities than 1:3 PA hydrogels since the former provides a higher specific surface area (smaller pore size). This in turn will provide more accessible electroactive ions to the hydrogel surface and, therefore, more charge storage. However, if we considered the SR%, the pore size difference will be reduced since the SR% is much bigger for the 1:1 PA than for the 1:3 PA. This means that the pore size difference between both hydrogels in the hydrated state is reduced compared to the lyophilized state.

FTIR spectroscopy was also used to detect the presence of both polymers**.** Figure 3.6.3 shows the spectra of pure alginate and pure PEDOT:PSS as well as those of 1:1 and 1:3 PA hydrogels. Alginate shows characteristic peaks denoting asymmetric and symmetric stretching vibrations of COO groups at 1598 $cm^{-1}$and 1419 cm^{-1}respectively; and the C–O stretching vibration mode at 1028 cm^{-1}.[30] Meanwhile, PEDOT:PSS shows characteristic peaks at 1564 $cm^{-1}$for the C=C stretching of the thiophene ring, 1270 and 1122 cm^{-1} for the C–C vibrations of the fused dioxane ring, and 862cm^{-1} for the C–S stretching of the thiophene ring in PEDOT. Moreover, the peaks at 1162 and 1060 cm^{-1} have been attributed to the S–O and S-phenyl vibration of PSS chains, respectively.[31] The PA hydrogel spectrum shows the characteristic peaks of both alginate and PEDOT. The same spectra were recorded in different points of the hydrogel confirming the homogeneous distribution of both polymers within it. These results are in agreement with those shown by EDS. Moreover, the shift of the main peaks of alginate and PEDOT in the hydrogel indicates the good interaction between both

polymers. In addition, the decrease in the intensity of the PSS peaks indicated the partial replacement of alginate, as predicted by DFT calculations. Finally, comparing the 1:1 and 1:3 PA hydrogel spectra we observed that the intensity of the PEDOT peaks increased as the content into the hydrogel was higher, as expected.

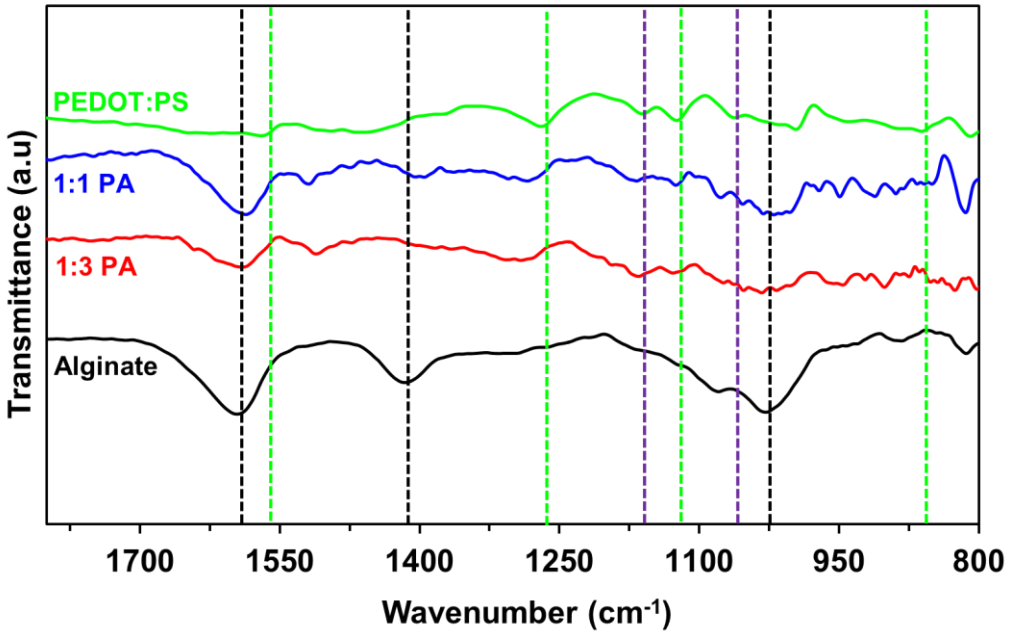

Figure 3.6.3. FTIR spectra of pure alginate and PEDOT:PSS as well as 1:1 and 1:3 PA hydrogels. Dashed black, green and violet lines correspond to the characteristic peaks of alginate, PEDOT and PSS, respectively.

3.6.4.3 Electrochemical characterization

Figure 3.6.4a shows the cyclic voltammetry (CV) curves of the 1:1 and 1:3 PA hydrogels. From a qualitatively point of view, both voltammograms are similar. They are non-quasi rectangular and symmetric in shape without redox peaks, which indicate the typical behavior of pseudocapacitive materials as well as good reversibility during the energy storage process, respectively.[8,32] Another two remarkable characteristics of such CV curves are: (*i*) they are deviated from ideal voltammetric curves (perfectly horizontal); and (*ii*) the recorded current is very low.

Both characteristics have been attributed to the low amount of PEDOT within the hydrogel.

The energy storage ability of a pseudocapacitive material depends on the electrolyte insertion/de-insertion into it, which is a diffusion-controlled process. Therefore, such process will be affected by the potential scan rate. As it can be observed in Figure 3.6.4b, the voltammograms are less ideal and deviate more from the horizontal when the scan rate increases from 50 to 200 mV/s. This behavior reflects that the higher the scan rate is, the lower the number of ions that successfully approach and interact with the hydrogel, since diffusion is limited. On the other hand, the low electrical conductivity of the PA hydrogels could also explain the angling of the voltammograms away from the ideal rectangular shape.[8] It is also worthy to mention that all the curves are symmetric, independently of the scan rate, indicating good reversibility even at the higher rates. Despite the similarities between the voltammograms of both hydrogels, the area enclosed within the CV curve is slightly higher for 1:1 PA than for 1:3 PA. This has been attributed not only to the higher amount of the pseudocapacitive PEDOT but also to the difference in the surface area (smaller pore size) in the 1:1 hydrogel.

Galvanostatic charge-discharge (GCD) experiments were performed to quantitatively evaluate the specific capacitance of the PA hydrogels (Figure 3.6.4c). GCD curves are slightly asymmetrical because the presence of the pseudocapacitive materials, as previously discussed. [33] Comparing both hydrogels, we can observe that the specific capacitance is higher for the 1:1 hydrogel (0.11 mF/cm^2) than for the 1:3 (0.025 mF/cm^2) due to the higher amount of the pseudocapacitive PEDOT and surface area. These results are in agreement with those obtained by cyclic voltammetry. GCD experiments were also performed at different current densities (Figure 3.6.4d). As expected, the higher the current density, the lower the capacitance. However, even when the current density increased by a factor of 10, around 70% of the initial capacitance was retained,

indicating a good rate capability of the hydrogel.[34] Moreover and despite the slight asymmetry in the GCD curves, the coulombic efficiency is reasonable (around 75%).

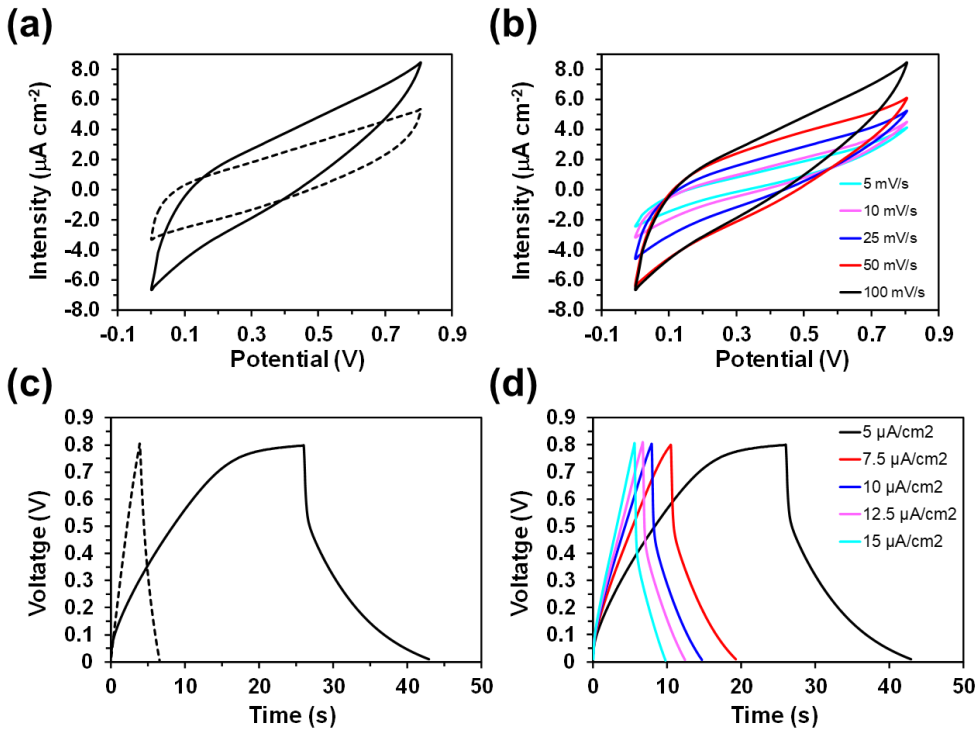

Figure 3.6.4. (a) Cyclic voltammograms of 1:1 (solid line) and 1:3 (dashed line) PA hydrogels at 100 mV/s. (B) Cyclic voltammetries of 1:1 PA hydrogels at different scan rates. (C) Galvanostatic charge-discharge curves of 1:1 (continuous line) and 1:3 (dashed line) PA hydrogels at 5 µA/cm^2. (D) Galvanostatic charge-discharge curves of 1:1 PA hydrogel at different applied current densities.

The resistance of the 1:1 and 1:3 PA hydrogels was determined using electrochemical impedance spectroscopy (EIS). Accordingly, the impedance was measured for frequencies ranging from 0.1 to 10^4 Hz using an electrochemical cell filled with 10 mL of 0.1 M $CaCl_2$. Results are illustrated in Figure 3.6.5 for the 1:1 PA, which contains the highest proportion of CP and exhibits lower resistance than 1:3 PA. Figure 3.6.5a displays the collected impedance as Nyquist plot, which consist in a capacitive semicircle in the high-frequency range and a straight ascending line in the low-frequency range. EIS data were fitted to the electric equivalent circuit (EEC) displayed in Figure 3.6.5b. The quality of the experimental data fitting to EEC was evaluated to estimate the percentage error associated with

each circuit element, being comprised between 0.4% and 5.9%. The R_S corresponds to the electrolyte resistance, which means the resistance of the solution inside the hydrogel pores, and depends on the ionic concentration, type of ions, temperature and the geometry of the area in which the current is carried (*i.e.* hydrogel pore area). In this work all hydrogels were prepared using a 0.1 M $CaCl_2$ solution, which explains its low resistance (108.6 Ω). The diameter of the semicircle corresponds to the charge transfer resistance (R_P) of the hydrogel. The value of R_P, 62.9 kΩ, captures both the intrinsic semi-conducting behavior of PEDOT-rich domains and insulating nature of alginate-rich domains.

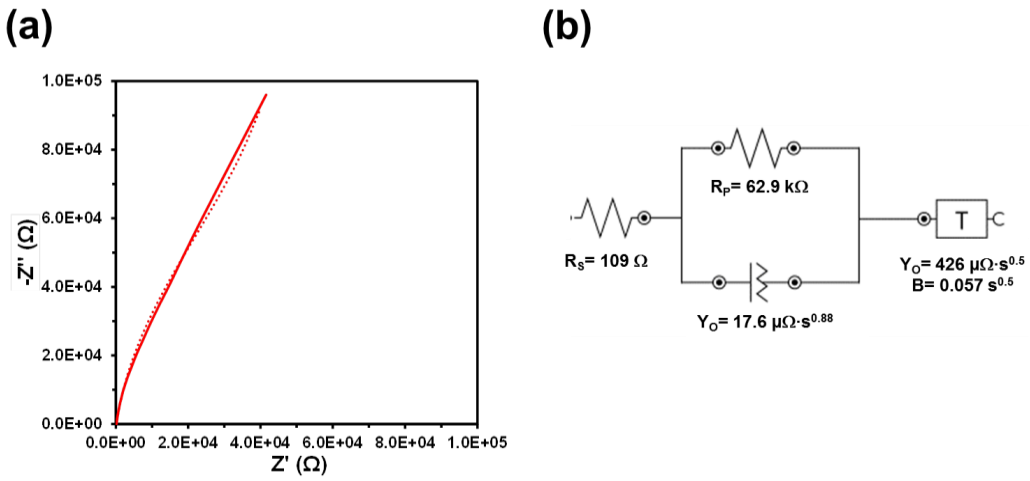

Figure 3.6.5. (a) Measured and fitted Nyquist plot (solid red line and dashed black line, respectively) for the 1:1 PA hydrogel. (d) EEC model used for numerical fitting of the EIS data. Numerical results from fitting the spectra are displayed for all the elements of EEC.

The capacitance values determined for both hydrogels are very low from a practical perspective. Therefore, both PA hydrogels were modified by incorporating PHMeDOT through *in situ* polymerization to improve their energy storage properties. This green polymerization process was performed using a simple 0.1 M $CaCl_2$ aqueous solution as electrolytic reaction medium. The HMeDOT monomer was selected because it is a water soluble EDOT derivative due to the exocyclic hydroxymethyl group present in its structure but also because the capacitance of PEDOT and PHMeDOT are very similar [15].

3.6.4.4 Improvement of hydrogels performance

PHMeDOT was anodically polymerized within the 1:1 PA hydrogel to improve its energy storage performance. In order to analyze the influence of the polymerization time on the morphology and electrochemical properties of the resulting 1:1 PAP hydrogels and chose the best electropolymerization conditions, four different electropolymerization times (*i.e.* 30, 60, 90 and 120 min) were considered. SEM analysis revealed the open structure with interconnected pores, as it was previously shown for the PA hydrogels, but partially covered with the newly electropolymerized PHMeDOT layer (Figure 3.6.6). This led to a reduction in the surface porosity. For example, the surface porosity of 1:1 PA hydrogel decreased from 60% to 54% after apply an electropolymerization time of 60 min. Also, it was observed that the higher the electropolymerization time, the higher the amount of PHMeDOT inside the hydrogel.

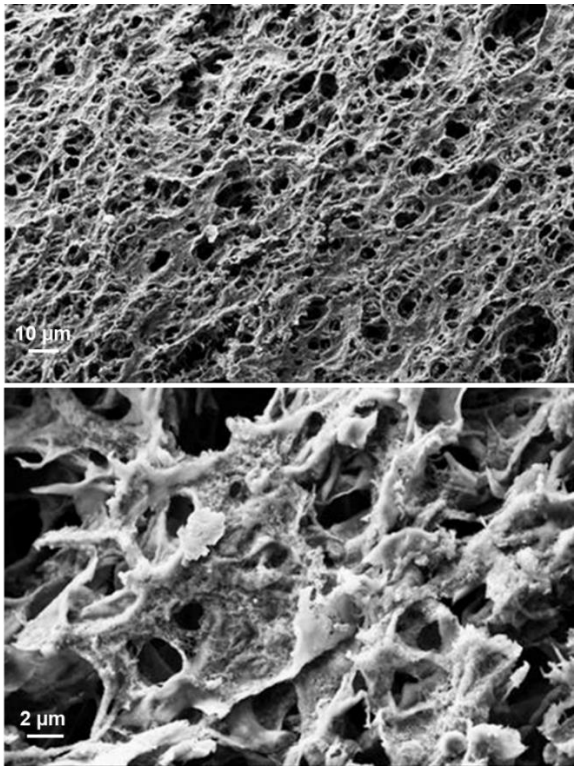

Figure 3.6.6. Cross-section SEM images of 1:1 PAP hydrogel obtained by applying an electropolymerization time of 60 min.

CV was used to qualitatively assess the effect of the electropolymerization time on the energy storage capability of 1:1 PAP hydrogels (Figure 3.6.7a). It is worth noting that the recorded intensity is two orders of magnitude higher than that obtained in 1:1 PA, which clearly reflects the successful incorporation of PHMeDOT. On the other hand, the voltammograms obtained for different electropolymerization times exhibit the same shape (*i.e.* non-quasi rectangular and symmetrical), even though they show different enclosed areas. The area increases with the electropolymerization time up to 60 min and, after that, the CV area decreases again. This trend has been attributed to changes in the organization of the pseudocapacitive PHMeDOT chains. Thus, the capacitance increases with the content of the PHMeDOT during the first 60 minutes of electropolymerization. However, longer deposition times cause the blocking of the interconnected pores by the newly formed polymer, reducing the effective surface area where the ion insertion/de-insertion takes place and leading to a reduction in the capacitance. Thus, a 60 min polymerization (associated charge of 69 mC/cm^2) yielded the highest area in the voltammogram, meaning that it is the optimum time to have hydrogels with the best electrochemical properties. On the other hand, as the content of the conducting polymer increases with time, the CV angles down as a consequence of an increase in the electrical conductivity of the hydrogel. This result is consistent with those previously discussed.

Based on the previous results, galvanostatic charge discharge experiments were performed on the 60 min electropolymerized hydrogel (Figure 3.6.7b). The most remarkable characteristic of the GCD curve is that the discharge time, and therefore the capacitance, is much higher than before electropolymerization. The calculated capacitance of the 1:1 PAP hydrogel is 10.2 ± 2.5 mF/cm^2. This value is more than 90 times the areal capacitance of 1:1 PA, reflecting a remarkable energy storage capacity of the hydrogel after electropolymerization in aqueous solution.

GCD curves display again a quasi-triangular shape with a slight curvature due to the pseudocapacitive behavior of PEDOT and PHMeDOT.

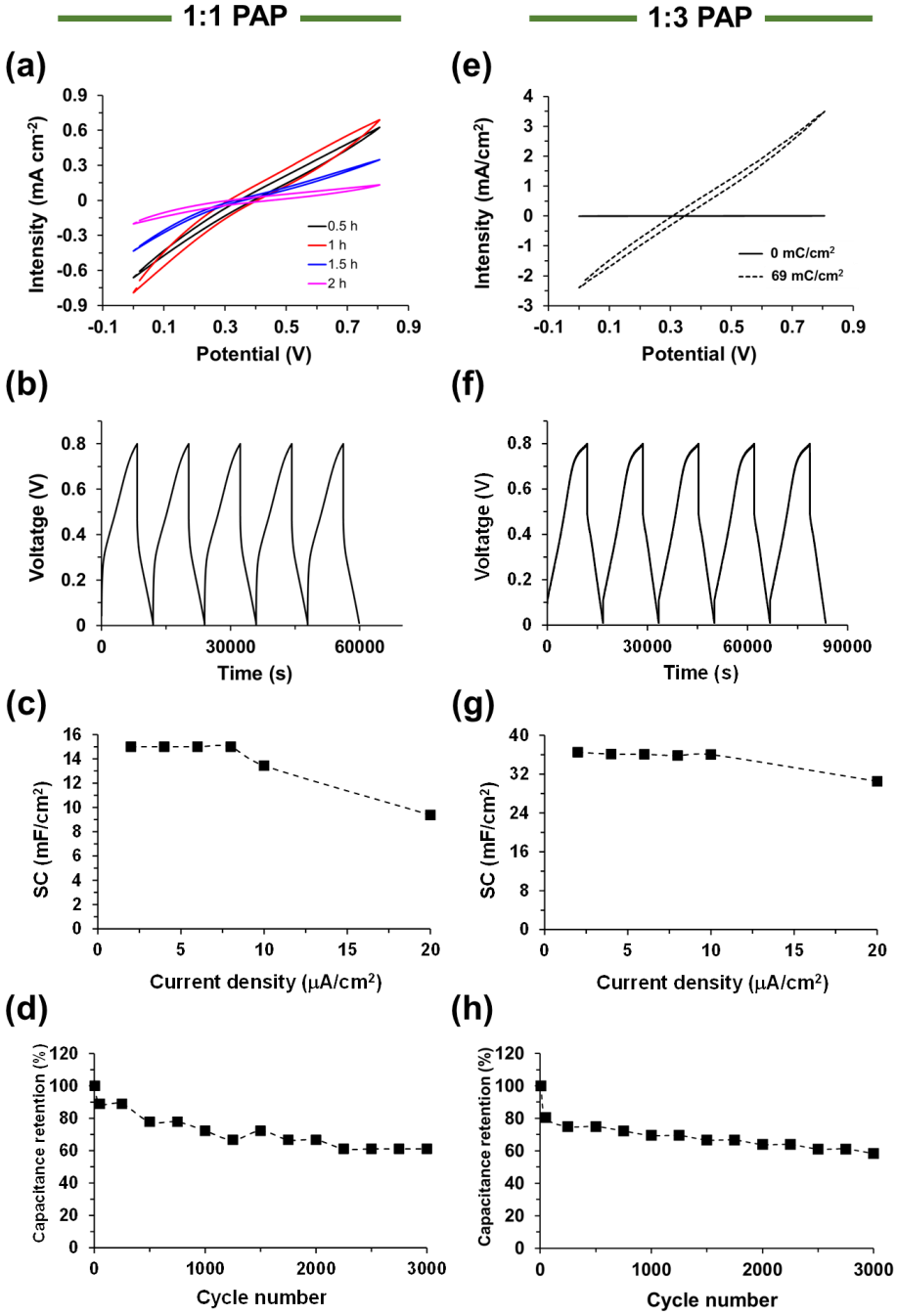

Figure 3.6.7. (a) Cyclic voltammograms for the 1:1 PAP hydrogels after different times of electropolymerization. (b) GCD curves for the 1:1 PAP hydrogel (t = 60 min) at a current density of 6 μA/cm^2. (c) Variation of the specific capacitance with the applied current density for the 1:1 PAP hydrogel (t = 60 min). (d) Stability performance of 1:1 PAP hydrogel over 3000 cycles. (e) Cyclic voltammograms for the 1:3 PAP after electropolymerization of PHMeDOT (69 mC/cm^2). (f) GCD curves for the 1:3 PAP hydrogel at a current density of 6 μA/cm^2. (g) Variation of the specific capacitance with the applied current density for the 1:3 PAP hydrogel. (h) Stability performance of 1:3 PAP hydrogel over 3000 cycles.

GCD experiments were also performed at various current densities (Figure 3.6.7c). Initially, the specific capacitance was kept constant when the applied current density was in the range 2 mA/cm^2 – 10 mA/cm^2. This indicates that ions can easily diffuse and reach the hydrogel surface area in the whole current density interval, which has been attributed to the open structure previously observed by SEM. However, capacitance decreases when current density was 20 mA/cm^2 as diffusion is being impeded. Despite the reduction in capacitance, around 63 % of the initial capacitance was retained even when the current density was increased by a factor of 20, indicating a good rate capability for the 1:1 PAP hydrogel.

After that, PHMeDOT was anodically polymerized within the 1:3 PA hydrogel. Based on the previous results for 1:1 PAP hydrogel, where the capacitance peaked when the electropolymerization charge was 69 mC/cm^2 (time = 60 min), we decided to electropolymerize the same charge within the 1:3 PA hydrogel. CV was run to evaluate the influence of PHMeDOT (Figure 3.6.7e). A remarkable increase in the intensity (300 times) was observed in comparison to the non-electropolymerized hydrogel samples, indicating again that PHMeDOT was successfully incorporated. Moreover, the recorded intensity was 3 times higher than that recorded for the 1:1 PAP hydrogel. To confirm all these results, GCD experiments were subsequently performed (Figure 3.6.7f). Results indicate the discharge time is greatly improved not only compared to the non-electropolymerized hydrogel but also compared to the 1:1 PAP hydrogel.

The calculated capacitance is 35 ± 2 mF/cm^2, which is more than 1000 times the capacitance of the 1:3 PA hydrogel and 3 times higher than that for the 1:1 PAP hydrogel. The difference between 1:1 and 1:3 PAP hydrogels can be explained as follows: PHMeDOT blocks the channels of the hydrogel due to the smaller pore size of the 1:1 PA hydrogel. However, we did not observe the same when electropolymerizing into the 1:3 PA hydrogels, where the pores were bigger. Therefore, PHMeDOT was electropolymerized onto the hydrogel surface within the

channels. Thus, the accessible surface area in the 1:3 PAP is higher than that in the 1:1 PAP one, leading to a higher specific capacitance. GCD curves also display a quasi-triangular shape with a slight curvature due to again the pseudocapacitive behavior of PEDOT and PHMeDOT.

The dependence of the capacitance on the applied current density was also evaluated for the 1:3 PAP hydrogel (Figure 3.6.7g). The specific capacitance is constant in the current density range from 2 mA/cm^2 to 10 mA/cm^2, indicating an easy ionic diffusion towards the hydrogel surface. Beyond this range, we observed a decrease in the capacitance as diffusion is being impeded. In spite of the reduction in capacitance, a good rate capability of the 1:3 PAP hydrogel is measured as around 80 % of the initial capacitance is retained even when the current density was increased by a factor of 20.

The capacitance values obtained are of the same order of magnitude than those reported for similar all organic PEDOT-based hydrogels (*e.g.* 4.7 and 32 mF/cm^2 for PEDOT:PSS and PEDOT:PSS/cellulose),[35,36] and even those obtained for PEDOT-based hydrogels containing inorganic nanomaterials (*e.g.* 25 and 38 mF/cm^2 for PEDOT/reduced graphene oxide and PANI/CNT hydrogels),[37] reflecting the good electrochemical behaviour of the PAP hydrogels.

Cycling performance is another key factor for practical applications. Figures 3.6.6d and 3.6.6h compare the performance of the 1:1 and 1:3 PAP hydrogels over 3000 charge-discharge cycles, exhibiting retention values of 61 ± 4 % and 58 ± 3 %, respectively. The efficiency in our study is slightly smaller than those published for CP-biopolymer hydrogels.[15] In further studies we will explore if we can improve life cycle stability of the hydrogels by coating or incorporating polypyrrole (PPy) as has been recently reported.[8] The influence of electrochemical cycling in the morphology of 1:1 PAP is reflected in Figure 3.6.8, which shows representative SEM micrographs of the such hydrogel after 3000 charge-discharge

cycles. Comparison with the micrographs displayed in Figure 3.6.6 reveals morphological changes that have been associated to an enhancement of the compactness. Thus, the hydrogel structure becomes more compact and less porous, the changes induced by GCD cycles leading to a reduction of both the pore size and the pore distribution. Indeed, the surface porosity decreased from 54% to 28% after 3000 GCD cycles. Furthermore, electropolymerized PHMeDOT also undergoes significant structural changes. Thus, the superficial CP clusters tend to collapse, reducing the porosity of the whole 1:3 PAP sample.

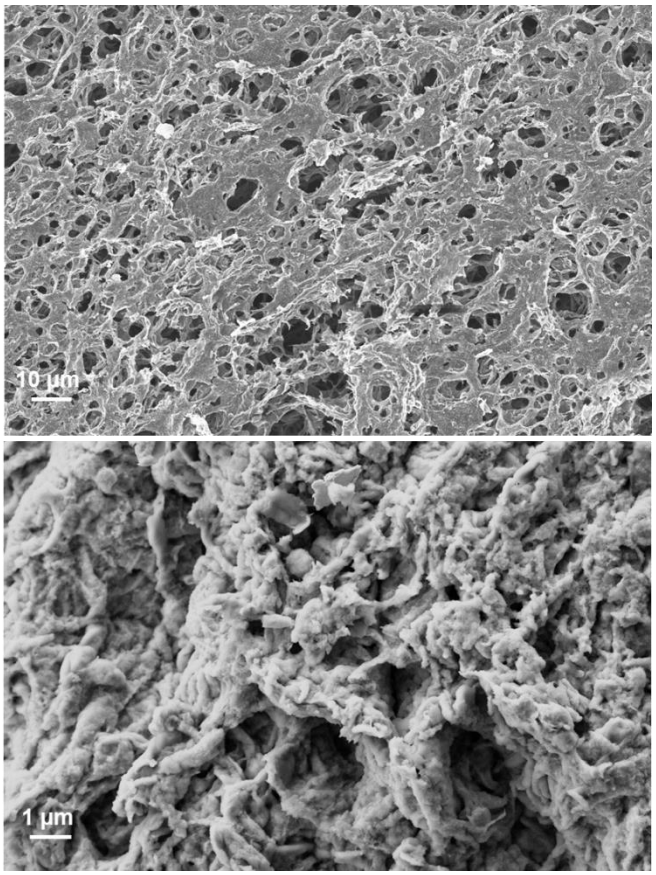

Figure 3.6.8. Cross-section SEM images of 1:1 PAP hydrogel after applying 3000 GCD cycles.

3.6.4.5 Self-healing of the PAP hydrogels

The developed hydrogel shows self-healing capacity as an additional functionality other than flexibility, biocompatibility and eco-friendliness. Self-healing was first assessed by cutting the hydrogel and contacting both parts again

to enable the self-healing process. After 10 min, the two pieces were completely self-healed and the entire hydrogel could be lifted (Figure 3.6.9a).

To go further, the electrochemical performance of the PAP hydrogels was evaluated by cyclic voltammetry after several cutting/healing cycles (Figure 3.6.9b). As it can be observed, all CV's are comparatively the same in terms of shape and intensity, which indicates that the hydrogel recovers its performance after each cutting/healing cycle (at least during the 10 cycles evaluated). The small differences observed in intensity can be attributed to small changes in the roughness and therefore in the area (*i.e.* the geometrical area is considered to calculate the current density). The self-healing ability of the hydrogel is probably associated to the diffusion of Ca^{2+} ions into the damage area through the open and interconnected structure of the hydrogel allowing again the cross-linking between alginate chains located in both pieces. It is important to highlight the fast self-healing capacity of the hydrogel. Only a few minutes after damage, the hydrogel recovers its structural integrity and functional properties probably due to the rapid diffusion of calcium ions into the damaged surface. No significant differences were observed between the 1:1 and 1:3 PAP hydrogels.

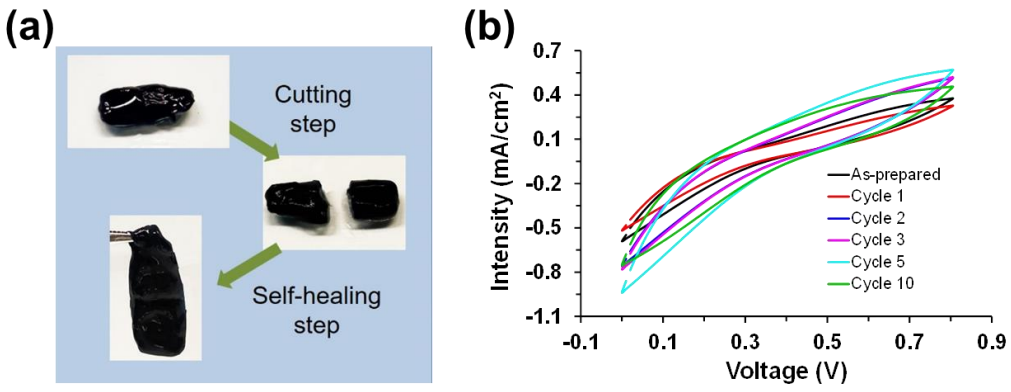

Figure 3.6.9. (a) Images showing the cutting/self-healing process. The self-healed hydrogel can hold its own weight. (b) Cyclic voltammograms for different cutting/healing cycles. Scan rate: 50 mV/s.

3.6.5 Conclusion

In summary, we have successfully developed PEDOT/Alginate/PHMeDOT (PAP) hydrogels by a simple water-based two-step process to get flexible and self-healable electrodes for supercapacitor applications. Initially, PEDOT:PSS/Alginate hydrogels in two different ratios 1:1 and 1:3 were obtained by simply mixing both components and cross-linking it in a $CaCl_2$ aqueous solution. These composite hydrogels, characterized by a porous and open interconnected structure, exhibited very low capacitance values (lower than 0.11 mF/cm^2). In a second step, PHMeDOT was incorporated into the previous hydrogels by *in situ* electropolymerization using the same electrolyte solution. The resulting composite hydrogels exhibited high capacitance values (35 mF/cm^2). Finally, the prepared hydrogels show a fast self-healing capacity without losing their electrochemical performance at least during 10 cutting/healing cycles. Thus, the combination of flexibility and self-healing together with the inherent properties of biocompatibility and eco-friendliness of the PEDOT:PSS and alginate polymers makes the obtained hydrogels promising for applications in wearable and implantable electronics.

References

1. González, Ander, Goikolea, Eider, Barrena, Jon Andoni & Mysyk, Roman. Review on supercapacitors: Technologies and materials. *Renew. Sustain. Energy Rev.* **58**, 1189–1206 (2016).

2. Shi, Xiaoyu, Pei, Songfeng, Zhou, Feng, Ren, Wencai, Cheng, Hui-Ming, Wu, Zhong-Shuai & Bao, Xinhe. Ultrahigh-voltage integrated micro-supercapacitors with designable shapes and superior flexibility. *Energy Environ. Sci.* **12**, 1534–1541 (2019).

3. Salanne, M., Rotenberg, B., Naoi, K., Kaneko, K., Taberna, P. L., Grey, C. P., Dunn, B. & Simon, P. Efficient storage mechanisms for building better supercapacitors. *Nat. Energy* **1**, 16070 (2016).

4. Dong, Xiaomei, Jin, Huile, Wang, Rongyue, Zhang, Jingjing, Feng, Xin, Yan, Chengzhan, Chen, Suqin, Wang, Shun, Wang, Jichang & Lu, Jun. High Volumetric Capacitance, Ultralong Life Supercapacitors Enabled by Waxberry-Derived Hierarchical Porous Carbon Materials. *Adv. Energy Mater.* **8**, 1702695 (2018).

5. Lv, Tian, Liu, Mingxian, Zhu, Dazhang, Gan, Lihua & Chen, Tao. Nanocarbon-Based Materials for Flexible All-Solid-State Supercapacitors. *Adv. Mater.* **30**, e1705489 (2018).

6. Kumaravel, Vignesh, Bartlett, John & Pillai, Suresh C. Solid Electrolytes for High-Temperature Stable Batteries and Supercapacitors. *Adv. Energy Mater.* **11**, 2002869 (2021).

7. Khattak, Abdul Muqsit, Yin, Huajie, Ghazi, Zahid Ali, Liang, Bin, Iqbal, Azhar, Khan, Niaz Ali, Gao, Yan, Li, Lianshan & Tang, Zhiyong. Three dimensional iron oxide/graphene aerogel hybrids as all-solid-state flexible supercapacitor electrodes. *RSC Adv.* **6**, 58994–59000 (2016).

8. Garcia-Torres, Jose & Crean, Carol. Multilayered Flexible Fibers with High Performance for Wearable Supercapacitor Applications. *Adv. Sustain. Syst.* **2**, 1700143 (2018).

9. Garcia-Torres, Jose, Roberts, Alexander J., Slade, Robert C. T. & Crean, Carol. One-step wet-spinning process of CB/CNT/MnO2 nanotubes hybrid flexible fibres as electrodes for wearable supercapacitors. *Electrochim. Acta* **296**, 481–490 (2019).

10. Liu, Zhiqiang, Liu, Ying, Zhong, Yuxue, Cui, Liang, Yang, Wenrong, Razal, Joselito M., Barrow, Colin J. & Liu, Jingquan. Facile construction of MgCo2O4@CoFe layered double hydroxide core-shell nanocomposites on nickel foam for high-performance asymmetric supercapacitors. *J. Power Sources* **484**, 229288 (2021).

11. Gao, Libo, Surjadi, James Utama, Cao, Ke, Zhang, Hongti, Li, Peifeng, Xu, Shang, Jiang, Chenchen, Song, Jian, Sun, Dong & Lu, Yang. Flexible Fiber-Shaped Supercapacitor Based on Nickel–Cobalt Double Hydroxide and Pen Ink Electrodes on Metallized Carbon Fiber. *ACS Appl. Mater. Interfaces* **9**, 5409–5418 (2017).

12. Kim, Jayoung, Campbell, Alan S., de Ávila, Berta Esteban-Fernández & Wang, Joseph. Wearable biosensors for healthcare monitoring. *Nat. Biotechnol.* **37**, 389–406 (2019).

13. Ray, Tyler R., Choi, Jungil, Bandodkar, Amay J., Krishnan, Siddharth, Gutruf, Philipp, Tian, Limei, Ghaffari, Roozbeh & Rogers, John A. Bio-Integrated Wearable Systems: A Comprehensive Review. *Chem. Rev.* **119**, 5461–5533 (2019).

14. Won, Sang Min, Wang, Heling, Kim, Bong Hoon, Lee, KunHyuck, Jang, Hokyung, Kwon, Kyeongha, Han, Mengdi, Crawford, Kaitlyn E., Li, Haibo, Lee, Yechan *et al.* Multimodal Sensing with a Three-Dimensional Piezoresistive Structure. *ACS Nano* **13**, 10972–10979 (2019).

15. Saborío, Mari Cruz G., Lanzalaco, Sonia, Fabregat, Georgina, Puiggalí, Jordi, Estrany, Francesc & Alemán, Carlos. Flexible Electrodes for Supercapacitors Based on the Supramolecular Assembly of Biohydrogel and Conducting Polymer. *J. Phys. Chem. C* **122**, 1078–1090 (2018).

16. Teng, Weili, Zhou, Qinqin, Wang, Xuekai, Che, Haibing, Hu, Peng, Li, Hongyi & Wang, Jinshu. Hierarchically interconnected conducting polymer hybrid fiber with high specific capacitance for flexible fiber-shaped supercapacitor. *Chem. Eng. J.* **390**, 124569 (2020).

17. Ding, Yangbin, Bai, Wei, Sun, Jinhua, Wu, Yu, Memon, Mushtaque A., Wang, Chao, Liu, Chengbin, Huang, Yong & Geng, Jianxin. Cellulose Tailored Anatase TiO2 Nanospindles in Three-Dimensional Graphene Composites for High-Performance Supercapacitors. *ACS Appl. Mater. Interfaces* **8**, 12165–12175 (2016).

18. Yu, Huimin, Rouelle, Nathalie, Qiu, Aidong, Oh, Jeong-A., Kempaiah, Devaraju M., Whittle, Jason D., Aakyiir, Mathias, Xing, Wenjin & Ma, Jun. Hydrogen Bonding-Reinforced Hydrogel Electrolyte for Flexible, Robust, and All-in-One Supercapacitor with Excellent Low-Temperature Tolerance. *ACS Appl. Mater. Interfaces* **12**, 37977–37985 (2020).

19. Pérez-Madrigal, Maria M., Edo, Miquel G., Saborío, Maricruz G., Estrany, Francesc & Alemán, Carlos. Pastes and hydrogels from carboxymethyl cellulose sodium salt as supporting electrolyte of solid electrochemical supercapacitors. *Carbohydr. Polym.* **200**, 456–467 (2018).

20. Zhang, Wei, Feng, Pan, Chen, Jian, Sun, Zhengming & Zhao, Boxin. Electrically conductive hydrogels for flexible energy storage systems. *Prog. Polym. Sci.* **88**, 220–240 (2019).

21. Xia, Shan, Song, Shixin, Jia, Fei & Gao, Guanghui. A flexible{,} adhesive and self-healable hydrogel-based wearable strain sensor for human motion and physiological signal monitoring. *J. Mater. Chem. B* **7**, 4638–4648 (2019).

22. Wang, Huanhuan, Bian, Linyi, Zhou, Peipei, Tang, Jian & Tang, Weihua. Core–sheath structured bacterial cellulose/polypyrrole nanocomposites with excellent conductivity as supercapacitors. *J. Mater. Chem. A* **1**, 578–584 (2013).

23. Ajjan, F. N., Casado, N., Rębiś, T., Elfwing, A., Solin, N., Mecerreyes, D. & Inganäs, O. High performance PEDOT/lignin biopolymer composites for electrochemical supercapacitors. *J. Mater. Chem. A* **4**, 1838–1847 (2016).

24. Guimard, Nathalie K., Gomez, Natalia & Schmidt, Christine E. Conducting polymers in biomedical engineering. *Prog. Polym. Sci.* **32**, 876–921 (2007).

25. Pal, Ramendra K., Kundu, Subhas C. & Yadavalli, Vamsi K. Fabrication of Flexible, Fully Organic, Degradable Energy Storage Devices Using Silk Proteins. *ACS Appl. Mater. Interfaces* **10**, 9620–9628 (2018).

26. Reid, Daniel O., Smith, Rachel E., Garcia-Torres, Jose, Watts, John F. & Crean, Carol. Solvent Treatment of Wet-Spun PEDOT: PSS Fibers for Fiber-Based Wearable pH Sensing. *Sensors (Basel).* **19**, (2019).

27. Fabregat, Georgina, Teixeira-Dias, Bruno, del Valle, Luis J., Armelin, Elaine, Estrany, Francesc & Alemán, Carlos. Incorporation of a Clot-Binding

Peptide into Polythiophene: Properties of Composites for Biomedical Applications. *ACS Appl. Mater. Interfaces* **6**, 11940–11954 (2014).

28. Mosa, Islam M., Pattammattel, Ajith, Kadimisetty, Karteek, Pande, Paritosh, El-Kady, Maher F., Bishop, Gregory W., Novak, Marc, Kaner, Richard B., Basu, Ashis K., Kumar, Challa V & Rusling, James F. Ultrathin Graphene–Protein Supercapacitors for Miniaturized Bioelectronics. *Adv. Energy Mater.* **7**, 1700358 (2017).

29. Yao, Bowen, Wang, Haiyan, Zhou, Qinqin, Wu, Mingmao, Zhang, Miao, Li, Chun & Shi, Gaoquan. Ultrahigh-Conductivity Polymer Hydrogels with Arbitrary Structures. *Adv. Mater.* **29**, 1700974 (2017).

30. Liu, Qiongqiong, Li, Qingtao, Xu, Sheng, Zheng, Qiujian & Cao, Xiaodong. Preparation and Properties of 3D Printed Alginate–Chitosan Polyion Complex Hydrogels for Tissue Engineering. *Polymers (Basel).* **10**, (2018).

31. Xu, Shunjian, Liu, Can, Xiao, Zonghu, Zhong, Wei, Luo, Yongping, Ou, Hui & Wiezorek, Jörg. Cooperative effect of carbon black and dimethyl sulfoxide on PEDOT:PSS hole transport layer for inverted planar perovskite solar cells. *Sol. Energy* **157**, 125–132 (2017).

32. Simon, Patrice, Gogotsi, Yury, Simon, Patrice, Gogotsi, Yury & Materials, Nature. Materials for electrochemical capacitors. *Nat. Mater.* **7**, 845–854 (2008).

33. Li, Xin & Wei, Bingqing. Facile synthesis and super capacitive behavior of SWNT/MnO2 hybrid films. *Nano Energy* **1**, 479–487 (2012).

34. Garcia-Torres, José & Crean, Carol. Ternary composite solid-state flexible supercapacitor based on nanocarbons/manganese dioxide/PEDOT:PSS fibres. *Mater. Des.* **155**, 194–202 (2018).

35. Cheng, Tao, Zhang, Yi-Zhou, Zhang, Jian-Dong, Lai, Wen-Yong & Huang, Wei. High-performance free-standing PEDOT:PSS electrodes for flexible and transparent all-solid-state supercapacitors. *J. Mater. Chem. A* **4**, 10493–10499 (2016).

36. Kurra, Narendra, Park, Jihoon & Alshareef, H. N. A conducting polymer nucleation scheme for efficient solid-state supercapacitors on paper. *J. Mater. Chem. A* **2**, 17058–17065 (2014).

37. Lehtimäki, Suvi, Suominen, Milla, Damlin, Pia, Tuukkanen, Sampo,

Kvarnström, Carita & Lupo, Donald. Preparation of Supercapacitors on Flexible Substrates with Electrodeposited PEDOT/Graphene Composites. *ACS Appl. Mater. Interfaces* **7**, 22137–22147 (2015).

3.7 Conductive, self-healable and reusable poly(3,4-ethylenedioxythiophene)-based hydrogels for highly sensitive pressure arrays

3.7.1 Summary

Although challenging, the preparation of pure conducting polymer (CP) hydrogels as conductive flexible networks for developing high-performance functional platforms is an outstanding alternative to conventional approaches, as for example those based on the cross-linking of insulating polymer with CP segments and the simple utilization of CPs as fillers of insulating hydrogel networks. In this work, we propose the employment of poly(3,4-ethylenedioxythiophene):poly(styrenesulfonate) (PEDOT:PSS) to prepare conductive hydrogels by partially replacing the PSS dopant by alginate (Alg) chains, which is energetically favoured. The capacity of Alg chains to be electrostatically cross-linked by Ca^{2+} ions has allowed us to obtain hydrogels with good electrical percolation response and mechanical properties. Hydrogels were prepared in a very simple one-step process by adding $CaCl_2$ to different mixtures of PEDOT:PSS and alginic acid (1:3, 1:1 and 3:1). After structural, chemical and physical characterization, the 1:3 PEDOT/Alg hydrogel was moulded to fabricate stretchable touch-pressure sensor arrays, which exhibited fast response and good spatial resolution of the pressure distribution. In addition, PEDOT/Alg hydrogel is self-healable which allowed us to prepare reusable pressure sensors (*i.e*. devices that can be reprocessed to be used in its original application) thanks to the reversibility of the noncovalent Ca^{2+} crosslinks. Reusable devices are in opposition to reclaimed and recycled devices as they are no longer use for the same application because the materials lose their properties. With our hydrogel we are a step closer to a circular economy by allowing the reuse of electronic devices and reducing electronic waste worldwide. Moreover, the superior performance of PEDOT/Alg hydrogel opens up its utilization as efficient and flexible pressure sensors for wearable human-electronic interfaces, in which reusability would be an added value.

3.7.2 Introduction

Conducting polymer (CP) hydrogels are usually prepared by combining an insulating polymer, which forms three-dimensional networks that have the capacity to absorb large amount of water, and a CP that mainly provides electrical conductivity and/or electrochemical activity[1–5]. However, the properties of the resulting hydrogels are typically compromised when CPs are added as simple fillers in hydrogel networks, this inherent limitation sometimes restricting their applicability. A much better approach, but also more complex from a chemical point of view, is to combine the unique properties of the insulating polymer and the CP by a proper coupling reaction between segments of such materials to produce an integrated network of cross-links.[6–11] The most advantageous approach, which is very recent, consists on the formation of pure CP hydrogels to produce outstanding conducting networks that can be integrated in high-performance functional platforms.[12–14]

Poly(3,4-ethylenedioxythiophene) (PEDOT) is one of the most studied CPs because of its excellent properties (*i.e.* great environmental stability, electrical conductivity, electrochemical activity, thermoelectric behaviour and high specific capacitance).[15–18] In particular, poly(styrenesulfonate) (PSS)-doped PEDOT is a very attractive material with good film forming properties, moderate to high conductivity, high visible light transmittance, excellent stability and, therefore, used in a wide number of technological applications (*e.g.* sensors, electrodes for supercapacitors, soft actuators, and as hole injection/extraction material in organic optoelectronics).[19–23] In PEDOT:PSS, the CP domains are embedded in an electronically insulating PSS matrix loosely cross-linked by hydrogen bonding.[22]

Due to its interesting properties, efforts on the preparation of pure CP hydrogels have been mainly focused on PEDOT:PSS. [13,14,24] In a very recent study, Zhao and coworkers[13] engineered a simple process to produce pure CP hydrogels by

interconnecting networks of PEDOT:PSS nanofibrils. This was achieved by mixing dimethyl sulfoxide (DMSO) into PEDOT:PSS aqueous dispersions followed by controlled dry-annealing and rehydration. The resulting hydrogels were proved to fulfil the properties desired for bioelectronic applications. Besides, Shi and coworkers[14] prepared CP hydrogels by thermal treatment of commercial PEDOT:PSS suspensions in diluted H_2SO_4 followed by partial removal of the PSS with concentrated H_2SO_4 and purification by washing with deionized water. The resulting hydrogels were dried and used to prepare highly conducting fibres, which were subsequently employed to fabricate flexible supercapacitors. In both cases, the transformation of PEDOT:PSS into a conducting hydrogel required several steps including both chemical and physical treatments.[13,14] More recently, Bao and co-workers developed an electrochemical gelation method for patterning PEDOT:PSS hydrogels on conductive templates using a sacrificial metal layer.[24] A few months ago, Khademhosseini and coworkers[25] reported the spontaneous formation of PEDOT:PSS hydrogel by injecting a mixture of the CP suspension with 4-dodecylbenzenesulfonic acid, which is a cytotoxic surfactant. The resulting hydrogel fibers were found to be self-healing.

In very recent studies PEDOT:PSS has been combined with other polymers to create stretchable and conducting systems. Wang *et al.* [26] constructed a 3D segregated structure in the carboxylated styrene butadiene latex films using PEDOT:PSS, which led to highly stretchable composite with sensitivity towards touchless stimuli. Also, an all inkjet-printed sensor for hydrazine detection has been prepared using a PEDOT:PSS electrode functionalized with ZnO and encapsulated in a Nafion matrix [27]. Wang *et al.* [28] blended PEDOT:PSS with graphene oxide on flexible polyethylene terephthalate for applications based on the piezoresistive properties of the resulting composite. Zhou *et al.* [29] nanostructured fibres anchoring a thin layer of polyaniline on PEDOT:PSS hydrogel for fibre supercapacitors. Teo *et al.* [30] prepared PEDOT:PSS / ionic liquid

hydrogels by microreactive inkjet printing for bioelectronic applications. The main disadvantage of these hybrid hydrogels refers to the cytotoxicity of the component that is mixed with PEDOT:PSS (*e.g.* polyaniline and ionic liquids are very cytotoxic materials), which hinders their utilization for some biomedical applications. Moreover, many of the mentioned hydrogels were not self-healing.

Herein, we report a new PEDOT hydrogel that combines high conductivity, flexibility and self-healing property with the outstanding capacity of reutilization, which in the context of this work should be understood as the capacity to be recycled for the same application (*i.e.* without loss of properties) by re-constituting it after complete disintegration. This hydrogel is rapidly formed in a very simple one step process from commercial PEDOT:PSS through the replacement of PSS dopant polyanions by alginate (Alg) chains. More specifically, the simply addition of a $CaCl_2$ solution to a mixture of PEDOT:PSS and alginic acid (AA) directly results in the formation of a hydrogel, hereafter named PEDOT/Alg-h. Furthermore, this hydrogel can be undone by disassembling the polymer chains through the replacement of Ca^{2+} by monovalent ions like Na^{+} and, subsequently, reconstituted by adding $CaCl_2$ again.

Alg is a biocompatible and biodegradable copolymer with homopolymeric blocks of 1,4-linked β-D-mannuronate and its C-5 epimer, α-L-guluronate, covalently linked in different sequences. The mannuronate / guluronate ratio and length of each block depend on the source of the Alg.[31] Alg is frequently employed in the form of hydrogel in biomedicine, mainly in wound healing, in vitro cell culture, drug delivery and tissue engineering.[32]

Taking advantage of the properties of the PEDOT hydrogel obtained by replacing PSS by Alg in a Ca^{2+}-containing medium, a reusable pressure sensor array with high capability for detecting both location and pressure of touches, as well as with excellent response time, has been prepared. Results demonstrate that the novel hydrogel, named PEDOT/Alg, can be considered as an ideal material for

many applications (*e.g.* textile devices, including wearable ones, keyboards, touchscreens and human-machine interfaces) in which the reconstitution of the sensor, instead of its replacement, could be considered as the most appropriated alternative.

3.7.3 Methods

3.7.3.1 Theoretical calculations

The strength of PEDOT···PSS and PEDOT···alginate interaction was examined using Density Functional Theory (DFT) calculations, which were performed using the Gaussian 09 computer package.[33] The geometries of the different investigated model complexes were fully optimized with the M06L[34,35] functional, which was developed by Zhao and Truhlar to account for dispersion, combined with the 6-31G(d,p) basis set. Geometry optimizations were performed in vacuum and in water (ε= 32.6), which was described through a simple Self Consistent Reaction Field (SCRF) method. More specifically, the Polarizable Continuum Model [36,37] (PCM) was used in the framework of the M06L/6-31G(d,p) level to represent bulk solvent effects. No symmetry constraints were used in the geometry optimizations.

3.7.3.2 Preparation of hydrogels.

PEDOT:PSS 1.3 wt. % dispersion in H_2O, **Alginic acid (AA) from Macrocystis pyrifera** (61% mannuronic acid and 39% guluronic acid; M_W= 240 kDa) **were purchased from Sigma-Aldrich, while** $CaCl_2$ was purchased from Scharlab.

The 1.3 wt% and 3.9 wt% AA solutions were prepared by dissolving the biopolymer in deionized water at 50 ºC with vigorous stirring for 1 h. Then, equal volumes of the 1.3 wt% PEDOT:PSS dispersion and each of these AA solutions were mixed at room temperature with vigorous stirring for 20 min. Hereafter, the mixtures coming from 1.3 wt% and 3.9 wt% AA solutions are denoted 1:1 PEDOT:PSS/AA and 1:3 PEDOT:PSS/AA. Also, the 3:1 PEDOT:PSS/AA mixture was prepared using 1.3 wt% AA and increasing three times the volume of PEDOT:PSS with respect to that of AA. Hydrogels were formed by immersing silicon rubber molds filled with 3 mL (5×3×0.3 cm^3 molds) or 1 mL (5×1×0.2 cm^3)

of the 1:1 or 1:3 mixture into a $CaCl_2$ 3 wt.% aqueous solution for 10 min. Silicon rubber molds were constructed with Ecoflex® 00-10, which is a platinum cure silicon rubber compound. It should be mentioned that the mold is not necessary for the formation of the hydrogels, which can be directly obtained by depositing the mixtures onto a cover glass or any other surface, even though it allows to control the dimensions of the hydrogel for reproducibility. Both PSS chains displaced by AA and the excess of negatively charged polymer chains were removed by thoroughly washing the samples with abundant water. Then, a blotting paper is applied to the surface of the hydrogels to remove excess water and thus prevent water leaking during measurements.

Blank samples -pure PEDOT:PSS and pure Alg hydrogels- were also fabricated for comparison purposes. While Alg hydrogels were obtained using the same procedure as before but using only the 1.3 wt% AA solution, pure PEDOT:PSS hydrogels were prepared with H_2SO_4 using the procedure described by Shi and coworkers.[14] Briefly, a PEDOT:PSS suspension (10.5 mg/mL, Clevios PH1000) containing H_2SO_4 (0.1 mol/L) was placed in a glass capillary tube and kept at 90ºC for 3h. Hydrogels for the electrochemical characterization were prepared onto an indium tin oxide (ITO)-coated polyethylene terephthalate (PET) sheet (purchased from Sigma-Aldrich).

3.7.3.3 Characterization

Attenuated total reflectance (ATR)-FTIR spectra were obtained with a FTIR 4100 spectrophotometer, equipped with a diamond crystal (Specac model MKII Golden Gate Heated Single Reflection Diamond ATR). The samples were evaluated using spectra manager software. For each sample 3 scans were performed between 4000 and 600 cm^{-1} with a resolution of 4 cm^{-1} at room temperature.

Raman spectra were acquired using a commercial Renishaw inVia Qontor confocal Raman microscope. The Raman setup consisted of two laser at 785 nm and 532 nm, both with a nominal 500 mW output power and directed through a microscope (specially adapted Leica DM2700 M microscope) to the sample, after which the scattered light is collected and directed to a spectrometer with a 1200 lines/mm grating and 2400 lines/mm grating, respectively. The exposure time was 10 s, the laser power was adjusted to 0.05% and 1%, respectively, of its nominal output power, and each spectrum was collected with three accumulations

The morphology of the prepared hydrogels was examined by scanning electron microscopy (SEM) using a Focused Ion Beam Zeiss Neon40 scanning electron microscope equipped with an energy dispersive X-ray (EDX) spectroscopy system and operating at 5 kV. All samples were sputter-coated with a thin carbon layer using a K950X Turbo Evaporator to prevent electron charging problems. Prior to SEM observation, samples were lyophilized (*i.e.* freeze-drying). The size of pores was determined from the SEM images using the software SmartTIFF (*v*1.0.1.2.).

Atomic force microscopy (AFM) images were obtained with a Molecular Imaging PicoSPM using a NanoScope IV controller under ambient conditions. The tapping mode AFM was operated at constant deflection. The row scanning frequency was set to 1 Hz. AFM measurements were performed on various parts of the films, which provided reproducible images similar to those displayed in this work. The root mean square roughness (RMS R_q), which is the average height deviation taken from the mean data plane, was determined using the statistical application of the NanoScope Analysis software (1.20, Veeco).

Measurements for water uptake were carried in distillate water. First, hydrogels were lyophilized by freeze-drying and weighted. Then, they were immersed in distilled water for 24 h (for measurements of water uptake). After that, the wet hydrogels were quickly wiped to remove the surface water with filter paper, and their weights were scored again. Water uptake was calculated as:

$$\text{Water uptake} = \frac{W_w - W_d}{W_d} x100\% \qquad \text{(E.3.7.1)}$$

where W_w is the weight of the swelled hydrogel and W_d is the weight of the lyophilized hydrogel. Three independent measurements were carried using similar sized samples to check for reproducibility. The average values were expressed in all cases.

Transmission electron microscopy (TEM) studies were performed using a JEOL J1010 (filament: tungsten) equipped with a Gatan *Orius* 1000 slow scan *CCD* and the *DigitalMicrograph* (Gatan) software. The accelerating voltage was 80 kV. A Sorvall Porter-Blum microtome (Sorwall, NT, USA) equipped with a diamond knife was used to cut the sample in thin sections that were subsequently lifted onto carbon-coated grids.

The electrical conductivity was determined using a Fluke 8840A Multimeter. Measurements were performed on hydrogel samples that were prepared inside smooth rubber molds of well-defined dimensions. The latter were built using Ecoflex® 00-10 platinum cure silicone rubber compound.

Electrochemical impedance spectroscopy (EIS) diagrams were taken at open circuit (OCP) over the frequency range of 10^5 kHz to 10 Hz with potential amplitude of 0.05 V using an AUTOLAB-302N potentiostat/galvanostat. All experiments were performed at room temperature.

Electrochemical cells in three-electrode configurations were assembled for electrochemical characterization. The working consisted on the hydrogel supported by an ITO-coated PET sheet (exposed area: 1 cm^2) while the counter electrode was platinum wire. An Ag|AgCl electrode containing saturated KCl aqueous solution (E^0 = 0.222 V *vs.* standard hydrogen electrode at 25 °C) was used as reference electrode. All electrochemical experiments were run in triplicate using a 0.1 M $CaCl_2$ solution as supporting electrolyte. The electrochemical activity was determined by cyclic voltammetry. The initial and final potentials were 0.0 V,

whereas the reversal potential was 0.8 V. All measurements were performed at room temperature using a scan rate comprised between 50 and 500 mV/s. On the other hand, galvanostatic charge-discharge curves between 0.0 and 0.8 V were run at 20 $\mu A/cm^2$. All electrochemical experiments were run in triplicate with a potentiostat-galvanostat Autolab PGSTAT101 equipped with the ECD module (Ecochimie, The Netherlands).

3.7.4 Results and discussion

3.7.4.1 Conceptualization

The energetic associated to the substitution of PSS polyanions by Alg chains in PEDOT:PSS has been evaluated using Density Functional Theory (DFT) calculations at the M06L/6-31G(d,p) level. The aqueous medium was described using the Polarizable Continuum Model (PCM), which is a well-stablished Self-Consistent Reaction Field method. Calculations were conducted on simple model systems involving a PEDOT chain with 4 or 8 repeat units and a charge of +0.5 per repeat unit (*i.e.* 4-EDOT^{+2} or 8-EDOT^{+4}) complexed to: *i)* a PSS chain with 2 or 4 repeat units and a charge of –1 per repeat unit (*i.e.* 2-SS^{2-} or 4-SS^{4-}); or ii) an Alg chain with two (one mannuronate and one guluronate residues; *m*= *n*= 1 in Scheme 3.7.1) or four (two mannuronate and two guluronate residues; *m*= *n*= 2 in Scheme 3.7.1) units, blocked at the ends with methyl groups, and a charge of –1 per unit (*i.e.* 2-Alg^{2-} or 4-Alg^{4-}). It is worth noting that the half positive charge used for each PEDOT repeat unit, which has been taken from previous measures of the doping level,[38] reflects the characteristic delocalized electronic distribution of heterocyclic CPs, while the negative charge of each PSS or Alg unit is specifically localized on the corresponding sulfonate or carboxylate group, respectively. In order to search for the most favourable interaction between the model molecules involved in each calculated complex, different relative orientations were considered as starting points for geometry optimizations (*i.e.* at least 5 different starting points were considered for each complex). Results are summarized in Figure 3.7.1.

The binding energies associated to the formation of PEDOT:PSS complexes indicate that this assembly process is more favoured in vacuum than in aqueous solution (Figure 3.7.1a). Water shields both the delocalized charges of PEDOT and the localized charges of the PSS, reducing the strength of the electrostatic interactions between the two species.

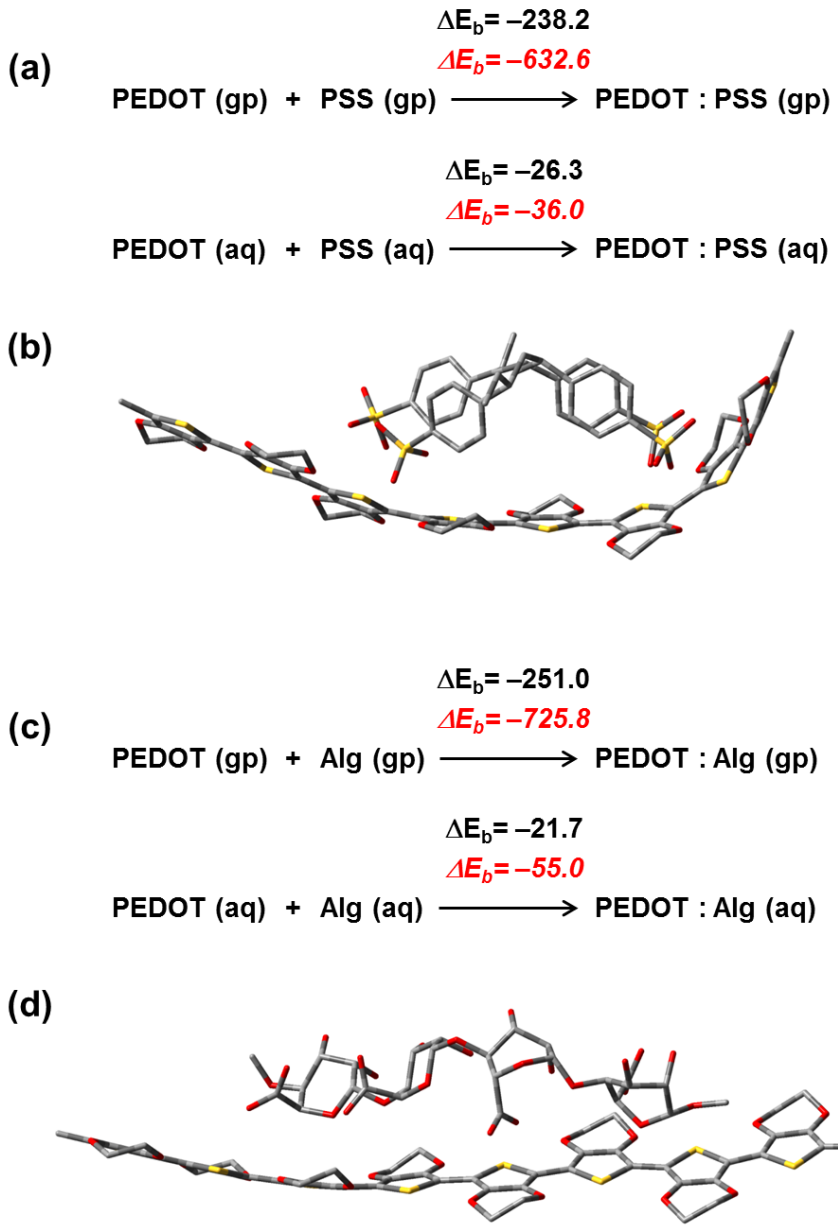

Figure 3.7.1. (a) Binding energies (ΔE_b, in kcal/mol) associated to the formation of 4-EDOT^{2+}:2-SS^{2-} (plain and black) and 8-EDOT^{4+}:4-SS^{4-} (italic and red) in vacuum (gp) and aqueous solution (aq) as determined by PCM-M06L/6-31G(d,p) calculations. (b) Lowest energy complex obtained for 8-EDOT^{4+}:4-SS^{4-}. (c) Binding energies (ΔE_b, in kcal/mol) associated to the formation of 4-EDOT^{2+}:2-Alg^{2-} (plain and black) and 8-EDOT^{4+}:4-Alg^{4-} (italic and red) in vacuum (gp) and aqueous solution (aq) as determined by PCM-M06L/6-31G(d,p) calculations. (d) Lowest energy complex obtained for 8-EDOT^{4+}:4-Alg^{4-}.

Besides, the strength of the interaction increases with the size of the model molecules. Thus, the binding energy becomes 2.6 (vacuum) and 1.4 (aqueous solution) times more attractive when the size of the model molecules used to

represent PEDOT and PSS increases from 4-EDOT^{+2} and 2-SS^{2-} to 8-EDOT^{+4} and 4-SS^{4-}. As shown in Figure 3.7.1b, which displays the most stable 8-EDOT^{+4}:4-SS^{4-} complex, the sulfonate groups preferentially interact with the oxidized thiophene rings.

Although the binding energies calculated for PEDOT:Alg (Figure 3.7.1c) show trends similar to those described for PEDOT:PSS, the influence of the size of the model is significantly more pronounced. More specifically, the binding energy becomes 2.9 and 2.5 times more attractive in vacuum and aqueous solution, respectively, when the size of model oligomers doubles. Consequently, the binding energies are more attractive for 8-EDOT^{+4}:4-Alg^{4-} than for 8-EDOT^{+4}:4-SS^{4-} (-93.2 and -19.0 kcal/mol in vacuum and aqueous solution, respectively), confirming that the substitution of PSS by Alg in PEDOT:PSS complexes is favoured from a thermodynamic point of view. This has been attributed to the flexibility of Alg chains, which permits the re-orientation of the carboxylate groups to achieve stronger electrostatic interactions with the thiophene ring. Figure 3.7.1d, which depicts the most stable 8-EDOT^{+4}:4-Alg^{4-} complex, shows that the carboxylate rings of 4-Alg^{4-} directly confront the oxidized thiophene rings. This structural re-orientation is more difficult in PEDOT:PSS since the bulk phenyl groups easily induce severe steric repulsions.

3.7.4.2 Preparation of PEDOT/Alg hydrogels

As DFT calculations indicated that PEDOT⋯Alg interactions are energetically favoured with respect to PEDOT⋯PSS, substitution of PSS by Alg was directly attempted using commercial PEDOT:PSS. Three different PEDOT:PSS/Alg hydrogels, named 1:3, 1:1 and 3:1, were prepared, this choice allowing to roughly scan the properties of the whole range of compositions. For this purpose, equal volumes of a 1.3 wt. % PEDOT:PSS aqueous dispersion and a 1.3 wt% or 3.9 wt%

AA water solution were mixed at room temperature with vigorous stirring for 20 min. Hereafter, the mixtures coming from 1.3 wt% and 3.9 wt% AA solutions are denoted 1:1 PEDOT:PSS/AA and 1:3 PEDOT:PSS/AA. Also, the 3:1 PEDOT:PSS/AA mixture was prepared using 1.3 wt% AA and increasing three times the volume of 1.3 wt. % PEDOT:PSS with respect to that of AA. These mixtures were transformed in hydrogels by immersing silicon rubber moulds of well-defined dimensions, which were previously filled with the corresponding PEDOT:PSS/AA mixture, into a $CaCl_2$ 3 wt.% aqueous solution for 10 min; or by depositing the corresponding mixture onto a substrate (*e.g.* cover glass) and, subsequently, adding $CaCl_2$ 3 wt.% aqueous solution. The excess of AA and the leaving PSS chains (*i.e.* those replaced by Alg) were eliminated by thoroughly washing the formed hydrogel with abundant water. Hydrogels prepared using this simple process, which is sketched in Scheme 3.7.1, are denoted 3:1, 1:1 or 1:3 PEDOT/Alg-h.

In the dispersion, the PEDOT:PSS complex is usually described as a micro-gel system, where a PEDOT-rich center is surrounded by excessive PSS. In addition, *PSS* plays the *role* of a primary *dopant agent* for *PEDOT. This is because of the electronic structure of negatively charged sulfonate groups that is stabilized by the aromatic phenyl rings. Substitution of PSS by Alg, which is also a very soluble polyelectrolyte, is expected to maintain the dispersion of the CP in the solution. This explains the observation of PEDOT-rich domains surrounded by Alg-rich in the prepared hydrogels (see next-subsection). However, the role of Alg as primary dopant agent is expected to be worse than that of PSS since in the former the negative charges are not stabilized by aromatic moieties. This is also consistent with the moderate conductivity of PEDOT/Alg-h, as shown below.*

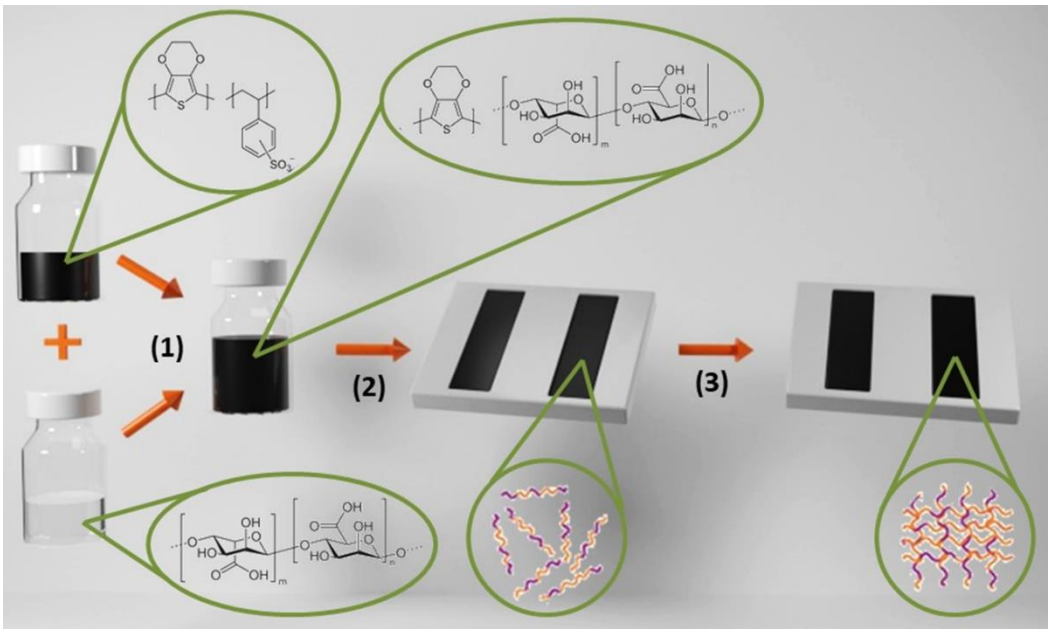

Scheme 3.7.1. Procedure used to prepare PEDOT/Alg-h. (1) Mixing of alginate solution and PEDOT:PSS dispersion and stirring for 20 min. (2) Pouring the mixture in the silicone rubber mould. (3) Cross-linking in 3 wt.% $CaCl_2$ solution for 3 min.

Besides, hydrogels derived from pure PEDOT:PSS and pure AA, hereafter named PEDOT-h and Alg-h, respectively, were used as controls. More specifically, PEDOT-h was obtained applying the H_2SO_4 treatment described by Shi and coworkers (see methods section for details),[14] while Alg-h was derived from a 1.3 wt% AA solution using the procedure described for PEDOT/Alg-h.

3.7.4.3 Characterization of PEDOT/Alg hydrogels

Figure 3.7.2a compares the FTIR spectra of PEDOT-h, Alg-h and 3:1, 1:1 and 1:3 PEDOT/Alg-h. In addition of the broad band at ~3400 cm^{-1} (not shown), which is attributed to the O–H stretching, the spectrum of Alg-h displays absorption bands assigned to carbonyl (C=O) asymmetric and symmetric stretching at 1598 and 1418 cm^{-1}, respectively, and the C–O–C stretching at 1028 cm^{-1}.[39] On the other hand, PEDOT-h shows the characteristic absorption bands of the CP at 1564 cm^{-1} for the C=C stretching in the thiophene ring, 1270 and 1122 cm^{-1} for the vibrations of the fused dioxane ring, and 862 cm^{-1} for the stretch of the C–S bond in the

thiophene ring. Moreover, the bands at 1162 and 1060 cm^{-1} have been attributed to the S–O and S–phenyl vibrations of residual PSS chains (*i.e.* those that were not removed by the acid treatment[14]). The FTIR spectra recorded for 3:1, 1:1 and 1:3 PEDOT/Alg-h are consistent with the concentration of PEDOT and AA in the starting mixtures. Most importantly, in all cases the bands associated to PSS are residual, reflecting that the substitution of this component by Alg chains is almost complete. Raman spectra recorded for the different compositions of PEDOT/Alg-h show that PEDOT bands predominate over Alg bands due to the resonance Raman effect (Figure 3.7.2b), which increases the intensity of the bands of the material when the laser energy coincides with the frequency of the electronic transition of the sample.[40,41]

To get some insights into the microstructure of the materials, we conducted scanning electron microscopy (SEM) studies of lyophilized hydrogels. Alg-h exhibits a homogeneous interconnected macroporous "open cell" structure with irregular large pores of 43 ± 7 μm in diameter (Figure 3.7.2c). Similarly, PEDOT-h forms a 3D network, even though in this case the pore diameter shows great variability (*i.e.* from 1 to 46 μm) with an average value of 12 ± 9 μm (Figure 3.7.2d). On the other hand, Alg-h is easy handling and shows mechanical integrity and stiffness (Figure 3.7.3a). These properties are due to the stability provided by the binding between the Ca^{2+} ions and the carboxylate groups of the guluronate blocks of two adjacent polymer chains (*i.e.* "egg-box" model). Instead, the mechanical behaviour of PEDOT-h is very poor, breaking by its own weight (Figure 3.7.3b) and making it difficult to handle even with the help of tweezers. This feature has been attributed to the weakness of the cross-linking interactions and explains that a drying process, which enhanced the strength of such interactions, was required to obtain mechanically strong porous PEDOT-h fibres.[14]

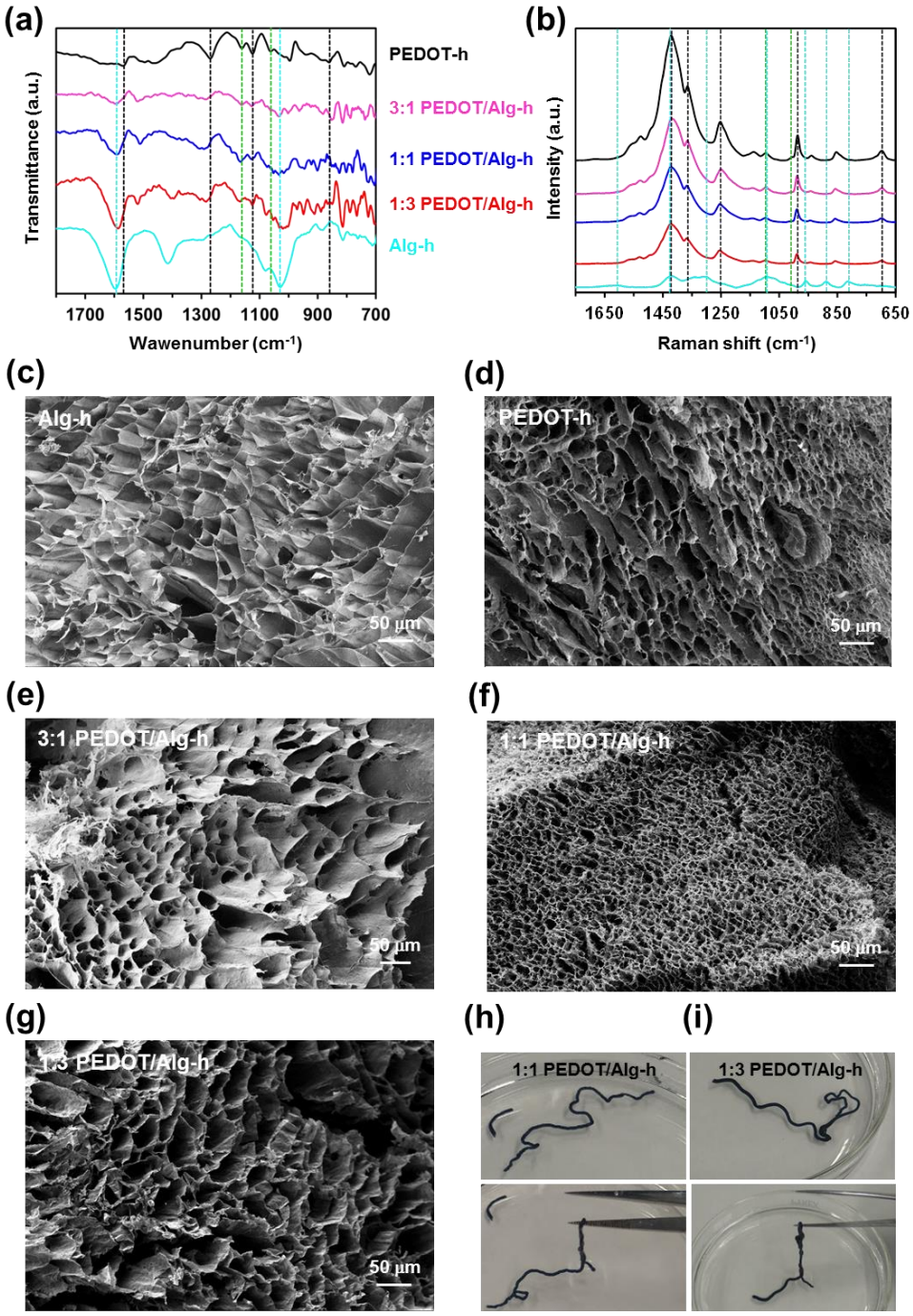

Figure 3.7.2. (a) FTIR and (b) Raman spectra of Alg-h, PEDOT-h and 3:1, 1:1 and 1:3 PEDOT/Alg-h. Characteristic bands of Alg (light blue), PEDOT (black) and PSS (green) are indicated by dashed lines and discussed in the text. SEM micrographs of (c) Alg-h, (d) PEDOT-h, (e) 3:1, (f) 1:1 and (g) 1:3 PEDOT/Alg-h. Photographic images of (h) 1:1 and (i) 1:3 PEDOT/Alg-h as prepared (top) and handled with tweezers (bottom).

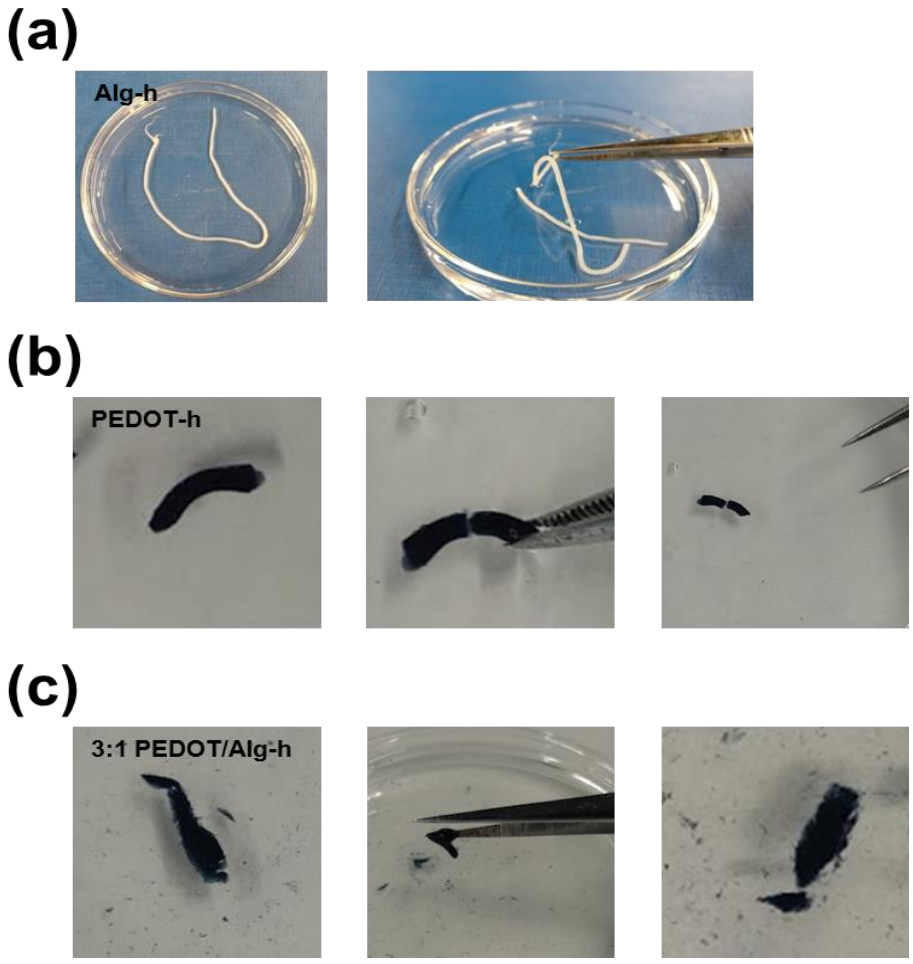

Figure 3.7.3. Photographic images of (a) Alg-h, (b) PEDOT-h and (c) 3:1 PEDOT/Alg-h as prepared, handled with tweezers and, for both PEDOT-h and 3:1 PEDOT/Alg-h, the hydrogel broken after this operation due to its own weight.

SEM micrographs of 3:1, 1:1 and 1:3 PEDOT/Alg-h are displayed in Figures 3.7.2e-f. The three systems present similar macroporous open structures, but the pore size is significantly affected by both the PEDOT content and the degree of replacement of PSS by Alg (*i.e.* 20 ± 5, 9 ± 2 and 68 ± 11 μm for the 3:1, 1:1 and 1:3 hydrogels, respectively). Additional SEM micrographs and energy dispersive X-ray (EDX) spectra, which indicate that the atomic compositions of the hydrogels are consistent with those of the PEDOT:PSS/AA feeding mixtures, are displayed in Figure 3.7.4. As occurred for PEDOT-h, the mechanical integrity and the easy of handling of 3:1 PEDOT:Alg-h are very poor (Figure 3.7.3c), which has been attributed to a combination of two factors. First, the high concentration of CP

weakens cross-linking interactions, as happens in PEDOT-h, which are responsible for the consistency of the material. Second, PEDOT and Alg chains are segregated in different domains, as is suggested by phase imaging atomic force microscopy (AFM). Recorded images show very significant phase shift signal, distinguishing between bright (PEDOT domains) and dark (Alg domains) separated patterns (Figure 3.7.3a).

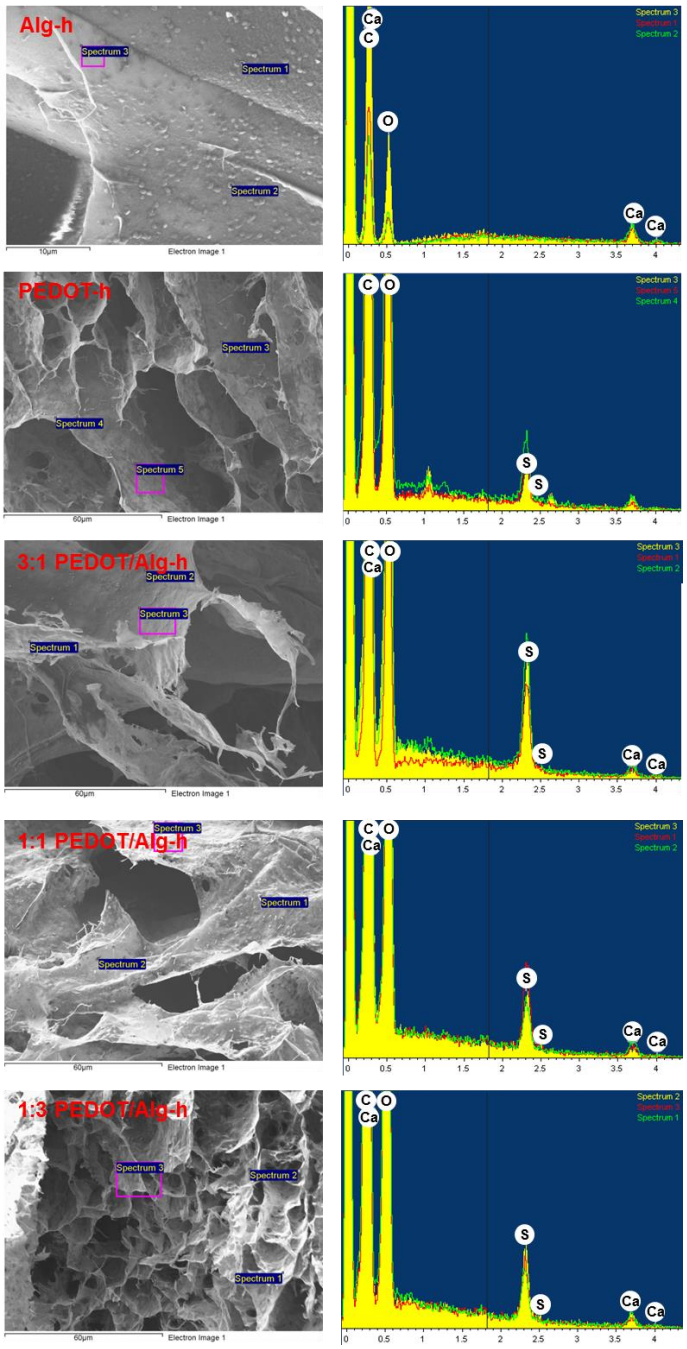

Figure 3.7.4.. SEM micrograph (left) and EDX spectra (right) of Alg-h, PEDOT-h and 3:1, 1:1 and 1:3 PEDOT/Alg-h.

Instead, 1:1 and 1:3 PEDOT/Alg-h show easy handle-ability and processability (Figures 3.7.2h-i), which justify the preparation of hydrogels with higher Alg content. Besides, height and phase-contrast AFM images show that the surface topography (*i.e.* the root mean square roughness, RMS R_q) and the microstructure (*i.e.* the distribution of PEDOT and Alg chains in the hydrogel) of PEDOT/Alg-h changes with the composition (Figure 3.7.5). While in the 1:1 hydrogel the Alg and CP chains are homogeneously distributed, as is shown by phase AFM images (Figure 3.7.5b), Alg chains form abundant domains of micrometric size in the 1:3 hydrogel (Figure 3.7.5c). However, in both cases, the content of Alg chains is high enough to form strong ionic cross-links in which the Ca^{2+} cations connect the carboxylate groups of different but close Alg chains. Indeed, the mechanical integrity, texture and, in general, the aspect of 1:1 and 1:3 PEDOT/Alg-h (Figures 3.7.2h-i) is similar to that of Alg-h (Figure 3.7.3a). The only exception to this resemblance is the color, which is dominated by the dark blue color of PEDOT. On the other, the RMS R_q increases with the Alg content, suggesting that the latter defines the surface topography.

The water uptake capacity (Eq E.3.7.1) of 1:1 and 1:3 PEDOT/Alg-h is 6392% ± 115% and 3640% ± 147%, indicating that the swelling of these hydrogels decreases with the content of Alg. This has been attributed to strong ionic Ca^{2+} mediated crosslinks between neighbouring alginate chains, which restrict the molecular movement in the 1:3 hydrogel. Instead, Ca^{2+}-alginate crosslinks are less abundant in the 1:1 PEDOT:Alg-h, facilitating alginate chains relaxation and water diffusion. Obviously, the dimensional stability of hydrogels increases with decreasing swelling ratio and, therefore, the stability of 1:3 PEDOT/Alg is expected to be superior.

Based on the aforementioned mechanical integrity, easy of handling and dimensional stability, the 1:3 hydrogel was selected for the evaluation of the

electrical and electrochemical properties and, subsequently, the fabrication of a reusable pressure sensor array.

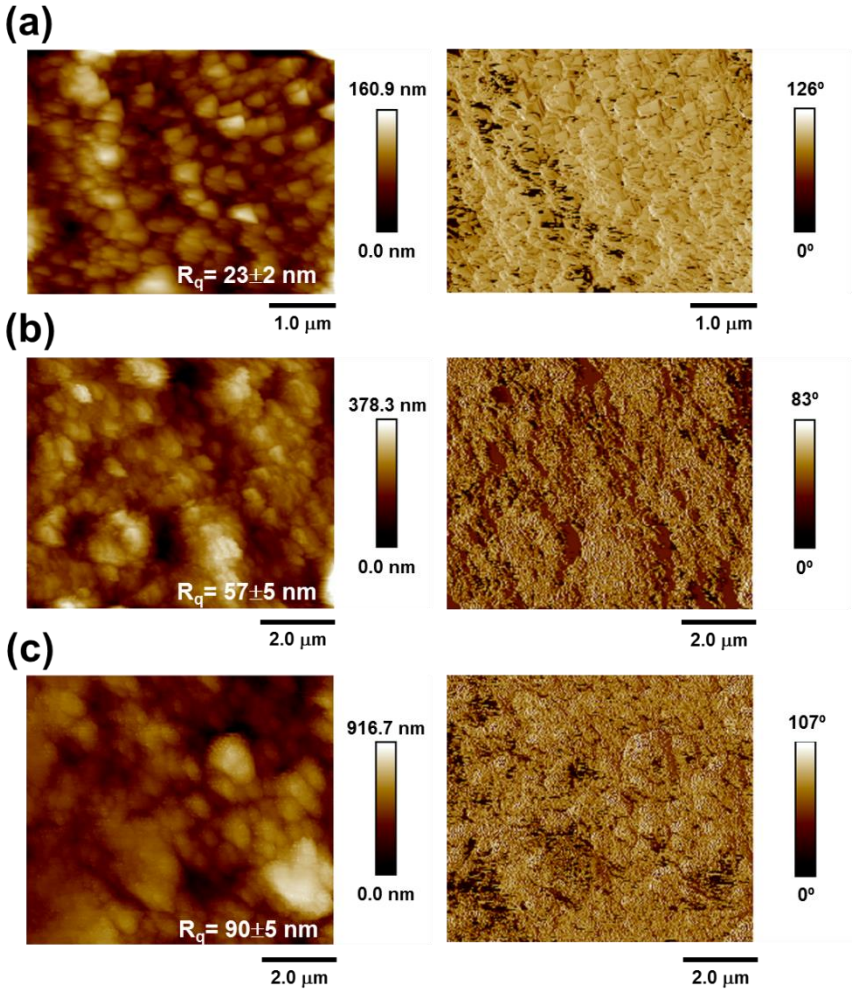

Figure 3.7.5.. Height (left) and phase (right) AFM images of (a) 3:1, (b) 1:1 and (c) 1:3 PEDOT/Alg-h. RMS roughness (R_q) values are indicated

3.7.4.4 Raman spectroscopy

Raman spectra recorded for the different compositions of PEDOT/Alg-h are displayed in Figure 3.7.2b. The main vibrational modes of PEDOT-h are located at 1423 cm^{-1} for the symmetric C_α=C_β stretching of the thiophene ring (the shoulder at 1488 cm^{-1} corresponds to the asymmetric C_α=C_β stretching), 1366 cm^{-1} for the C_β=C_β stretching, and 1256 cm^{-1} for the inter-ring stretching vibrations.[42,43] Other important bands are located at 693 and 990 cm^{-1} which have been assigned to the symmetric C–S–C and oxyethylene ring respectively. Unfortunately, some of these

bands overlap the most characteristic bands of Alg-h which appear at 1427 cm^{-1} for the symmetric COO-stretching bounded to Ca^{2+}, at 1301 and 1085 cm^{-1} for C–H and C–O deformations, respectively, and at 955, 886 and 811 cm^{-1} for skeletal stretching deformation and ring breathing.[44] Instead, the asymmetric COO-stretching appears as a very weak and broad band at 1610 cm^{-1} probably due to the effect of the mass of Ca^{2+} in this mode. Although the Raman spectra of PEDOT/Alg-h prove the presence of the CP, Alg chains are practically undetectable. The Raman fingerprints of PSS phases are typically located at the vibration modes of 1000 and 1100 cm^{-1} .[45,46] The very low intensity of these bands is consistent with the residual presence of PSS in both PEDOT-h and PEDOT/Alg-h.

3.7.4.5 Electrical and electrochemical properties of 1:3 PEDOT/Alg-h

Electrical and electrochemical properties were measured using hydrogel strips of $5 \times 3 \times 0.3$ cm^3 that were prepared in silicone rubber moulds, as shown in Figure 3.7.7a. After removing the excess of water, the electronic conductivity (σ) of 1:3 PEDOT/Alg-h was determined to be σ = 7.9($\pm$0.3)$\cdot 10^{-5}$ S/cm. This value is one order of magnitude higher than that obtained for Alg-h and similar to those of soft composites obtained by chemically polymerizing CPs inside Alg-h networks.[47] However, it is much lower than those reported for pure PEDOT hydrogels that ranged from 0.46 to 8.8 S/cm, depending on the characteristics of the treatment with concentrated H_2SO_4.[14] The conductivities of 1:1 and 3:1 PEDOT/Alg-h, which were determined for sake of completeness, were σ = 5.1($\pm$0.5)$\cdot 10^{-3}$ and 8.7($\pm$0.6)$\cdot 10^{-2}$ S/cm, respectively. The progressive reduction of the conductivity with increasing Alg content has been attributed to the detrimental effect of

micrometric polysaccharide-rich domains on the conduction paths, as suggested by phase imaging AFM (Figure 3.7.5c).

The ionic conductivity of the 1:3 PEDOT/Alg-h was also determined using electrochemical impedance spectroscopy (EIS) as the high-water content can contribute to the total hydrogel conductivity. Accordingly, the impedance was measured for frequencies ranging from 10^{-1} to 10^{4} Hz using a previously reported through-plane impedance cell.[48] Figure 3.7.6 displays the collected impedance (*Z*) data for three independent replicas as Nyquist plots. The hydrogel showed a typical semicircle in the high frequency region, whose diameter represents the charge-transfer resistance of the interface (R_{ct}). In all cases, the diameter is very small with an average value of R_{ct}= 48.9 ± 9.8 kΩ/cm^2, indicating that 1:3 PEDOT/Alg-h possesses a high ionic conductivity (ca. 10^{-5} S/cm). Besides, the straight ascending line at low frequencies with an angle higher than 45º has been attributed to diffusion of ionic species from the hydrogel to the electrode.

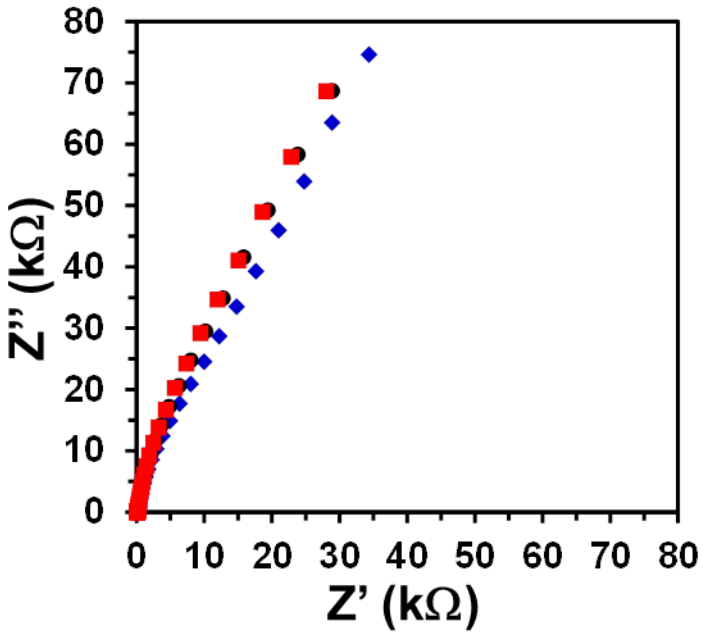

Figure 3.7.6.. Nyquist plots recorded for 1:3 PEDOT/Alg-h.

As a complement to AFM images, transmission electron microscopy (TEM) was performed not only for negatively stained hydrogels (using 1% uranyl acetate (UAc)

solution) (Figure 3.7.7b) but also for unstained hydrogels (Figure 3.7.7c). TEM images of the stained samples show dark regions corresponding to the anionic sites of Alg that were selectively stained with UAc. These higher contrast regions correspond to Alg-rich domains, which are clearly distinguished from the bright regions with a high content of PEDOT (grey). Thus, TEM micrographs of the unstained samples (Figure 3.7.7c) show that the latter zones are dominated by the remarkable electron scattering properties of PEDOT. In fact, the contrast of PEDOT-rich domains in unstained samples is relatively similar to that of Alg-rich domains negatively stained with UAc. In spite of this segregation, both TEM and AFM images suggest that this separation is not complete in 1:3 PEDOT/Alg-h. Thus, PEDOT-rich domains contain a fraction of Alg and vice-versa, which is essential to preserve stable and repetitive conduction paths across the samples (as proved below).

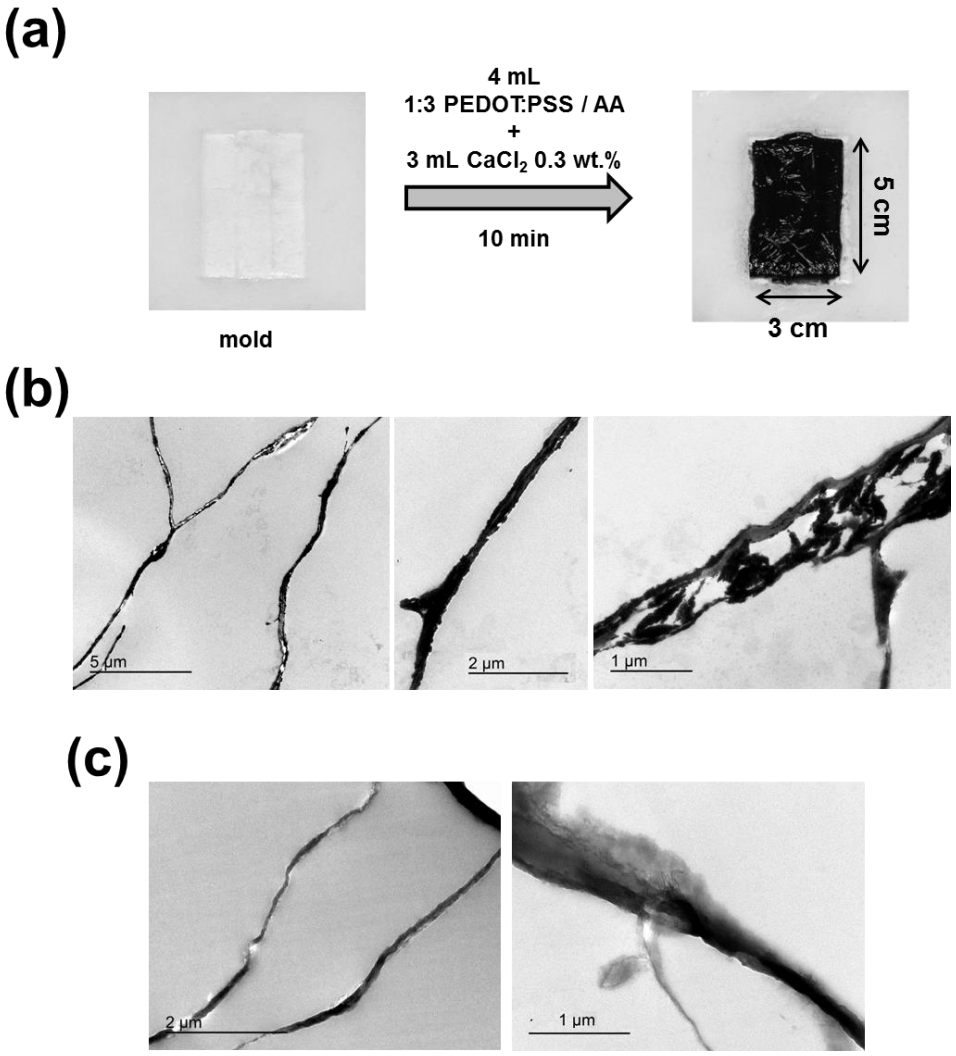

Figure 3.7.7. (a) Preparation of 1:3 PEDOT/Alg-h pieces in a silicon rubber mold. (b,c) TEM micrographs of 1:3 PEDOT/Alg-h samples (b) stained with UAc and (c) unstained.

The electrical percolation response of 1:3 PEDOT/Alg-h was evaluated by monitoring the change in resistivity as a function of the applied pressure. For this purpose, hydrogels were maintained in the rubber moulds shown in Figure 3.7.7a and coated with a thin rubber sheet (thickness: 1 mm). Individual cylindrical weights with a nominal mass between 1 g and 100 g were carefully deposited on the rubber coating, avoiding direct contact with the hydrogel, and the resistivity was measured using a multimeter that was directly connected to the hydrogel. As shown in Figure 3.7.8a, the resistivity decreases linearly with increasing loading, evidencing that the hydrogel is able to detect very low pressures (*i.e.* as low as $6 \cdot 10^{-5}$ Pa).

Repeatability was observed when independently prepared hydrogels were employed. This reproducibility is reflected in Figure 3.7.8a, which displays the calibration curves of three independent hydrogels, indicating that 1:3 PEDOT/Alg-h exhibits an outstanding electrical percolation response that reminds the called "*piezoresistive response*" of PEDOT:PSS/latex[26] and PEDOT:PSS/graphene oxide[28] composites.

Cyclic voltammograms recorded for the 1:3 PEDOT/Alg-h (Figure 3.7.8b) in a three electrode system in the potential window from 0.0 to 0.8 V at different scan rates do not exhibit a rectangular shape, reflecting a deviation from the quasi-reversible electrochemical double layer capacitive behaviour typically observed for PEDOT films.[49,50] However, the current density varies linearly with the square root of the scan rate, as is reflected in Figure 3.7.8c for the current density at the reversal (anodic current density, j_a) and the initial potential (cathodic current density, j_c). This regime indicates that the electrochemical processes at 1:3 PEDOT/Alg-h are controlled by diffusion.

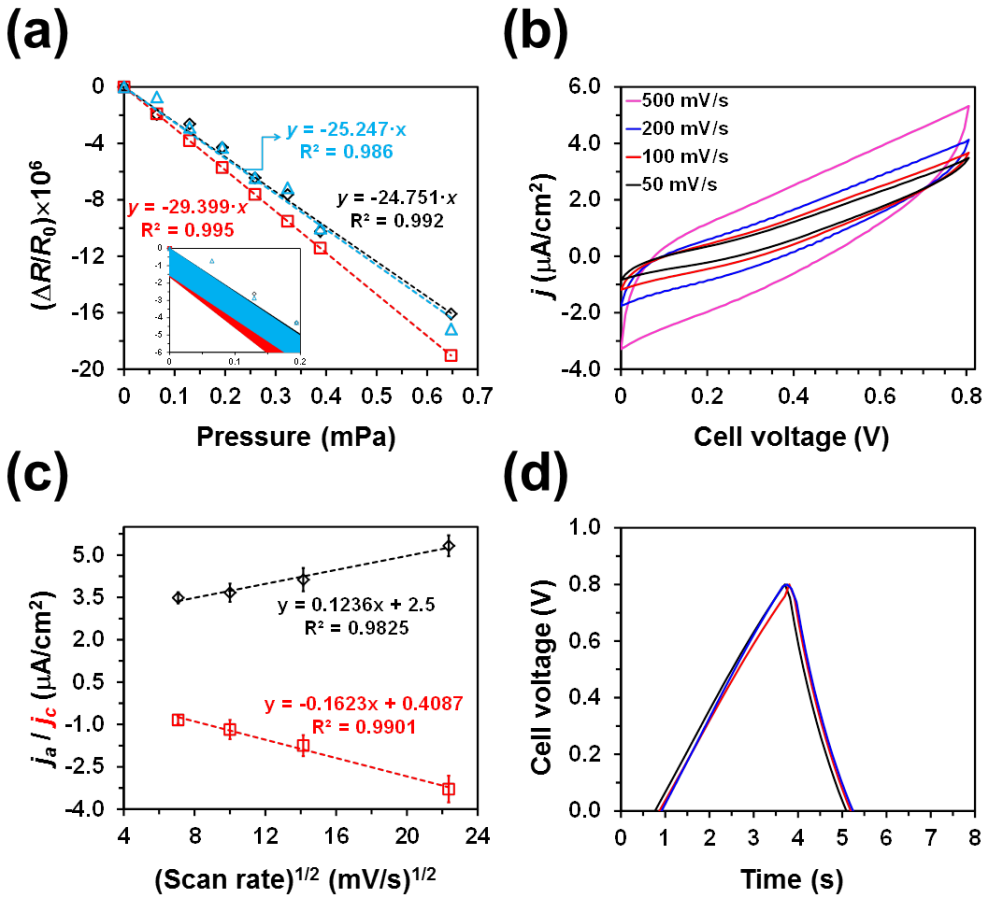

Figure 3.7.8. (a) Relative change of the resistivity with the pressure (results for three independent experiments are shown). (b) Cyclic voltammograms recorded from 0.0 to 0.8 V at different scan rates. (c) Variation of the anodic (black) and cathodic (red) current density (j_a and j_c, respectively) against the square root of the scan rate. (d) Galvanostatic charge-discharge curves (fifth cycle) recorded from 0 to 0.8 V at a current density of 20 μA/cm^2 (results for three independent samples are shown).

Figure 3.7.8d shows galvanostatic charge-discharge curves between 0.0 and 0.8 V at a current density of 20 μA/cm^2. Charge and discharge profiles are linear and, therefore, curves exhibit a typical triangular shape. Although the voltage drop at the beginning of the discharging step is very small (*i.e.* < 0.05 V), charge and discharge processes are not symmetric. Specifically, the discharge is twice faster than the charge, reducing the coulombic efficiency of the system. Moreover, the low discharge times and therefore the low capacitance limit the utilization of the 1:3 PEDOT/Alg-h for the construction of efficient supercapacitors. Instead, porous fibres obtained by drying PEDOT:PSS hydrogel fibres treated with H_2SO_4 showed

a very high Coulombic efficiency (*i.e.* the charge step was faster than the discharge one). In summary, although 1:3 PEDOT/Alg-h exhibits electrochemical activity, its properties are more appropriated for the fabrication of highly sensitive pressure sensors than for the production energy storage devices.

3.7.4.6 Preparation of PEDOT-based pressure sensor array and proof of concept

In order to investigate the potential sensing applications of 1:3 PEDOT/Alg-h, four 5×1×0.2 cm^3 hydrogel strips were distributed in two crossed layers separated by a 1 mm-thick silicone rubber film acting as dielectric. The schematic design of the 2×2 pressure sensor array with the dimensions of each component is sketched in Figure 3.7.9a, while the silicone rubber mould used to prepare the two hydrogel strips of each layer is displayed in Figure 3.7.9b. Hydrogel strips were contacted by copper wires (wire diameter = 0.1 mm) for detection of pressure through a control device. The wires were place inside the moulds and before the preparation of the hydrogels to assure good connection after cross-linking. Figure 3.7.9c exhibits a photograph (left) of the two separated layers, each one consisting in a rubber mould with two hydrogel strips prepared by filling each mould with 1 mL of the 1:3 PEDOT:PSS/AA mixture and immersing the whole later into a $CaCl_2$ 3 wt.% aqueous solution. After drying the excess of water from the surface of the formed hydrogels, the pressure sensor was assembled forming a 2×2 array with two crossed layers separated by a thin silicone rubber film (Figure 3.7.9c, right).

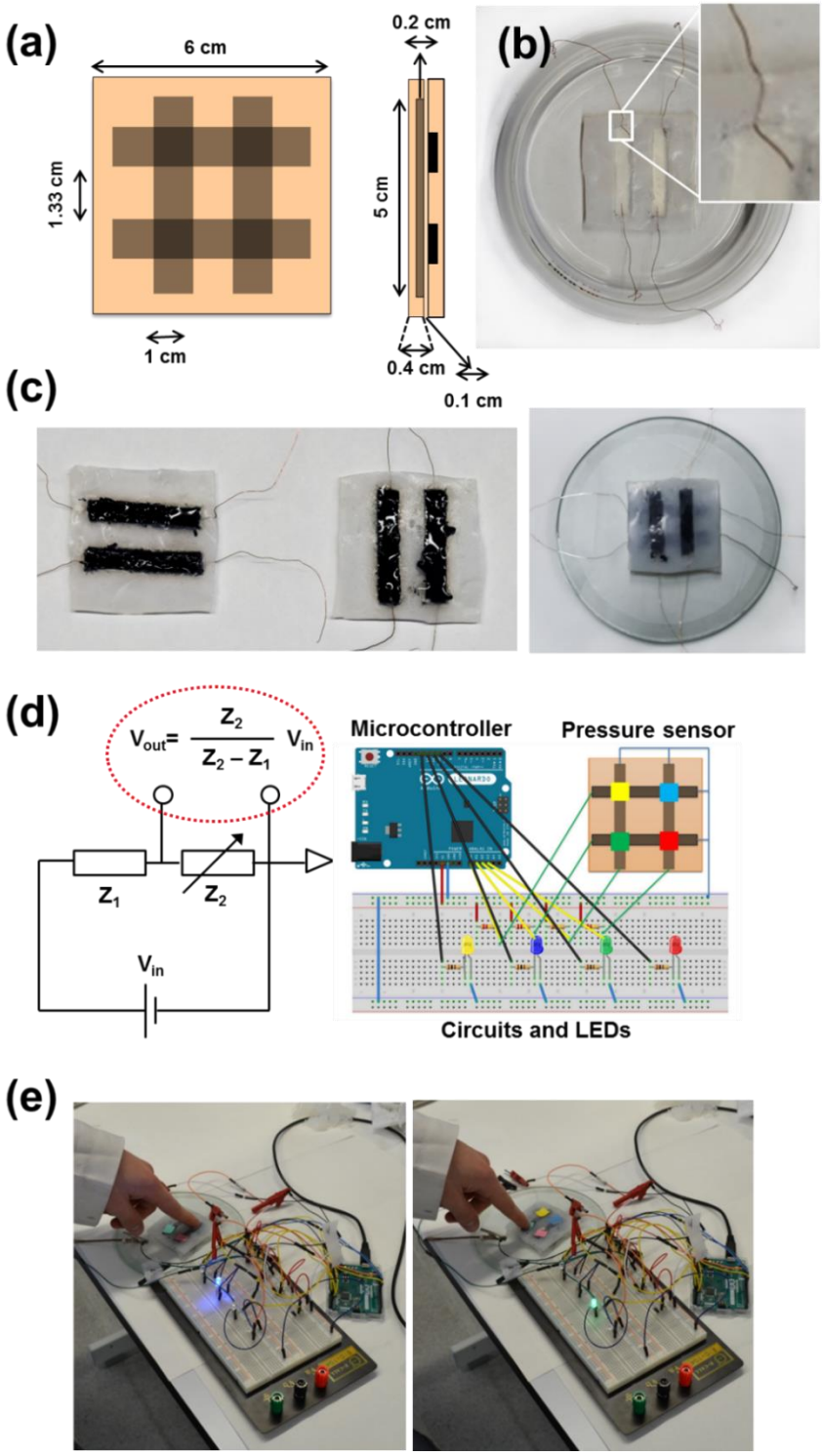

Figure 3.7.9.. (a) Schematic design of the pressure sensor and dimensions of each component. (b) Silicon rubber mold used to prepare each layer of the pressure sensor. (c) Two silicon rubber layers containing 2 hydrogel strips with embedded copper electrodes before (left) and after assembly into a 2×2 crossed array (right). (d) Sketches showing the circuit used to calculate the output voltage (V_{out}) via an Arduino® UNO platform (V_{in} is the input voltage, while Z_1 and Z_2 are the resistance of non-touched and touched hydrogels) and the connections among the microcontroller, the pressure sensor array and the yellow, blue, green and red LEDs. (e) Demonstration of the sensing capacity of the tactile pressure sensor array in terms of location and pressure of touches

The evaluation of the prepared array as stretchable touch-pressure sensor was first conducted by demonstrations of controlled illumination of light emitting diodes (LEDs) of different colours (*i.e.* yellow, blue, green and red). Figure 3.7.9d shows a schematic diagram of the voltage divider circuit used to transform the input voltage (V_{in}) into the output voltage (V_{out}) by pressing the hydrogel. Thus, V_{in} is affected by the change in resistance of the strip hydrogel when touched, varying from Z_1 to Z_2. The change in the voltage is controlled via an Arduino® Leonardo platform that is connected to the pressure sensor array and the different LEDs, as is sketched in Figure 3.7.9d.

The microcontroller is responsible for detecting changes in V_{out} through the pins and turn on the corresponding LED, thus obtaining a tactile pressure sensor with spatial resolution. Figure 3.7.9e illustrates the excellent sensing capacity of the tactile pressure sensor array, which exhibits very fast response and good spatial resolution of the pressure distribution through the outstanding electrical percolation response of hydrogel strips. As it is shown, LEDs light up depending on the location of the pressure exerted by touching the device.

3.7.4.7 Self-healing and reusability

Hydrogels stabilized by ionic bonds can be self-healable by modulating the formation and disruption of reversible electrostatic interactions between oppositely charged moieties. Electrostatic interactions can occur between oppositely charged polymers or through ionic bridges between charged polymers mediated by oppositely charged ions.[51,52] An example of the latter are skin inspired conductive self-healable hydrogels with 3D printability,[51] which were achieved through dynamic ionic interactions between the carboxylic groups of poly(acrylic acid) and ferric ions. Also, Alg-h made of negatively charged alginate chains that cross-link

into a hydrogel through divalent ions, belongs to this class of self-healing hydrogels.[53,54]

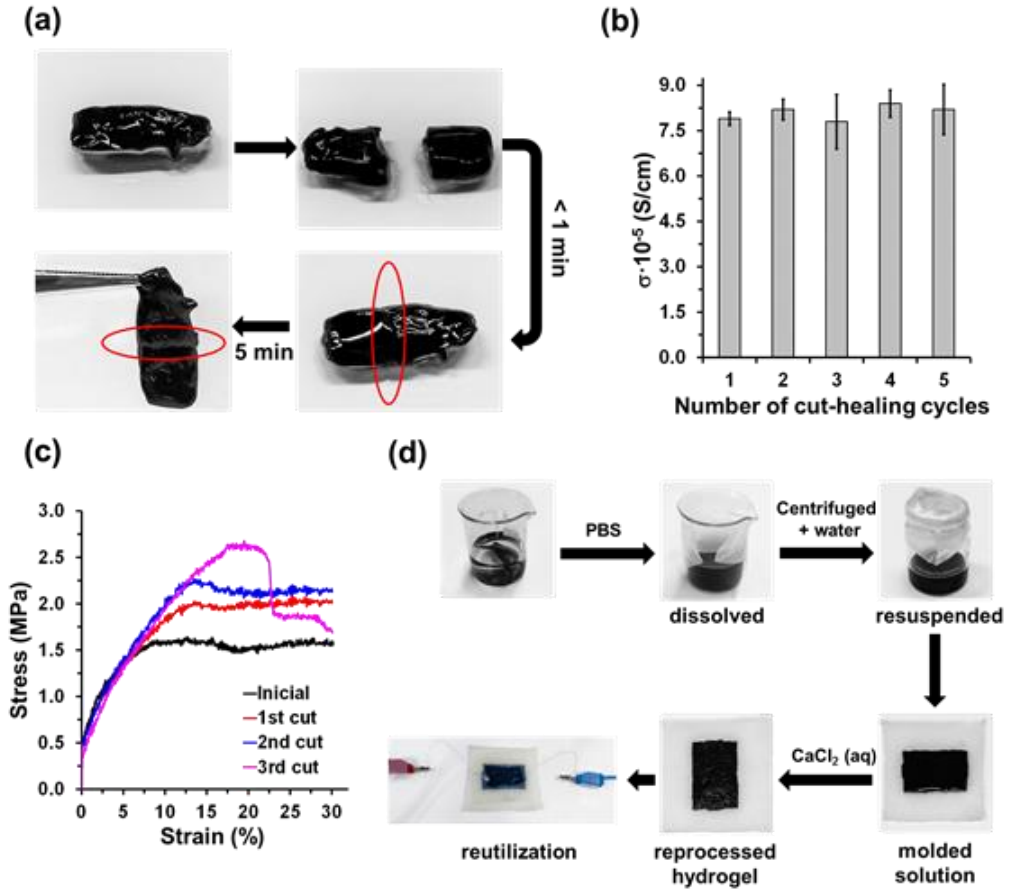

Figure 3.7.10. (a) Demonstration of the autonomous self-healing by the 1:3 PEDOT/Alg-h. The healed hydrogel can hold its own weight. (b) Electrical conductivity of the hydrogel as prepared and after successive cut-healing steps at different locations. (c) Strain-stress curves of the hydrogel as prepared and after successive cut-healing steps at the same location. (d) Disassembly-reprocessing steps for the reutilization of the 1:3 PEDOT/Alg-h as pressure sensor: dissolution of the hydrogel in PBS; centrifugation to recover both PEDOT and Alg; re-suspension and homogenization in water; and crosslinking in a silicon rubber mold by adding $CaCl_2$ 3 wt.% aqueous solution.

Figure 3.7.10a provides optical evidence of the self-healing ability of 1:3 PEDOT/Alg-h. When a hydrogel strip was cut into two halves by a scalpel and the freshly generated surfaces were brought into contact to allow autonomous healing, the segments merged very rapidly into one piece, adhering to each other with well-bonded interface in less than 1 min. After 5 min, the fused hydrogel can be lifted with tweezers or suspended between the two surfaces. On the other hand, the

conductivity of the self-healed hydrogel is practically identical to that of the original one, σ= 7.9(±0.3)·10^{-5} S/cm, demonstrating its excellent stability and reproducibility for practical applications. Successive cut and healing steps were carried out on the hydrogel at different locations, the restoration of the electrical conductivity confirming the repeatable electrical self-healing (Figure 3.7-10b).

Figure 3.7.10c shows nominal strain vs stress curves in tensile of 1:3 PEDOT/Alg-h strips that were submitted to successive cut and healing steps at the same location. The Young moduli of the pristine and the self-healed 1:3 PEDOT/Alg-h are in the range of 0.5-3.0 MPa, which are several orders of magnitude lower than those of conventional polymers. Besides, the elastic limit is higher for the self-healed hydrogels than for the pristine one. This has been attributed to the dynamics of the Ca^{2+}-mediated crosslinks, which favours the formation of entanglements between Alg-rich domains at the damaged regions. On the other hand, the strain (*e*) of the hydrogel is maintained at around 30% until the 3^{rd}-4^{th} cut-healing steps, depending on the sample. After this, the breakage is systematically observed at $e \approx$ 15%, indicating that the self-healing capacity of the same interfaces is limited. This should be attributed to the effects of the cut-healing steps on the distribution of charged groups at the healed interfaces. Thus, coulombic repulsions at such interfaces probably increase with the number of cut-healing steps due to the accumulation of Ca^{2+} and Alg chains. This favours the loss of stretchability and the rupture.

On the hand, the reusability of functional devices based on conductive hydrogels is still an unresolved challenge. It would be highly desirable that hydrogel-based electronic devices, such as pressure sensors, that have worn out and fails to work properly for different reasons (*e.g*. mechanical failure and dehydration) could be reused for the same electronic functionality using a simple procedure. This reusable capacity is significantly important for addressing the problem of recycling and reprocessing electronic devices, especially taking into

account the massive electronic waste produced worldwide. In addition, the reutilization of electronic products reduces the number of items to be manufactured, which in turn has a favourable impact on the conservation of natural resources and raw materials necessary for the manufacture of such products. In addition, once marketed, it is expected that reusable electronic products capable of maintaining their functionality will help consumers reduce costs compared to the purchase of single-use electronic items.

Although the development of reusable hydrogels has been recently claimed by different authors,[55,56] in such studies the term "*reusability*" was not associated to disassembling and reprocessing steps but to regeneration and recycling. Liu *et al* [55] restored the swelling property of polyacrylamide-alginate hydrogels for wearable force sensors, alleviating the fall of functionality induced by the structure shrinkage associated to the loss of water. However, this reusability, which was based on a simple rehydration by casting in water, should be considered simply as a clean regeneration treatment to preserve the functionality of the hydrogel. Instead, Pereira and coworkers,[56] proved the recycling ability of cellulose-based hydrogel sticker films, which were applied as electrolyte-gated sensors in transistors. In this case, the material was completely dissolved and, subsequently, reconstituted with the resulting solution. However, the electrical performance of the reprocessed hydrogel as electrolyte-gated sensor was worse than that of pristine hydrogel, suggesting that its recycling to a different application would be the most appropriated.

In this work the concept of reusable hydrogels has been clearly established and differentiated from regenerated and recyclable hydrogels. Thus, the conception of reusable hydrogels is not based on treatments to preserve the functionality of already formed hydrogels (*i.e.* regeneration) or the utilization of reconstituted hydrogels for applications other than the initial one due to a loss of properties (*i.e.* recycling) but on the use of the reprocessed hydrogel in its original application.

Figure 3.7.10d shows the steps followed in this work to disassemble an already prepared 1:3 PEDOT/Alg-h and, subsequently, reprocess it maintaining its properties. First, the hydrogel is submerged in a PBS solution with slight magnetic stirring until disassembly occurs and its components are incorporated into the solution. After this, the solution is centrifuged at 11000 rpm for 45 min at 4 ° C to recover both PEDOT and Alg. The mixture is re-suspended with 3 mL of water and, then, stirred to homogenize. The solution is poured into the silicone rubber mould and, finally, the crosslinking is carried out by adding $CaCl_2$ 3 wt.% aqueous solution. The reprocessed hydrogel can be reutilized as pressure sensor without loss of properties (Figure 3.7.11).

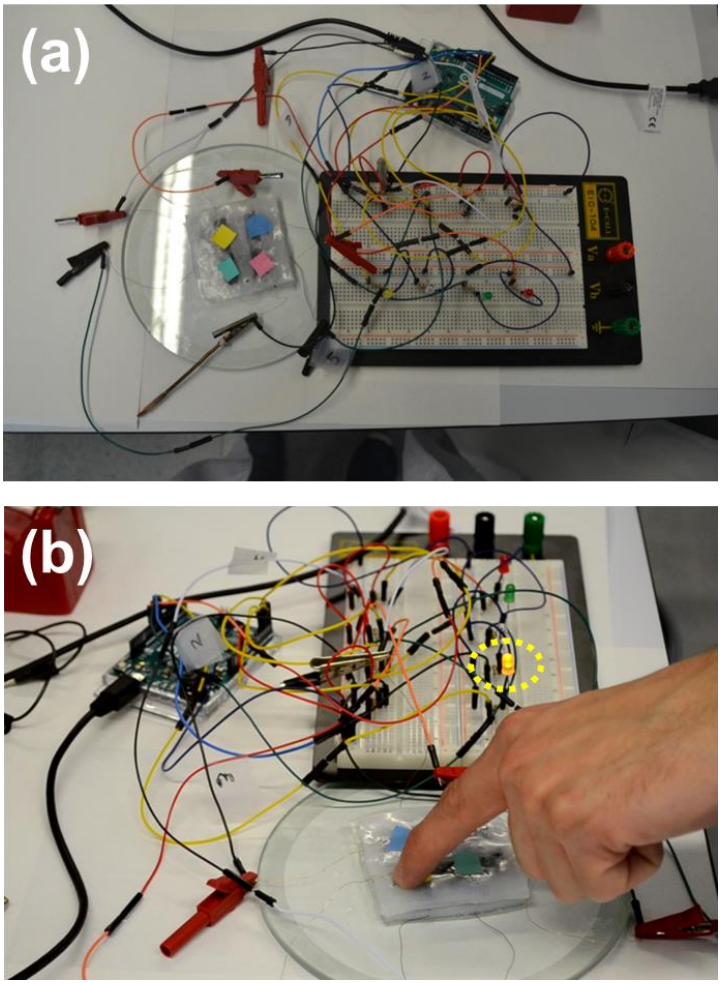

Figure 3.7.11. Demonstration of the sensing capacity of the reprocessed tactile pressure sensor array in terms of location and pressure of touches: (a) voltage divider device constructed using the reprocessed sensor array; and (b) demonstration of the sensing capacity of the reprocessed sensor array.

3.7.5 Conclusions

In summary, we demonstrated a flexible pressure sensor with fast response and good spatial resolution of the pressure distribution using a PEDOT-based hydrogel. This hydrogel was obtained by mixing a commercial PEDOT:PSS aqueous dispersion with an AA aqueous solution. The substitution of PSS by Alg as dopant agent, which is thermodynamically favoured as proved by DFT calculations, promotes the gelation process when the mixture enters in contact with a $CaCl_2$ solution. After characterization of the structure and properties of hydrogels derived from 3:1, 1:1 and 1:3 PEDOT:PSS/AA mixtures, the 1:3 hydrogel was found to be the most appropriated for the fabrication of sensors because of its mechanical integrity, ease of handling and dimensional stability. The internal structure of the 1:3 hydrogel with Alg-rich domains contacting conductive PEDOT-containing networks provides electrical percolation response and self-healing behaviour. The spatial resolution was proved using a 2×2 array as stretchable touch-pressure sensor that was able to control the illumination of LEDs. The sensor was reusable because of the reversibility of noncovalent Ca^{2+}-based crosslinks. Thus, the hydrogel was disassembled and, subsequently, reprocessed to be reused for the same application, which represents a step forward in terms of sustainability overcoming concepts such as regenerability and recyclability. Overall, demonstrations of the performance of 1:3 PEDOT/Alg-h as reusable sensitive pressure sensor further uncover the promising perspective of hydrogel wearable electronics for the cutting-edge human-electronic interfaces.

References

1. Chen, Fang, Chen, Qing, Song, Qun, Lu, Han & Ma, Mingming. Strong and Stretchable Polypyrrole Hydrogels with Biphase Microstructure as Electrodes for Substrate-Free Stretchable Supercapacitors. *Adv. Mater. Interfaces* **6**, 1900133 (2019).

2. Shih, Chien-Chung, Lin, Yan-Cheng, Gao, Mengyao, Wu, Mercedes, Hsieh, Hui-Ching, Wu, Nae-Lih & Chen, Wen-Chang. A rapid and green method for the fabrication of conductive hydrogels and their applications in stretchable supercapacitors. *J. Power Sources* **426**, 205–215 (2019).

3. Gan, Donglin, Han, Lu, Wang, Menghao, Xing, Wensi, Xu, Tong, Zhang, Hongping, Wang, Kefeng, Fang, Liming & Lu, Xiong. Conductive and Tough Hydrogels Based on Biopolymer Molecular Templates for Controlling in Situ Formation of Polypyrrole Nanorods. *ACS Appl. Mater. Interfaces* **10**, 36218–36228 (2018).

4. Spencer, Andrew R., Primbetova, Asel, Koppes, Abigail N., Koppes, Ryan A., Fenniri, Hicham & Annabi, Nasim. Electroconductive Gelatin Methacryloyl-PEDOT:PSS Composite Hydrogels: Design, Synthesis, and Properties. *ACS Biomater. Sci. Eng.* **4**, 1558–1567 (2018).

5. Deng, Zexing, Guo, Yi, Zhao, Xin, Ma, Peter X. & Guo, Baolin. Multifunctional Stimuli-Responsive Hydrogels with Self-Healing, High Conductivity, and Rapid Recovery through Host–Guest Interactions. *Chem. Mater.* **30**, 1729–1742 (2018).

6. Chen, Jingsi, Peng, Qiongyao, Thundat, Thomas & Zeng, Hongbo. Stretchable, Injectable, and Self-Healing Conductive Hydrogel Enabled by Multiple Hydrogen Bonding toward Wearable Electronics. *Chem. Mater.* **31**, 4553–4563 (2019).

7. Hu, Shiqian, Zhou, Lei, Tu, Lingjie, Dai, Cong, Fan, Lei, Zhang, Kejia, Yao, Tiantian, Chen, Junqi, Wang, Zhengao, Xing, Jun, Fu, Ruming, Yu, Peng, Tan, Guoxin, Du, Jianqiang & Ning, Chengyun. Elastomeric conductive hybrid hydrogels with continuous conductive networks. *J. Mater. Chem. B* **7**, 2389–2397 (2019).

8. Yang, Chunying, Zhang, Pengfei, Nautiyal, Amit, Li, Shihua, Liu, Na, Yin, Jialin, Deng, Kuilin & Zhang, Xinyu. Tunable Three-Dimensional

Nanostructured Conductive Polymer Hydrogels for Energy-Storage Applications. *ACS Appl. Mater. Interfaces* **11**, 4258–4267 (2019).

9. Chakraborty, Priyadarshi, Guterman, Tom, Adadi, Nofar, Yadid, Moran, Brosh, Tamar, Adler-Abramovich, Lihi, Dvir, Tal & Gazit, Ehud. A Self-Healing, All-Organic, Conducting, Composite Peptide Hydrogel as Pressure Sensor and Electrogenic Cell Soft Substrate. *ACS Nano* **13**, 163–175 (2019).

10. Guo, Baolin, Finne-Wistrand, Anna & Albertsson, Ann-Christine. Degradable and Electroactive Hydrogels with Tunable Electrical Conductivity and Swelling Behavior. *Chem. Mater.* **23**, 1254–1262 (2011).

11. Guo, Baolin, Finne-Wistrand, Anna & Albertsson, Ann-Christine. Versatile functionalization of polyester hydrogels with electroactive aniline oligomers. *J. Polym. Sci. Part A Polym. Chem.* **49**, 2097–2105 (2011).

12. Zhou, Kun, He, Yuan, Xu, Qingchi, Zhang, Qin'e, Zhou, An'an, Lu, Zihao, Yang, Li-Kun, Jiang, Yuan, Ge, Dongtao, Liu, Xiang Yang & Bai, Hua. A Hydrogel of Ultrathin Pure Polyaniline Nanofibers: Oxidant-Templating Preparation and Supercapacitor Application. *ACS Nano* **12**, 5888–5894 (2018).

13. Lu, Baoyang, Yuk, Hyunwoo, Lin, Shaoting, Jian, Nannan, Qu, Kai, Xu, Jingkun & Zhao, Xuanhe. Pure PEDOT:PSS hydrogels. *Nat. Commun.* **10**, 1043 (2019).

14. Yao, Bowen, Wang, Haiyan, Zhou, Qinqin, Wu, Mingmao, Zhang, Miao, Li, Chun & Shi, Gaoquan. Ultrahigh-Conductivity Polymer Hydrogels with Arbitrary Structures. *Adv. Mater.* **29**, 1700974 (2017).

15. Bubnova, Olga, Khan, Zia Ullah, Wang, Hui, Braun, Slawomir, Evans, Drew R., Fabretto, Manrico, Hojati-Talemi, Pejman, Dagnelund, Daniel, Arlin, Jean-Baptiste, Geerts, Yves H. *et al.* Semi-metallic polymers. *Nat. Mater.* **13**, 190–194 (2014).

16. Kayser, Laure V & Lipomi, Darren J. Stretchable Conductive Polymers and Composites Based on PEDOT and PEDOT:PSS. *Adv. Mater.* **31**, 1806133 (2019).

17. Sappia, Luciano D., Piccinini, Esteban, Marmisollé, Waldemar, Santilli, Natalia, Maza, Eliana, Moya, Sergio, Battaglini, Fernando, Madrid, Rossana

E. & Azzaroni, Omar. Integration of Biorecognition Elements on PEDOT Platforms through Supramolecular Interactions. *Adv. Mater. Interfaces* **4**, 1700502 (2017).

18. Groenendaal, L., Jonas, F., Freitag, D., Pielartzik, H. & Reynolds, J. R. Poly(3,4-ethylenedioxythiophene) and Its Derivatives: Past, Present, and Future. *Adv. Mater.* **12**, 481–494 (2000).

19. Lim, Ji-Eun, Lee, Sang-Mok, Kim, Seok-Soon, Kim, Tae-Woong, Koo, Hyun-Woo & Kim, Han-Ki. Brush-paintable and highly stretchable Ag nanowire and PEDOT:PSS hybrid electrodes. *Sci. Rep.* **7**, 14685 (2017).

20. Teo, Mei Ying, Kim, Nara, Kee, Seyoung, Kim, Bong Seong, Kim, Geunjin, Hong, Soonil, Jung, Suhyun & Lee, Kwanghee. Highly Stretchable and Highly Conductive PEDOT:PSS/Ionic Liquid Composite Transparent Electrodes for Solution-Processed Stretchable Electronics. *ACS Appl. Mater. Interfaces* **9**, 819–826 (2017).

21. Li, Yuda, Liu, Meiyue, Li, Yuan, Yuan, Kai, Xu, Lijia, Yu, Wei, Chen, Runfeng, Qiu, Xueqing & Yip, Hin-Lap. Perovskite Solar Cells: Poly(3,4-Ethylenedioxythiophene): Methylnaphthalene Sulfonate Formaldehyde Condensate: The Effect of Work Function and Structural Homogeneity on Hole Injection/Extraction Properties (Adv. Energy Mater. 6/2017). *Adv. Energy Mater.* **7**, (2017).

22. Stöcker, Thomas, Köhler, Anna & Moos, Ralf. Why does the electrical conductivity in PEDOT:PSS decrease with PSS content? A study combining thermoelectric measurements with impedance spectroscopy. *J. Polym. Sci. Part B Polym. Phys.* **50**, 976–983 (2012).

23. Taccola, Silvia, Greco, Francesco, Sinibaldi, Edoardo, Mondini, Alessio, Mazzolai, Barbara & Mattoli, Virgilio. Toward a New Generation of Electrically Controllable Hygromorphic Soft Actuators. *Adv. Mater.* **27**, 1668–1675 (2015).

24. Feig, Vivian Rachel, Tran, Helen, Lee, Minah, Liu, Kathy, Huang, Zhuojun, Beker, Levent, Mackanic, David G. & Bao, Zhenan. An Electrochemical Gelation Method for Patterning Conductive PEDOT:PSS Hydrogels. *Adv. Mater.* **31**, 1902869 (2019).

25. Zhang, Shiming, Chen, Yihang, Liu, Hao, Wang, Zitong, Ling, Haonan,

Wang, Changsheng, Ni, Jiahua, Çelebi-Saltik, Betül, Wang, Xiaochen, Meng, Xiang, Kim, Han-Jun, Baidya, Avijit, Ahadian, Samad, Ashammakhi, Nureddin, Dokmeci, Mehmet R., Travas-Sejdic, Jadranka & Khademhosseini, Ali. Room-Temperature-Formed PEDOT:PSS Hydrogels Enable Injectable, Soft, and Healable Organic Bioelectronics. *Adv. Mater.* **32**, 1904752 (2020).

26. Wang, Zhiyong, Wang, Tao, Zhuang, Mengdi & Xu, Hangxun. Stretchable Polymer Composite with a 3D Segregated Structure of PEDOT:PSS for Multifunctional Touchless Sensing. *ACS Appl. Mater. Interfaces* **11**, 45301–45309 (2019).

27. Beduk, Tutku, Bihar, Eloise, Surya, Sandeep G., Castillo, Aminta N., Inal, Sahika & Salama, Khaled N. A paper-based inkjet-printed PEDOT:PSS/ZnO sol-gel hydrazine sensor. *Sensors Actuators B Chem.* **306**, 127539 (2020).

28. Wang, Jer-Chyi, Karmakar, Rajat Subhra, Lu, Yu-Jen, Chan, Shun-Hsiang, Wu, Ming-Chung, Lin, Kun-Ju, Chen, Chin-Kuo, Wei, Kuo-Chen & Hsu, Yung-Hsin. Miniaturized Flexible Piezoresistive Pressure Sensors: Poly(3,4-ethylenedioxythiophene):Poly(styrenesulfonate) Copolymers Blended with Graphene Oxide for Biomedical Applications. *ACS Appl. Mater. Interfaces* **11**, 34305–34315 (2019).

29. Zhou, Qinqin, Teng, Weili, Jin, Yuhong, Sun, Ling, Hu, Peng, Li, Hongyi, Wang, Lianzhou & Wang, Jinshu. Highly-conductive PEDOT:PSS hydrogel framework based hybrid fiber with high volumetric capacitance and excellent rate capability. *Electrochim. Acta* **334**, 135530 (2020).

30. Teo, Mei Ying, RaviChandran, Narrendar, Kim, Nara, Kee, Seyoung, Stuart, Logan, Aw, Kean C. & Stringer, Jonathan. Direct Patterning of Highly Conductive PEDOT:PSS/Ionic Liquid Hydrogel via Microreactive Inkjet Printing. *ACS Appl. Mater. Interfaces* **11**, 37069–37076 (2019).

31. Lee, Kuen Yong & Mooney, David J. Alginate: Properties and biomedical applications. *Prog. Polym. Sci.* **37**, 106–126 (2012).

32. Braccini, Isabelle & Pérez, Serge. Molecular Basis of Ca2+-Induced Gelation in Alginates and Pectins: The Egg-Box Model Revisited. *Biomacromolecules* **2**, 1089–1096 (2001).

33. Frisch, M. & Clemente, F. Gaussian 09, Revision A. 01, MJ Frisch, GW

Trucks, HB Schlegel, GE Scuseria, MA Robb, JR Cheeseman, G. *Scalmani, V. Barone, B. Mennucci, GA Petersson, H. Nakatsuji, M. Caricato, X. Li, HP Hratchian, AF Izmaylov, J. Bloino, G. Zhe* (2009).

34. Zhao, Yan & Truhlar, Donald G. A new local density functional for main-group thermochemistry, transition metal bonding, thermochemical kinetics, and noncovalent interactions. *J. Chem. Phys.* **125**, 194101 (2006).

35. Zhao, Yan & Truhlar, Donald G. The M06 suite of density functionals for main group thermochemistry, thermochemical kinetics, noncovalent interactions, excited states, and transition elements: two new functionals and systematic testing of four M06-class functionals and 12 other function. *Theor. Chem. Acc.* **120**, 215–241 (2008).

36. Miertuš, S., Scrocco, E. & Tomasi, J. Electrostatic interaction of a solute with a continuum. A direct utilizaion of AB initio molecular potentials for the prevision of solvent effects. *Chem. Phys.* **55**, 117–129 (1981).

37. Miertuš̃, S. & Tomasi, J. Approximate evaluations of the electrostatic free energy and internal energy changes in solution processes. *Chem. Phys.* **65**, 239–245 (1982).

38. Ocampo, Cintia, Oliver, Ramon, Armelin, Elaine, Alemán, Carlos & Estrany, Francesc. Electrochemical Synthesis of Poly(3,4-ethylenedioxythiophene) on Steel Electrodes: Properties and Characterization. *J. Polym. Res.* **13**, 193–200 (2006).

39. Hua, Shuibo, Ma, Haizhen, Li, Xun, Yang, Huixia & Wang, Aiqin. pH-sensitive sodium alginate/poly(vinyl alcohol) hydrogel beads prepared by combined Ca2+ crosslinking and freeze-thawing cycles for controlled release of diclofenac sodium. *Int. J. Biol. Macromol.* **46**, 517–523 (2010).

40. Shakoor, Abdul & Rizvi, Tasneem Zahra. Raman spectroscopy of conducting poly (methyl methacrylate)/polyaniline dodecylbenzenesulfonate blends. *J. Raman Spectrosc.* **41**, 237–240 (2010).

41. Salvatierra, Rodrigo V, Moura, Luciano G., Oliveira, Marcela M., Pimenta, Marcos A. & Zarbin, Aldo J. G. Resonant Raman spectroscopy and spectroelectrochemistry characterization of carbon nanotubes/polyaniline thin film obtained through interfacial polymerization. *J. Raman Spectrosc.*

43, 1094–1100 (2012).

42. Han, Yu-Kai, Chang, Mei-Ying, Huang, Wen-Yao, Pan, Hsin-Yu, Ho, Ko-Shan, Hsieh, Tar-Hwa & Pan, Sin-Yu. Improved Performance of Polymer Solar Cells Featuring One-Dimensional {PEDOT} Nanorods in a Modified Buffer Layer. *J. Electrochem. Soc.* **158**, K88 (2011).

43. Farah, Abdiaziz A., Rutledge, Steven A., Schaarschmidt, Antje, Lai, Roger, Freedman, Justin P. & Helmy, Amr S. Conductivity enhancement of poly(3,4-ethylenedioxythiophene)-poly(styrenesulfonate) films post-spincasting. *J. Appl. Phys.* **112**, 113709 (2012).

44. Koburger, Susanne, Bannerman, Alistair, Grover, Liam M., Müller, Frank A., Bowen, James & Paxton, Jennifer Z. A novel method for monitoring mineralisation in hydrogels at the engineered hard-soft tissue interface. *Biomater. Sci.* **2**, 41–51 (2014).

45. Sun, Bingjie, Wang, Zhijian, He, Qiguang, Fan, Wei & Cai, Shengqiang. Porous double network gels with high toughness{,} high stretchability and fast solvent-absorption. *Soft Matter* **13**, 6852–6857 (2017).

46. Shi, Xiao-Ning, Wang, Wen-Bo & Wang, Ai-Qin. Effect of surfactant on porosity and swelling behaviors of guar gum-g-poly(sodium acrylate-co-styrene)/attapulgite superabsorbent hydrogels. *Colloids Surfaces B Biointerfaces* **88**, 279–286 (2011).

47. Bodenberger, Nicholas, Kubiczek, Dennis, Abrosimova, Irina, Scharm, Annika, Kipper, Franziska, Walther, Paul & Rosenau, Frank. Evaluation of methods for pore generation and their influence on physio-chemical properties of a protein based hydrogel. *Biotechnol. reports (Amsterdam, Netherlands)* **12**, 6–12 (2016).

48. Müller, Franciélli, Ferreira, Carlos A., Azambuja, Denise S., Alemán, Carlos & Armelin, Elaine. Measuring the proton conductivity of ion-exchange membranes using electrochemical impedance spectroscopy and through-plane cell. *J. Phys. Chem. B* **118**, 1102–1112 (2014).

49. Gualandi, Isacco, Tonelli, Domenica, Mariani, Federica, Scavetta, Erika, Marzocchi, Marco & Fraboni, Beatrice. Selective detection of dopamine with an all PEDOT:PSS Organic Electrochemical Transistor. *Sci. Rep.* **6**, 35419 (2016).

50. Aradilla, David, Azambuja, Denise, Estrany, Francesc, Casas, Maria T., Ferreira, Carlos A. & Alemán, Carlos. Hybrid polythiophene–clay exfoliated nanocomposites for ultracapacitor devices. *J. Mater. Chem.* **22**, 13110–13122 (2012).

51. Darabi, Mohammad Ali, Khosrozadeh, Ali, Mbeleck, Rene, Liu, Yuqing, Chang, Qiang, Jiang, Junzi, Cai, Jun, Wang, Quan, Luo, Gaoxing & Xing, Malcolm. Skin-Inspired Multifunctional Autonomic-Intrinsic Conductive Self-Healing Hydrogels with Pressure Sensitivity, Stretchability, and 3D Printability. *Adv. Mater.* **29**, 1700533 (2017).

52. Shao, Changyou, Wang, Meng, Meng, Lei, Chang, Huanliang, Wang, Bo, Xu, Feng, Yang, Jun & Wan, Pengbo. Mussel-Inspired Cellulose Nanocomposite Tough Hydrogels with Synergistic Self-Healing, Adhesive, and Strain-Sensitive Properties. *Chem. Mater.* **30**, 3110–3121 (2018).

53. Augst, Alexander D., Kong, Hyun Joon & Mooney, David J. Alginate Hydrogels as Biomaterials. *Macromol. Biosci.* **6**, 623–633 (2006).

54. Alegre-Requena, Juan V, Häring, Marleen, Herrera, Raquel P. & Díaz Díaz, David. Regulatory parameters of self-healing alginate hydrogel networks prepared via mussel-inspired dynamic chemistry. *New J. Chem.* **40**, 8493–8501 (2016).

55. Liu, Hao, Li, Moxiao, Ouyang, Cheng, Lu, Tian Jian, Li, Fei & Xu, Feng. Biofriendly, Stretchable, and Reusable Hydrogel Electronics as Wearable Force Sensors. *Small* **14**, 1801711 (2018).

56. Cunha, Inês, Barras, Raquel, Grey, Paul, Gaspar, Diana, Fortunato, Elvira, Martins, Rodrigo & Pereira, Luís. Reusable Cellulose-Based Hydrogel Sticker Film Applied as Gate Dielectric in Paper Electrolyte-Gated Transistors. *Adv. Funct. Mater.* **27**, 1606755 (2017).

3.8 Electroresponsive Alginate-Based Hydrogel for Controlled Release of Hydrophobic Drugs

3.8.1 Summary

Stimuli-responsive biomaterials have attracted significant attention for the construction of on-demand drug release systems. The possibility of using external stimulation to trigger drug release is particularly enticing for hydrophobic compounds, which are not easily released by simple diffusion. In this work, an electrochemically active hydrogel, which has been prepared by gelling a mixture of poly(3,4-ethylenedioxythiophene): polystyrene sulfonate (PEDOT:PSS) and alginate (Alg), has been loaded with curcumin (CUR), a hydrophobic drug with a wide spectrum of clinical applications. The PEDOT/Alg hydrogel is electrochemically active and organizes as segregated PEDOT- and Alg-rich domains, explaining its behaviour as an electroresponsive drug delivery system. When loaded with CUR, the hydrogel demonstrates a controlled drug release upon application of a negative electrical voltage. Comparison with the release profiles obtained applying a positive voltage and in absence of electrical stimuli, indicates that the release mechanism dominating this system is complex due not only to the intermolecular interactions between the drug and the polymeric network but also to the loading of a hydrophobic drug in a water-containing delivery system.

3.8.2 Introduction

Intrinsically conducting polymers (CPs) have gained much attention as materials capable of stimuli-responsive drug delivery [1-6]. Among CPs, poly(3,4-ethylenedioxythiophene) (PEDOT) has evolved as a highly promising platform for delivering therapeutic agents, as it has excellent electroactive properties, stability, biocompatibility and is relatively simple to prepare [7-12]. Tunable drug release from PEDOT is based on electrically driven alterations in redox state, causing subsequent changes in polymer properties (*e.g.* changes in volume and hydrophilic/hydrophobic balance) [13]. Moreover, PEDOT has been used for drug delivery from carriers in different formats, for example, PEDOT nanoparticles [14,15], fibers [16-18], films [19-22], and hydrogels [23-25].

Hydrogels-based delivery systems can leverage therapeutic beneficial outcomes and have found clinical use. This is because hydrogels not only can provide spatial and temporal control over the release of small molecules and macromolecular drugs [26-33], but also exhibit tunable physical properties, controllable degradability, the capability to protect labile drugs from degradation and responsiveness to external stimuli. Therefore, hydrogels can serve as potential drug delivery platforms in which the release of loaded drugs is controlled by physicochemical interactions that can be easily modified by physical parameters (*e.g.* voltage, light, and temperature). Despite such interesting properties, the amount of drug release studies involving PEDOT-based hydrogels is very scarce [23-25,33]. Kleber *et al.* [23] studied the release of fluorescein and dexamethasone from iridium oxide electrodes coated by a conducting hydrogel that was obtained by photo-crosslinking poly(dimethylacrylamide-*co*-4-methacryloyloxy benzophenone-*co*-4-styrenesulfonate) and, subsequently, electropolymerizing PEDOT through the hydrogel network. Molina *et al.* [24] regulated the release of vitamin K3 from a semi-interpenetrated hydrogel prepared by electropolymerizing a hydrophilic

PEDOT derivative within a poly-γ-glutamic acid biohydrogel containing PEDOT nanoparticles. Zhang and co-workers [25] formed hydrogels by mixing a β-cyclodextrin polymer solution with a dispersion of PEDOT, which was obtained by oxidative polymerization in the presence of adamantyl-modified sulfate alginate. This matrix was used to encapsulate and to proliferate myoblast cells, which were released by adding the β-cyclodextrin monomer. On the other hand, Chikar *et al.* [33] formed a dual coating system by depositing an RGD-functionalized alginate hydrogel on an electrode previously coated with PEDOT. Interestingly, a trophic factor loaded inside the hydrogel was released by electrostimulating the coated electrode.

In this study, a new PEDOT-based electroactive hydrogel is explored as a carrier platform for electrically triggered drug delivery. The hydrogel is easily prepared by mixing polystyrenesulfonate-doped PEDOT (PEDOT:PSS), a biocompatible CP widely used for bioelectronics and tissue engineering,[34-37] and alginic acid (AA) aqueous solution. Although alginate-based hydrogels are extensively used in biomedicine [38-40], the incorporation of CP confers electric-field responsive properties to the resulting material, hereafter named PEDOT/Alg-h. Drug delivery assays have been conducted using curcumin (CUR), a hydrophobic compound with a wide spectrum of biological and pharmacological activity, such as antioxidant, anti-inflammatory, antimicrobial, anticarcinogenic, hepatic- and nephroprotective, and hypoglycemic effects, among others [41-45]. The release of *in situ* loaded CUR is controlled by applying a potential of –1.0 V to the hydrogel. Due to the advantages associated with the simplicity of the synthetic and loading processes, the outstanding properties of the hydrogel, and its response to the electric field for the dosage-controlled release of a drug, PEDOT/Alg-h should be considered as a promising carrier for on-demand release of bioactive substances.

3.8.3 Methods

3.8.3.1 Materials

PEDOT:PSS 1.3 wt. % dispersion in H2O, alginic acid (AA) from Macrocystis pyrifera (61% mannuronic acid and 39% guluronic acid; MW= 240 kDa), curcumin (CUR), Indium tin oxide coated polyethylene terephthalate films and ethanol (99%) were purchased from Sigma-Aldrich, while CaCl2 was purchased from Scharlab.

For cell culture experiments, fibroblast derived human normal skin (Hff) and fibroblast derived from osteosarcoma (MG-63) cells were selected and purchased from ATCC (USA). Dulbecco's phosphate buffered saline (PBS) solution without calcium chloride and magnesium chloride, Dulbecco's modified Eagle's medium (DMEM, with 4500 mg L−1 glucose, 110 mg L−1 sodium pyruvate and 2 mM L-glutamine), penicillin–streptomycin, 3-(4,5-dimethylthiazol-2-yl)2,5-diphenyltetrazolium bromide (MTT, 97.5%) and trypsin EDTA solution (0.05% trypsin, 0.02% EDTA) were purchased from Sigma-Aldrich (USA). Fetal bovine serum (FBS) was purchased from Gibco (UK).

3.8.3.2 Preparation of hydrogels

The four hydrogels prepared in this work are:

- PEDOT/Alg-h: hydrogel obtained by mixing PEDOT:PSS and AA aqueous solution;
- PEDOT/Alg(CUR)-h: CUR-loaded PEDOT/Alg-h;
- Alg-h: control hydrogel obtained by gelling a AA solution;
- Alg(CUR)-h (CUR-loaded control Alg-h).

PEDOT/Alg-h. The unloaded hydrogel was prepared by dissolving AA (1.6 g) in a mixture of deionized water and ethanol (16 and 4 mL, respectively) at 50 ºC with vigorous stirring for 1 h. After this, the resulting AA solution was mixed with 20 mL of the 1.3 wt% PEDOT:PSS dispersion at room temperature with vigorous stirring for 20 min. 0.7 mL of the PEDOT:PSS + AA mixture were deposited on a indium thin oxide (ITO) coated polyethylene terephthalate (PET) sheet (4×2 cm^2), which was sandwiched between two cover glasses separated (1 mm) by plastic sheets. This sandwich was introduced in a petri dish that was, subsequently, filled with 10 wt.% $CaCl_2$ aqueous solution for gelation.

PEDOT/Alg(CUR)-h. The hydrogel loaded with CUR was prepared using the procedure described for PEDOT/Alg-h but dissolving previously the CUR (20 mg) in the ethanol (4 mL) used to prepare the AA solution. The concentration of CUR loaded in the resulting hydrogel was of 0.5 mg/mL.

Alg-h. AA (0.8 g) was dissolved in a mixture of deionized water and ethanol (18 and 2 mL, respectively) at 50 ºC with vigorous stirring for 1 h. The gelling process was performed with $CaCl_2$, as described for PEDOT/Alg-h.

Alg(CUR)-h. For the CUR-loaded control hydrogel, the drug (10 mg) was previously dissolved in the ethanol (2 mL). Then, the resulting solution was employed to prepare the AA solution using the procedure described for Alg-h, which was gelled with a 10 wt.% $CaCl_2$ aqueous solution.

3.8.3.3 Cell Viability

Cellular assays were performed using fibroblast from skin (Hff) and osteosarcoma (MG-63) cells. Cells were cultured in DMEM supplemented with 15% FBS, penicillin (100 units/mL), and streptomycin (100 µg/mL). The cultures were maintained in a humidified incubator with an atmosphere of 5% CO2 and 95% O2 at 37 ºC. Culture media were changed every two days.

Small hydrogel squares (1 × 1 cm^2) were attached to the 24-well polystyrene plates using biocompatible silicon and sterilized using UV irradiation for 15 min in a laminar flux cabinet. Our control (Ctrl) group were the bare polystyrene wells. For adhesion and proliferation assays 1 mL of 40000 and 20000 cells/mL were deposited, respectively, on each well. After 24 h, an [3-(4, 5-dimethylthiazol-2-yl)-2, 5-diphenyltetrazolium bromide] assay (MTT) was performed to quantify the cell adhesion and after 7 days to evaluate the cell proliferation rate.

Cell viability was evaluated by the colorimetric MTT assay. This assay measures the ability of the mitochondrial dehydrogenase enzyme of viable cells to cleave the tetrazolium rings of the MTT and form formazan crystals, which are impermeable to cell membranes and, therefore, are accumulated in healthy cells. This process is detected by a color change: the characteristic pale yellow of MTT transforms into the dark-blue of formazan crystals. Specifically, 1 mL of MTT solution in DMEM were added to each well. After 2 h of incubation, samples were washed three times with PBS supplemented with 2 mM $CaCl_2$. In order to dissolve formazan crystals, 1 mL of DMSO/methanol/water (70/20/10 % v/v) was added. Finally, the absorbance was measured in a plate reader at 570 mm. The viability results, derived from the average of four replicates (n= 4) for each independent experiment, were normalized to the control, for relative percentages. Statistical analysis was performed using two-way ANOVA with a Tukey's multiple comparison test.

3.8.3.4 Characterization

FTIR spectra were recorded on a Jasco 4100 spectrophotometer through an attenuated total reflection accessory (Top-plate) with a diamond crystal (Specac model MKII Golden Gate Heated Single Reflection Diamond ATR). Samples were

evaluated using spectra manager software and, for each sample 64 scans were performed between 4000 and 600 cm^{-1} with a resolution of 4 cm^{-1}.

The swelling rate (SR) was determined using distillate water. First, hydrogels were lyophilized by freeze-drying and weighted. Then, they were immersed in distilled water for 24 h (for measurements of water uptake). After that, the wet hydrogels were quickly wiped to remove the surface water with filter paper, and their weights were scored again. SR was calculated as:

$$\mathrm{SR} = \frac{\mathrm{W}_w - W_d}{W_d} \times 100 \qquad \text{(E.3.8.1.)}$$

where W_w is the weight of the swelled hydrogel and W_d is the weight of the lyophilized hydrogel. Three independent measurements were carried using similar sized samples to check for reproducibility. The average values of four replicas were expressed in all cases.

The morphology of the prepared hydrogels was examined by scanning electron microscopy (SEM) using a Focused Ion Beam Zeiss Neon40 scanning electron microscope equipped with an energy dispersive X-ray (EDX) spectroscopy system and operating at 5 kV. All samples were sputter-coated with a thin carbon layer using a K950X Turbo Evaporator to prevent electron charging problems. Prior to SEM observation, samples were lyophilized (*i.e.* freeze-drying).

Transmission electron microscopy (TEM) studies were performed using a JEOL J1010 (filament: tungsten) equipped with a Gatan *Orius* 1000 slow scan *CCD* and the *DigitalMicrograph* (Gatan) software. The accelerating voltage was 80 kV. A Sorvall Porter-Blum microtome (Sorwall, NT, USA) equipped with a diamond knife was used to cut the sample in thin sections that were subsequently lifted onto carbon-coated grids.

Electrochemical characterization by cyclic voltammetry (CV) and galvanostatic charge-discharge (GCD) was performed using a microcomputer-controlled potentiostat/galvanostat Autolab with PGSTAT101 equipment and Anova

software. All assays were performed at room temperature using a three-electrode one compartment configuration cell. The cell was filled with 5 mL of $CaCl_2$ 5% wt. aqueous solution, as supporting electrolyte. The ITO-coated PET sheet covered with the hydrogel was used as working electrode, Ag|AgCl|KCl (3 mol/L) as the reference electrode, and a silver wire as counter electrode.

In all CV experiments the potential was scanned from -0.20 to 0.60 V at a scan rate of 100 mV/s. The ability to exchange charge reversibly (*i.e*. the electrochemical activity) and the electrochemical stability were determined through direct measurement of the anodic and cathodic areas in the control voltammograms. The loss of electroactivity (LEA, in %) was expressed as:

$$\text{LEA}\ (\%)\ \frac{\Delta Q}{Q_i} \times 100 \quad \text{(E.3.8.2)}$$

where ΔQ is the difference in voltammetric charges (in C) between the second and the last cycle, and Q_i is the voltammetric charge corresponding to the second cycle.

For GCD experiments, the potential was varied between 0.0 and 0.8 or 1.0 V at different current densities (*i.e.* 1.0, 1.5 and 2.0 μA/cm^2). The areal capacitance was calculated from GCD curves recorded in a three-electrode system (Eq. E.3.8.3):

$$C = \frac{I\, t_d}{A\, \Delta V} \quad \text{(E.3.8.3)}$$

where I is the applied current, t_d is the discharge time, ΔV is the potential window and A the surface area (geometric area) of the hydrogel.

3.8.3.5 Drug release

Washed PEDOT/Alg(CUR)-h and Alg(CUR)-h were cut into small squares (1×1 cm^2) and placed into Eppendorfs. Then, 1mL of the release medium, which consisted of 5 % wt. $CaCl_2$ aqueous solution, was added. Eppendorfs were maintained at 37 ºC under agitation (80 rpm). At selected time intervals (*i.e.* 15 min, 30 min, 1 h, 1 day, 2 days and 9 days), 1 mL of each tube was extracted and

deposited into a new Eppendorf in order to be quantified afterwards. Subsequently, the sample containing Eppendorf was supplemented with 1 mL of the liberation medium to keep the volume. Quantification was performed by measuring the absorbance at 400 nm using an EZ Read 400 microplate reader.

After 9 days, samples were taken from the Eppendorf with the aqueous solution and deposited into new Eppendorf with 1 mL of ethanol (99%). Quantification of the released CUR was performed after 2 and 4 days using the procedure described above.

Calibration curves in 5 % wt. $CaCl_2$ aqueous solution and ethanol were obtained using CUR concentrations ranging from 1.0 to 62.5 μg/mL.

3.8.3.6 Effects of the electrical voltage on drug release

A three electrodes configuration was used: the glassy carbon bar coated with the corresponding hydrogel, PEDOT/Alg(CUR)-h or Alg(CUR)-h, as a working electrode, a bar of glassy carbon as counter electrode, and Ag | AgCl as reference electrode. 2.5 mL of 5 % wt. $CaCl_2$ aqueous solution was used as electrolytic medium. A constant electrical voltage was applied for 2 h, interrupting for *ca*. 5 min to extract every 15 min to: 1) extract 1 mL of electrolytic medium for release quantification; 2) supplemented with 1 mL of the liberation medium to keep the volume in the cell; and 3) record a cyclic voltammetry. Quantification was performed by determined the absorbance at 400 nm using an EZ Read 400 microplate reader. All the measures were performed at 37 ºC and repeated at least six times.

3.8.4 Results and discussion

3.8.4.1 Preparation of unloaded and drug-loaded hydrogels

The process used to prepare PEDOT/Alg-h is sketched in Figure 3.8.1a. More specifically, equal volumes (20 mL) of a 1.3 wt.% PEDOT:PSS aqueous dispersion and an 8 wt.% alginic acid (AA) water:ethanol (4:1 v/v) solution were mixed at room temperature with vigorous stirring for 20 min. To prepare hydrogel films with a controlled, reproducible and homogeneous thickness, an indium tin oxide (ITO) coated polyethylene terephthalate (PET) sheet (4 cm × 2 cm x 0.01 cm) was sandwiched between two cover glasses separated 1 mm by plastic strips, which allowed creating a cavity with a defined volume. Then, a fixed volume of the PEDOT:PSS + AA mixture (0.7 mL) was introduced in the cavity to get films with reproducible thicknesses (see Figure 3.8.1). Finally, the previous assembly was immersed in a petri dish containing a 10 wt.% $CaCl_2$ aqueous solution to gel the mixture and obtain the hydrogel. The assembly was kept in the $CaCl_2$ solution for at least 24 h to assure complete gelation. The excess of AA and the leaving PSS chains (*i.e.* those replaced by Alg) were removed from the hydrogel by thoroughly washing it with abundant water. After disassembling, the hydrogels remained onto the ITO-coated PET sheet for the electrochemical studies.

CUR-loaded PEDOT/Alg-h samples, hereafter named PEDOT/Alg(CUR)-h, were obtained by applying the previous procedure but using a CUR ethanol solution (5 mg/mL) for preparing the 8 wt.% AA water:ethanol (4:1 v/v) solution. Besides, CUR-loaded and unloaded alginate hydrogels, hereafter abbreviated Alg(CUR)-h and Alg-h, respectively, were used as controls. Alg(CUR)-h was obtained by gelling with $CaCl_2$ (10 wt.%; 24 h) a 4 wt.% AA water:ethanol (9:1 v/v) solution, which was prepared again using the CUR ethanol solution. Alg-h was attained using the same procedure detailed above but without including CUR in the ethanol used to prepare the AA solution. After the crosslinking, the

concentration of CUR loaded in both PEDOT/Alg(CUR)-h and Alg(CUR)-h was 0.492 ± 0.005 and 0.474 ± 0.006 mg/mL, respectively. A complete description of the procedures used to prepare PEDOT/Alg-h, PEDOT/Alg(CUR)-h, Alg-h, and Alg(CUR)-h, which are shown in Figure 3.8.1b, is provided in the methods section. The dark blue color of PEDOT/Alg-h and PEDOT/Alg(CUR)-h corresponds to the color of PEDOT:PSS, which dominates over those of Alg and CUR. Instead, translucent Alg-h samples become opaque and orange when CUR loads.

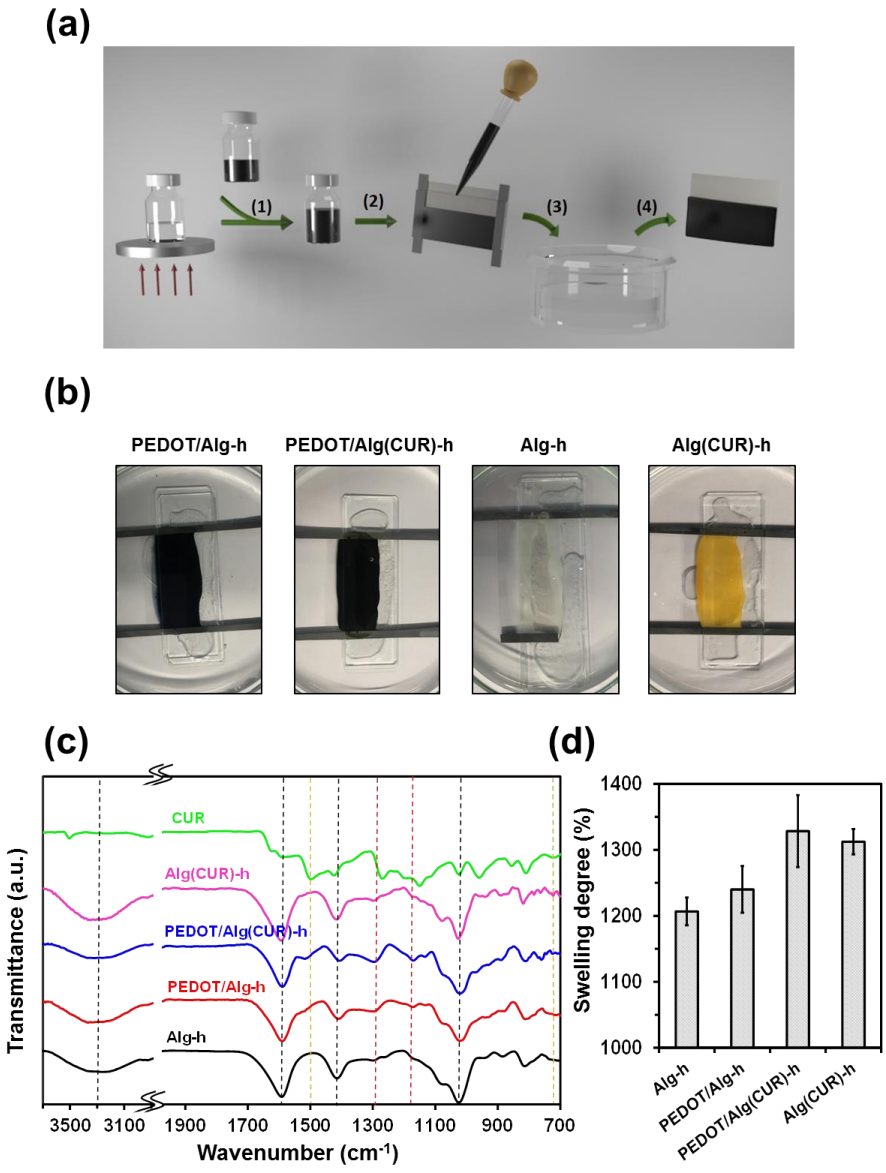

Figure 3.8.1. (a) Sketch illustrating the procedure used to prepare PEDOT/Alg(CUR)-h: (1) equal volumes of PEDOT:PSS aqueous dispersion and AA solution in water:ethanol were mixed; (2) 0.7 mL of the PEDOT:PSS + AA mixture were deposited on a ITO sheet, which was subsequently sandwiched between two cover glasses separated by plastic strips; (3) the sandwiched ITO

sheet was placed in a petri dish that was subsequently filled with a $CaCl_2$ solution; and (4) the formed hydrogels were extracted and washed after 24 h. (b) Photographs of the prepared hydrogels just after the gelling step. (c) FTIR spectra and (d) swelling ratio of the prepared hydrogels.

All hydrogels were initially characterized by FTIR spectroscopy. Structural fingerprints of all the components in the hydrogel were identified in the spectra (Figure 3.8.1c). Thus, all spectra show the following absorption bands characteristic of alginate hydrogels: (1) asymmetric and symmetric C=O stretching (1597 and 1413 cm^{-1}, respectively), C–O–C stretching (1028 cm^{-1}) and O–H stretching (broad band at ~3300 cm^{-1}) [46]. In contrast, PEDOT-containing hydrogels show additional bands at 1289 and 1127 cm^{-1} (vibrations of the fused dioxane ring) and 761 cm^{-1} (stretch of the C–S bond). Moreover, the band at 1162 cm^{-1} has been associated with the S–O vibrations of residual PSS chains (*i.e.* those that were not substituted by the Alg chains). Finally, even though some of the characteristic bands of CUR overlap with those of PEDOT and specially those of alginate, CUR presence is also detected in the FTIR spectra of PEDOT/Alg(CUR)-h and Alg(CUR)-h. The peaks at 1522 and 756 cm^{-1} can be attributed to the C=O stretching and *cis*-CH vibration of CUR, which proves the incorporation of the drug in PEDOT/Alg(CUR)-h and Alg(CUR)-h.

The swelling ratio (SR), which expresses the ability to absorb water, was very high for all evaluated hydrogels (Figure 3.8.1d). The SR for Alg-h and PEDOT/Alg-h were similar (*i.e.* 1207% ± 21% and 1240% ± 35%, respectively) suggesting that the crosslinking density is comparable for both systems. According to the classical "*egg-box*" model, chain-chain associations in Alg-h occur by the ionic binding of each divalent Ca^{2+} ion with two alginate chains through the corresponding guluronate blocks [47]. Apparently, this binding model does not undergo major alterations by oxidized PEDOT chains, which are positively charged, and can compete with Ca^{2+} ions for interacting with Alg chains. On the other hand, the SR is higher for Alg(CUR)-h and PEDOT/Alg(CUR)-h than for unloaded hydrogels (*i.e.*

SR increases 9% and 7% in comparison to Alg-h and PEDOT/Alg-h, respectively). This observation suggests that the drug has some adverse effect on the crosslinked structures of the hydrogels, slightly reducing the density of crosslinks and, therefore, increasing the free volume. Thus, the CUR would preferentially interact with Ca^{2+} ions and PEDOT chains, reducing their ability to bind Alg chains and, consequently, the crosslinking density concerning unloaded hydrogels.

3.8.4.2 Cytotoxicity

Since the final application of the developed material is its therapeutic utilization as a drug carrier, it is essential to study the biocompatibility of the employed material itself (*i.e.* without the drug). For this purpose, *in vitro* cell adhesion and cell proliferation studies were performed by MTT assays on Alg-h and PEDOT/Alg-h, which served as substrates for fibroblasts derived from normal skin (Hff) and osteosarcoma (MG-63) cells.

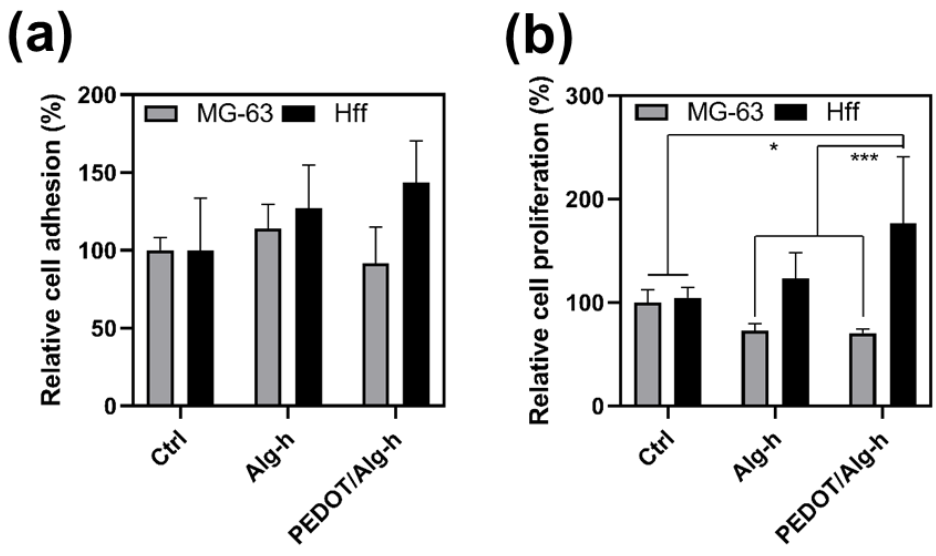

Figure 3.8.2. (a) Cell adhesion (24 h) and (b) cell proliferation (7 days) of Hff and MG-63 cells on Alg-h and PEDOT/Alg-h. The relative viabilities were established in relation to tissue culture polystyrene (TCPS), which was considered as a control substrate. Asterisk mark represents a significant difference among the other samples at $p < 0.05$ (*) and $p < 0.001$ (***).

Figure 3.8.2 displays cell viabilities after 24 h (cell adhesion) and 7 days (cell proliferation) for the hydrogels and the tissue culture polystyrene (TCPS) used as a control substrate. These results reveal a clear dependence of the proliferation rate on cell type. It is well-known that cell tissues present different mechanical properties and this may affect cell behavior [48-51]. As expected, cells had a similar adhesion to both systems without exhibiting a reduction in cell viability (Figure 3.8.2a). After 7 days (Figure 3.8.2b), Hff cells exhibited a higher affinity towards both Alg-h and PEDOT/Alg-h than MG-63 cells. This has been attributed to the stiffness of the material. Alg-based hydrogels without additional either covalent crosslinking or inorganic fillers are too low in stiffness to promote proliferation and spreading of hard tissue cells like bone. This hypothesis is strongly supported by previous microindentation results, which showed that the elastic modulus of the dermis is ~35 kPa [52] while that for bone is in the 10.4–20.7 GPa range [53]. Therefore, PEDOT/Alg-h would be more suitable to be used in soft tissues like skin, nervous system, adipose, and cardiac tissues.

3.8.4.3 Morphology of unloaded and drug-loaded hydrogels

High and low magnification SEM micrographs of the cross-section and surface of the loaded and unloaded hydrogels are displayed in Figure 3.8.3a. As can be observed, the cross-sections of all hydrogels are qualitatively the same and they are characterized by showing an open and interconnected porous structure. The cross-section porosity is higher for PEDOT/Alg-h, PEDOT/Alg(CUR)-h, and Alg(CUR)-h than for Alg-h, which is consistent with the higher electrochemical activity of the formers (see below). However, different pore sizes and pore areas are measured for the different hydrogels as shown in the histograms in Figures 3.8.3b-3.8.3c. The average diameters of the cross-sectional pores increase as follows: Alg-h (0.9 ± 0.3 μm) < Alg(CUR)-h (1.9 ±0.6 μm) < PEDOT/Alg-h (2.0 ±

1.0 µm) < PEDOT/Alg(CUR)-h (2.6 ± 0.8 µm). Obviously, the area of the pores follows the same trend Alg-h (0.9 ± 0.6 μm^2) < Alg(CUR)-h (2.8 ± 1.6 μm^2) < PEDOT/Alg-h (3.2 ± 1.5 μm^2) < PEDOT/Alg(CUR)-h (4.6 ± 2.5 μm^2). These results suggest that the presence of either CUR or PEDOT in the hydrogel could increase the distance between alginate chains, explaining the presence of bigger pores compared to the bare alginate hydrogel. No significant differences are observed between Alg(CUR)-h and PEDOT/Alg-h. However, the simultaneous presence of CUR and PEDOT within the hydrogel results in a new increase in pore size and pore area meaning that a new reduction in the cross-linking takes place. On the other hand, the surface morphology presents no pores and a smooth appearance. Besides, the superficial and cross-sectional morphology of the CUR-loaded hydrogels is very similar to that of the unloaded ones, suggesting that the drug is homogeneously distributed.

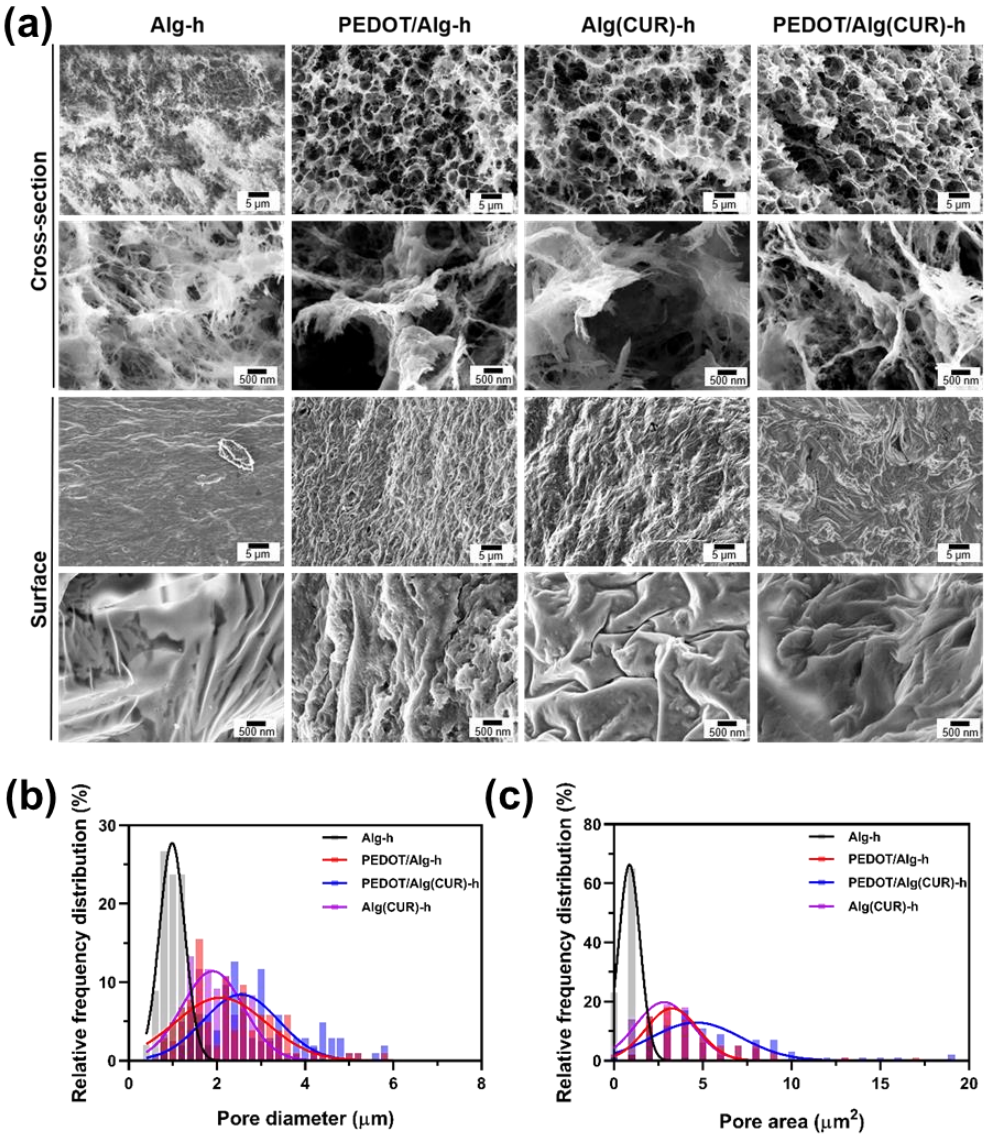

Figure 3.8.3 (a) Cross-sectional (low and high magnification at top and bottom, respectively) and surface (low and high magnification at top and bottom, respectively) SEM micrographs of: Alg-h; PEDOT/Alg-h; Alg(CUR)-h and PEDOT/Alg(CUR)-h. Bars in high and low-resolution micrographs: 500 nm and 5 µm, respectively. Histograms displaying (b) the diameter and (c) area of the pores observed in the cross-sections

TEM images of the stained PEDOT/Alg-h are shown in Figure 3.8.4a. Dark regions correspond to the anionic sites of Alg that were selectively stained with 1% uranyl acetate (UAc), while bright grey regions correspond to PEDOT.

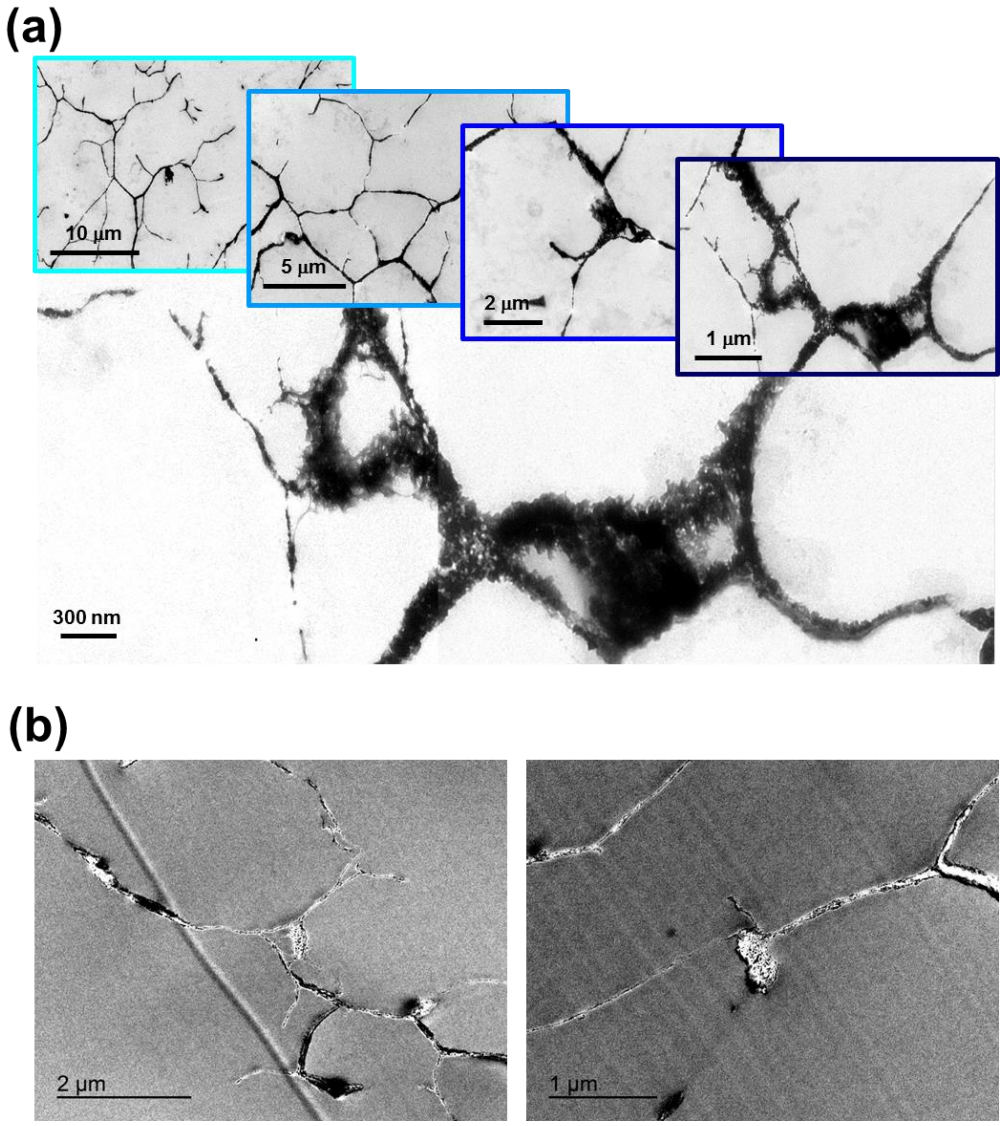

Figure 3.8.4. (a) TEM micrographs with different magnifications (from low at the left to high at the right and bottom) of the same region of stained PEDOT/Alg-h. (b) TEM micrographs of unstained PEDOT/Alg-h.

Although contrast regions associated with Alg-rich domains present a continuous structure, which explains the mechanical integrity of the hydrogel, bright regions can be distinguished. In some cases, the latter PEDOT-rich domains appear as interconnected nanometric grey spots embedded inside Alg-rich domains, while in other cases PEDOT-rich domains appear as micrometric (~1 µm) corpuscles interrupting the Alg-rich regions. The identification Alg-rich domains, in which PEDOT chains coexist with the predominant Alg chains, as well as of PEDOT-rich domains with the opposite organization, fully support the influence of

the CP on the cross-linking between Alg chains. This partially segregated structure is also clearly reflected in TEM micrographs of unstained samples (Figure 3.8.4b), in which dark regions correspond to PEDOT-rich domains due to the remarkable electron scattering properties of the CP. The microstructure showed by both stained and unstained samples of PEDOT/Alg-h with both components coexisting in many regions has an impact on electroactivity, as shown below.

3.8.4.4 Electrochemical characterization

Unloaded and CUR-loaded PEDOT/Alg-h and Alg-h were characterized by cyclic voltammetry (CV) and galvanostatic charge-discharge (GCD) using a $CaCl_2$ 5 wt.% aqueous solution as supporting electrolyte. Figure 3.8.5a shows the control cyclic voltammograms recorded for the different hydrogels. As can be observed, all the voltammograms are qualitatively the same: quasi-rectangular and symmetric in shape without redox peaks which are attributed to the reversibility of the non-faradaic adsorption/desorption process of Ca^{2+} ions onto the hydrogel surface during the potential scan. Thus, both the Alg-rich phases of PEDOT/Alg-h and Alg-h are considered ionically conductive since Alg chains are negatively charged and the formed hydrogels contain an aqueous electrolyte inside (*i.e.* $CaCl_2$ dissolved in water). Comparison of the unloaded hydrogels indicates that the electrochemical activity is slightly higher for PEDOT/Alg-h than for Alg-h which can be attributed to the electronic contribution of PEDOT but also the higher SR both making the Ca^{2+} adsorption/desorption process more efficient.

CUR-loaded hydrogels display an increment in the area of the voltammograms compared to the unloaded ones, which is very significant for Alg(CUR)-h. The higher electrochemical activity of Alg(CUR)-h indicates that the diffusion and migration of ions during the potential scan experienced a drastic increase, which is fully consistent with the high SR value obtained for the Alg(CUR)-h. Thus, the

increment in the voltammetric area of Alg(CUR)-h with respect to Alg-h suggests that CUR preferentially interacts with Ca^{2+}, reducing the crosslinking density and facilitating the ion diffusion with respect to the unloaded hydrogel in the potential range from –0.20 V to 0.60 V. Instead, the moderate variation of the electrochemical activity of PEDOT/Alg(CUR)-h compared to PEDOT/Alg-h is consistent with the preferential interaction between the drug and PEDOT chains

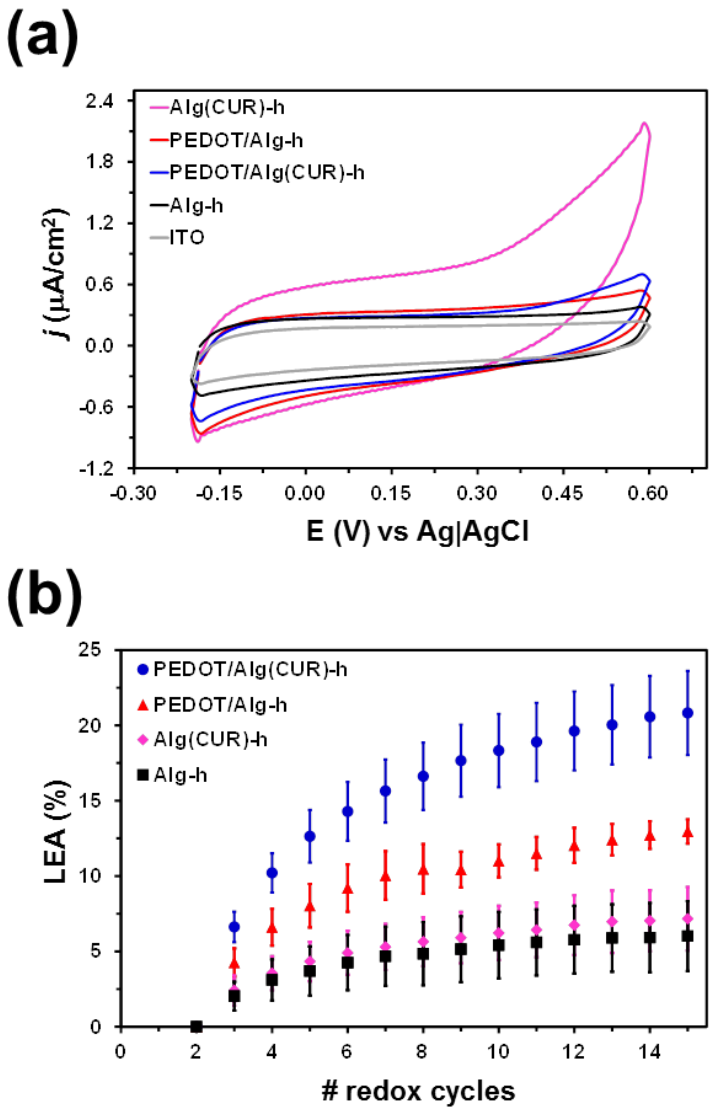

Figure 3.8.5. For PEDOT/Alg(CUR)-h, PEDOT/Alg-h, Alg(CUR)-h and Alg-h: (a) Cyclic voltammograms recorded from –0.20 to 0.60 V at a scan rate of 100 mV/s; and (b) Variation of the loss of electrochemical activity (LEA) against the number of consecutive redox cycles.

The preferred CUR···PEDOT interaction over CUR···Ca^{2+} one has a clear implication: CUR limits access to the electrically conductive polymer. On the other hand, the voltammograms recorded for PEDOT/Alg(CUR)-h and Alg(CUR)-h exhibit an increase in current density at around + 0.4 V which corresponds to CUR oxidation. No reduction peak is observed in the scanned potential range because the oxidation of CUR is an irreversible or quasi-irreversible process (depending on the experimental conditions), which agrees with the literature [14,54].

The electrochemical stability, represented as the loss of electrochemical activity (LEA; Eq E.3.8.2) with the number of consecutive oxidation-reduction cycles, is shown in Figure 3.8.5b. In all cases the area of the voltammograms and, therefore, the voltammetric charge decreased with the number of cycles, reflecting a loss electrochemical stability. The two PEDOT-containing hydrogels, especially the CUR-loaded one, display the lowest stability. This feature suggests that the interface between the PEDOT and Alg domains becomes seriously affected by the consecutive potential scan cycles. Moreover, this effect is enhanced in PEDOT/Alg(CUR)-h since, apparently, redox processes also affect the PEDOT···CUR interactions, which is expected to be beneficial for the controlled delivery of the drug. It should be noted that the stabilization of the LEA around 20% after 15 redox cycles limits the utilization of PEDOT/Alg-h for applications related with energy storage (e.g. fabrication of electrodes for devices), which require preserving the electrochemical activity for thousands of redox cycles. However, such LEA value does not represent a drawback for the release of drugs in medical applications since in those cases the number of redox cycles needed is relatively low, even for multiple stimulation processes. On the other hand, the structure of Alg-h and Alg(CUR)-h undergoes much fewer changes during the consecutive redox processes, the value of LEA keeping below 10% after 15 cycles.

3.8.4.5 Non-stimulated release of CUR

A main disadvantage of Ca^{2+}-crosslinked Alg is the low mechanical stability in absence of Ca^{2+}-rich environments, which may affects the drug release rate in biorelevant media by increasing it. Although this drawback can be easily overcome using a number of well-known methods (*e.g.* coating with chitosan, adding selected of anions and using an ion diffusion approach during the crosslinking step) [38,55-57], application of such procedures is out of the scope of this work, which is focused on the preparation, characterization, properties and electrochemical response of PEDOT/Alg-h for drug delivery. Accordingly, in order to avoid distortions in the release results due to the loss of mechanical integrity, a $CaCl_2$ 5 % wt. aqueous solution was used as release medium. However, we are aware that stabilization of the hydrogel will be required in a future for *ex vivo* and/or *in vivo* studies

Due to its hydrophobic nature, CUR is poorly soluble in water, even though it is readily soluble in some organic solvents such as ethanol [58]. PEDOT/Alg(CUR)-h and Alg(CUR)-h square pieces of 1×1 cm^2 were cut and immersed in the aqueous release medium using Eppendorfs. At predefined time intervals (*i.e.* 15 min, 30 min, 1 h, 1 day, 2 days, and 9 days), the release medium (1 mL) was withdrawn from the tube and analyzed by UV-Vis spectroscopy. The amount of released CUR was quantified by UV-vis spectroscopy, using the absorption band centered at 400 nm, and the calibration curve displayed in Figure 3.8.6a. More details of the experimental procedure are provided in the methods section.

As shown in Figure 3.8.7a, the drug was slowly but progressively released to the medium during the first 1 h. More specifically, 3.6% $\pm$ 1.0% and 7.1% $\pm$ 1.0% of CUR from PEDOT/Alg(CUR)-h and Alg(CUR)-h, respectively, was released after this time period. This low release has been attributed to the weak affinity of CUR for water molecules, preferring the interactions with the components of the hydrogels and despite the high SR observed for the loaded hydrogels. This trend

was confirmed after 9 days when the accumulated released drug was kept at practically the same values (*i.e.* 3.3% ± 1.0% and 6.9% ± 1.0%, respectively). In order to accelerate the release, the aqueous medium was substituted by ethanol (99%) at day 9, the corresponding calibration curve is displayed in Figure 3.8.6b. After two days, the released CUR increased to 12.9% ± 1.7% and 9.1% ± 1.4% for PEDOT/Alg(CUR)-h and Alg(CUR)-h, respectively (see a pale yellow rectangle in Figure 3.8.7a). However, no additional release was observed after another two days in ethanol. The higher released observed for the PEDOT/Alg(CUR)-h can be explained by the higher SR measured for this hydrogel compared to the Alg(CUR)-h one.

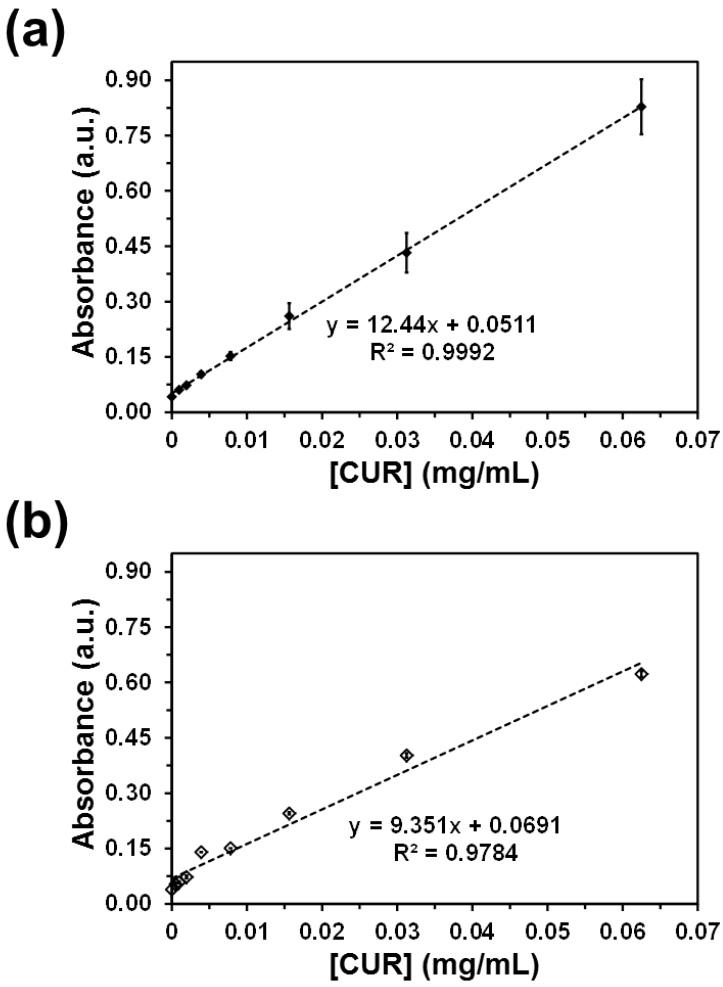

Figure 3.8.6. Calibration curves used for the CUR release quantification in (a) 5 % wt. $CaCl_2$ aqueous solution and (b) ethanol (99%).

These results indicate that the CUR, a highly hydrophobic drug is not released from the tested hydrogels by a simple diffusion mechanism. In general, the drug release rate depends on (1) drug affinity towards the release medium; (2) desorption of the adsorbed drug from the polymeric molecules, (3) drug diffusion out of the polymeric matrix once desorbed; and (4) the synergy between matrix stimulation and drug diffusion processes. Results displayed in Figure 3.8.7a shows that both PEDOT/Alg(CUR)-h and Alg(CUR)-h exhibit small burst and sustained release effects. Considering that the pores of the studied hydrogels are large enough to facilitate the drug diffusion (Figure 3.8.3), such effects have been associated not only to the hydrophobicity of CUR but also to the strength of the interactions between the drug and the component of the polymer matrixes, as the results obtained in ethanol demonstrate. In the case of Alg(CUR)-h, the interactions between the drug and Ca^{2+} ions apparently form relatively large hydrophobic complexes, probably with several CUR molecules surrounding each Ca^{2+} ion, causing lower burst effect and slower release than in PEDOT/Alg(CUR)-h. This could explain that the release in ethanol is lower for Alg(CUR)-h than for PEDOT/Alg(CUR)-h, in which CUR molecules presumably interact individually with PEDOT repeat units. This assumption has been taken as an advantage to explore the CUR release when the PEDOT-containing hydrogel is electrostimulated. Overall, the release profile displayed in Figure 3.8.7a reflects that stimuli-assisted drug release devices are necessary to achieve efficient delivery of hydrophobic drugs.

3.8.4.6 Electrostimulated release of CUR

The electrochemically controlled release of the drug from the hydrogels was carried out in an electrochemical cell filled with 2.5 mL of aqueous solution, as described in the ESI. Electrostimulation was conducted applying an external

voltage of either +1.0 V or –1.0 V. The voltage was applied for 2 h interrupted at regular time intervals (every 15 min) for a few minutes to extract the liberation medium for afterward quantification of the released drug, to supplement with fresh liberation medium to keep the volume constant and to record a cyclic voltammogram.

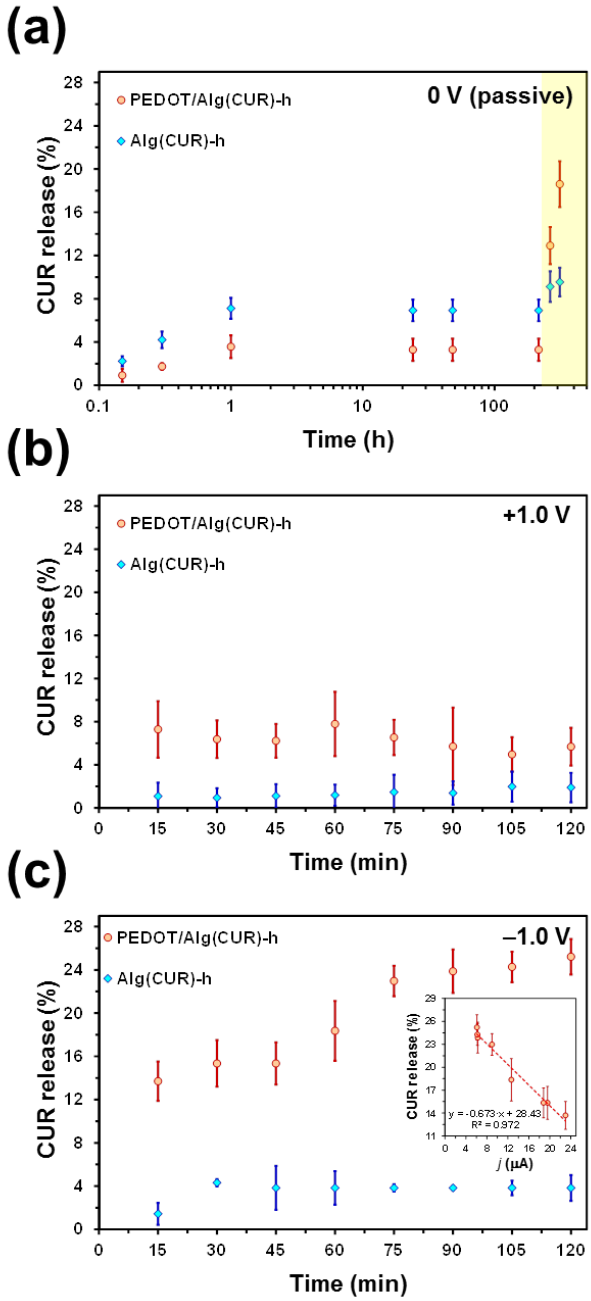

Figure 3.8.7. CUR release from PEDOT/Alg(CUR)-h and Alg(CUR)-h samples by (a) diffusion (passive release) after immersion in an aqueous solution for 9 days and ethanol (pale yellow rectangle) for four days, and by applying a constant potential of (b) +1.0 V or (c) –1.0 V for 2 h in aqueous solution. The inset in (c)

shows the correlation between the current density (from cyclic voltammograms) and the amount of CUR released from the hydrogel.

The release profiles obtained for PEDOT/Alg(CUR)-h and Alg(CUR)-h using voltages of +1.0 V and –1.0 V are shown in Figures 3.8.7b and 6c, respectively; while Figure 3.8.8. displays the cyclic voltammograms recorded every 15 min. Figure 3.8.9. shows SEM micrographs of the hydrogels after the 2 h electrostimulation and the histograms variation of the pore diameter upon electrostimulation, while the variation of pore area is shown in Figure 3.8.10.

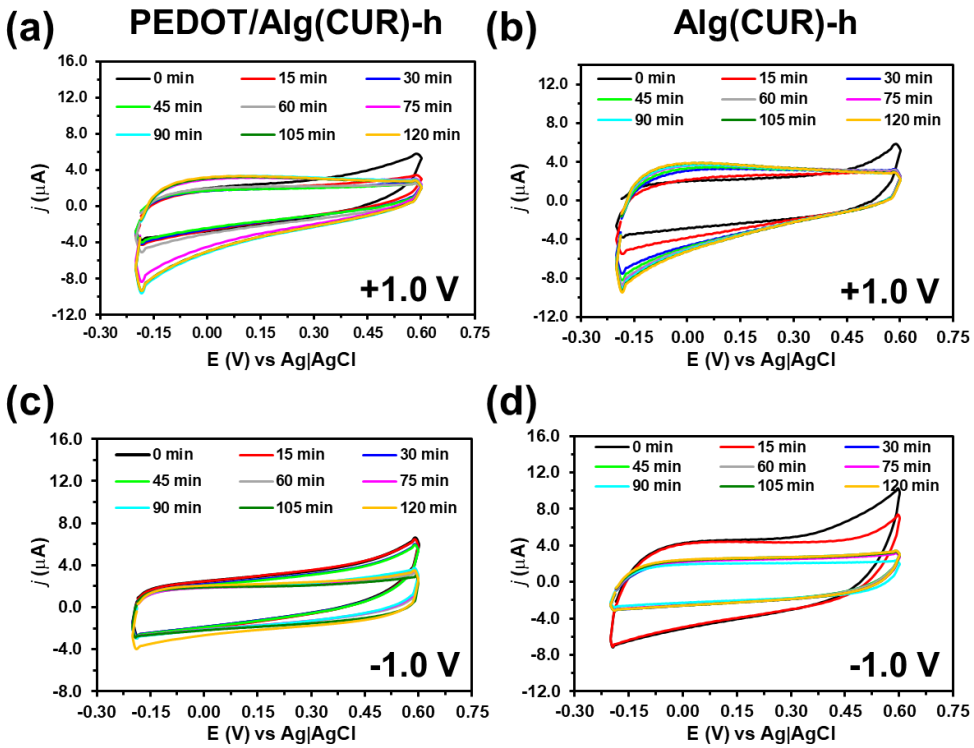

Figure 3.8.8. Cyclic voltammograms recorded at 15 min intervals for (a, c) PEDOT/Alg(CUR)-h and (b, d) Alg(CUR)-h electrostimulated by applying a constant voltage of (a, b) +1.0 V or (c, d) –1.0 V. All voltammograms were obtained in the potential window comprised between –0.20 and 0.60 V at a scan rate of 100 mV/s.

The application of a voltage of +1.0 V does not significantly affect the release of CUR from PEDOT/Alg(CUR)-h (Figure 3.8.7b). Although the amount of drug released after 15 min of electrostimulation (7.3% ± 2.6%) is higher than that achieved by simple diffusion after 1 h (3.6% ± 1.0%) (Figure 3.8.7a), beyond 15 min the amount of released CUR does not increase with the electrostimulation time, suggesting that PEDOT⋯CUR interactions are not affected by the application of oxidative potentials. The small difference between the profiles obtained for unstimulated and stimulated with +1.0 V at very short times has been attributed to the changes induced by the voltage in the structure of the hydrogel, which are discussed below. However, these structural changes are not enough to affect the CUR release at higher times. This interpretation is supported by the cyclic voltammograms recorded at periodic time intervals (Figure 3.8.8a), which are all practically identical, reflecting that the hydrogel is not altered by the electrostimulation process. Indeed, the only difference among all of them is a slight decrease in the anodic current, which can be explained by the lesser amount of CUR in the hydrogel because of its release. Also, the CUR oxidation reaction may occur, even though no change in the color of the hydrogel or the release medium was observed. Figure 3.8.11. shows the UV spectra of PEDOT/Alg(CUR)-h after the electrical stimuli, the peak is maintained at 400 nm in washed hydrogel even after stimulation at +1.0 V during 2 h, whereas the flat spectrum recorded for unloaded PEDOT/Alg-h (blank) is shown in Figure 3.8.12. Although there is an increase in the cross-section pore diameter from 2.6 ± 0.8 µm (for unstimulated hydrogel, Figure 3.8.3b) to 6.7 ± 2.0 µm (for +1.0 V stimulated hydrogel (Figure 3.8.9c), it seems no affecting significantly the CUR release at +1.0 V. No pores are observed on the surface of the hydrogel. On the other hand, Figure 3.8.11 also shows that when CUR is surrounded by an organic environment, the absorbance peak appears at 425 nm

Exposure of Alg(CUR)-h to a potential of +1.0 V for 2 h resulted in a CUR release of 1.9% ± 1.4% only (Figure 3.8.7b). The latter value, which is reached after only 15 min, is lower than that achieved in absence of stimulus by a factor of 3.6, suggesting that electrostimulation affects the structure of the Alg matrix. The evolution of the cathodic and anodic areas of the voltammograms recorded at periodic time intervals allows us to confirm this hypothesis (Figure 3.8.8b).

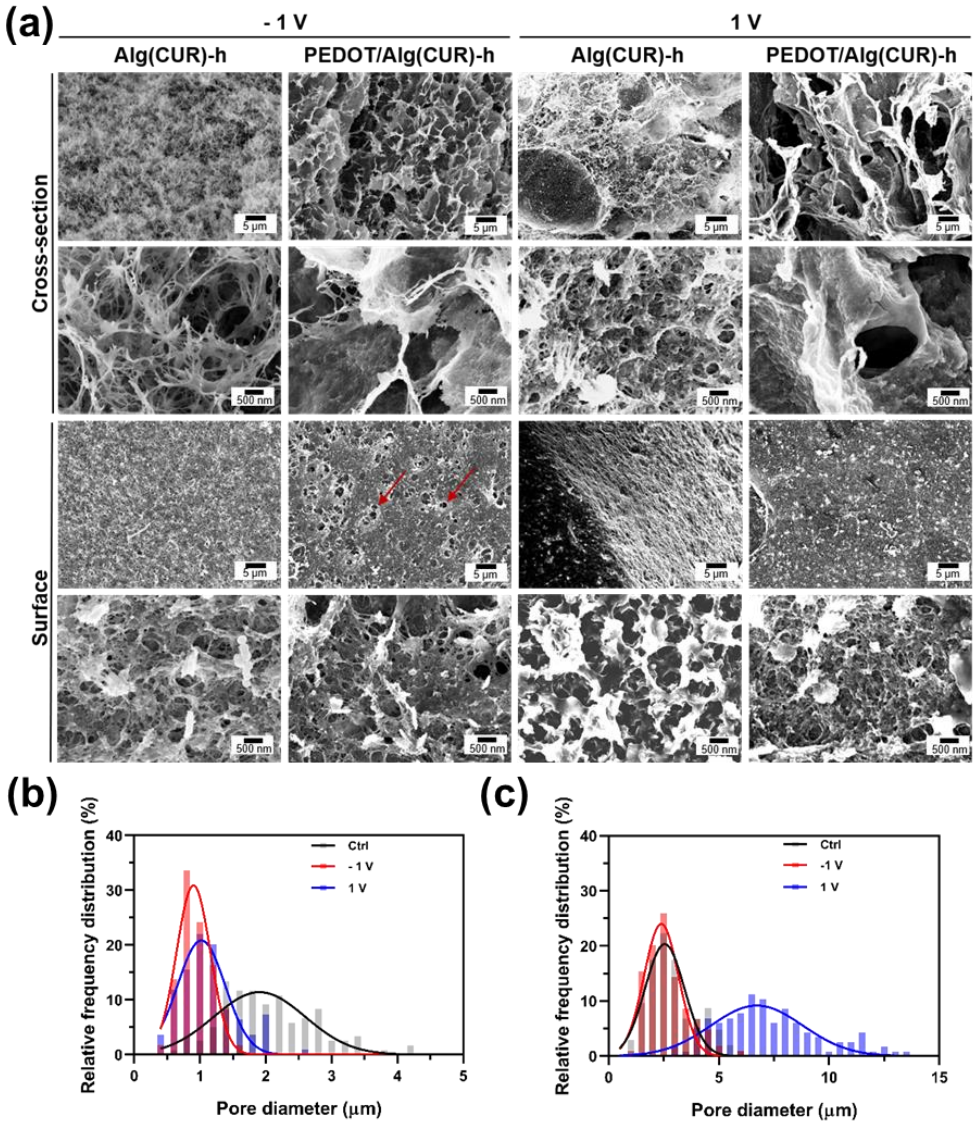

Figure 3.8.9 (a) Cross-sectional (low and high magnification at top and bottom, respectively) and surface (low and high magnification at top and bottom, respectively) SEM micrographs of Alg(CUR)-h and PEDOT/Alg(CUR)-h after undergoing –1.0 or +1 V electrostimulation (left and right, respectively). Bars in high and low-resolution micrographs: 500 nm and 5 µm, respectively. Histogram representing the diameter of the pores found on the cross-sectional profiles in (b)

Alg(CUR)-h and (c) PEDOT/Alg(CUR)-h before (Ctrl) and after applying the electrical stimuli

Thus, the electrochemical activity of the hydrogel decreases substantially with increasing time of exposition to the potential until t= 105 min. The reduction of the electroactivity is due to the greater difficulties that dopant ions have in entering into and escaping from the polymer matrix during oxidation and reduction scans, respectively. Thus, the application of the voltage affects the structure of the Alg-h, which becomes more compact, and makes difficult not only the transport of dopant ions but also the delivery of drug molecules. As expected, the average pore diameter of the cross-sectional decreased from 1.9 ± 0.6 to 0.9 ± 0.2 μm after +1.0 V stimulation (Figure 3.8.9b). A comparison between the voltammograms displayed in Figure 3.8.8a-3.8.8b indicates that the response of PEDOT/Alg(CUR)-h to chronoamperometric electrostimulation is dominated by the CP domains, even though the Alg domains are expected to be damaged by the applied voltage, like in Alg(CUR)-h.

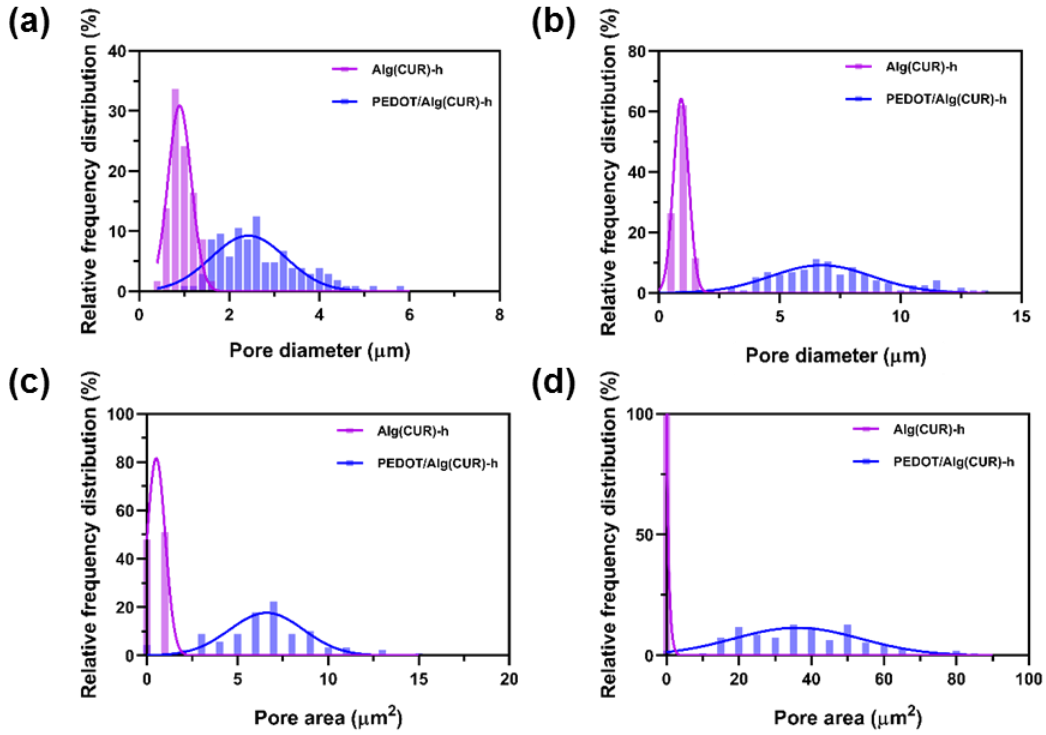

Figure 3.8.10. Histograms representing (a, b) the diameter and (c, d) area of Alg(CUR)-h and PEDOT/Alg(CUR)-h pores after applying the electrical stimuli of –1.0 V (a, c) and +1.0 V (b, d).

The release of drug from Alg(CUR)-h increased by ~2% when electrostimulation was performed applying a voltage of –1.0 V (Figure 3.8.7c) instead of +1.0 V. Moreover, the release profile obtained for –1.0 V recalls the shape of that achieved in absence of electrostimulation, suggesting that the negative voltage has a lower effect on the porosity of Alg hydrogel than the positive one, even though the diameter of the pores decreased to 1.0 ± 0.3 μm (Figure 3.8.9b). This is supported by the cyclic voltammograms displayed in Figure 3.8.8d, which show that the reduction of electrochemical activity at increasing electrostimulation time is much less noticeable than in Figure 3.8.8b. Also, denoting that Alg hydrogels, in which the electrochemical response is only associated with the diffusion of ions, cannot be employed as electroresponsive drug delivery systems.

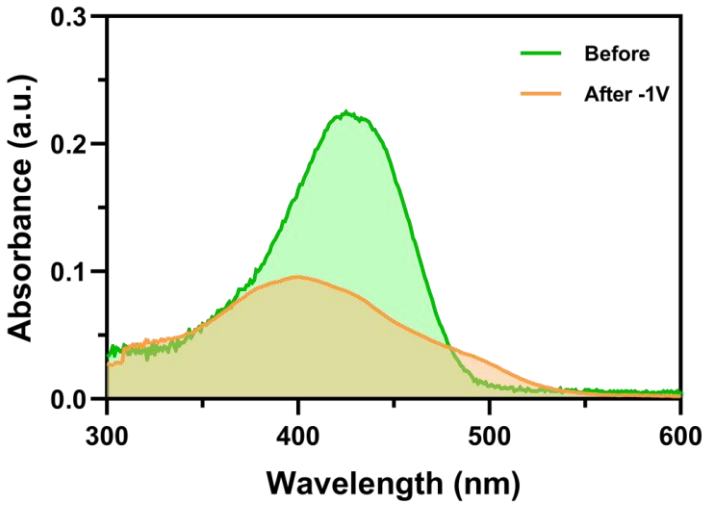

Figure 3.8.11. UV-Vis spectrum of PEDOT/Alg(CUR)-h hydrogel after applying the electrical stimuli of +1.0 V for 2 h and without applying any stimuli. In order to explain the shift of the peak from 425 nm, as is typically observed for ethanol CUR solutions, to 400 nm, the non-stimulated hydrogel was only scarcely washed with water (rather than thoroughly washed with abundant water). Accordingly, some of the ethanol used to dissolve the drug remained inside the hydrogel, surrounding CUR molecules, and the intense peak appeared at around 425 nm

Instead, the electrical stimulation of PEDOT/Alg(CUR)-h, with a sustained application of a voltage of –1.0 V, results in a significant and progressive CUR release (Figure 3.8.7c). After only 15 min, the amount of drug found in the release medium is approximately twice and fifteen times higher than those delivered by applying a voltage of +1.0 V (Figure 3.8.7b) and simple diffusion (Figure 3.8.7a), respectively. Moreover, the release profile reflects a slow but continued release when the negative voltage is applied, reaching a value of ~25% after 2 h. This represents an increment of ~22% with respect to the non-stimulated delivery achieved after 9 days immersed in an aqueous release medium and of ~19% with respect the stimulated delivery applying a voltage of +1.0 V. The progressive release of CUR is fully consistent with the lower intensity observed in the cyclic voltammograms recorded at intervals of 15 min (Figure 3.8.8c). Indeed, the current density in the CV linearly correlates (R^2= 0.972) with the amount of CUR released from the hydrogel, as shown in the inset of Figure 3.8.7c. On the other hand, the

angling of the voltammograms decreases with increasing electrostimulation time, suggesting the electrical contact between PEDOT rich domains increases. This effect can be attributed to released CUR molecules that facilitate the approach of PEDOT chains and/or to the voltage-induced degradation of Alg-rich domains that, despite being lower than for the positive voltage (as discussed above), may be enough to enhance the contact among PEDOT-rich domains. Interestingly, after 2 h electrostimulation, the average pore diameter did not present significant changes (from 2.6 ± 0.8 μm to 2.4 ± 0.7 μm), while the surface changed from a smooth to a rugose with pores morphology, which is not observed in any of the other cases and has been attributed to the release of CUR. These suggest that the damage that occurred on the surface of the hydrogel also contributes to CUR release.

The fact that the total amount of released CUR reached only ~25% of the initial dose after 2 h of electrostimulation may be explained by the formation of potential specific interactions between CUR and PEDOT chains (*e.g.* π-π stacking and/or hydrogen bonds). The reduction of the CP by applying a negative electrical voltage probably affects the strength of intermolecular CUR···PEDOT interactions, which become weaker or even cease. This facilitates the release of the drug, even though it is restricted by its hydrophobic characteristics, which hampers the diffusion of CUR (as observed in Figure 3.8.7a).

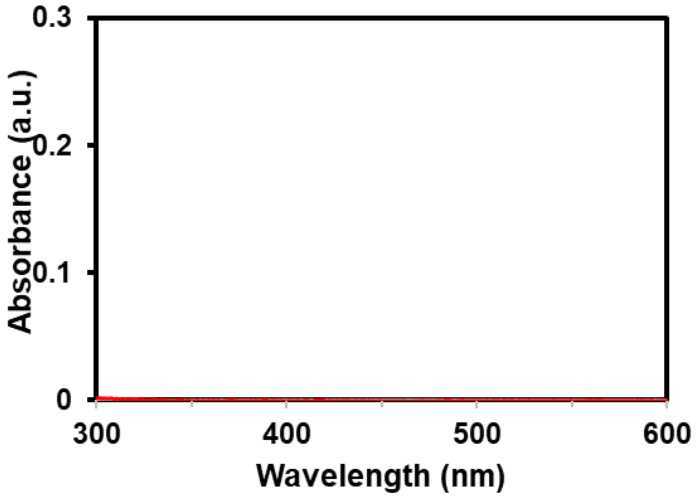

Figure 3.8.11. UV-Vis spectrum of PEDOT/Alg-h hydrogel after applying the electrical stimuli of +1.0 V for 2 h and without applying any stimuli. The profile remained absolutely flat after apply the electrical stimuli of +1.0 V for 2 h (not shown).

In addition to the effect of the voltage on the specific interactions and the structure of the hydrogel, the CUR release profiles displayed in Figure 3.8.7b-3.8.7c could be also influenced by other factors, as the change of pH in the hydrogel environment.[59-65] More specifically, the production of oxygen and protons due to the oxidation of water molecules when a voltage of + 1.0 V is applied (Eq E.3.8.4), may cause a pH reduction inside the hydrogel:

$$2\ H_2O \rightarrow O_2(g) + 4\cdot H^+(aq) + 4\cdot e^- \qquad \text{(E.3.8.4)}$$

Obara *et al.* [59] reported that, in acidic conditions, the carboxylate groups from Alg chains and the protons bond together, promoting the contraction of the hydrogel due to the neutralization of electrostatic repulsion between the carboxylate groups (Figure 3.8.13a). Therefore, the hydrogel becomes more compact, hindering the CUR diffusion.

Instead, water molecules reduce at –1.0 V voltage:

$$4\cdot H_2O + 4e^- \rightarrow 2\cdot H_2 + 4\cdot OH^- \qquad \text{(E.3.8.5)}$$

The basic environment caused by the hydroxyl ions favors the deprotonation of carboxylic acid groups from the Alg chain, increasing the amount of negatively

charged carboxylate groups and, therefore, the electrostatic repulsion among them (Figure 3.8.13a). This favors the swelling of the hydrogel and facilitates the diffusion (Figure 3.8.13b). However, it should be emphasized that the poor release profile obtained for Alg(CUR)-h upon the application of–1.0 V (Figure 3.8.7c) suggests that, the influence of the pH on the release of the drug from PEDOT/Alg(CUR)-h is very small or even practically null. This feature supports that the influence of the voltage in the structure of the hydrogel and the specific interactions between the drug and polymeric matrix are probably the main driving forces for the release mechanism from such system.

More work needs to be performed to better identify the nature and strength of specific interactions in PEDOT/Alg(CUR)-h, as well as to optimize the release profile. Both the sustained response of the PEDOT/Alg polymeric matrix to the negative voltage and the progressive delivery of CUR support the necessity of future investigations on PEDOT/Alg-h as a promising system for on-demand release. Details about the specific interactions involved in PEDOT/Alg(CUR)-h are expected to be obtained in the near future using computer simulations at the molecular level. Besides, to improve the efficiency of PEDOT/Alg-h as a drug delivery system, future work will focus on optimizing the value of the applied negative voltage and the application of short potential pulse protocols (*i.e.* on/off application of the electrical voltage). Also, investigations using drugs with a less pronounced hydrophobic profile than that of CUR are necessary to alter the balance of the intermolecular interaction. The relative strength between the interactions involving the loaded drug and the molecular species contained in the polymeric matrix and the release medium is a crucial point to regulate the on-demand release. Accordingly, identification of the optimum drug chemical profile for a given polymeric system is necessary to diagnose its effectivity as a drug delivery system.

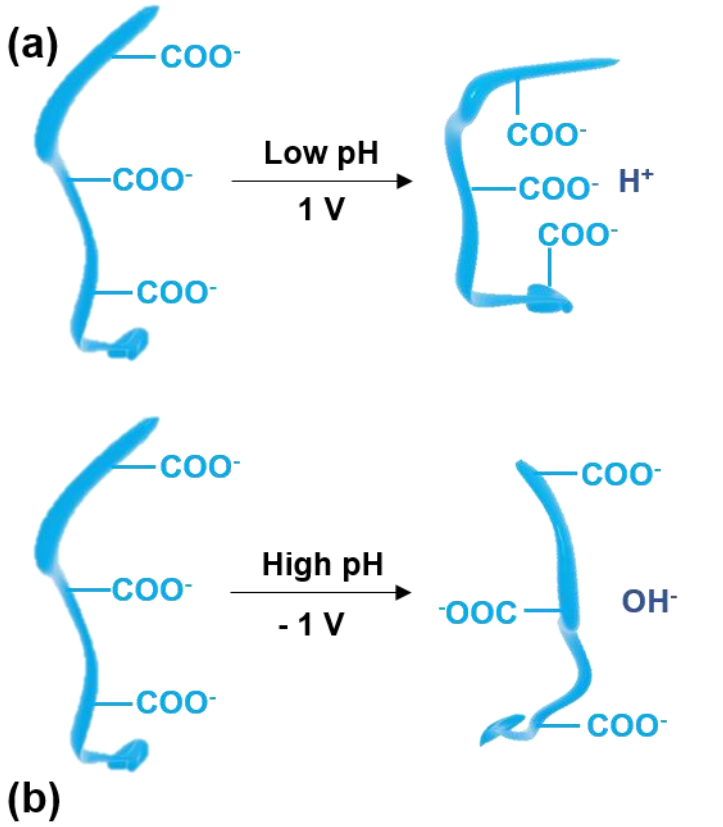

Figure 3.8.13. (a) Effect of pH and electrical stimuli on the Alg chain. (b) Scheme of PEDOT/Alg(CUR)-h hydrogel changes after undergoing – 1.0 V electrostimulation

3.8.5 Conclusions

PEDOT/Alg hydrogel capable of drug delivery were fabricated. Hydrogels are prepared using a very simple and effective method, which consists of gelling a PEDOT:PSS + AA mixture by adding a $CaCl_2$ solution. CUR is loaded *in situ* during the gelling process by dissolving the drug with the AA in ethanol before mixing with PEDOT:PSS. Despite PEDOT- and Alg-rich domains are partially segregated, TEM micrographs reveal the presence of conduction paths in the hydrogels, explaining the electroresponsive behavior. Because of both its hydrophobicity and the formation of intermolecular specific interactions, CUR is slowly released from PEDOT/Alg(CUR) and Alg(CUR) hydrogels by simple diffusion (*i.e.* around 3% only), even when the aqueous release medium is replaced by ethanol. However, the release of drug from PEDOT/Alg(CUR)-h is enhanced in response to electrical stimulation by applying a negative voltage (*i.e.* around 25% in 2 h), which affects intermolecular interactions. Such a stimuli-responsive drug delivery system may find use as drug delivery implants, where the release of the drug can be regulated, according to the patient's requirements through the application of an electrical stimulus.

References

1. Puiggalí-Jou, A.; del Valle, L. J.; Alemán, C. Drug Delivery Systems Based on Intrinsically Conducting Polymers. *J. Control. Release* **2019**, *309*, 244–264.
2. Boehler, C.; Oberueber, F.; Asplund M. Tuning Drug Delivery From Conducting Polymer Films for Accurately Controlled Release of Charged Molecules. *J. Control. Release* **2019**, *304*, 1404–1454.
3. Wu, J. G.; Chen, J. H.; Liu, K. T.; Luo, S. C. Engineering Antifouling Conducting Polymers for Modern Biomedical Applications. *ACS Appl. Mater. Interfaces* **2019**, *11*, 21294–21307.
4. Mondal, S.; Das, S.; Nandi, A. K. A Review on Recent Advances in Polymer and Peptide Hydrogels. *Soft Matter* **2020**, *16*, 1404–1454.
5. Tandon, B.; Magaz, A.; Balint, R.; Blaker, J. J.; Cartmell, S. H. Electroactive Biomaterials: Vehicles for Controlled Delivery of Therapeutic Agents for Drug Delivery and Tissue Regeneration. *Adv. Drug Deliv. Rev.* **2018**, *129*, 148–168.
6. Uppalapati, D.; Boyd, B. J.; Garg, S.; Travas-Sejdic, J.; Svirkis, D. Conducting Polymers with Defined Micro- or Nanostructures for Drug Delivery. *Biomaterials* **2016**, *111*, 149–162.
7. Gueye, M. N.; Carella, A.; Faure-Vincent, J.; Demadrille, R.; Simonato, J. P. Progress in Understanding Structure and Transport Properties of PEDOT-Based Materials: A Critical Review. *Prog. Mater. Sci.* **2020**, *108*, 100616.
8. Bubnova, O.; Khan, Z. U.; Wang, H.; Braun, S.; Evans, D. R.; Fabretto, M.; Hojati-Talemi, P.; Dagnelund, D.; Arlin, J. B.; Geerts, Y. H.; Desbief, S.; Breiby, D. W.; Andreasen, J. W.; Lazzaroni, R.; Chen, W. M.; Zozoulenko, I.; Fahlman, M.; Murphy, P. J.; Berggren, M.; Crispin, X. Semi-Metallic Polymers. *Nat. Mater.* **2014**, *13*, 190−194.
9. Kayser, L. V.; Lipomi, D. J. Stretchable Conductive Polymers and Composites Based on PEDOT and PEDOT:PSS. *Adv. Mater.* **2019**, *31*, 1806133.
10. Sappia, L. D.; Piccinini, E.; Marmisolle, W.; Santilli, N.; Maza, E.; Moya, S.; Battaglini, F.; Madrid, R. E.; Azzaroni, O. Integration of Biorecognition Elements on PEDOT Platforms through Supramolecular Interactions. *Adv. Mater. Interf.* **2017**, *17*, 1700502.

11. del Valle, L. J.; Estrany, F.; Armelin, E.; Oliver, R.; Alemán, C. Cellular Adhesion, Proliferation and Viability on Conducting Polymer Substrates. *Macromol Biosci.* **2008**, *8*, 1144−1151.
12. S. C. Luo, E. M. Ali, N. C. Tansil, H. H. Yu, S. Gao, E. A. B. Kantchev, J. Y. Ying. Poly(3,4-ethylenedioxythiophene) (PEDOT) Nanobiointerfaces: Thin, Ultrasmooth, and Functionalized PEDOT Films with In Vitro and In Vivo Biocompatibility. *Langmuir* **2008**, *24*, 8071−8077.
13. Puiggalí-Jou, A.; del Valle, L. J.; Alemán, C. Drug Delivery Systems Based on Intrinsically Conducting Polymers. *J. Control. Release* **2019**, *309*, 244−264.
14. Puiggalí-Jou, A.; Micheletti, P.; Estrany, F.; del Valle, L. J.; Alemán, C. *Electrostimulated Release of Neutral Drugs from Polythiophene* Nanoparticles*: Smart Regulation of* Drug-*Polymer Interactions. Adv. Healthc. Mater.* **2017**, *6*, 1700453.
15. Puiggalí-Jou, A.; del Valle, L. J.; Alemán, C. Encapsulation and Storage of Therapeutic Fibrin-Homing Peptides Using Conducting Polymer Nanoparticles for Programmed Release by Electrical Stimulation. *ACS Biomater. Sci. Eng.* **2020**, *6*, 2135−2145.
16. Esrafilzadeh, D.; Razal, J. M.; Moulton, S. E.; Stewart, E. M.; Wallace; G. G. Multifunctional Conducting Fibres with Electrically Controlled Release of Ciprofloxacin. *J. Control. Release* **2013**, *169*, 313−320.
17. Chen, C.; Chen, X.; Zhang, H.; Zhang, Q.; Wang, L.; Li, C.; Dai, B.; Yang, J.; Liu, J.; Sun, D. Electrically-Responsive Core-Shell Hybrid Microfibers for Controlled Drug Release and Cell Culture. *Acta Biomater.* **2017**, *55*, 434−442,
18. Puiggali-Jou, A.; Cejudo, A.; del Valle, L. J.; Aleman, C. Smart Drug Delivery from Electrospun Fibers Through Electro-Responsive Polymeric Nanoparticles. *ACS Appl. Bio Mater.* **2018**, *1*, 1594−1605.
19. Woeppel, K. M.; Zheng, X. S.; Schulte, Z. M.; Rossi, N. L.; Cui X. Y. T. Nanoparticle Doped PEDOT for Enhanced Electrode Coatings and Drug Delivery. *Adv. Healthc. Mater.* **2019**, *8*, 1900622.
20. Boehler, C.; Oberueber, F.; Asplund, M. Tuning Drug Delivery from Conducting Polymer Films for Accurately Controlled Release of Charged Molecules. *J. Control. Release* **2019**, *304*, 173−180.
21. Carli, S.; Fioravanti, G.; Armirotti, A.; Ciarpella, F.; Prato, M.; Ottonello, G.; Salerno, M.; Scarpellini, A.; Perrone, D.; Marchesi, E.; Ricci, D.; Fadiga, L. A

New Drug Delivery System Based on Tauroursodeoxycholic Acid and PEDOT. *Chem. Eur. J* **2019**, *25*, 2322−2329.

22. Krukiewicz, K.; Cinchy, M.; Ruszkowski, P.; Turnzyn, R.; Jarosz, T.; Zak, J. K.; Lapkoski, M.; Bednarczyk-Cwynar; B. Betulin-Loaded PEDOT Films for Regional Chemotherapy. *Mat. Sci. Eng. C Mater.* **2017**, *73*, 611−615.
23. Kleber, C.; Lienkamp, K.; Ruhe, J.; Asplund. M. Electrochemically Controlled Drug Release from a Conducting Polymer Hydrogel (PDMAAp/PEDOT) for Local Therapy and Bioelectronics. *Adv. Healthc. Mater.* **2019**, *8*, 1801488.
24. Molina, B. G.; Dominguez, E.; Armelin, E.; Alemán, C.. Assembly of Conducting Polymer and Biohydrogel for the Release and Real-Time Monitoring of Vitamin K3. *Gels* **2018**, *4*, 86.
25. Xu, Y.; Cui, M.; Patsis, P.; Günter, M.; Yang, X.; Eckert, K.; Zhang, Y. Reversibly Assembled Electroconductive Hydrogel via a Host−Guest Interaction for 3D Cell Culture. *ACS Appl. Mater. Interfaces* **2019**, *11*, 7715−7724.
26. Walker, B. W.; Lara, R. P.; Mogadam, E.; Yu, C. H.; Kimball, W.; Annabi, A. Rational Design of Microfabricated Electroconductive Hydrogels for Biomedical Applications. *Prog. Polym. Sci.* **2019**, *92*, 135−157.
27. Mayr, J.; Diaz Diaz, D. Release of Small Bioactive Molecules from Physical Gels. *Chem. Soc. Rev.* **2018**, *47*, 1484−1515.
28. Culver, H. R.; Clegg, J. R.; Peppas, N. A. Analyte-Responsive Hydrogels: Intelligent Materials for Biosensing and Drug Delivery. *Acc. Chem. Res.* **2017**, *50*, 170−178.
29. Oliva, N.; Conde, J.; Wang, K.; Artzi, N. Designing Hydrogels for On-Demand Therapy. *Acc. Chem. Res.* **2017**, *50*, 669−679
30. Neguyen, M. K.; Alsberg, E. Bioactive Factor Delivery Strategies from Engineered Polymer Hydrogels for Therapeutic Medicine. Prog. Polym. Sci. **2014**, *39*, 1235−1265.
31. Vermonden, T.; Censi, R.; Hennink, W. E. Hydrogels for Protein Delivery. Chem. Rev. 2012, 112, 2853−2888.
32. Li, Y.; Rodrigues, J.; Tomas, H. Injectable and Biodegradable Hydrogels: Gelation, Biodegradation and Biomedical Applications. *Chem. Soc. Rev.* **2012**, *41*, 2193−2221.
33. Chikar, J. A.; Hendricks, J. L.; Richarson-Burns, S. M.; Raphael, Y.; Pfingst, B. E.; Martin, D. C. The Use of a Dual PEDOT and RGD-Functionalized Alginate Hydrogel Coating to Provide Sustained Drug Delivery and Improved Cochlear Implant Function. *Biomaterials* **2012**, *33*, 1982−1990.

34. Marzocchi, M.; Gualandi, I.; Calienni, M.; Zironi, I.; Scavetta, E.; Castellani, G.; Fabroni, B. Physical and Electrochemical Properties of PEDOT:PSS as a Tool for Controlling Cell Growth. *ACS Appl. Mater. Interfaces* **2015**, *7*, 17993−18003.
35. Stritsky, S.; Markova, A.; Vitecek, J.; Safarikova, E.; Hrabal, M.; Kubac, L.; Kubala, L.; Weiter, M.; Vala, M. Printing Inks of Electroactive Polymer PEDOT:PSS: The Study of Biocompatibility, Stability, and Electrical Properties. *J. Biomed. Mater. Res. A* **2018**, *106*, 1121−1128.
36. Heo, D. N.; Lee, S. J.; Timsina, R.; Qiu, X. Y.; Castro, N. J.; Zhang. L. G. Development of 3D Printable Conductive Hydrogel with Crystallized PEDOT:PSS for Neural Tissue Engineering. *Mat. Sci. Eng. C Mater.* **2019**, *99*, 582−590.
37. Guex, A. G.; Puetzer, J. L.; Armgarth, A.; Littmann, E.; Stavrinidou, E.; Giannelis, E. P.; Malliaras, G. G.; Stevens, M. M. Highly Porous Scaffolds of PEDOT:PSS for Bone Tissue Engineering. *Acta Biomater.* **2017**, *62*, 91−101.
38. Lee, K. Y.; Mooney, D. J. Alginate: Properties and Biomedical Applications. *Prog. Polym. Sci.* **2012**, *37*, 106–26.
39. Reakasame, S.; Boccaccini, A. R. Oxidized Alginate Based Hydrogels for Tissue Engineering Applications: A Review. *Biomacromolecules* **2018**, *19*, 3–21.
40. Szekalska, M.; Puciłowska, A.; Szymańska, E.; Ciosek, P.; Winnicka, K. Alginate: Current Use and Future Perspectives in Pharmaceutical and Biomedical Applications. *Int. J. Polym. Sci.* **2016,** *2016*, 1–17.
41. Anand, P.; Kunnumakkara, A. B.; Newman, R. A.; Aggarwal, B. B. Bioavailability of Curcumin: Problems and Promises. *Mol. Pharm.* **2007**, *4*: 807–818.
42. Mahady, G. B.; Pendland, S. L.; Yun, G.; Lu, Z. Z. Turmeric (Curcuma longa) and Curcumin Inhibit the Growth of Helicobacter Pylori, a Group 1 Carcinogen. *Anticancer Res*. **2002**, *22*, 4179–4181.
43. Reddy, R. C.; Vatsala, P. G.; Keshamouni, V. G.; Padmanaban, G.; Rangarajan, P. N. Curcumin for Malaria Therapy. *Biochem. Biophys. Res. Commun.* **2005**, *326*, 472–474.
44. Venkatesan N.; Punithavathi, D.; Arumugam, V. Curcumin Prevents Adriamycin Nephrotoxicity in Rats. *Br. J. Pharmacol.* **2000**, *129*, 231–234.
45. Arun, N.; Nalini, N. Efficacy of Turmeric on Blood Sugar and Polyol Pathway in Diabetic Albino Rats. *Plant. Foods Hum. Nutr*. **2002**, *57*, 41–52.

46. Pérez-Madrigal, M. M.; Torras, J.; Casanovas, J.; Häring, M.; Alemán, C.; Díaz Díaz, D. Paradigm Shift for Preparing Versatile M2+-Free Gels from Unmodified Sodium Alginate. *Biomacromolecules* **2017**, *18*, 2967−2979.
47. Plazinski,W.; Drach,M. Calcium-_-l-Guluronate Complexes: Ca^{2+} *Binding Modes from DFT-MD Simulations. J. Phys. Chem. B* **2013**, *117*, 12105–12112.
48. Yang, C.; Tibbitt, M. W.; Basta, L.; Anseth, K. S. Mechanical Memory and Dosing Influence Stem Cell Fate. *Nat. Mater.* **2014**, *13*, 645–652.
49. Ma, Y; Lin, M.; Huang, G.; Li, Y.; Wang, S.; Bai, G.; Lu, T. J.; Xu, F. 3D Spatiotemporal Mechanical Microenvironment: A Hydrogel-Based Platform for Guiding Stem Cell Fate. *Adv. Mater.* **2018**, *30*, 1–27.
50. Guimarães, C. F.; Gasperini, L.; Marques, A. P.; Reis, R. L. The Stiffness of Living Tissues and Its Implications for Tissue Engineering. *Nat. Rev. Mater.* **2020**, **5**,351–370 (2020).
51. Pailler-Mattei, C.; Bec, S.; Zahouani, H. In Vivo Measurements of the Elastic Mechanical Properties of Human Skin by Indentation Tests. *Med. Eng. Phys.* **2008**, *30*, 599–606.
52. Rho, J. Y.; Ashman, R. B.; Turner, C. H. Young's Modulus of Trabecular and Cortical Bone Material: Ultrasonic and Microtensile Measurements. *J. Biomech.* **1993**, *26*, 111–119.
53. Li, X.; Wei, B. Facile Synthesis and Super Capacitive Behavior of SWNT/MnO_2 Hybrid Films. Nano *Energy* **2012**, *1*, 479–487.
54. Masek, A.; Chrzescijanska, E.; Zaborski, M. Characteristics of Curcumin Using Cyclic Voltammetry, UV–Vis, Fluorescence and Thermogravimetric Analysis. *Electrochim. Acta* **2013**, *107*, 441–447.
55. Bajpai, M.; Shukla, P.; Bajpai, S. K. Enhancement in the Stability of Alginate Gels Prepared with Mixed Solution of Divalent Ions Using a Diffusion Through Dialysis Tube (DTDT) Approach. *J. Macromol. Sci., Part A* **2017**, *54*, 301–310.
56. Matricardi, P.; di Meo, C.; Coviello, T.; Alhaique, F. Recent Advances and Perspectives on coated Alginate Microspheres for Modified Drug Delivery. *Expert Opin. Drug Del*. **2008**, *5*, 417–425.
57. Abasalizadeh, F.; Moghaddam, S. V.; Alizadeh, E.; Akbari, E.; Kashani, E.; Fazljou, S.; Torbati, M.; Akbarzadeh, A. Alginate-Based Hydrogels as Drug Delivery Vehicles in Cancer Treatment and Their Applications in Wound Dressing and 3D Bioprinting. *J. Biol. Eng.* **2020**, *14*, 8.

58. Priyadarsini, K. I. Photophysics Photochemistry and Photobiology of Curcumin. Studies from Organic Solutions Bio-mimetics and Living Cells. *J. Photochem. Photobiol. C* **2009**, *10*, 81–95.
59. Obara, S.; Yamauchi, T.; Tsubokawa, N. Evaluation of the Stimulus Response of Hydroxyapatite/ Calcium Alginate Composite gels. *Polym. J.* **2010**, *42*, 161–166.
60. Shi, X.; Zheng, Y.; Wang, C.; Yue, L.; Qiao, K.; Wang, G.; Wang, L.; Quan, H. Dual Stimulus Responsive Drug Release Under the Interaction of pH Value and Pulsatile Electric Field for a Bacterial Cellulose/Sodium Alginate/Multi-Walled Carbon Nanotube Hybrid Hydrogel. *RSC Adv.* **2015**, *5*, 41820–41829.
61. Shi, X., Zheng, Y., Wang, G., Lin, Q.; Fan, J. Ph- and Electro-Response Characteristics of Bacterial Cellulose Nanofiber/Sodium Alginate Hybrid Hydrogels for Dual Controlled Drug Delivery. *RSC Adv.* **2014**, *4*, 47056–47065.
62. Abd El-Ghaffar, M. A.; Hashem, M. S.; El-Awady, M. K.; Rabie, A. M. Ph-Sensitive Sodium Alginate Hydrogels for Riboflavin Controlled Release. *Carbohydr. Polym.* **2012**, *89*, 667–675.
63. Lima, D. S.; Tenório-Neto, E. T.; Lima-Tenório, M. K.; Guiherme, M. R.; Scariot, D. B.; Nakamura, C. V.; Muniz, E. C.; Rubira, A. F. pH-Responsive Alginate-Based Hydrogels for Protein Delivery. *J. Mol. Liq.* **2018**, *262*, 29–36.
64. Ben Messaoud, G.; Sánchez-González, L.; Probst, L.; Jeandel, C.; Arab-Tehrany, E.; Desobry, S. Physico-Chemical Properties of Alginate/Shellac Aqueous-Core Capsules: Influence of Membrane Architecture on Riboflavin Release. *Carbohydr. Polym.* **2016**, *144*, 428–437.
65. Nayak, A. K.; Pal, D. Development of pH-Sensitive Tamarind Seed Polysaccharide-Alginate Composite Beads for Controlled Diclofenac Sodium Delivery Using Response Surface Methodology. *Int. J. Biol. Macromol.* **2011**, *49*, 784–793.

4. Conclusions

1. A new UPEA-h has been synthesized and characterized by photo-crosslinking UPEA chains bearing phenylalanine, butenediol and fumarate as building blocks.
2. The morphology of UPEA-h is appropriated for its utilization as SE in ESCs while the biocompatibility and biodegradability confers applicability in the biomedical field.
3. ESCs prepared using PEDOT as electrode material and UPEA-h as SE exhibit excellent performance: the SC obtained by CV and GCD extends from 100 to 49 F/g and 179 to 114 F/g, respectively, depending on the scan rate and the current density; high cyclic stability and Coulombic efficiency; low self-discharging tendency; and small leakage current.
4. Molecular simulations of doped UPEA-h hydrogels have shown that the diffusion coefficients of Cl– and, especially, of Na+ increase linearly with the size of the pore. This effect is also influenced by the hydration degree since the amount of Na+···UPEA-Phe interactions is inversely proportional to the hydration degree.
5. Simulation results have been used to design doped UPEA-Phe hydrogels with higher pore size. For this purpose, the exposure to UV radiation has been reduced from 8 h to 4 h.
6. By taking advantage of the reduction of the pore size and structure, the ion migration improves considerably. More specifically, the SC determined by CV increases 54% in average, while the SC obtained by GCD increases 14%. Also, the leakage current decreases one order of magnitude with increasing pore size.
7. The electrochemical parameters achieved by ESCs prepared using UPEA-h as electrolyte are outstanding not only with respect to liquid electrolytes,

but also with respect to other biodegradable and biocompatible doped hydrogels based on polypeptides and polysaccharides, when identical electrodes and experimental conditions are compared.

8. The polyesteramide hydrogel shows low electrical resistance, high capacitance and good interfacial contact with the electrode, thus meeting the electrical requirements of solid-like electrolytes for supercapacitors.
9. In general, doped polyesteramide hydrogel, which displays a homogeneous distribution of micro- and nanopores, presents better properties as a solid-like electrolyte than doped biohydrogels derived from polysaccharides and polypeptides with pseudo-honey-comb and compact heterogeneous structures.
10. The performance as electrodes for electrochemical supercapacitors of self-standing multilayered films made of alternated nanometric layers of nanofeatured PLA and electrochemically polymerized PEDOT, has been evaluated. For this purpose, both 4- and 5-layered films, which differ in the chemical nature of the external layer, which is PEDOT and nanoperforated PLA, respectively, have been prepared and characterized.
11. Electrochemical assays show that the voltammetric charge and the stability of 4-layered films is significantly higher than that of 5-layered ones. Indeed, the AC is 69% and 33% higher for the former than for the latter as determined by CV and GCD, respectively. Moreover, 4-layered films exhibit a self-stabilizing behavior with increasing number of cycles that is not detected in 5-layered films.
12. 4-Layered (2PLA/2PEDOT) electrodes exhibited the best performance in terms of current leakage and the self-discharging, opening new perspectives for the technological application of self-standing multilayered films in the biomedical and textile fields.

13. The influence of the oxidation state on the pores size has been studied in PEDOT films using theoretical calculations and experimental measures.
14. The quasi-monoclicic structure obtained for b-dedoped PEDOT evolves towards a triclinic system after doping with ClO4– anions. Although the s-models of PEDOT keep structures similar to those b-models, the volume of s-doped is 12.5% higher than that of s-dedoped.
15. np-Dedoped models maintain structural similarities with s-models, the incorporation of ClO4– dopant anions causing important changes in the supercell dimensions. The size of the pore created as a structural defect in the np-dedoped model increases by 15.1% in the np-doped one (~21 % after a cell parameter correction).
16. The structural tendencies predicted by theoretical calculations have been confirmed by experimental observation. Thus, the averaged pore size of PEDOT/poxd was measured to be 25.2 % larger than that of PEDOT/pred.
17. PEDOT/Alginate/PHMeDOT (PAP) hydrogels have been by a simple water-based two-step process to get flexible and self-healable electrodes for supercapacitor applications. PEDOT/Alginate hydrogels present a porous and open interconnected structure but exhibit very low capacitance values. Therefore, PHMeDOT was incorporated into the previous hydrogels by in situ electropolymerization using the same electrolyte solution.
18. PAP hydrogels exhibited high capacitance values (35 mF/cm2) and fast self-healing capacity without losing their electrochemical performance. The combination of flexibility and self-healing together with the inherent properties of biocompatibility and eco-friendliness of the PEDOT and alginate polymers makes PAP hydrogels promising for applications in wearable and implantable electronics.

19. A flexible pressure sensor with fast response and good spatial resolution of the pressure distribution was developed using a PEDOT-based hydrogel. This hydrogel, which was prepared using a 1:3 PEDOT:PSS/AA mixture, showed mechanical integrity, ease of handling and dimensional stability. Furthermore, the internal structure of the 1:3 hydrogel was appropriated to provide electrical percolation response and self-healing behavior.
20. The spatial resolution of the pressure sensor was proved using a 2×2 array as stretchable touch-pressure sensor that was able to control the illumination of LEDs. The sensor was reusable because of the reversibility of noncovalent Ca2+-based crosslinks.
21. PEDOT/Alg hydrogel capable of drug delivery was fabricated by gelling a 1: 1 mixture of PEDOT:PSS and alginic acid in a CaCl2 solution. CUR was loaded in situ during the gelling process by dissolving the drug with the alginic acid before mixing with PEDOT:PSS.

CUR is slowly released from PEDOT/Alg(CUR) hydrogel by simple diffusion (i.e. around 3% only). However, the release of drug from PEDOT/Alg(CUR)-h is enhanced in response to electrical stimulation by applying a negative voltage (i.e. around 25% in 2 h), which affects intermolecular interactions